

Dynamic behaviour of the Sognefjord bridge

Analysis and review of the world's largest floating bridge design

Eduard Hendriksen

July 9, 2018

Dynamic behaviour of the Sognefjord bridge
July 9, 2018

A master thesis report submitted to the Faculty of Civil Engineering and Geosciences

By

Eduard Hendriksen, 4063171
e.c.hendriksen@gmail.com

Graduation committee:

Prof. Dr. A. Metrikine	<i>Committee chair</i>	Delft University of Technology, Faculty of Civil Engineering and Geosciences, Engineering Structures Department, Section Dynamics of Structures
Dr. Ir. A. Tsouvalas		Delft University of Technology, Faculty of Civil Engineering and Geosciences, Hydraulic Engineering Department, Section Offshore Engineering
Dr. Ir. M. A. N. Hendriks		Delft University of Technology, Faculty of Civil Engineering and Geosciences, Materials- Mechanics- Management & Design Department, Section Applied Mechanics
Ir. F. Amico		IV-Consult B.V.

Preface

I would like to take the opportunity to thank a few people. The first of which is Fabio Amico, my supervisor within IV-Consult and a steady source of sensible advice and jokes. You made my time with the company more enjoyable and really helped me with setting the scope of this thesis. The next person I would like to thank is Apostolos Tsouvalas; for listening to my iteration schemes and especially for the extensive flow of information that inevitably followed. The following thank you is for Prof. Metrikine; for taking the time to see me during cancelled and moving meetings, seeing solutions where they were hidden and asking tough questions. Max Hendriks deserves a thank you, too; for being there when asked and the flexibility to reduce the impact of my poor planning. My girlfriend deserves a thank you and an apology, both of them for you remaining calm and supportive while my mind was adrift in a Norwegian fjord. I hope you haven't suffered too much from my graduation syndrome. A thank you is also in order for taking the time to read this piece of work. To my parents I direct a big thank you, for supporting me throughout my time at this university and even more so in the time before I started here. Your comments on this work improved it greatly and I suspect that you may be the only people happier than I am about my graduation. My brother also deserves a thank you; your offer to read this thesis is part of the reason for its length.

After almost seven and half months of research I present this study as end result and finish my master's degree in Structural Engineering. I hope it is as enjoyable for the reader as it was for me.

Abstract

A project is under way to replace the ferry crossings in Norway's highway E39 with fixed links, such as highway bridges or tunnels. This thesis research is on the crossing located at the Sognefjord, the widest and deepest of the straight crossings in the E39 highway. Previous thesis projects at IV-Consult have yielded a design for a floating bridge supported on twenty-two pontoons. The bridge is moored using a sub-sea cable system. The bridge design reaches a height of 70 m at its 465 m wide mid-span and is dimensioned on the basis of static calculations of the structural elements.

The goal of this thesis research is to calculate the dynamic response of the bridge system to environmental loads and to determine if the current bridge design is sufficient in relation to this response. To reach this goal, several models have been developed for the structural elements that compose the bridge; the continuous bridge deck girder, the pylons supporting this girder, the floating pontoons supporting these and the sub-sea cable mooring system fixing the structure in place. First a structural model for the bridge structure is developed with special attention being placed on the sub-sea mooring system. For these cables an internal design is made and a calculation method is developed to model and determine the internal hysteretic damping in the cables due to inter-wire friction. Second, a mechanical model describing the linear dynamic response of the pontoons for small rotations has been developed. The pontoons themselves are modelled as rigid bodies. Third, the bridge deck girder is modelled as an equivalent Euler-Bernoulli beam. Finally, a load model is developed for the wave and current loads at the bridge location. Diffraction theory is used to calculate wave loads on the large pontoons and the current loading is identified and modelled according to prevailing design codes. Six critical wave load cases are formulated.

Models of the bridge structure are built using the SACS and Scia Engineer software packages. A non-linear solver is written in Python to implement the cable model for static calculation, utilizing Scia Engineer's non-linear solver. Verification calculations of SACS software results are performed.

The steady state response of the bridge structure is calculated using SACS software for the six critical wave load cases formulated. In conjunction with this analysis, the cable damping is calculated according to the cable model. The bridge deck motion and cable fatigue damage are evaluated and are found to be well within design limits, leading to the conclusion that wave loading will not lead to critical failure in the bridge design.

An analysis of vortex induced vibrations of the bridge system caused by cross-flow loading of the bridge pontoons is performed. The analysis is performed using Ansys Fluent in conjunction with the SACS Dynamic Response module to model the fluid-structure coupling. A large sensitivity to vortex induced vibrations is found for the bridge system, several potential solutions to this problem are presented and recommendations are made for further research into this phenomenon for the bridge design.

A verification calculation of the Fluent-SACS model introduced in this thesis is performed using a coupled wake oscillator model. The verification is based on only the cross-flow motion of a single pontoon in the bridge system and yields comparable results in terms of load and displacement amplitudes for both models.

Contents

1	Introduction	6
1.1	Project description	6
1.2	State of the project	7
1.3	Project overview	9
2	Design information	10
2.1	Local environment	10
2.2	Design requirements	11
2.2.1	Design lifetime	11
2.2.2	Ship clearance requirements	11
2.2.3	Traffic requirements	11
2.2.4	Servicability limits	11
2.3	Environmental data	12
2.3.1	Wind	12
2.3.2	Waves	13
2.3.3	Currents	14
2.3.4	Tidal effects	15
2.3.5	Temperature	15
2.3.6	Marine growth	15
2.4	Current design	15
3	Research question and scope	17
3.1	Scope	17
4	Structural model	18
4.1	Girders	18
4.2	Pylons	19
4.3	Pontoons	19
4.4	Cable system	20
4.4.1	Cross section	20
4.4.2	Cable stiffness	20
4.4.3	Cable damping	21
4.4.4	Lay angle	22
4.4.5	Cable design	23
4.5	Numerical model	24
5	Load model	25
5.1	Wave loading	25
5.2	Current loading	26
5.3	Load cases	27
6	Dynamic analyses	28
6.1	Steady state response calculation	28
6.1.1	Goals	28
6.1.2	Methodology	28
6.1.2.1	Cable damping	28
6.1.2.2	Steady state motion bridge deck	30

6.1.2.3	Cable fatigue	30
6.1.3	Defining results and conclusions	30
6.1.3.1	Cable damping	30
6.1.3.2	Steady state motion bridge deck	31
6.1.3.3	Cable fatigue	32
6.2	Vortex induced vibrations	33
6.2.1	Goal	33
6.2.2	Methodology	33
6.2.3	Defining results and conclusions	34
7	Conclusions and recommendations	41
7.1	Research questions	41
7.1.1	Main question	41
7.1.2	Sub questions	41
7.2	Further recommendations	43
	Appendices	48
A	Current bridge design	51
A.1	Overview	51
A.2	Bridge girder	52
A.3	Pylons	53
A.4	Pontoons	55
A.4.1	Buoyancy and restoring moment	58
A.5	Cable System	65
B	Loads	66
B.1	Wave loading	66
B.2	Current loading	78
B.3	Traffic loading	79
B.4	Wind loading	79
B.4.1	Wind load on bridge girder	81
B.4.2	Wind load on bridge pylons and pontoons	92
B.5	Load cases	96
C	Cable design	97
C.1	Cross section type	97
C.2	Cross section design	98
C.3	Elasticity module	100
C.4	Bending stiffness	101
C.5	Conclusion	109
D	Cable damping	111
D.1	Hysteretic damping	111
D.2	Modelling cable damping	111
D.2.1	Overview	112
D.2.2	Equilibrium	113
D.2.3	Mode shapes	113
D.2.4	Undamped steady state solution	113
D.2.5	Pre-set displacement	113
D.2.6	Integration	114
D.2.7	Equivalent systems	116
D.2.8	Structural damping factor	117
D.3	Results	117
D.4	Conclusions	118

E	Waves steady state displacement	119
E.1	Theory	119
E.2	Set-up	121
E.3	Results	122
E.4	Conclusions	130
F	Nonlinear analysis	131
F.1	Nonlinear analysis	131
F.2	Linear analysis	136
G	SACS modelling	137
G.1	Cables	137
G.1.1	Verification of the SACS cable model	137
G.1.1.1	Static analysis	138
G.1.1.2	Eigenfrequency analysis	139
G.2	Pontoons	141
G.2.1	Static analysis	142
G.2.2	Eigenfrequency analysis	142
G.3	Pylons	145
G.4	Girders	145
G.5	Bridge model	145
G.5.1	Dimensions and axis system	145
G.5.2	Component coordinates	146
G.5.3	Connections	147
G.5.4	Full model	148
G.5.4.1	SACS Input file	148
G.5.4.2	Graphical presentation	150
G.6	Waves and current	151
G.6.1	Modelling	151
G.6.2	Verification	152
H	SACS dynamic analysis	156
H.1	Eigenfrequency analysis	156
H.1.1	Stiffness matrix reduction	157
H.1.2	Mass matrix generation	157
H.1.3	Result calculation	157
H.2	Steady state analysis	157
H.3	Time history analysis	158
I	Pontoon decoupling	159
I.1	Methodology	160
I.2	Results	162
I.3	Significance	162
J	Vortex induced vibrations	163
J.1	Theory	163
J.1.1	Ansys Fluent turbulent flow modelling	164
J.1.1.1	Constitutive equations	164
J.1.1.2	Boundary conditions	167
J.1.1.3	Moving boundaries in Fluent	167
J.2	Methodology	170
J.3	Research and results	170
J.3.1	Shared parameters	170
J.3.2	'Semi-2D' analysis	175
J.3.2.1	Set-up	175
J.3.2.2	Results	175
J.3.2.3	Conclusions	176
J.3.3	Wake effect influence	177
J.3.3.1	Set-up	177

J.3.3.2	Results	178
J.3.3.3	Conclusions	181
J.3.4	3D analysis	181
J.3.4.1	Set-up	181
J.3.4.2	Results	184
J.3.4.3	Conclusions	185
J.3.5	3D draught comparison	186
J.3.5.1	Set-up	186
J.3.5.2	Results	187
J.3.5.3	Conclusions	188
J.3.6	Coupled analysis using decoupling springs	188
J.3.6.1	Set-up	189
J.3.6.2	Results	189
J.3.6.3	Conclusions	190
J.3.7	Coupled analysis	190
J.3.7.1	Set-up	190
J.3.7.2	Results	192
J.3.7.3	Displacement table	197
J.3.7.4	Conclusions	199
J.3.8	Model verification	201
J.3.8.1	Coupled wake oscillator model	201
J.3.8.2	Set-up	202
J.3.8.3	Results and conclusions	204
J.3.9	Possible solutions	207
J.3.9.1	Helical strakes	207
J.3.9.2	Changing the pontoon shape	208
J.3.9.3	Dynamic absorber (tuned mass damper)	212
J.4	Conclusions	212
K	Cable fatigue	213
K.1	Theory	213
K.2	Set-up	215
K.3	Results	216
K.4	Conclusions	219

Chapter 1

Introduction

Norway has a rough coastline with deep fjords cutting into the mainland. Although this creates a beautiful natural environment, the possibilities for road-based transport are greatly reduced. This has led the Norwegian Statens Vegvesen, the Public Roads Administration, to commission a series of studies into the feasibility of spanning the fjords in the coastal highway with fixed crossings, such as bridges or tunnels.

1.1 Project description

The coastal highway, the E39, is 1100 km long and currently includes eight ferry crossings. It connects an area producing 50 % of Norwegian traditional export value. Eliminating all ferry crossings reduces travel time for the complete stretch of highway by about 9 h, which will positively influence trade and industry for the entire region [Ell12]. The entire route is depicted in Figure 1.1. As one can imagine, the crossings not yet replaced with fixed links are the widest and deepest in the coastal highway and of these crossings, the Sognefjord is the most challenging. This is due to its combination of a very large water depth of 1200 m, compared to 450-500 m in other fjords, its width of almost 4 km and the 2-300 m of muddy soil deposits that make up the fjord bed. It is clear that this fjord crossing is a benchmark project.



Figure 1.1: Overview of the crossings in the E39 highway [Ell12].

This thesis project is part of an ongoing feasibility study on the possibility of spanning the Sognefjord with a floating bridge design within IV-Consult. Although it is the fourth study performed on this subject, it is the first to research the dynamic behaviour of this floating bridge design.

1.2 State of the project

The feasibility study on a floating bridge design to cross the Sognefjord at IV-consult has been investigated in three design iterations prior to this study. To define a starting point for this thesis, a description of the goals and accomplishments of these projects and an introduction into the current design of the Sognefjord bridge are given in this section.

The first study on the Sognefjord crossing conducted at IV-Consult has been carried out by Hermans (2014). It investigated the local environmental conditions, provided an overview of factors influencing design choices and investigated the prevailing construction codes for this project. The end result of the study was a preliminary bridge design, from which some elements have endured to the present design. The elements that have endured to the present design include the circular, spar-like, shape and spacing for the pontoons and the recognizable S-shaped curve the bridge deck follows. All design choices are based on static calculations of the loads. This study makes a clear distinction between different construction elements in the bridge design, which is continued in all studies since, including this one. These elements are the bridge deck girder, the pylons supporting this girder, the floating pontoons to which they are attached and the sub-sea cable mooring system fixing the structure in place. A first estimation of their dimensions and influence on the total model is made. A visual representation of the resulting design is depicted in Figure 1.2. This design has unfortunately been proven to be infeasible [Her14].

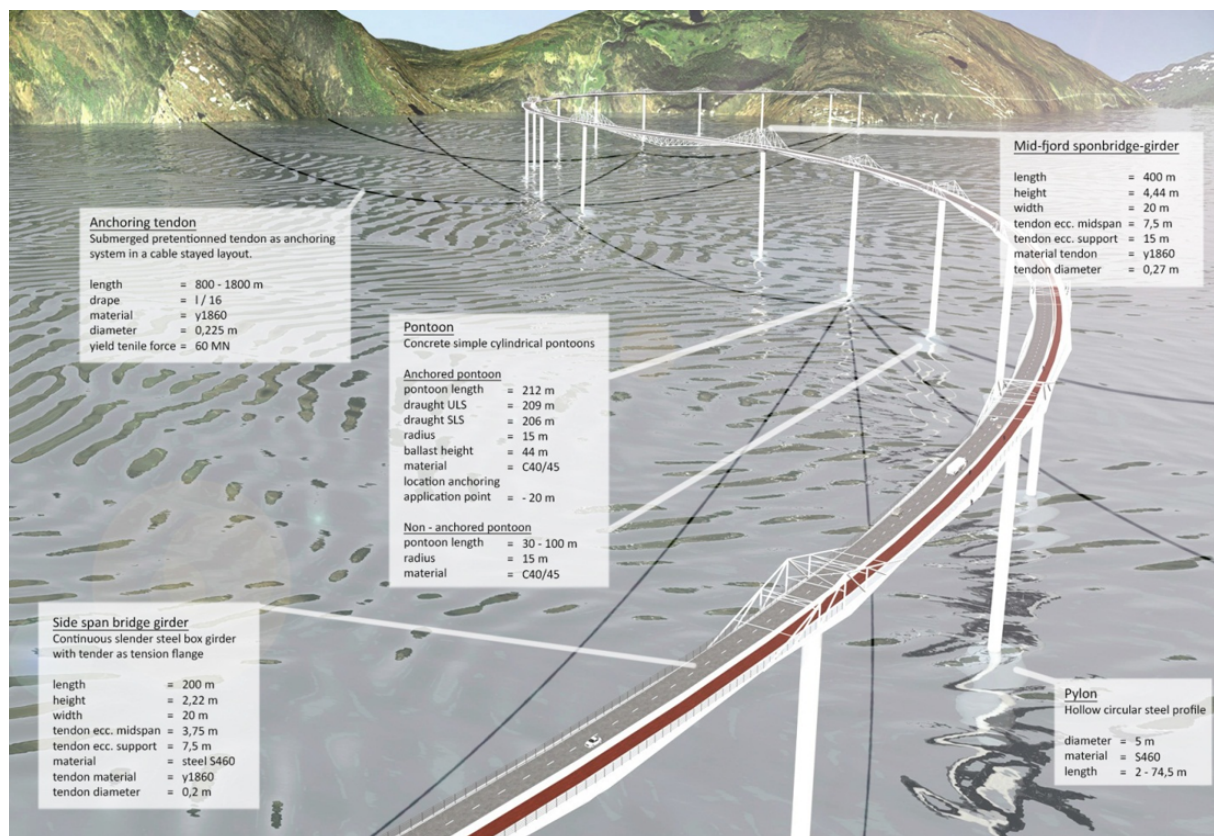


Figure 1.2: First bridge design for the Sognefjord crossing created at IV-Consult [Her14].

The second study has been performed by Yip (2015). It took the recommendations and methods introduced in the first study and focussed on the cable system mooring the pontoons. Special care was given to the above-water portion of the bridge design, which is redesigned to a more aesthetically pleasing form in conjunction with an architectural design firm. Additional effort was placed on the construction methods for the sub-sea part of the bridge design and design choices were made based on the construction method. This design was based on static calculations. The final design of this study only includes the circular shape for the spar-like pontoons and the original pontoon spacing previously introduced. The bridge girder, pylons and cable system are redesigned, resulting in the bridge design depicted in Figures 1.3 and 1.4.



Figure 1.3: Second bridge design for the Sognefjord crossing created at IV-Consult [Yip15].

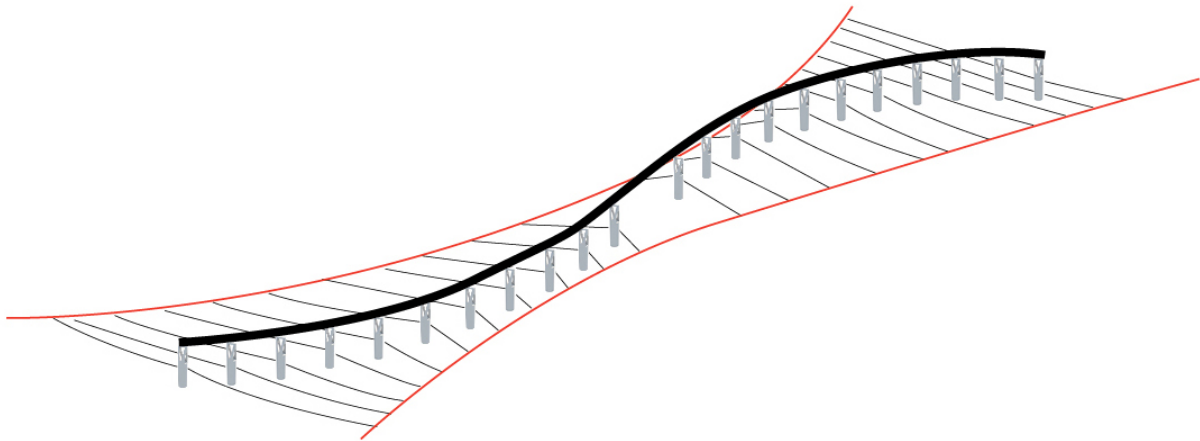


Figure 1.4: Sub-sea portion of the second bridge design for the Sognefjord crossing created at IV-Consult [Yip15].

The third study has finished recently by Cijssouw (2018). It primarily focussed on the optimization of the bridge girder in an effort to reduce its weight and in an effort to reduce the maintenance requirement of the bridge structure. A complete redesign of the bridge girders is put forward, including a new set-up of the connections between the girder and the supporting pylons. Design recommendations are made for the internal design of the pontoons, based on a ship impact- and subsequent damage analysis. The cable system, pontoons and pylons are left unchanged. The design calculations performed in this thesis were static calculations, too.

To conclude: The dynamic behaviour of the Sognefjord bridge design has not been investigated yet. This is a void this thesis aims to fill.

1.3 Project overview

This section outlines the steps taken in this thesis to provide an answer to the research question and its sub questions. A visual overview is shown in Figure 1.5.

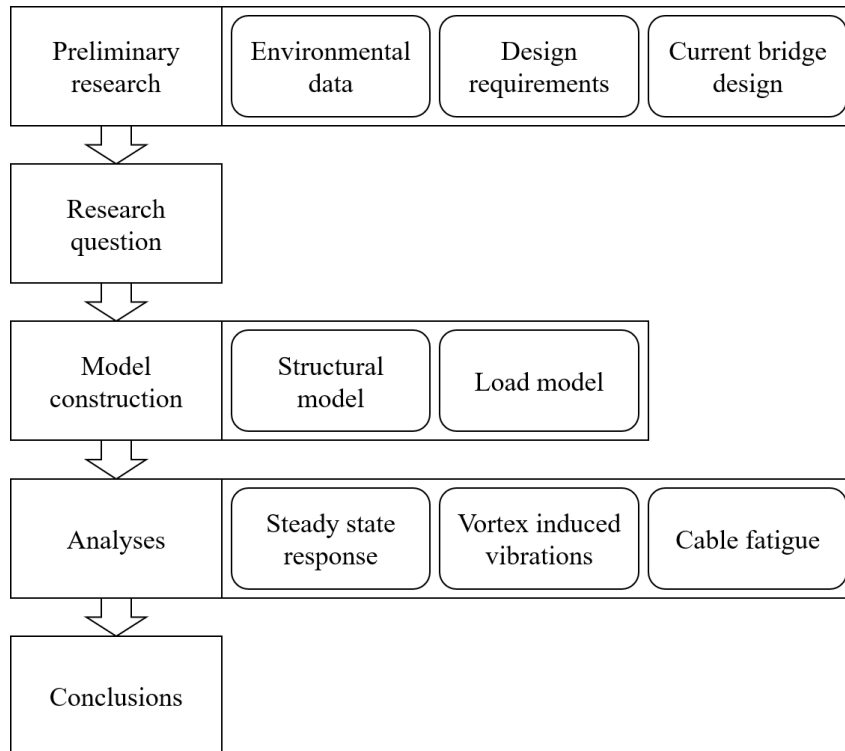


Figure 1.5: Research overview.

The preliminary research phase includes the investigation of the local environment, design requirements put forward to the design and the current bridge design. The investigation into the local environment is meant to yield information on the load-inducing environmental factors, such as wind, waves and current. The design requirements give a framework in which the bridge design must fit when put into motion by these environmental loads. Finally, the current bridge design provides the basis for this feasibility study. The information obtained in the preliminary research allows the formulation of an informed research question, to cover the investigation performed in this thesis. To analyse and calculate the dynamic behaviour of the bridge system and provide an answer to the research question, a model of the bridge design and the environment at the bridge location must be constructed. In the model construction phase models are designed for both the structure and the environmental loading. During the different analyses performed in this study the structural and load models meet and results are calculated. Finally, the calculated results are discussed and recommendations are made for improvements and further research.

Chapter 2

Design information

This chapter includes design information for the Sognefjord Bridge.

2.1 Local environment

The floating bridge is to span the Sognefjorden in Norway. It connects highway E39 and the towns of Lavik and Oppdal on opposite sides of the fjord. The bridge location is about 25 km from the sea. The two towns and highway are currently connected by a ferry crossing. Figure 2.1 displays the location of Sognefjord and the bridge location in the Sognefjord.

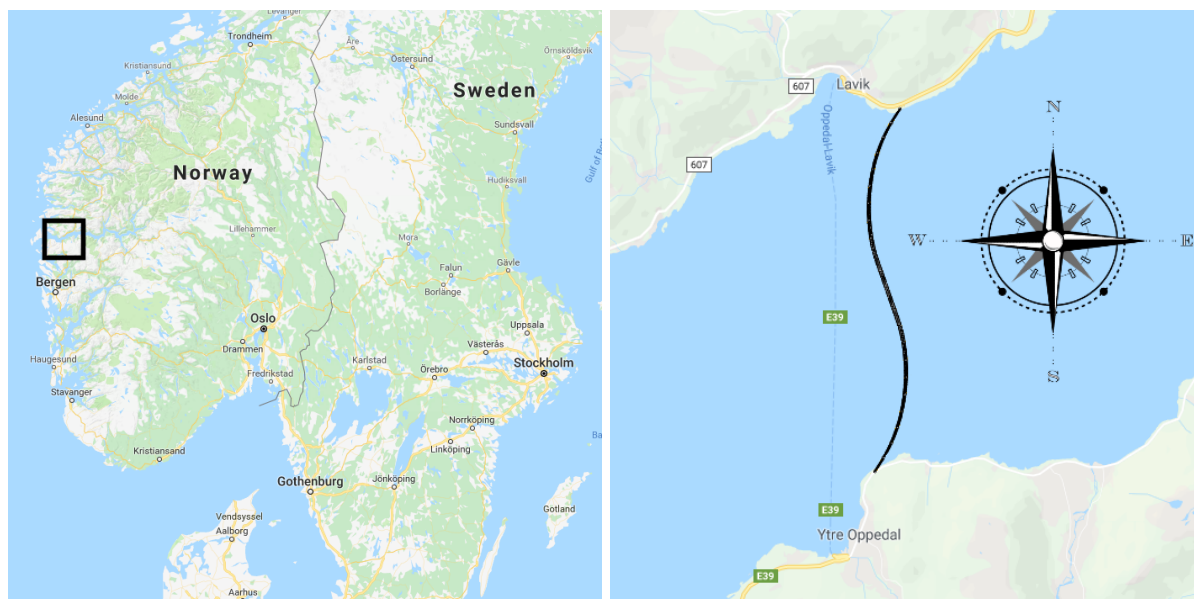


Figure 2.1: Location of the bridge (Google Maps).

The fjord is about 3700 m wide and the deepest point is 1250 m below mean sea level. As can be seen in Figure 2.2, the fjord slope is relatively mild near-shore, but increases in steepness to about 30° to 50° . The soil at the bottom of the fjord consists of 200-300 m of soft clay and the steep sides are rocky.

Because support structures would either need to support the bridge from the depth of the fjord plus the depth of the soft clay layer or be built to a significant depth on the fjord's steep sides, the need for a crossing design that does not rely on bottom founded support structures is clear.

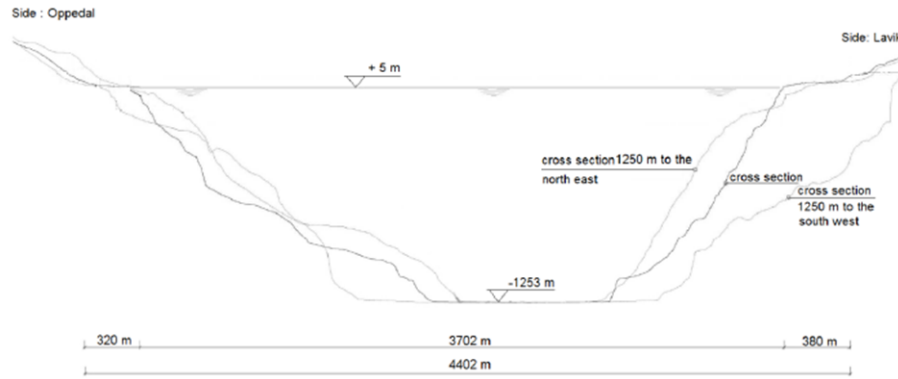


Figure 2.2: Cross section of the fjord at the bridge location [Fje12].

2.2 Design requirements

In this section the design requirements specified by the Norwegian Statens Vegvesen are presented.

2.2.1 Design lifetime

The design lifetime for the bridge is to be at minimum 100 years. It is required that no significant maintenance jobs, such as the replacement of complete structural elements, are needed within this time period. Therefore, the design lifetime of each structural element is set at 100 years.

2.2.2 Ship clearance requirements

The ship clearance requirements are specified in Table 2.1.

Ship clearance at the middle fairway	
Width passage	400 m
Height passage	70 m
Draught	20 m
Ship clearance outside the middle fairway	
Height passage	70 m
Draught	20 m

Table 2.1: Ship clearance requirements.

2.2.3 Traffic requirements

The traffic requirements are specified in Table 2.2.

Average daily traffic	12000 vehicles
Design speed	80 km h ⁻¹
Road class	H7, double lane in each direction
Road width	20 m (excluding pedestrian and cycling lanes)
Clearance height	4.5 m

Table 2.2: Traffic requirements.

2.2.4 Servicability limits

There are requirements posed for the largest rotations, deformations and accelerations allowed in the bridge deck. These requirements are specified in Table 2.3.

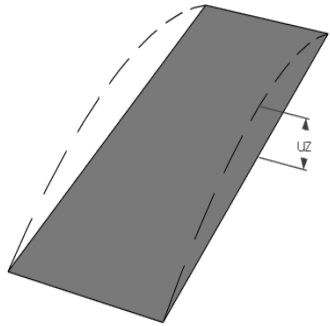
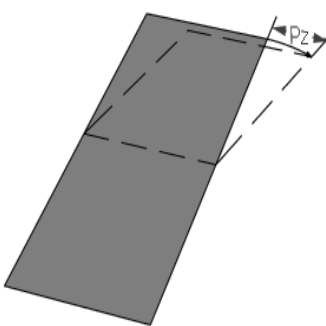
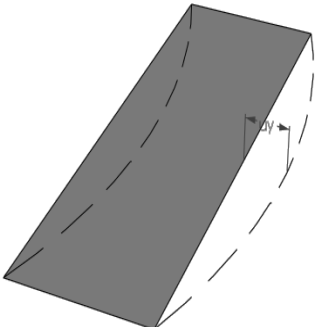
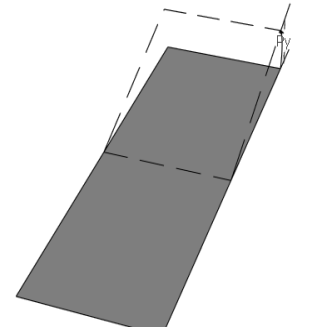
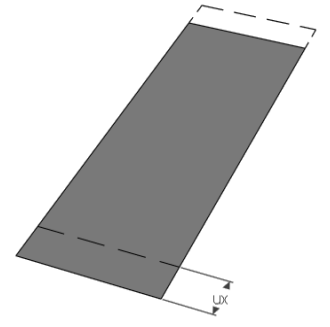
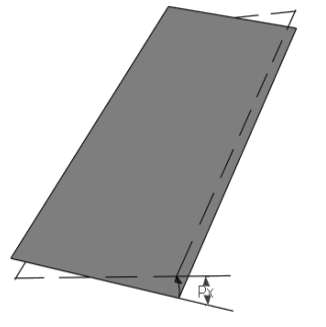
Vertical deformation		Lateral plane rotation	
			
$u_z \leq L/200 \text{ m}$	$a_z \leq 0.7 \text{ m s}^{-2}$	$\phi_z \leq 0.060 \text{ rad}$	$\zeta_z \leq 0.050 \text{ rad s}^{-2}$
Lateral deformation		Cross section plane rotation	
			
$u_y \leq L/200 \text{ m}$	$a_y \leq 0.5 \text{ m s}^{-2}$	$\phi_y \leq 0.044 \text{ rad}$	$\zeta_y \leq 0.107 \text{ rad s}^{-2}$
Longitudinal deformation		Vertical section plane rotation	
			
Not considered	$a_x \leq 0.5 \text{ m s}^{-2}$	$\phi_x \leq 0.060 \text{ rad}$	$\zeta_y \leq 0.070 \text{ rad s}^{-2}$

Table 2.3: Bridge deck deformation and acceleration limits.

2.3 Environmental data

The environmental loads at the bridge location are based upon research performed by SINTEF [al11] and Reinertsen [Fje12] for the Norwegian Statens Vegvesen.

2.3.1 Wind

The wind loading is based on wind speeds with a return period of 100 years. The 10-minute and hourly mean wind velocity at a reference height of 10 m are shown in Table 2.4.

The direction of the extreme mean wind velocity ranges from 180° to 240° relative to the North. The extreme wind velocity at a height of 10 m (U_{10}) versus the direction relative to the North are displayed in Figure 2.3 [al11].

The wind profile is extrapolated using the logarithmic function specified in DNV-RP-C205 [DNV10], since it coincides with the profile extrapolated using the function specified in EN 1991-1-4:2005+A1

Averaging period	Wind velocity [m s^{-1}]
10 min	35
1 h	32

Table 2.4: Mean wind velocity at a reference height of 10 m at the bridge location.

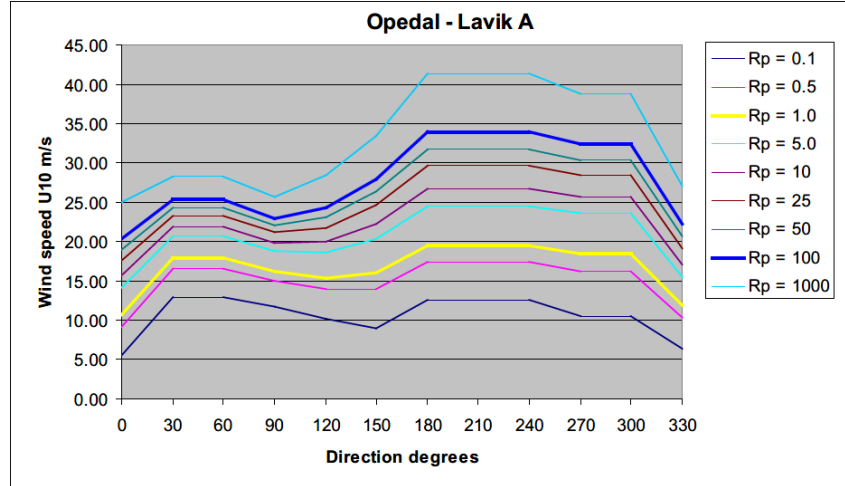


Figure 2.3: Extreme wind velocity at a height of 10 m per reference period vs. direction at the bridge location [al11].

[ECS10]. This wind profile is shown in Figure 2.4.

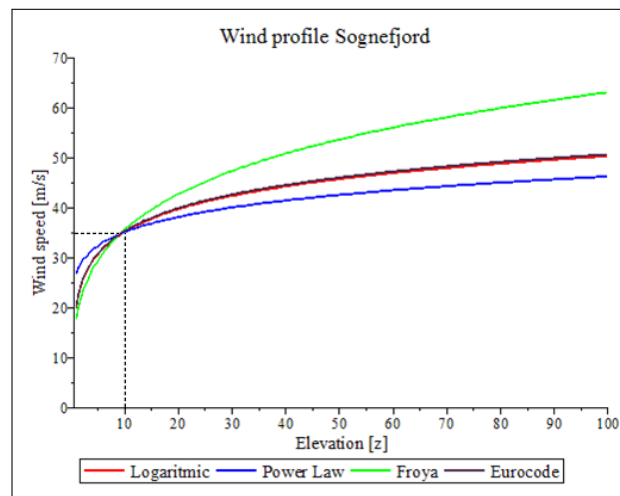


Figure 2.4: Wind profiles extrapolated from the mean wind velocity at a height of 10 m at the bridge location.

DNV-RP-C205 specifies methods to be used to model spatial and temporal variations in wind speeds from wind measurements to be used in modelling wind loads [DNV10].

2.3.2 Waves

Wind waves have been measured at three locations in the fjord crossing: the north shore, the middle of the fjord and at the south shore. The extreme values of the wind wave height, relative to the North, obtained from these measurements are displayed in Figure 2.5, while the different wave characteristics are presented in Table 2.5.

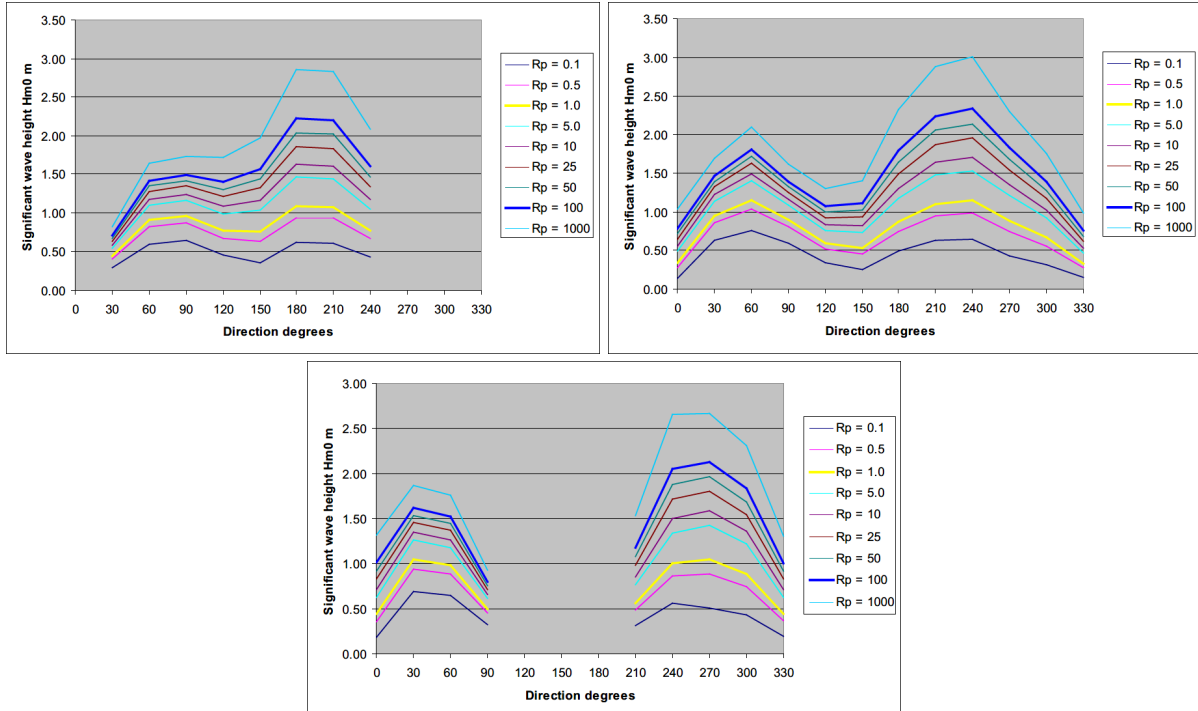


Figure 2.5: Extreme values wind wave height per reference period vs. direction at respectively, the north shore, mid-fjord and the south shore [al11].

Parameter		Wind waves		
		North side	Mid-fjord	South side
Significant wave height	H_s [m]	2.22	2.34	2.13
Spectral top period	T_p [s]	4.6	4.8	4.8
Direction	[$^\circ$]	180	240	270
Maximum single wave height	H_{max} [m]	4.55	4.79	4.36
Wave length	λ [m]	33	36	36

Table 2.5: Wave characteristics at the bridge location.

2.3.3 Currents

The current flow direction is assumed to be along the axis of the fjord, which corresponds to an angle of 60° relative to the North. The current flow is assumed to be uniform for the fjord. The current velocities at the bridge location are presented in Table 2.6.

Mid-fjord			
Water depth [m]	Outwards velocity [m s^{-1}]	Mean velocity [m s^{-1}]	Inwards velocity [m s^{-1}]
0 - 10	-1.06	-0.53	1.27
30	-0.55	0.26	0.48
75	-0.44	0.26	0.39

Table 2.6: Characteristic current velocity at the bridge location.

2.3.4 Tidal effects

The tidal motion is expected to change the water level uniformly over the full fjord's width at the bridge location. Since no tidal information is available on at the bridge location, tidal measurements at Ålesund are taken as representative for the Sognefjord, too. The tidal characteristics at the bridge location are presented in Table 2.7.

Lowest astronomical tide (LAT)		0.00 m
Mean sea level (MSL)		+1.20 m
Highest astronomical tide (HAT)		+2.39 m
Return period [y]	Highest sea level [m]	Lowest sea level [m]
1	+2.61	-0.10
10	+2.88	-0.27
20	+2.97	-0.32
100	+3.05	-0.38

Table 2.7: Tidal characteristics at the bridge location.

2.3.5 Temperature

The design air and water temperature at the bridge location are displayed in Table 2.8.

	T_{min} [°C]	T_{max} [°C]
Air temperature at water surface	-20	32
Water temperature at water surface	4	20

Table 2.8: Temperatures at the bridge location.

2.3.6 Marine growth

According to DNV-RP-C205, marine growth will develop as shown in Table 2.9.

Depth [m]	Thickness [mm]	Dry mass [kg m^{-2}]	Submerged weight [N m^{-2}]
+2 to -40	80	106	255
Below -40	40	53	128

Table 2.9: Marine growth on the submerged parts of the bridge.

2.4 Current design

An overview of the current bridge design analysed in this thesis is presented in this section. For a more detailed treatment of the bridge design reference is made to appendix A. Figure 2.6 shows the main bridge dimensions and gives an insight into the spacing of the different structural elements. The bridge deck rests on twenty-two pylons, which in turn are supported by twenty-two floating pontoons. Figure 2.7 provides the numbering used for the pylons and pontoons in this thesis. The pontoons are subsequently secured in place by forty-four lateral cables, which connect to two main cables spanning the width of the fjord. The main cables are connected to shore at water level.

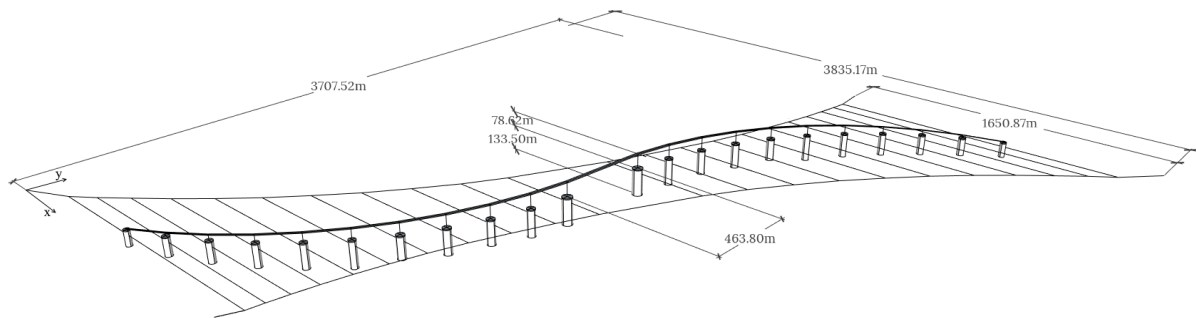


Figure 2.6: An overview of the bridge model including dimensions.

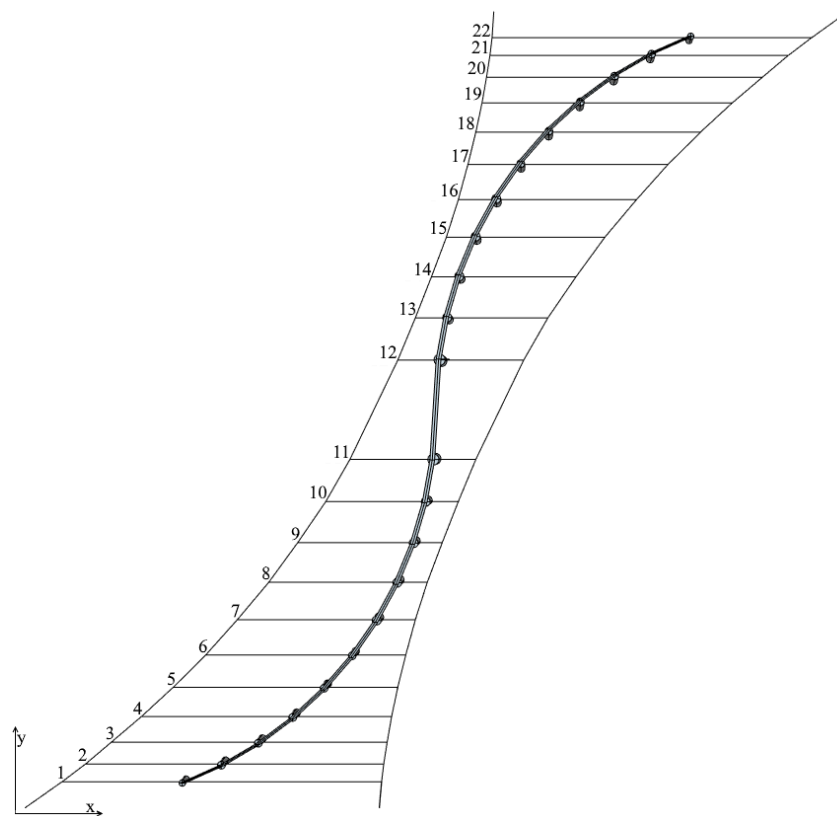


Figure 2.7: Pylon and pontoon numbering.

Chapter 3

Research question and scope

The research question this thesis aims to answer is the following;

”What is the dynamic response of the current bridge structure design, as a result of wave and current loading?”

To which the following sub questions are posed:

- i ”Considering the dynamic response of the system, will the bridge deck motion or cable fatigue damage exceed design limits?”
- ii ”Which design measures, specifically focusing on the pontoon and cable system design, can be taken to improve the system’s dynamic behaviour?”

3.1 Scope

For this thesis the following scope has been chosen;

- i It has been chosen to focus on wave and current induced loading, excluding wind loading because this thesis is focussed on the sub-sea portion of the bridge design. A preliminary calculation of wind loading, included in section B.4, indicates that the wind loading will be a big factor in the bridge design.
- ii Traffic loads are not a part of this thesis. The current bridge design has been dimensioned taking into account static traffic loading according to the prevailing design codes. It is not expected that moving traffic loads will induce a large dynamic response.
- iii The rigid body motions of the pontoons are investigated. To model the pontoons as rigid bodies, they are modelled as numerically ”infinitely” stiff beam elements.
- iv Vortex induced vibration analysis only considers the inward current, since the velocity of the inward current is higher and thus this is expected to be the critical current direction.
- v Vortex induced vibration analysis is limited to the loading applied by the current to the pontoons, excluding the loading on the cables, because it is expected that the pontoon loading will be most critical to the bridge design.

Chapter 4

Structural model

This chapter describes the structural model used to model the bridge. The model has been built using two FEM software packages; SACS and Scia engineer.

4.1 Girders

The continuously connected girders spanning the 200 m wide side- and 465 m wide main span are modelled as prismatic Euler-Bernoulli beam elements with properties obtained from a previous study [Cij18]. This representation is chosen because this model is adequate to model the response of these relatively slender elements in the low frequency domain. An important aspect is the connections between the girders and the pylons. The support conditions are such that the girders are free to rotate in their longitudinal direction, or around their local y -axis, in their normal direction, or around their local x -axis, and are fixed for rotations around the vertical axis, or around their local z -axis. Figure 4.1 displays the local girder axes and indicates the allowed girder support rotations.

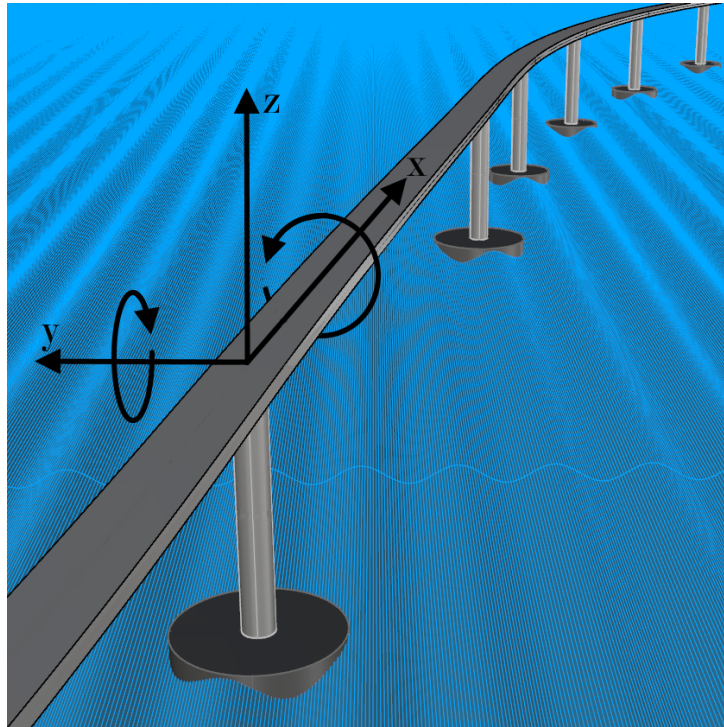


Figure 4.1: Girder local axes and allowed girder support rotations.

For precise listing of all girder properties and dimensions, reference is made to section A.2. The girders are modelled in SACS according to the method described in section G.4.

4.2 Pylons

The pylons are still in the preliminary design phase. The aesthetically pleasing model shown in Figure 4.2 is not dimensioned based on calculations. Therefore, the pylon sections are modelled as steel tubular cylinders in this thesis and a recommendation is made for future research to fully dimension the pylons. The pylons are also modelled as Euler-Bernoulli beam elements and they are connected rigidly to the pontoons. The rotations allowed by their connections to the bridge girders are depicted in Figure 4.1. For the precise structural properties adopted for the pylons and the way they are modelled in SACS, reference is made to sections A.3 and G.3.



Figure 4.2: Pylon design [Yip15].

4.3 pontoons

The pontoons are modelled in this thesis as rigid bodies, by using extremely stiff Euler-Bernoulli tubular elements, since their internal dynamic behaviour take place at much higher frequencies. An example of a pontoons cross section and the related mechanical model adopted for small rotations is displayed in Figures 4.3 and 4.4. The mechanical model utilizes rotational springs, attached to the pontoon center of gravity, with a spring stiffness based on a linearisation of the pontoon restoring moment for small rotations. A translational spring is also used; attached to the center of buoyancy of the pontoon, it models buoyant force as the vertical position of the pontoon changes. The precise pontoon properties and locations are described in full in section A.4. For the full derivation and calculation of the pontoon mechanical model, reference is made to section A.4.1.

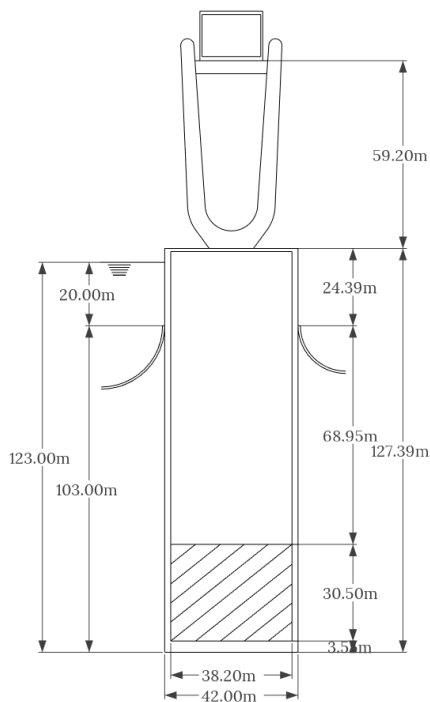


Figure 4.3: Example pontoon cross section.

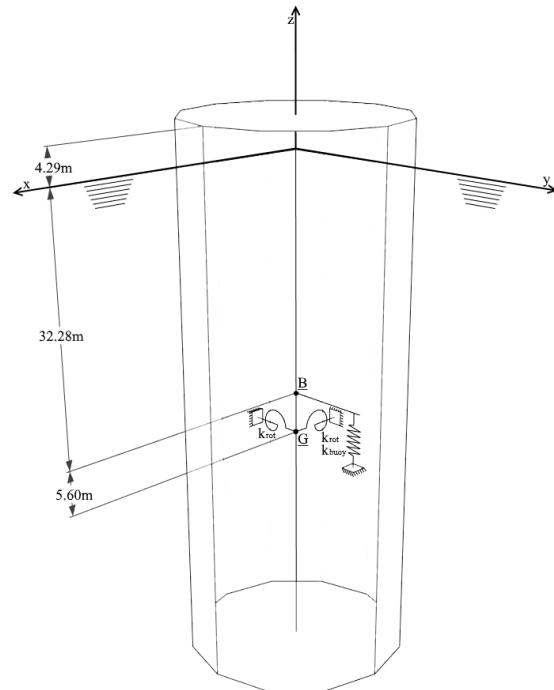


Figure 4.4: Mechanical model for the pontoons.

4.4 Cable system

The current cable system design is the result of research focused on its layout. Therefore, the current model for the main and lateral cables is a prismatic circular beam with a steel area large enough to withstand the static loads imposed on the bridge structure. A detailed description of the current cable system properties is given in section A.5.

For the purpose of this thesis, this preliminary design is not sufficient. For the analysis of the dynamic behaviour of the bridge system as a whole, the internal damping properties of the cables have an influence that can not be neglected. These properties are not a part of the present cable model. Therefore, a detailed design for both the main- and lateral cables is made and the method for the calculation of the internal cable damping is presented. The entire design process for the main and lateral cable designs is described in depth in appendix C. This section outlines the resulting design, the choices motivating this design and the adopted model for the cables.

4.4.1 Cross section

For the cross section layout type the open spiral rope with plastic sheathing has been chosen. The open spiral rope has been chosen due the general better fatigue- and design lifetime of open spiral ropes. The plastic sheathing is added to ensure a proper corrosion protection. The layout of the cables' strands and rope cross section have been calculated using a Python script, developed for this purpose, which optimizes the steel area used in the rope design against the steel area required based on the previous cable design. The resulting strand and rope cross section layout for the lateral cables is shown in Figure 4.5.

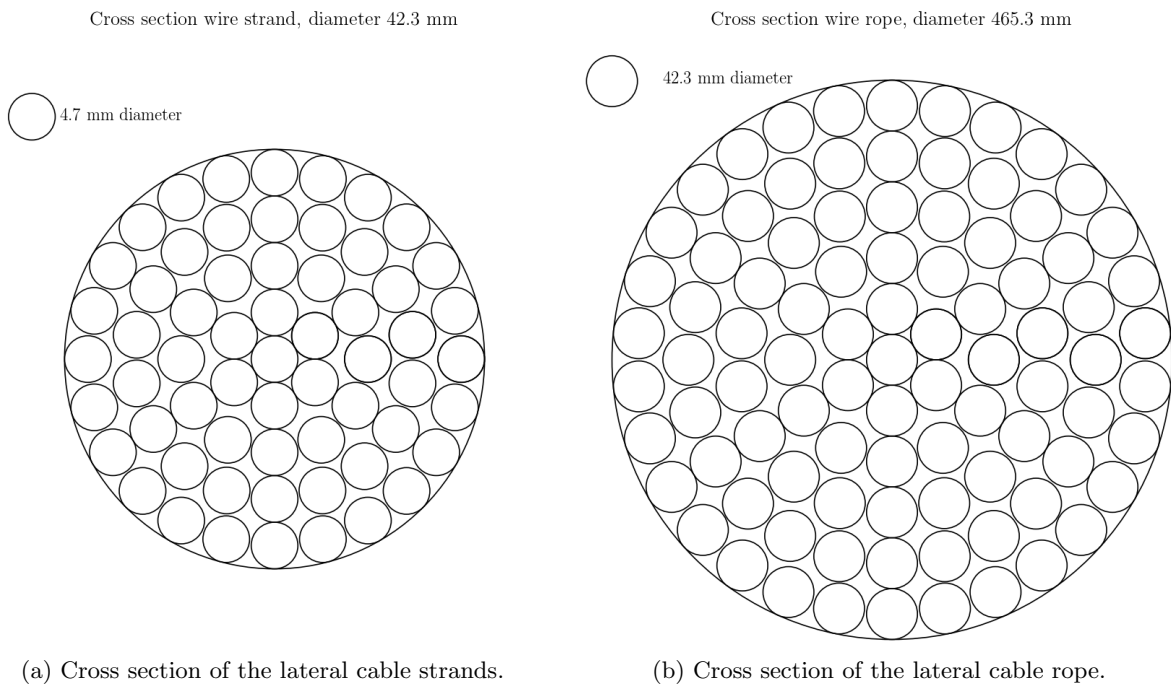


Figure 4.5: Cross sections of the lateral cable strands and total rope

4.4.2 Cable stiffness

In the mechanical model adopted for the cables in this thesis, the bending stiffness of the cables is modelled to be variable as a function of the cable curvature. This is because when the cable is stretched, all wires in the cable 'stick' together and they act as a solid material. As the cables bend, the wires slip past each other and the bending stiffness decreases, until all wires act individually. A visual representation of this phenomenon is shown in Figure 4.6, in which a cable is first shown completely straight and then bent over an angle of 2α . The situation in which the cable is completely straight is the situation where the cable bending stiffness is maximal and at approximately the same level as a solid steel circular cross section of the same diameter. The situation where all wires have slipped is the situation where the cable bending stiffness is minimal. No wire stress transfer is taking place and the bending stiffness of individual wires

is summed [Pap97]. An example of the variable bending stiffness versus curvature for the main cable at different strand lay angles, tensioned by an axial load of 530 MN is depicted in Figure 4.7. For the calculation of the variable cable bending stiffness reference is made to section C.4.

This method has been developed for much smaller scale cables than the ones used for the lateral- and main cables in this thesis. Therefore it is recommended that the results of these calculations are verified with measurements.

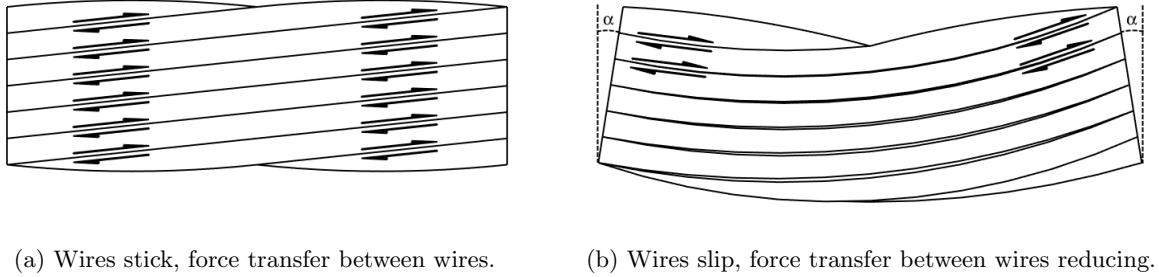


Figure 4.6: Unbent cable segment (left) and cable segment bent over an angle 2α

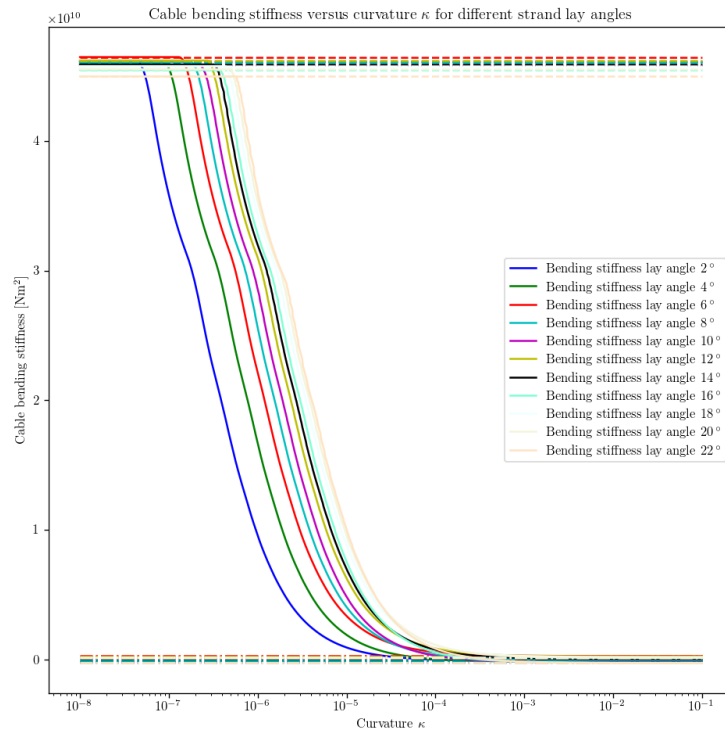


Figure 4.7: Variable bending stiffness versus curvature for the main cable with different strand lay angles, tensioned at 530 MN.

4.4.3 Cable damping

Hysteretic damping is a new subject in this thesis. It is the damping of cable motions due to inter-wire friction and pure material damping in the wires themselves. Friction between the strands and wires in the cables are the main contribution to this phenomenon and only a negligible contribution is made by damping in the wire material itself [Spa13].

Hysteretic damping is caused by the dissipation of energy due to inter-wire friction as the cables deform under loading. This can be visualised using a force-displacement hysteresis curve. An example of a wire rope hysteresis curve is depicted in Figure 4.8. In this Figure, the load sequence is depicted with numbers 1 – 4. In this load sequence, the load path during unloading is different than during loading, creating the shaded area in the Figure. The area contained in this load path is the energy extracted from the motion by the internal hysteretic damping during this load cycle.

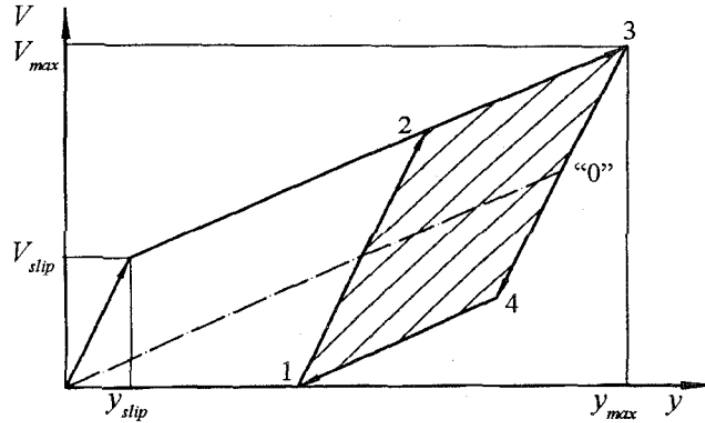


Figure 4.8: An example force-deflection hysteresis curve [Pap97].

A method to model the effect of this hysteretic damping due to inter-wire friction is to model the cable with a variable bending stiffness, dependant upon the curvature and tension of the cable [Pap97]. For each analysis step, the bending stiffness is updated, reflecting the state of the cable. As the internal cable damping is modelled to be dependant upon its changing curvature, it can only be calculated during dynamic analysis. Therefore the full treatment of the cable damping is performed in conjunction with a dynamic analysis at a later point in this thesis.

4.4.4 Lay angle

The lay angle of wires in a steel wire rope is the angle at which the wires in the layers surrounding the cable core are twisted around this core. Figure 4.9 displays an example of the lay angle of wires in a steel wire rope. The lay angle of the wires in the cable strands, and of the strands themselves, are a critical design choice as they influence all mechanical properties of the cable.

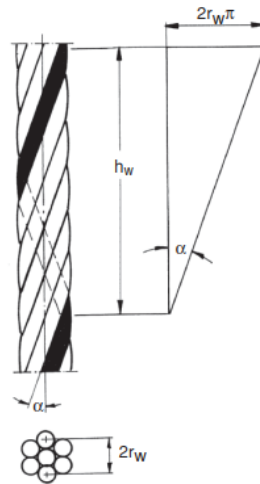


Figure 4.9: Example steel wire rope with wire lay angle indicated by α [Fey07].

The desired properties of the rope should lead to a long fatigue life, low extension under tensile stress, good environmental protection and high hysteretic damping. Both a long fatigue life and low tensile extension are achieved by choosing low lay angles for these axially loaded stay cables. The environmental protection should mainly be achieved by the plastic sheathing added to the cross section. However, by giving both the strands and the wires in the strands a small lay angle, the containment of the rope lubricating agent in all rope parts will be improved, improving the fatigue life of the rope [Fey07].

Hysteretic damping, as described in section 4.4.3, has a positive contribution to the cable system's dynamic behaviour, reducing vibration amplitudes and reducing the time needed for the system to return to equilibrium after excitation. Previous studies showed that when loaded under its own weight, most

cable segment curvatures fall between 10^{-3} to 10^{-5} . To maximize hysteretic damping, a lay angle should be chosen that maximizes the stiffness change in this curvature range. As the damping is achieved mainly through inter-wire friction, this will most likely be detrimental to the fatigue life of the cable.

4.4.5 Cable design

Taking the considerations outlined in the previous sections into account and balancing the different advantages and disadvantages has led to the main and lateral cable properties displayed in Table 4.1. The lay angle of the wires in the cable strands is kept at a low 2° , as this has a large influence on the elasticity modulus of the cable as a whole and thus the cable extension under axial loading. The cable strands' lay angle is slightly higher at 6° as this allows a better 'lock in' of lubricating agent in the ropes. At 6° the change in bending stiffness in the regarded curvature range is already quite significant, while further increases in lay angle yield smaller increases in the variability of the bending stiffness. It is expected that these values for the lay angles provide a good balance between fatigue life and damping. The bending stiffness versus curvature for the main and lateral cables is shown in Figures 4.10 and 4.11.

	Material	Type	Wire lay angle	Wire diameter [mm]	Wire layers	Strand lay angle	Strand diameter [mm]	Strand layers
Main cable	Y1860	Spiral rope	2°	3.0	20	6°	123	6
Lateral cable	Y1860	Spiral rope	2°	4.7	4	6°	42.3	5

Table 4.1: Cable wire rope properties.

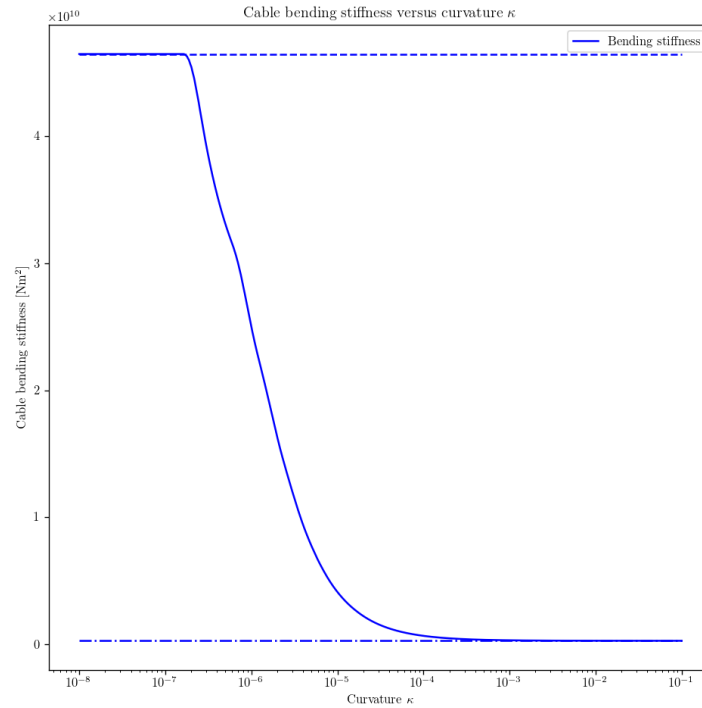


Figure 4.10: Main cable bending stiffness versus curvature.

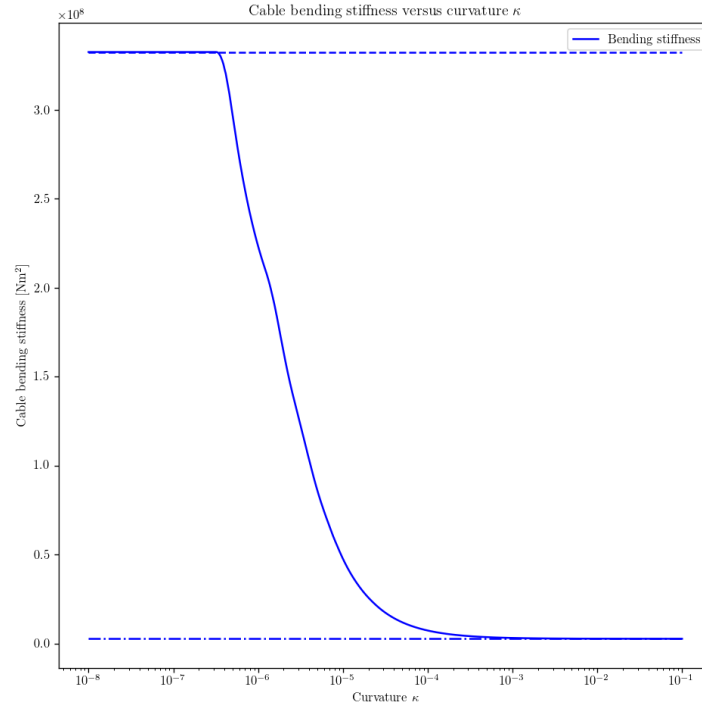


Figure 4.11: Lateral cable bending stiffness versus curvature.

4.5 Numerical model

All the structural elements handled in this chapter have been modelled in the SACS software package. A complete description of the model created in SACS, as well as verification calculations for portions of the model, is given in appendix G.

Chapter 5

Load model

This chapter outlines the environmental loads taken into account for this thesis; the wave and current loading.

5.1 Wave loading

For a full description and calculation of the wave loads on the pontoons, reference is made to section B.1. This section provides an outline of the calculation method and the results. Table 5.1 contains the critical wave conditions at the bridge location.

Parameter		Wind waves		
		North side	Mid-fjord	South side
Significant wave height	H_s [m]	2.22	2.34	2.13
Spectral top period	T_p [s]	4.6	4.8	4.8
Direction	[°]	180	240	270
Maximum single wave height	H_{max} [m]	4.55	4.79	4.36
Wave length	λ [m]	33	36	36

Table 5.1: Wave characteristics at the bridge location.

The common method of calculating wave loads on structures is to apply the Morison equation [Zhu93]. This method of calculation is valid for structures whose presence in the wave field does not create a significant disturbance of the wave field. Objects of the size of the pontoons in the bridge model, however, may significantly alter the wave field. This depends upon the structures' dimensions in relation to the incident wave length. As is described in section B.1, the pontoons are large compared to the wave lengths and therefore the Morison equation is not applicable. Thus, for the pontoons used in the bridge design, the diffraction theory of wave scattering is to be used.

For the calculation of the resulting loads on the pontoons, an analytical equation derived by MacCamy (1954) is used [Mac54]. This analytical equation has been derived for the 'linear' or 'airy' wave theory. It has been concluded that the waves found in the Sognefjord are best described using Stokes 3rd wave theory [Sto47]. Therefore the loads calculated using the MacCamy equation provide a close approximation of the wave loading on the pontoons.

To model the wave loading on the bridge structure, the SACS SeaState module is used. This module allows the user to input the waves according to their characteristics and applicable wave theory. The software then calculates the loading on the structural elements using the Morison equation. Since this approach is not applicable to the bridge design in this thesis a method has been found to apply the loading calculated using the MacCamy expression with the Morison expression. This is done by modifying the C_M value in the Morison expression, or effective inertia value, for each pontoon per different wave case. This method is also applicable in SeaState, as it allows for member properties to be modified per load

condition. The calculated effective inertia values per pontoon, per wave condition are displayed in Table 5.2.

A detailed description of modelling using the SeaState program and a verification of its load calculations is found in section G.6.

Pontoon number	Wind wave direction 180°	Wind wave direction 240°	Wind wave direction 270°
1	0.3312	0.3771	0.3771
2	0.2521	0.2872	0.2872
3	0.2521	0.2872	0.2872
4	0.2521	0.2872	0.2872
5	0.2521	0.2872	0.2872
6	0.2521	0.2872	0.2872
7	0.2	0.228	0.228
8	0.2	0.228	0.228
9	0.2	0.228	0.228
10	0.2	0.228	0.228
11	0.1451	0.1654	0.1654

Table 5.2: Effective inertia values per pontoon per wave condition.

5.2 Current loading

The in- and outgoing current velocities at the bridge location are displayed in Table 5.3. The current direction is shown in Figure 5.1. The resulting profile is calculated using a curve fitting regression tool developed for this purpose with the power law expression specified in the DNV-RP-C205 and is depicted in Figure 5.2.

Inwards - 60°		Outwards - 240°	
Depth	Velocity	Depth	Velocity
10 m	1.27 m s ⁻¹	10 m	1.06 m s ⁻¹
30 m	0.48 m s ⁻¹	30 m	0.55 m s ⁻¹
70 m	0.39 m s ⁻¹	70 m	0.44 m s ⁻¹

Table 5.3: In- and outward current profile.

For analyses involving wave loading, it is sufficient to model the current as a constant flow and add the static load this flow exerts on the structure to the total loading of the structure [DNV10]. This calculation is performed by the SACS module SeaState after the user inputs the current profile and direction. A description of this and a verification of the load calculation is given in section G.6.

For the research into vortex induced vibrations due to the current loading, the inward current is used as this provides the highest flow velocities.

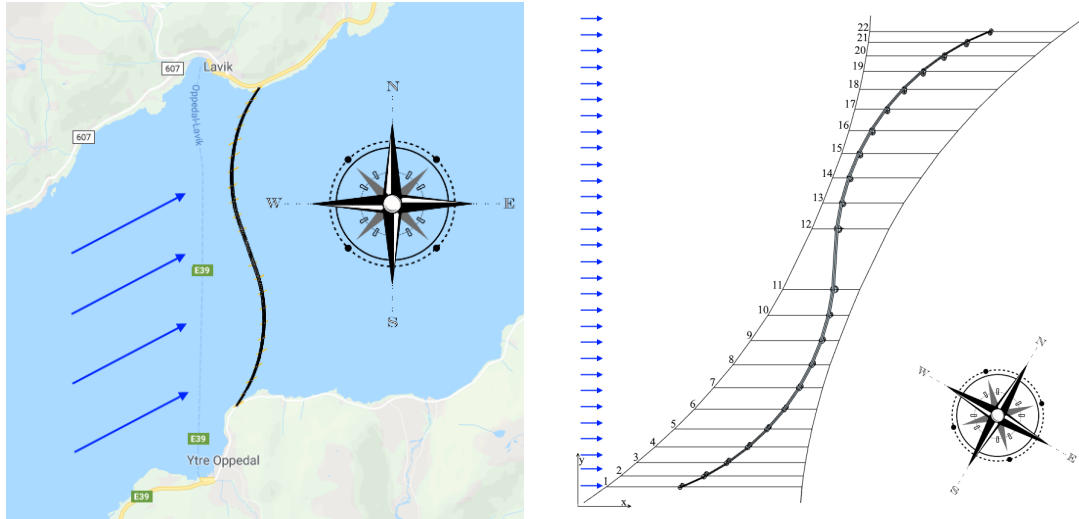


Figure 5.1: Current flow direction in reality (left, Google Maps) and in the bridge model (right).

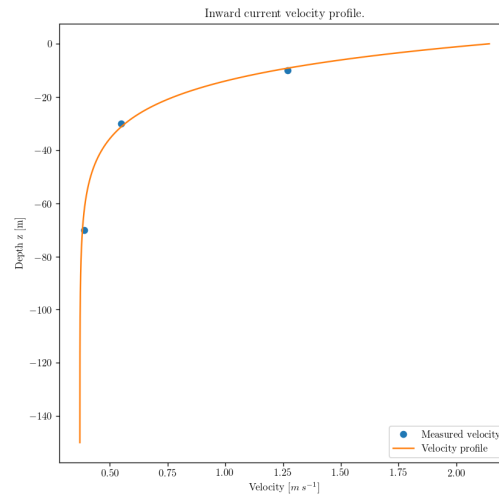


Figure 5.2: Inward current velocity profile.

5.3 Load cases

The load cases used for the different analyses are outlined in this section. For the wave loading, six distinct load cases have been created. Each critical wave direction is coupled to both the in- and outward current. This is displayed in Table 5.4.

Loadcase	Wave direction - height - wavelength	Current direction
1	180° - 4.55 m - 33 m	Inwards
2	180° - 4.55 m - 33 m	Outwards
3	240° - 4.79 m - 36 m	Inwards
4	240° - 4.79 m - 36 m	Outwards
5	270° - 4.36 m - 36 m	Inwards
6	270° - 4.36 m - 36 m	Outwards

Table 5.4: Wave load cases.

Another load case is the inward current, which is used on its own for the research into vortex induced vibrations of the bridge structure, for which reference is made to appendix J.

Chapter 6

Dynamic analyses

This chapter describes the dynamic analyses performed in this study. First, the steady state response analysis is described, then the vortex induced vibrations analysis. For each analysis, the goals, used methodology, defining results and related conclusions are described.

6.1 Steady state response calculation

This section describes the steady state analysis performed in this study. It outlines the goals of the analysis, the methodology, the defining results and the conclusions that can be drawn from these results.

6.1.1 Goals

The goals of this analysis are the following;

Calculate the cable internal structural damping.

Calculate the steady state motion of the bridge system to verify if the bridge deck motion is within serviceability limits.

Calculate the internal loading during the steady state motion to investigate cable fatigue.

6.1.2 Methodology

The methodology to attain the goals of this analysis is described in this section. All steady state analyses are performed for the six critical wave load cases described in section 5.3.

6.1.2.1 Cable damping

The methodology to calculate the internal cable damping is described in this section and displayed in Figure 6.1. For the full description of the cable damping analysis, reference is made to appendix D.

The definition for the structural damping factor used in this thesis is the following; The critical damping ratio per mode of vibration, commonly known as the "modal damping ratio", is fixed at a single value for all modes of vibration. This is a simplification of reality. The procedure to include the cable damping is as follows;

- i An equilibrium situation (in terms of displacement u_0 , cable bending stiffness EI_0 and tension T_0) of the bridge model loaded by its self-weight is obtained through iterative non-linear FEM analysis. An iterative solver is written in Python for this task. It operates in combination with the FEM software Scia Engineer as described in appendix F. Figure 6.2 displays an isometric view of the equilibrium situation calculated using the this solver.
- ii Taking the bridge model in this equilibrium situation, an eigenvalue analysis is performed in order to calculate mode shapes, mode frequencies and mass M and stiffness K_0 matrices using the Dynpac module of the SACS software package. Reference is made to section H.1.

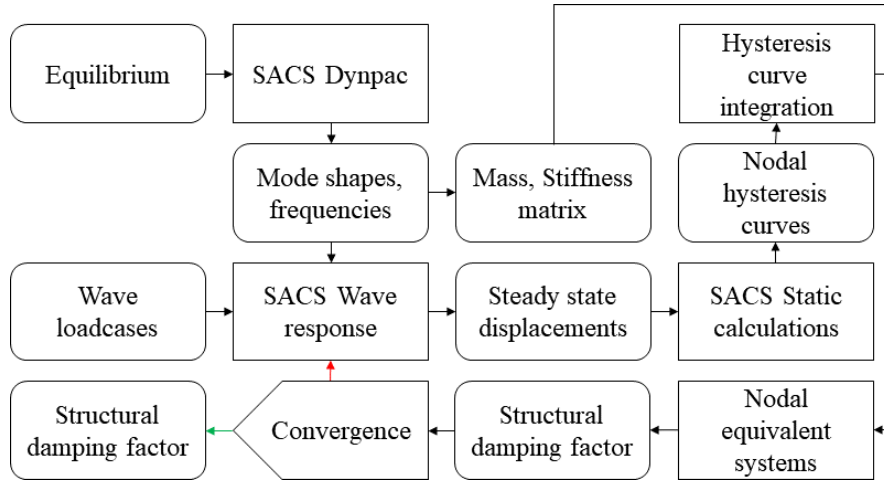


Figure 6.1: Work-flow for the structural damping calculation.

- iii Use the SACS wave response program to pre-calculate the steady state response of the model without damping and with constant cable bending stiffness EI_0 , calculated previously, to the different wave load cases as described in section G.6. Reference is made to appendix E and section H.2.
- iv Create a set of linear analyses in which the model is deformed according to the steady state displacements calculated earlier, time-stepping the model through the displacement to obtain hysteresis curves per node. The cable bending stiffness EI is updated per time step.
- v These hysteresis curves are integrated to calculate the dissipated energy per node during the steady state excitation.
- vi Per node, per degree of freedom, single mass-spring-dashpot systems are used as equivalent systems to mimic the local hysteretic dissipation of energy. The spring stiffness k is determined from the global stiffness matrix K_0 . The viscous damping is to be determined.
- vii Hysteretic damping factors μ are determined per degree of freedom per node by equating the dissipated energy in the hysteretic curves to the dissipated energy in the equivalent system.
- viii An energy consistent structural damping factor for the entire system is calculated from the nodal damping factors.

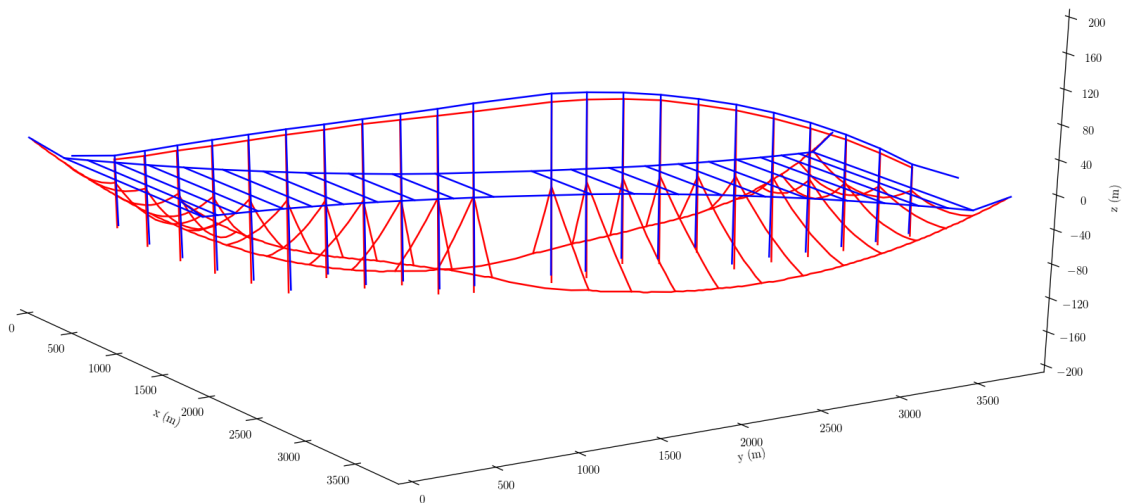


Figure 6.2: Isometric view of the undeformed (blue) and deformed (red) equilibrium bridge structure shape as calculated using the Sciapthon solver.

6.1.2.2 Steady state motion bridge deck

The steady state motion of the bridge deck is calculated using the SACS Wave Response module in combination with the structural damping calculated earlier. From this motion, the maximum displacements, rotations and accelerations are calculated and compared to the given limits. For the full description of this analysis, reference is made to appendix E.

6.1.2.3 Cable fatigue

Cable fatigue is investigated by calculating the internal cable system loads during the steady state motion and calculating fatigue damage to the cable system during the load cycles. By calculating the fatigue damage caused by the critical wave load cases, an indication of the probability of fatigue damage to the cable system due to wave loading being a critical factor for the bridge design can be given. For the full description of this analysis and the theory behind wire rope fatigue, reference is made to appendix K.

6.1.3 Defining results and conclusions

This section provides the defining results and related conclusions of the analyses.

6.1.3.1 Cable damping

The results of the cable damping calculations are presented in Table 6.1. The resulting cable deflection amplitudes are shown for the load cases causing the highest and lowest cable deflection amplitude in Figure 6.3.

Load case	Undamped ζ	Iteration 1 ζ	Iteration 2 ζ	Iteration 3 ζ
1	1.894 %	0.912 %	1.644 %	1.624 %
2	1.850 %	0.878 %	1.768 %	1.776 %
3	7.145 %	5.568 %	5.403 %	
4	6.958 %	5.365 %	5.612 %	
5	2.377 %	2.347 %		
6	2.347 %	2.337 %		

Table 6.1: Structural damping factors per load case.

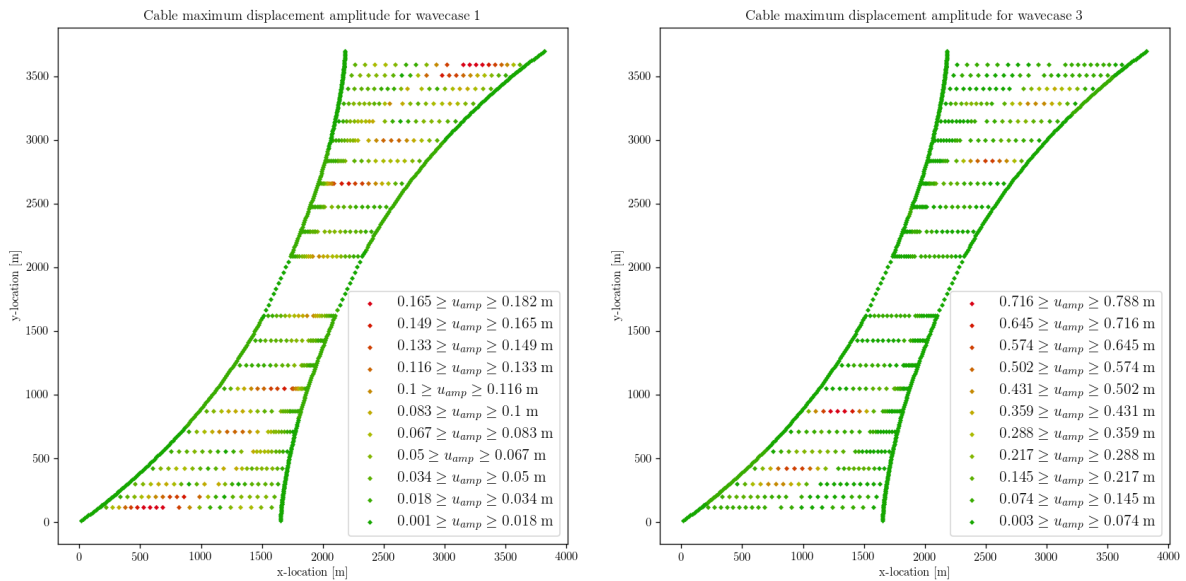


Figure 6.3: Cable node displacement amplitude values for load case 1 and 3.

As can be seen, the structural damping factor is highly dependent upon the wave excitation and almost insensitive to the change in current loading. That the damping factors are the same for the in- and outgoing current cases coupled to the same wave loading provides a simple sanity check for the entire damping calculation, because it is expected that these values match closely. It is clear that when the wave loading remains the same, the damping factor remains mostly the same. As the wave loading changes and excites more modes of vibration of the structure, the structural damping increases. This is expected, since the source of the structural damping is the friction between the strands and wires in the steel cables. If the steel cables move less, there is less friction and the damping is less. This is illustrated by the difference in displacement amplitude visible between the highly damped load case three and the much less damped load case one. The solution is quick to converge, which makes this method quite effective to obtain a constant structural damping factor for all modes of vibration quickly. It is clear that for every loading scenario, a recalculation of the cable structural damping is necessary to obtain the structural damping as applicable for that specific load case.

A point of attention is the fact that the results obtained from this analysis have to be verified and potentially modified after experiments with steel cables whose properties approach the cables used in this design.

6.1.3.2 Steady state motion bridge deck

The results for the two load cases containing the maximal values of displacement, rotation and acceleration are shown in Table 6.4 per measure of deformation. The serviceability design limits are given in Tables 6.2 and 6.3.

Vertical deformation		Lateral plane rotation	
$u_z \leq L/200$ m	$a_z \leq 0.7 \text{ m s}^{-2}$	$\phi_z \leq 0.060 \text{ rad}$	$\zeta_z \leq 0.050 \text{ rad s}^{-2}$
Lateral deformation		Cross section plane rotation	
$u_y \leq L/200$ m	$a_y \leq 0.5 \text{ m s}^{-2}$	$\phi_y \leq 0.044 \text{ rad}$	$\zeta_y \leq 0.107 \text{ rad s}^{-2}$
Longitudinal deformation		Vertical section plane rotation	
Not considered	$a_x \leq 0.5 \text{ m s}^{-2}$	Not considered	

Table 6.2: Bridge deck deformation serviceability limits.

Deck number	Length [m]	Maximum displacement [m]
1 to 11 and 13 to 23	200	1
12	465	2.325

Table 6.3: Maximum allowed deck displacements.

Measure of deformation	Maximum value	Loadcase(s)	U.C.
Maximum total displacement	0.198 m	3, 4	0.198
Maximum total acceleration	0.008 m s^{-2}	5, 6	0.016
Maximum lateral rotation	0.000 64 rad	5, 6	0.1066
Maximum cross section plane rotation	0.0001 rad	3, 4	0.0023
Maximum lateral angular acceleration	$2.6 \cdot 10^{-5} \text{ rad s}^{-2}$	5, 6	0.0005
Maximum cross section plane angular acceleration	$2.8 \cdot 10^{-5} \text{ rad s}^{-2}$	3, 4	0.0002

Table 6.4: Bridge deck deformation serviceability limits.

The serviceability limit states for the bridge deck aren't broken during any of the steady state analyses. Therefore it is concluded, that bridge deck motion due to wave excitation is not excessive and well below the serviceability limits.

6.1.3.3 Cable fatigue

The results of the cable fatigue analysis are presented here in terms of the Woehler diagrams for the main- and lateral cables in Figure 6.4. The allowed load cycles until failure are plotted in the diagrams for the internal loads per cable element for all load cases. The two S-N curves are calculated at two distinct minimum load levels. Figure 6.5 displays the maximal axial load amplitude values calculated during this analysis.

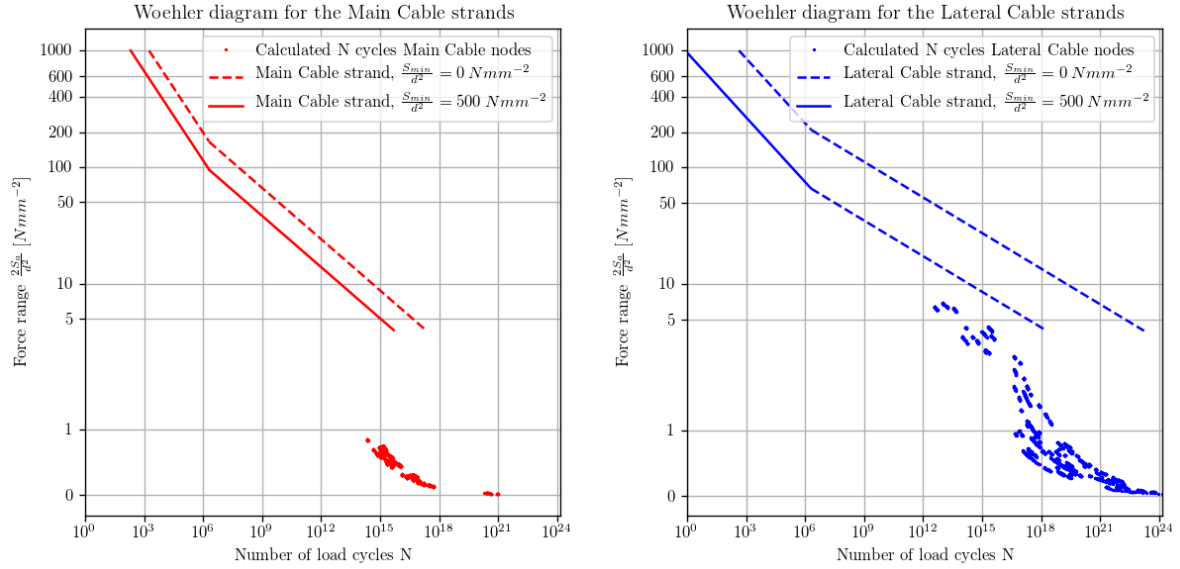


Figure 6.4: Woehler diagram for the main- and lateral cable strands with calculated maximum cycles for the loads observed in the main- and lateral cable nodes.

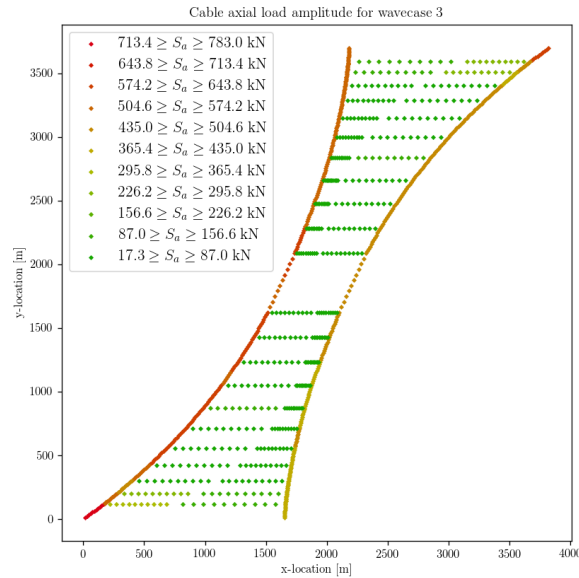


Figure 6.5: Load amplitude values for load case 3.

The conclusion to be drawn from this analysis is simple; fatigue induced by wave loading should not be an issue for the bridge design. This is clearly visible in the two Woehler diagrams. A quick calculation using the minimum calculated cycles and minimum wave period out of the load cases shows that for the main cable to experience a single strand failure due to the wave loads would take, at minimum, $10^{13} \cdot 4.6 \text{ s} = 1.46 \cdot 10^6$ years. For the lateral cable this number is slightly lower at $10^{12} \cdot 4.6 \text{ s} = 1.46 \cdot 10^5$ years.

This is explained by the load amplitudes calculated, too. The maximal axial load amplitude calculated is 783 kN. Comparing this to the design static axial load values for the main- and lateral cables, 930 MN and 53 MN, respectively, shows the difference in order of magnitude.

Bending stresses have not been a part of the study presented here and will have an influence on the fatigue life. Their influence is, however, expected to be marginal and it is not expected that their inclusion will lead to cable fatigue due to wave loading being decisive in the bridge design.

6.2 Vortex induced vibrations

This section describes the vortex induced vibration analyses performed in this study. It outlines the goal of the analysis, the methodology, the defining results and accompanying conclusions.

6.2.1 Goal

The goal of this analysis is to determine if the bridge design is sensitive to vortex induced vibrations and, if it is sensitive, determine the extent of the motion caused by this phenomenon. For more detailed information on the theory behind vortex induced vibration, reference is made to section J.1.

6.2.2 Methodology

This section outlines the methodology and different analyses performed to investigate vortex induced vibrations in the bridge system. The fluid flow analyses are carried out using the program Ansys Fluent and all structural calculations are performed using SACS. The steps taken in the process are the following:

- i First the pontoon modal eigenfrequencies are calculated from the model developed in appendix F using the method described in section H.1.
- ii Next a 'semi-2D' analysis is performed on stationary pontoon models and the resulting cross-flow loading frequencies are compared to the pontoon modal eigenfrequencies. This is detailed further in section J.3.2.
- iii After this, the influence of pontoon spacing relative to the flow direction on the loading is investigated, as a pontoon being in the wake region where vortices are shed by preceding pontoons may influence the loading on that pontoon. More on this can be found in section J.3.3.
- iv If the preceding analyses indicate sensitivity to vortex induced vibrations, a 3D analysis is performed on stationary pontoon models for a more realistic calculation of the cross-flow loading frequencies. These are then compared to the modal eigenfrequencies of the bridge model. This analysis can be found in section J.3.4.
- v To verify the calculation model calculating the loads on four representative pontoons out of the twenty-two, a verification calculation is performed for pontoons with matching diameters and different draughts. This analysis is found in section J.3.5.
- vi If the system is deemed sensitive to vortex induced vibrations based on the preceding analysis, a coupled analysis is performed. In this coupled analysis the influence of the pontoon motion on the fluid flow is taken into account, leading to a more accurate depiction of reality and a calculation of the bridge motion due to vortex induced vibrations. The performed analysis can be found in section J.3.7. A trial analysis using a different meshing method is found in section J.3.6.
- vii A verification calculation of the model to calculate vortex induced vibrations introduced in this thesis (the Fluent-SACS model) is performed using a wake oscillator model based on the work by Ogink and Metrikine (2010) [OM10]. The verification is performed for the motion of a single pontoon, pontoon 11, in just the cross-flow direction. The theory behind this model and the detailed set-up of this analysis is found in section J.3.8.
- viii If all analyses show that vortex induced vibrations will be a problem for the bridge design, possible solutions to the problem are presented. This can be found in section J.3.9.

6.2.3 Defining results and conclusions

This section contains the defining results and accompanying conclusions of the analysis. These are displayed per partial analysis performed.

Apart from the pontoon modal eigenfrequencies, the eigenfrequencies of the entire bridge structure are calculated. The first five are depicted in Table 6.5.

Mode number	Eigenfrequency [Hz]	Eigenperiod [s]
1	0.006231	160.5
2	0.008432	118.6
3	0.008974	111.4
4	0.009476	105.5
5	0.009677	103.3

Table 6.5: Bridge system eigenfrequencies of the first five modes.

The results of the 'semi-2D' analysis in terms of the calculated load periods compared to the first two pontoon eigenperiods with matching values shown in bold text are shown in Table 6.6. The load periods for a pontoon in a flow with velocity 1.27 m s^{-1} are close to one of the two eigenperiods of four pontoons. Since this flow velocity is found in the inward current velocity profile, there is at least part of the pontoon loaded at the calculated frequencies and it can be stated that the pontoons appear sensitive to vortex induced vibrations.

Pontoon number	Diameter	First eigenperiod [s]	Second eigenperiod [s]	"Semi-2D" VIV load period [s]
1	30 m	79.167	57.187	78.9
2	36 m	96.987	59.388	89.1
3	36 m	110.123	67.436	89.1
4	36 m	122.226	75.277	89.1
5	36 m	125.271	83.525	89.1
6	36 m	128.881	89.194	89.1
7	42 m	130.616	89.712	104.0
8	42 m	131.444	92.492	104.0
9	42 m	133.908	96.640	104.0
10	42 m	132.461	100.173	104.0
11	52 m	137.071	106.649	136.6

Table 6.6: Pontoon eigenperiods and "Semi-2D" VIV load periods.

The results of the wake effect analysis in terms the average change in the cross-flow loading parameters are shown in Table 6.7. There is a wake effect present in the part of the model analysed. The wake effect provides, on average, a -10% decrease in the cross-flow load amplitude for pontoons affected by the wake of preceding pontoon. This is a positive effect. The average increase of about 15% of the load period is not necessarily a positive effect since it moves the load frequency away from the second eigenperiods of the pontoons, which are between 59.4s and 75.3s , but towards the first eigenperiods of the pontoons, which are between 97s and 122.2s . The influence of this wake effect is dwarfed by the influence the 3D calculation has on cross-flow loading parameters, as is shown next. Therefore the results of this analysis are not taken into account further in this thesis and a recommendation is made to investigate wake effects in 3D flow.

The results of the 3D load calculations on stationary pontoons in terms of the loading period compared to the first two pontoon- and bridge system eigenperiods are displayed in Table 6.8. At first sight the results of the 3D analysis seem to indicate that the pontoons are less sensitive to vortex induced vibrations than may have been expected from the results of the 'semi-2D' analysis. The primary cross-flow loading periods have moved quite a bit away from the corresponding pontoons first two eigenperiods.

Affected load parameter	Average change
Load periods	+ 15 %
Load amplitude	- 10 %

Table 6.7: Average change in cross-flow load parameters due to wake effects.

The main indication that these results only show a larger sensitivity to vortex induced vibrations is given when the eigenfrequencies of the entire bridge structure are taken into account. When comparing the first eigenfrequency of the entire bridge to the main loading periods calculated in this analysis it becomes obvious that the main loading period for pontoon 6 coincides with the bridge structure's first eigenperiod. Under the assumption that the cross-flow loading for different pontoon lengths does not change significantly, this means that ten out of the twenty-two pontoons will be subject to loading at the structure's first eigenfrequency. This indicates a very high sensitivity to vortex induced vibrations due to the current as present at the bridge location. Furthermore, as a coupled analysis may show, the range of load frequencies which are shifted to a frequency closer to eigenfrequencies of the bridge structure may be large enough to 'capture' even more of the load frequencies found.

Structure	Diameter	First eigenperiod [s]	Second eigenperiod [s]	3D VIV main loading period [s]
Pontoon 1	30 m	79.167	57.187	142.9
Pontoon 6	36 m	128.881	89.194	166.7
Pontoon 10	42 m	132.461	100.173	200.4
Pontoon 11	52 m	137.071	106.649	189.8
Entire bridge	-	160.5	118.6	-

Table 6.8: Pontoon eigenperiods and 3D VIV load periods.

The result of the draught comparison analysis is shown in Figure 6.6 in terms of the frequency spectra of the cross-flow loading on the pontoons. Visual comparison of the spectra for the two pontoons considered in the draught influence analysis shown in Figure 6.6 shows a large discrepancy in the location of the peaks - and thus in the energy content per load frequency. The main issue is the difference in the locations of the peaks, with minima visible where the other spectrum is maximal. This indicates that the loading on the pontoons is definitely not just scaled based on the draught over which the current load acts. So it must be concluded that the assumption that the total load on a pontoon with a larger draught can be scaled to be used on a pontoon with a smaller draught is not valid for all draughts. Therefore it is recommended to further investigate the difference pontoon draught makes on cross-flow loading. Perhaps this means that all twenty-two pontoons must be included separately in vortex induced vibration analysis.

The defining results of the coupled analysis are shown in Figure 6.7 and Table 6.9. Figure 6.7 displays the calculated displacement for pontoon eleven for each of the iterations. Table 6.9 displays the main cross-flow loading frequency calculated for the four representative pontoons for each iteration. The first conclusion that must be drawn from the coupled analysis is that the bridge structure is highly sensitive to vortex induced vibrations. This is clear from the fact that the fluid-structure interaction causes cross-flow loading frequencies over a wide band (0.005 Hz - 0.072 Hz) to move toward the structure's first modal eigenfrequency. This may be partially caused by the chosen load model, which will be discussed later.

Diameter [m]	Iteration 1 [Hz]	Iteration 2 [Hz]	Iteration 3 [Hz]	Iteration 4 [Hz]
30	0.0072	0.0064	0.0061	0.0061
36	0.0064	0.0064	0.0064	0.0061
42	0.005	0.005	0.0064	0.0064
52	0.0053	0.0061	0.0061	0.0064

Table 6.9: Cross flow load frequencies per pontoon diameter for four iterations

The shape of the first mode of vibration of the bridge structure is a slight deformation of the rigid

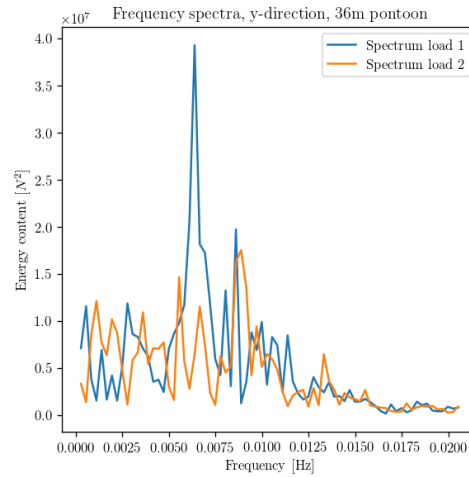


Figure 6.6: Comparison of the cross-flow load spectrum for pontoon 6 (load 1) and pontoon 2 (load 2).

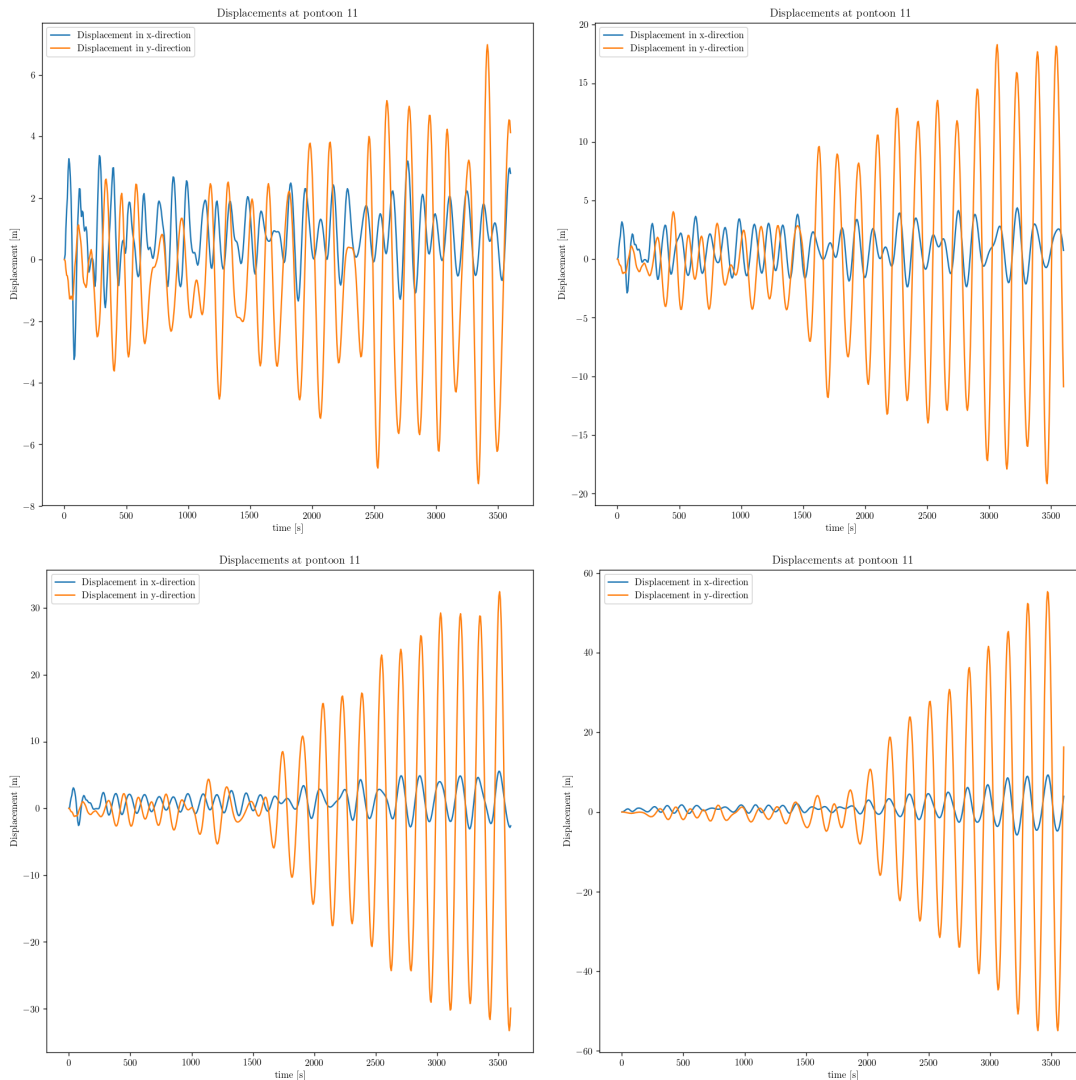


Figure 6.7: Displacements plotted against time for pontoon 11 for the four coupled iterations performed.

bridge deck in which the pontoons mainly move in the cross-flow direction relative to the current, depicted in Figures 6.8 and 6.9. This further contributes to the structure's sensitivity to cross-flow loading at

frequencies in a range near the first eigenfrequency.

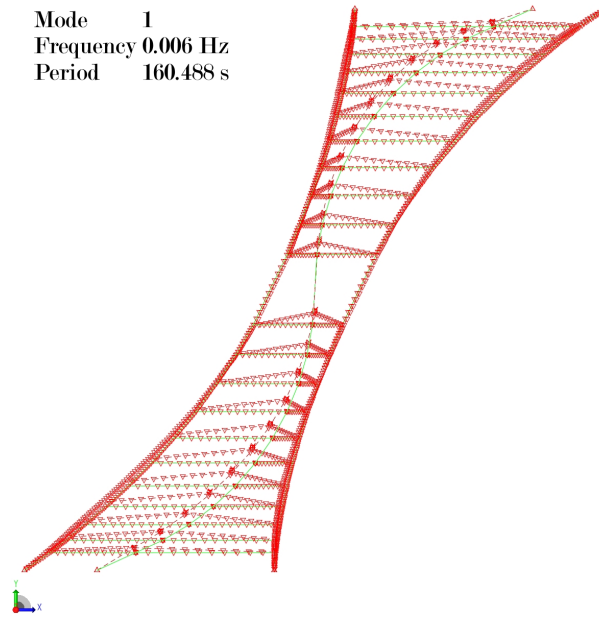


Figure 6.8: Top view of the first eigenmode shape (in red) of the bridge structure and the undeformed structure (green).

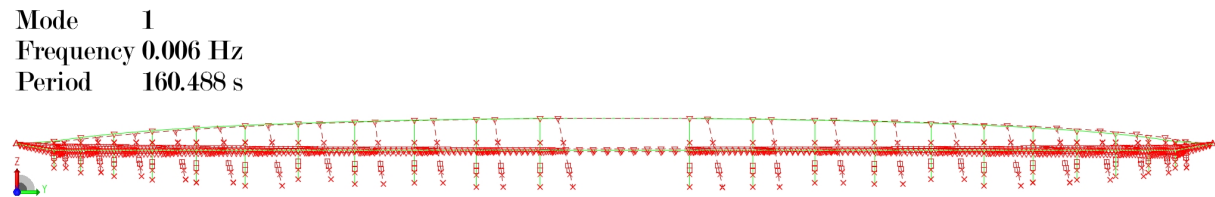


Figure 6.9: Side view of the first eigenmode shape (in red) of the bridge structure and the undeformed structure (green).

Despite the structure's high sensitivity to vortex induced vibrations, the fact that the vibrations are this pronounced casts doubt on the results obtained. Furthermore, the fact that the displacement reaches values that are larger than the pontoon diameters raises red flags, as experimental results indicate the maximum displacements in cross-flow direction should be in the range of 0.6 - 0.8 times the pontoon diameter [OM10] and the results indicate displacements as large as 1.2 times the pontoon diameter. Therefore, the results must be examined critically and reasons for the larger results must be found.

Another point of attention is the fact that the fluid loading is calculated using the shape, and motion, of only four pontoons out of the twenty-two. After which it is scaled to the draught of the remaining pontoons of the same diameter. The assumption that this is a realistic model for the loading of stationary pontoons has been proven wrong for at least one combination of pontoons with the same diameter and different draughts in section J.3.5. Performing this operation leads to ten out of the twenty-two pontoons (all those with a 36 m diameter) being loaded at the first modal frequency of the bridge structure for the first iteration. Furthermore, due to the fact that the resulting motion of only four pontoons is taken into account for the calculation of the new fluid forces per iteration, this leads to a perfect line-up of forcing frequencies across all pontoons with the same diameter, which may be possible, but is improbable due to variations in structural boundary conditions for the different pontoons.

For further research into this phenomenon, it is recommended to extend the calculation of fluid forces to all of the pontoons separately for each iteration, increasing the computation time by at least a factor five, but eliminating the assumptions leading to the issues described earlier.

Another remarkable element of the results is that the fluid force - structure interaction appears to increase each other with each iteration without an apparent maximum, although there are some clues in the results a maximum may have been reached. One of the reasons there is no conclusive result proving a maximum amplitude of vibration is the fact that the time-span for the analysis has been set

too short. The first potential apparent 'plateauing' of the results appear after 3300s into the analysis and increasing the analysis time should lead to a conclusive answer to the question of the maximum amplitude's existence.

The results of the coupled wake oscillator model are shown in Figures 6.10 and 6.12 for the cross-flow loading and displacement.

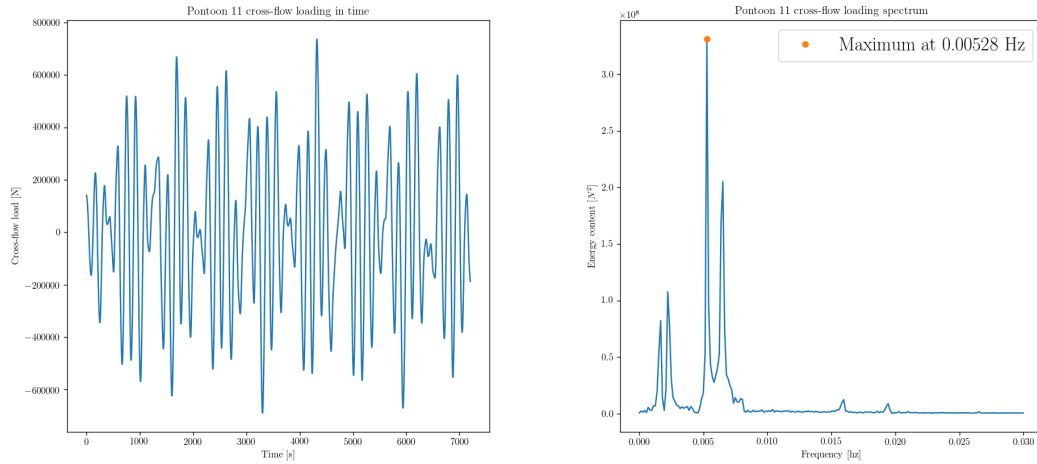


Figure 6.10: Cross-flow loading calculated using the wake oscillator model for pontoon 11 in both the time (left) and frequency domain (right).

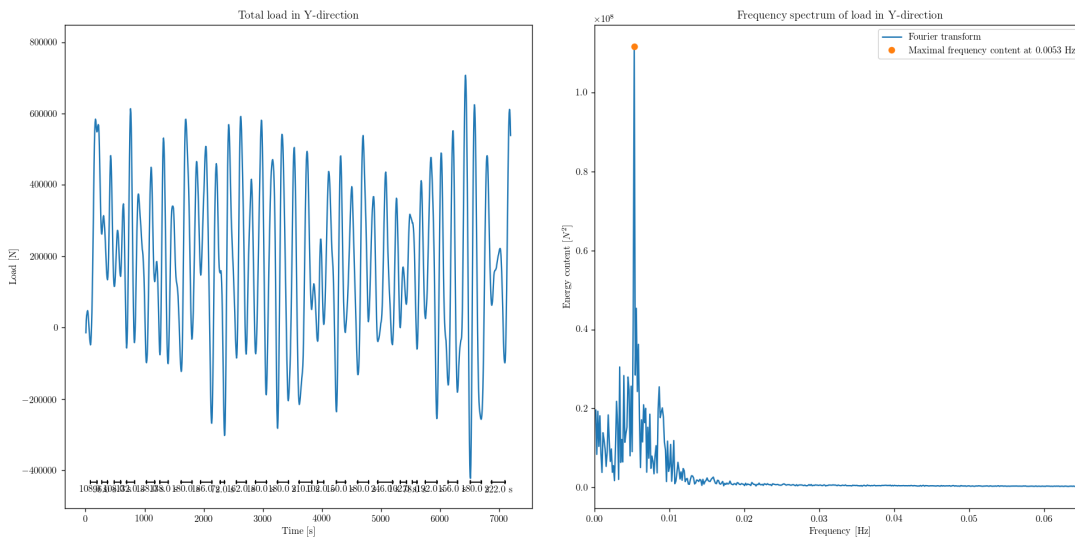


Figure 6.11: Cross-flow loading calculated using the Ansys-Fluent model for pontoon 11 in both the time (left) and frequency domain (right).

Figures 6.11 and 6.13 show the results of the final iteration performed with the Fluent-SACS model. Once again, the solution has not converged and shows no signs of nearing convergence. The reason for this will be explained later.

The results show that the Ansys-Fluent model and the wake oscillator model calculate both loads and displacements with comparable amplitudes. Differences are found once the results in the are examined in the frequency domain. The cross-flow loading using the wake oscillator model shows four distinct peaks, even in this coupled analysis, while the Fluent-SACS loading is mainly concentrated in one frequency. There are peaks near the same frequencies as in the wake oscillator model, but they are far less pronounced. For both the wake oscillator and the Fluent-SACS model the loading is not very different from the loading on a stationary pontoon. This is expected when the displacement amplitude is

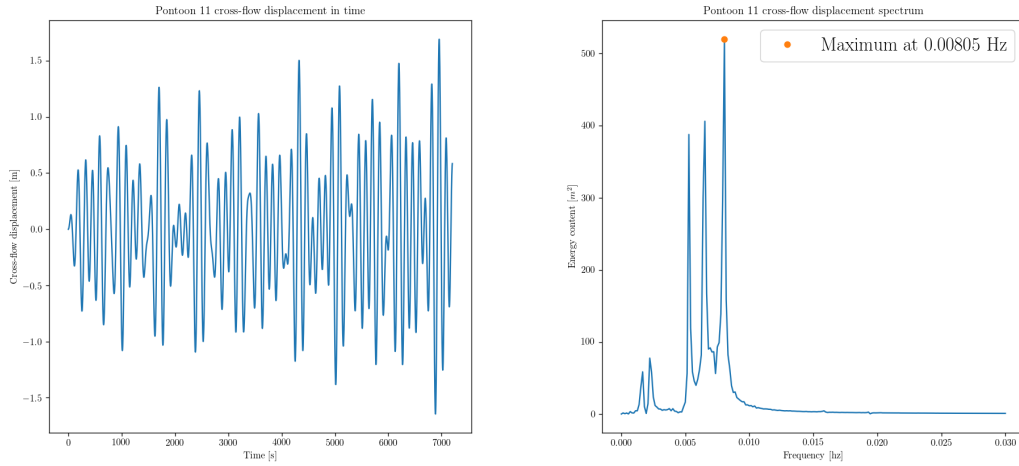


Figure 6.12: Cross-flow displacement calculated using the wake oscillator model for pontoon 11 in both the time (left) and frequency domain (right).

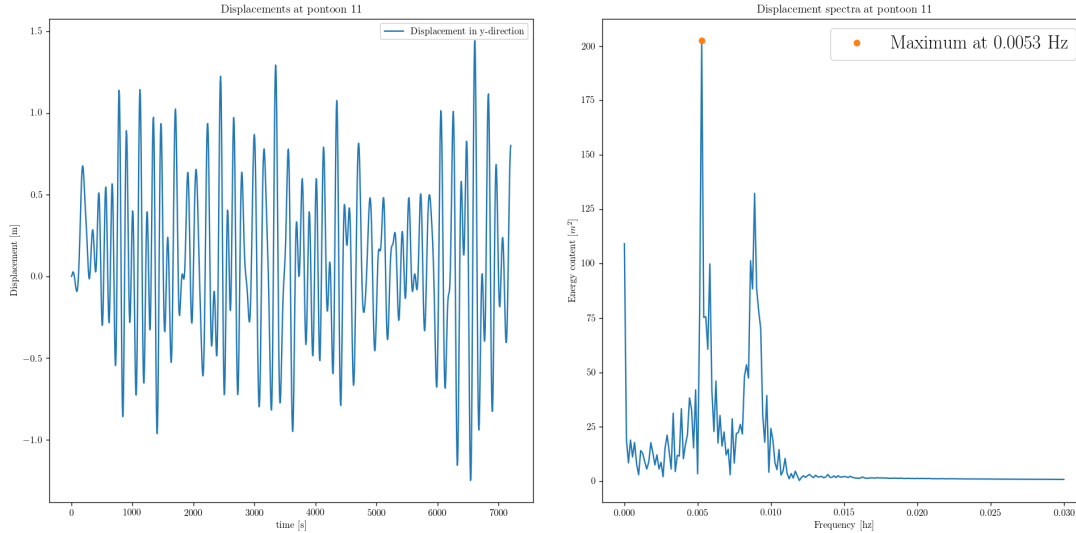


Figure 6.13: Cross-flow displacement calculated using the Ansys-Fluent model for pontoon 11 in both the time (left) and frequency domain (right).

considered with respect to the pontoon diameter; 1.5 m versus 52 m, or a 0.029 amplitude over diameter ratio. The pontoon is nearly stationary. The wake oscillator model finds the pontoon's eigenfrequency as main frequency of vibration, while the Fluent-SACS model finds that the pontoon mainly vibrates at the amplitude of the loading and has a smaller peak at the pontoon eigenfrequency. This difference is explained by looking at the exciting frequencies for both models; the wake oscillator model has a pronounced peak close to the pontoon eigenfrequency, while the Fluent-SACS model is almost exclusively loaded at 0.0053 Hz. If further improvements are made to make the loading by the wake oscillator model more closely resemble the Fluent-SACS model loading, it is expected that the displacement results will also be more in line in terms of frequency. What can be concluded from this analysis is that both methods produce comparable results for this case and thus that the Fluent-SACS model is applicable for the calculation of pontoon motion.

Then there is the matter of the Fluent-SACS model not converging. The reason for this is found when the simulation time of the wake oscillator model is extended. Figure 6.14 shows the cross-flow motion of pontoon 11 over a time period of 28 800 s, or 8 hours. The figure shows that it takes about 22 500 s, or 6.25 hours, for the coupled system to reach a steady state in terms of vibration amplitude. This means that even at a simulation time of 2 hours, the modelled systems are still in the transient

phase, making comparison of results and especially calculating convergence a futile effort. Once again, the recommendation is made to extend simulation time even further for this analysis, to see if the Fluent-SACS model finds a comparable steady state motion.

One point of interest is the small peak near a frequency of 0.0063 Hz in the Fluent-SACS model's displacement in the frequency spectrum (shown on the right in Figure 6.13). This value corresponds to the frequency of the first mode of vibration of the entire bridge structure and apparently it is already excited when only a single pontoon is loaded by cross-flow lift forces at mainly a very different frequency. This lends credence to the conclusion that the bridge is very susceptible to vortex induced vibrations.

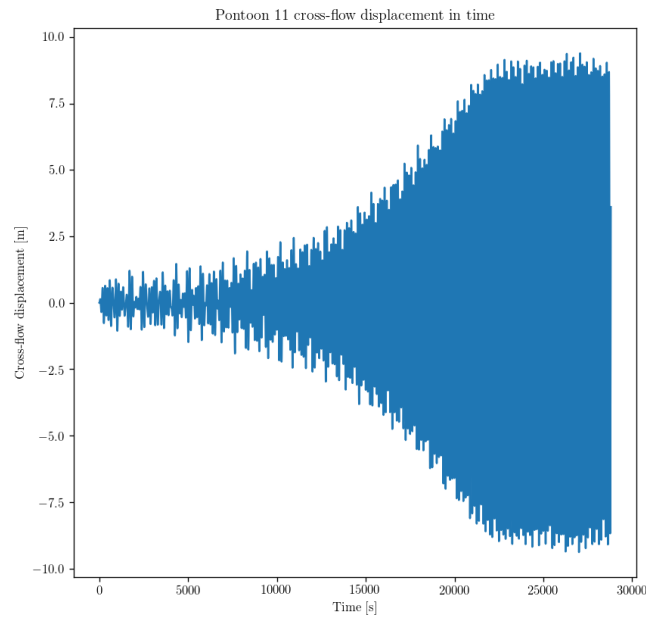


Figure 6.14: Cross-flow displacement calculated using the wake oscillator model for pontoon 11 in time, for a period of 8 hours.

Chapter 7

Conclusions and recommendations

This chapter contains the conclusions drawn in this study and recommendations for both the bridge design and further research. These are first given in relation to the research questions, after which further recommendations are given.

7.1 Research questions

7.1.1 Main question

What is the dynamic response of the current bridge structure design, as a result of wave and current loading?

The steady state response of the structure due to wave and current loading has been calculated for six representative critical load cases. The displacement and internal loads have been used to answer the research sub questions. The dynamic response to the current in terms of vortex induced motion has been shown to be significant and a critical factor in the design of the bridge structure. The bridge system is found to be excited in its first mode of vibration as a result of the cross-flow loading by the inward current. The precise extent of the vortex induced motion has not been determined with certainty in this study. A verification calculation of the model used in this thesis has partially verified the results provided by this model, however a more complete verification is needed and can be achieved by extending the simulation time. The same applies to the coupled analysis performed for the entire bridge structure in this thesis. Increasing the calculation time should lead to evidence of the self-limiting effect of vortex induced vibrations being present in the model. Further refining of the model will lead to more accurate and potentially more realistic results. This can be achieved by calculating the fluid loading on each pontoon separately, at the cost of an enormous increase in computation time.

7.1.2 Sub questions

Considering the dynamic response of the system, will the bridge deck motion or cable fatigue damage exceed design limits?

Considering the steady state response of the system due to current and wave loading, a definitive answer to this question has been found in this thesis. The bridge deck motion and fatigue damage are well within design limits for the critical wave load cases considered. Therefore, bridge deck motion and fatigue damage due to any wave condition found at the bridge location is deemed to be insignificant and not critical to the bridge design.

When the results obtained for the vortex induced vibrations are considered, it is clear that bridge deck motion will exceed design limits by an impressive margin and lead to complete structural failure of the bridge design. Therefore, the calculation of cable fatigue damage is foregone. Since the displacement results obtained from the vortex induced vibration calculation are deemed to be uncertain until verified, the answer to this sub-question considering vortex induced motion remains uncertain, too. It is considered to be very likely that both bridge deck motion and cable fatigue damage will exceed design limits due to vortex induced motion.

Which design measures, specifically focusing on the pontoon and cable system design, can be taken to improve the system's behaviour?

To improve the system's behaviour in relation to wave loading, no further design steps are necessary. To solve the bridge system's sensitivity to vortex induced vibrations, multiple solutions are available. An extended treatment of some of the solutions is found in section J.3.9 and a summary is given here.

The first possible solution is the addition of one, or multiple, helical strakes to the pontoons. Figure 7.1 depicts an example of a helical strake attached to a pontoon. Helical strakes, when applied well, reduce the amplitude of the cross-flow loading, 'spread' the frequency of vortex shedding over more frequencies and create a phase difference in vortex shedding along the pontoon draught. All of these combined lead to a reduced structural response to the current in cross-flow direction. However, the drag in the in-flow direction is increased, which is undesirable. Furthermore, strake functioning is reduced by marine growth, which, as shown in section 2.3.6, is significant at the bridge location. This leads to an increased maintenance requirement or a significant increase in cost due to expensive coatings, which is both highly undesirable. Strakes are designed to reduce vortex induced vibrations in multidirectional flows. Usually this property outweighs the negative side effects of their inclusion. Since the flow direction at the bridge location is known and unidirectional, this may not be the case for this bridge design.

Therefore, a recommendation is made to investigate the effect and required shape of strakes applied to the pontoons and determine if the negative side effects mentioned are too significant for this solution to be viable.

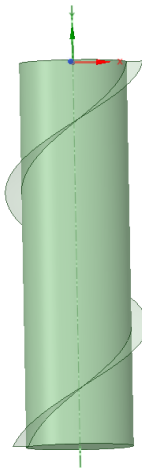


Figure 7.1: Example of a helical strake attached to a pontoon.

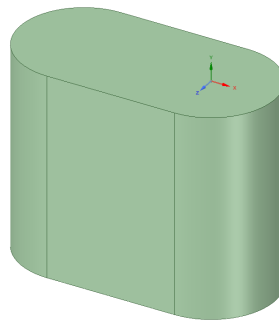


Figure 7.2: Possible different pontoon shape.

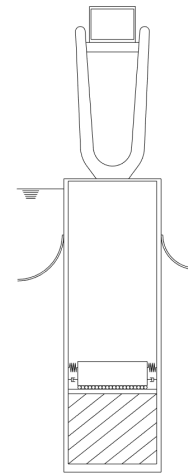


Figure 7.3: Dynamic absorber in a pontoon.

Another possible solution is redesigning the pontoons into something with a more aerodynamic shape. An analysis of a simple redesign is found in section J.3.9.2. The results of this analysis show that the amplitude of cross-flow loading is much lower than for the original pontoon. This is a positive improvement and it is deemed likely that further research into possible pontoon shapes can lead to huge improvements in the vortex induced vibrations of the bridge system. Furthermore, redesigning the pontoons to something with a larger section plane cut by the water line leads to a higher restoring moment in the enlarged direction. This is an improvement which may lead to smaller amplitudes of motion of both the bridge deck and the cable mooring system. A recommendation is made to investigate a redesign of the pontoons in relation to vortex induced vibrations.

Another change that can be made to the pontoons is the inclusion of a dynamic absorber, or tuned mass damper. These systems improve dynamic behaviour by changing the frequency of vibration of the mode(s) of vibration of the system, or by damping the response at a certain frequency of vibration. The first is difficult to implement, since the main mode of vibration of the bridge system is considered. The latter may be possible to implement within the confines of the pontoons. This system damps the primary structure response by 'absorbing' the energy of certain vibrations from the primary structure by vibrating itself. An example of the set-up of such a system is shown in Figure 7.3. A recommendation is made to investigate the scale and effectiveness of the system needed to damp the bridge design's primary mode of vibration.

A redesign of the cable mooring system is recommended. The recommendation is made to research the possibilities for restraining the cross-flow motion of the pontoons, as this particular direction of motion is currently almost unrestrained. An example of this could be replacing the single lateral cables, spanning

in the flow direction, with multiple cables at angles with the flow direction, restraining the cross-flow motion.

7.2 Further recommendations

This section includes further recommendations made on the basis of this study that have not yet been stated.

- i The cable model adopted in this thesis, in which the cable bending stiffness changes based on cable curvature, is developed for the calculation of internal damping of transmission line conductors. These steel cables are vastly different in dimensions compared to the cables designs used in this thesis. Therefore, a recommendation is made to verify the cable model adopted in this thesis for cables of the dimensions used in the bridge design through testing.
- ii For the vortex induced vibration analysis, the current load on cables has not been investigated. The main cables may well be sensitive to vortex induced vibrations in the current velocities found at the bridge location. The lateral cables are expected to be affected by this phenomenon too, since they are inclined in the flow direction. It is recommended to investigate the sensitivity of both the main- and lateral cables to vortex induced vibrations.
- iii This thesis has focused on the bridge structure's response to wave and current loading, omitting wind loading. Due to the large lever arm wind loading on the bridge deck has with respect to the centers of rotation of the bridge structure, wind loading may be an issue here. Furthermore, the precise loading applied to the bridge structure by the wind has to be investigated using either wind tunnel testing or a detailed flow model. A recommendation is made to investigate the loading applied to the bridge structure by the wind at the bridge location and the bridge structure's response to the wind loading.
- iv With the design of the cable's cross sections in this thesis, most structural elements used in the bridge have received a detailed design. The elements still in need of such a treatment are the bridge pylons and, to a lesser extent, the pontoons. Since the redesign of the pontoons has been recommended earlier, a recommendation for the detailed design of the pylons is made here.
- v From the investigation performed into the wake effect for the bridge design it has become clear that there is an interaction between pontoon wakes and subsequent pontoons. Due to the large difference observed between results obtained using 'semi-2D'- and 3D models, it is recommended to investigate the wake effect using a 3D model, too.

Bibliography

- [Sto47] G.G. Stokes. “On the theory of oscillatory waves”. In: *Transactions of the Cambridge Philosophical Society* 8 (1847), pp. 441–455.
- [Rie51] B. Riemann. *Grundlagen für eine allgemeine Theorie der Functionen einer veränderlichen complexen Grösse*. Adalbert Rente, 1851.
- [Mac54] R.C. MacCamy. *Wave Forces on Piles: A Diffraction Theory*. U.S. Army Corps of Engineers Beach Erosion Board, 1954. URL: http://acwc.sdp.sirsi.net/client/en_US/default/index.assetbox.assetactionicon.view/1007800?rm=TECHNICAL+MEMO2%7C%7C%7C1%7C%7C%7C0%7C%7C%7Ctrue.
- [Rom55] W. Romberg. “Vereinfachte numerische Integration”. In: *Det Kongelige Norske Videnskabers Selskab Forhandlinger* 28 (1955), pp. 30–36.
- [CT65] J. W. Cooley and J. W. Turkey. “An algorithm for the machine calculation of complex Fourier series”. In: *Math. Comput.* 19 (1965), pp. 297–301.
- [Cha74] G. Chaikin. “An algorithm for high speed curve generation.” In: *Computer Graphics and Image Processing* 3 (1974), pp. 346–349.
- [MGB74] A. Mood, F. Graybill, and D. Boes. *Introduction to the Theory of Statistics (3rd ed.)*. 1974.
- [DP80] R. Dormand and P. J. Prince. “A family of embedded Runge-Kutta formulae”. In: *Journal of Computational and Applied Mathematics* 6 (1980), pp. 19–26.
- [KEN83] JOHN T. KENT. “Information gain and a general measure of correlation”. In: *Biometrika* 70.1 (1983), pp. 163–173. DOI: 10.1093/biomet/70.1.163. URL: <http://dx.doi.org/10.1093/biomet/70.1.163>.
- [Cha87] S. K. Chakrabarti. *Hydrodynamics of Offshore Structures*. Springer Verlag, 1987.
- [HH88] Chen Su Huan and Pan H. H. “Guyan reduction”. In: *Communications in Applied Numerical Methods* 4.4 (1988), pp. 549–556. DOI: 10.1002/cnm.1630040412. URL: <https://onlinelibrary.wiley.com/doi/abs/10.1002/cnm.1630040412>.
- [Hai89] E. Haibach. VDI-Verlag, 1989.
- [Cas93] N. F. Casey. “The fatigue endurance of wire ropes for mooring offshore structures.” In: *OIPEEC Round Table Conference 1993* (1993), pp. I.21–I.49. ISSN: 9037000916 9789037000917.
- [Zhu93] S. Zhu. “Diffraction of Short-Crested Waves Around a Circular Cylinder”. In: *Ocean Engineering* (1993). URL: http://www.sciencedirect.com.tudelft.idm.oclc.org/science/article/pii/002980189390003Z?_rdoc=1&_fmt=high&_origin=gateway&_docanchor=&md5=b8429449ccfc9c30159a5f9aeaa92ffb&ccp=y.
- [Men94] F. R. Menter. “Two-Equation Eddy-Viscosity Turbulence Models for Engineering Applications”. In: *AIAA Journal* 32 (1994), pp. 1598–1605.
- [al96] Feriani et al. “The Formation of Viscous Damping Matrices for the Dynamic Analysis of MDOF Systems”. In: *Earthquake Engineering and Structural Dynamics* (1996). URL: [http://onlinelibrary.wiley.com.tudelft.idm.oclc.org/doi/10.1002/\(SICI\)1096-9845\(199607\)25:7%3C689::AID-EQE575%3E3.0.CO;2-L/abstract](http://onlinelibrary.wiley.com.tudelft.idm.oclc.org/doi/10.1002/(SICI)1096-9845(199607)25:7%3C689::AID-EQE575%3E3.0.CO;2-L/abstract).
- [Pap97] K. O. Papailiou. “On the Bending Stiffness of Transmission Line Conductors”. In: *IEEE Transactions on Power Delivery* (1997). URL: <http://ieeexplore.ieee.org.tudelft.idm.oclc.org/document/634178/>.
- [DS98] N. R. Draper and H. Smith. *Applied regression analysis*. 1998.

- [Bel99] A. G. Belyaev. "A Note on Invariant Three-Point Curvature Approximations". In: (1999). URL: <http://www.kurims.kyoto-u.ac.jp/~kyodo/kokyuroku/contents/pdf/1111-16.pdf>.
- [Weh00] Klopfer Wehking K.-H. "Lebensdauer und Ablegereife von Drahtseilen unter Zugschwellbeanspruchung." In: *Abschlussbericht d. Forschungsprojekts AVIF und DRAHT 51* (2000), pp. 138–144.
- [ECS02] ECS. *Steel wire and wire products - steel wire for ropes*. EN 10264-1:2002. Design Code. European Committee for Standardization, 2002. URL: <https://www.nen.nl/NEN-Shop/Norm/NENEN-1026412012-en.htm>.
- [Fey07] K. Feyrer. *Wire Ropes*. Springer, 2007. ISBN: 978-3-540-33831-4. URL: <https://doi-org.tudelft.idm.oclc.org/10.1007/978-3-540-33831-4>.
- [Apo09] J. A. Apolinário. *QRD-RLS Adaptive Filtering*. 2009. ISBN: 978-0-387-09734-3. DOI: <https://doi-org.tudelft.idm.oclc.org/10.1007/978-0-387-09734-3>.
- [al10] Babuska et al. "Modeling and Experimental Validation of Space Structures with Wiring Harnesses". In: *Journal of Spacecraft and Rockets* (2010). URL: <https://doi.org/10.2514/1.48078>.
- [DNV10] DNV. *Environmental Conditions and Environmental Loads*. DNV-RP-C205. Recommended Practice. Det Norske Veritas, 2010. URL: <https://rules.dnvg1.com/docs/pdf/dnv/codes/docs/2010-10/rp-c205.pdf>.
- [ECS10] ECS. *Eurocode 1: Actions on structures - Part 1-4: General actions - Wind actions*. EN 1991-1-4:2005+A1. Design Code. European Committee for Standardization, 2010. URL: <http://www.phd.eng.br/wp-content/uploads/2015/12/en.1991.1.4.2005.pdf>.
- [OM10] R.H.M. Ogink and A.V. Metrikine. "A wake oscillator with frequency dependent coupling for the modeling of vortex-induced vibration". In: *Journal of Sound and Vibration* 329.26 (2010), pp. 5452–5473. ISSN: 0022-460X. DOI: <https://doi.org/10.1016/j.jsv.2010.07.008>. URL: <http://www.sciencedirect.com/science/article/pii/S0022460X10004621>.
- [al11] Lothe et al. *Mulighetsstudie for Kryssing av Sognefjorden Opedal - Lavik: Estimert På Bølger og Strøm*. Feasibility study. SINTEF, 2011.
- [Sim11] A. Simone. *An Introduction to the Analysis of Slender Structures*. 2011.
- [Cam12] F.C. Campbell. ASM International, 2012. ISBN: 978-1-61503-976-0. URL: <https://app.knovel.com/hotlink/toc/id:kpFFUB0001/fatigue-fracture-understanding/fatigue-fracture-understanding>.
- [Ell12] O. Ellefsen. *Project Overview Coastal Highway Route E39*. Statens vegvesen, 2012.
- [Fje12] A. Fjeld. *Feasibility Study for Crossing Sognefjorden - Submerged Floating Tunnel*. Feasibility Study. Reinertsen, 2012. URL: https://www.vegvesen.no/_attachment/513902/binary/828560?fast_title=Mulighetsstudie+for+kryssing+av+Sognefjorden+-+Neddykket+r%C3%B8rbru.pdf.
- [Adh13] S. Adhikari. *Structural Dynamic Analysis with Generalized Damping Models*. 1st ed. Mechanical Engineering and Solid Mechanics. Wiley-ISTE, 2013. ISBN: 9781848215214.
- [Spa13] K. et al. Spak. "Cable Modeling and Internal Damping Developments". In: *Applied Mechanics Reviews* (2013). URL: <http://appliedmechanicsreviews.asmedigitalcollection.asme.org.tudelft.idm.oclc.org/article.aspx?articleid=1678950>.
- [CGZ14] Xiangju Cheng, John S. Gulliver, and Dantong Zhu. "Application of Displacement Height and Surface Roughness Length to Determination Boundary Layer Development Length over Stepped Spillway". In: *Water* 6.12 (2014), pp. 3888–3912. ISSN: 2073-4441. DOI: 10.3390/w6123888. URL: <http://www.mdpi.com/2073-4441/6/12/3888>.
- [Her14] R. Hermans. "Buoyancy Aided Crossing for Bridging Extreme Widths". Delft University of Technology, 2014.
- [Lal14] Christian Lalanne. John Wiley and Sons, 2014. ISBN: 978-1-84821-647-1. URL: <https://app.knovel.com/hotlink/toc/id:kpMVSAVF03/mechanical-vibration/mechanical-vibration>.

- [DNV15a] DNV. *Offshore mooring steel wire ropes*. DNVGL-OS-E304. Offshore standard. Det Norske Veritas, 2015. URL: <https://rules.dnvgl.com/docs/pdf/dnvgl/os/2015-07/DNVGL-OS-E304.pdf>.
- [DNV15b] DNV. *Position mooring*. DNVGL-OS-E301. Offshore standard. Det Norske Veritas, 2015. URL: <https://rules.dnvgl.com/docs/pdf/dnvgl/os/2015-07/DNVGL-OS-E301.pdf>.
- [Yip15] T. Yip. “Long Span Buoyance Bridge with Submerged Cable Anchoring”. Delft University of Technology, 2015.
- [DX16] R. Dhanak and N. Xiros. *Springer Handbook of Ocean Engineering*. 2016. ISBN: 978-3-319-16649-0. DOI: <https://doi-org.tudelft.idm.oclc.org/10.1007/978-3-319-16649-0>.
- [al17] Visser et al. “Sognefjord Buoyancy Bridge Feasibility and Sensitivity Analysis”. In: *Proceedings of Eurosteel 2017* (2017).
- [Cij18] W. Cijssouw. “A continuous superstructure for the Sognefjord bridge”. Delft University of Technology, 2018.

Appendices

Appendices

A.1	Overview	51
A.2	Bridge girder	52
A.3	Pylons	53
A.4	Pontoons	55
A.4.1	Buoyancy and restoring moment	58
A.5	Cable System	65
B.1	Wave loading	66
B.2	Current loading	78
B.3	Traffic loading	79
B.4	Wind loading	79
B.4.1	Wind load on bridge girder	81
B.4.2	Wind load on bridge pylons and pontoons	92
B.5	Load cases	96
C.1	Cross section type	97
C.2	Cross section design	98
C.3	Elasticity module	100
C.4	Bending stiffness	101
C.5	Conclusion	109
D.1	Hysteretic damping	111
D.2	Modelling cable damping	111
D.2.1	Overview	112
D.2.2	Equilibrium	113
D.2.3	Mode shapes	113
D.2.4	Undamped steady state solution	113
D.2.5	Pre-set displacement	113
D.2.6	Integration	114
D.2.7	Equivalent systems	116
D.2.8	Structural damping factor	117
D.3	Results	117
D.4	Conclusions	118
E.1	Theory	119
E.2	Set-up	121
E.3	Results	122
E.4	Conclusions	130
F.1	Nonlinear analysis	131
F.2	Linear analysis	136
G.1	Cables	137
G.1.1	Verification of the SACS cable model	137
G.1.1.1	Static analysis	138
G.1.1.2	Eigenfrequency analysis	139
G.2	Pontoons	141
G.2.1	Static analysis	142
G.2.2	Eigenfrequency analysis	142
G.3	Pylons	145
G.4	Girders	145
G.5	Bridge model	145
G.5.1	Dimensions and axis system	145
G.5.2	Component coordinates	146
G.5.3	Connections	147
G.5.4	Full model	148
G.5.4.1	SACS Input file	148
G.5.4.2	Graphical presentation	150
G.6	Waves and current	151
G.6.1	Modelling	151
G.6.2	Verification	152
H.1	Eigenfrequency analysis	156

H.1.1	Stiffness matrix reduction	157
H.1.2	Mass matrix generation	157
H.1.3	Result calculation	157
H.2	Steady state analysis	157
H.3	Time history analysis	158
I.1	Methodology	160
I.2	Results	162
I.3	Significance	162
J.1	Theory	163
J.1.1	Ansys Fluent turbulent flow modelling	164
J.1.1.1	Constitutive equations	164
J.1.1.2	Boundary conditions	167
J.1.1.3	Moving boundaries in Fluent	167
J.2	Methodology	170
J.3	Research and results	170
J.3.1	Shared parameters	170
J.3.2	'Semi-2D' analysis	175
J.3.2.1	Set-up	175
J.3.2.2	Results	175
J.3.2.3	Conclusions	176
J.3.3	Wake effect influence	177
J.3.3.1	Set-up	177
J.3.3.2	Results	178
J.3.3.3	Conclusions	181
J.3.4	3D analysis	181
J.3.4.1	Set-up	181
J.3.4.2	Results	184
J.3.4.3	Conclusions	185
J.3.5	3D draught comparison	186
J.3.5.1	Set-up	186
J.3.5.2	Results	187
J.3.5.3	Conclusions	188
J.3.6	Coupled analysis using decoupling springs	188
J.3.6.1	Set-up	189
J.3.6.2	Results	189
J.3.6.3	Conclusions	190
J.3.7	Coupled analysis	190
J.3.7.1	Set-up	190
J.3.7.2	Results	192
J.3.7.3	Displacement table	197
J.3.7.4	Conclusions	199
J.3.8	Model verification	201
J.3.8.1	Coupled wake oscillator model	201
J.3.8.2	Set-up	202
J.3.8.3	Results and conclusions	204
J.3.9	Possible solutions	207
J.3.9.1	Helical strakes	207
J.3.9.2	Changing the pontoon shape	208
J.3.9.3	Dynamic absorber (tuned mass damper)	212
J.4	Conclusions	212
K.1	Theory	213
K.2	Set-up	215
K.3	Results	216
K.4	Conclusions	219

Appendix A

Current bridge design

This chapter lays out the most current design for the floating bridge crossing the Sognefjord on which this thesis is based and handles previous studies performed on this subject.

A.1 Overview

The current bridge design is an S-shaped bridge in the horizontal plane, which gradually inclines to the required height for the mid-span. The bridge deck rests on aesthetically pleasing pylons which transfer the loads to 22 pontoons, which provide the necessary buoyancy. To aid in maintaining the relative position of the pontoons, a sub-sea cable system has been designed which consists of 44 lateral and 2 main cables. Each pontoon is connected to two lateral cables to restrain its motion. The current design for the above sea level portion of the bridge is displayed in Figures A.1 [al17]. The bridge design is rotationally point symmetric in the middle point of the main span, meaning that rotating the bridge by 180° degrees around this points will provide the same structure.



Figure A.1: An overview of the current bridge design [Yip15].

An overview of the current bridge design including the subsea cable system and coordinate system origin is found in Figure A.2. As previously mentioned, the main cables span from shore to shore over a distance of approximately 4 km and the lateral cables connect the pontoons to the main cables. The figure also displays the bridge designs' outer- and main span dimensions.

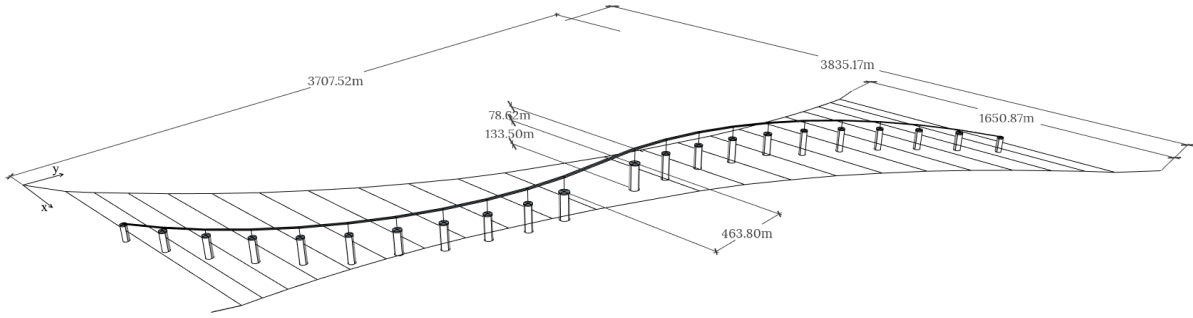


Figure A.2: An overview of the bridge dimensions.

A.2 Bridge girder

The bridge girder has different characteristics across the bridge design. Three girder designs are used; the main, intermediate and side girders. The main girder is the largest, as it spans the main, 465 m, span. This girder is flanked by the two intermediate girders, which span 200 m and are continuously connected to the main girder. The rest of the 200 m spans are spanned by side girders, which are also continuous. Figure A.3 displays the three girder types.

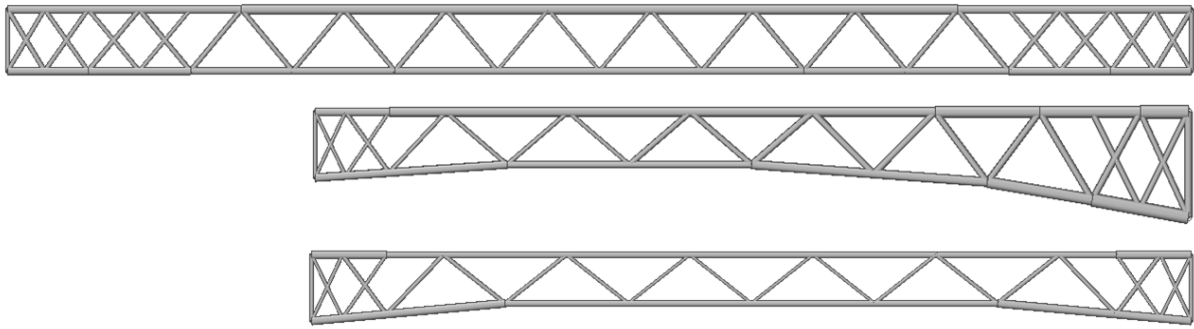


Figure A.3: Main (top), intermediate (middle) and side (bottom) span girders [Cij18].

All girders are supported on hinged connections at their respective pylon supports. These supports allow free rotation about the x- and y-axes and fix the girders to the pylons for rotation about the vertical z-axis. Figure A.4 displays the mechanical model for the center spans (not scaled to size).



Figure A.4: Mechanical model for the center bridge spans.

The precise characteristics of the bridge girder types are specified in Tables A.3 and A.2, and explanation of the symbols used is given in Table A.1.

Length	L
Height	Z
Width	Y
Cross sectional area	A
Shear area in Y-direction	$A_{shear,y}$
Shear area in Z-direction	$A_{shear,z}$
Torsional moment of inertia	I_t
Moment of inertia about Y-axis	I_y
Moment of inertia about Z-axis	I_z
Self weight	G

Table A.1: An overview of the symbols used in the following tables.

Steel Type	S460			
Young's modulus	E	200	$\cdot 10^3$	N mm $^{-2}$
Shear modulus	G	80	$\cdot 10^3$	N mm $^{-2}$
Yield stress	f_y	460		N mm $^{-2}$

Table A.2: Girder steel properties.

Girder	L [m]	Z [m]	Y [m]	A [m 2]	$A_{shear,y}$ [m 2]	$A_{shear,z}$ [m 2]	I_t [m 4]	I_y [m 4]	I_z [m 4]	G [kN m $^{-1}$]
Main	468	27	21.5	4.342	1.7	2.6	$1.3 \cdot 10^3$	$2.9945 \cdot 10^2$	$1.1245 \cdot 10^2$	408
Intermediate	200	16.8	21.5	1.8829	0.76	1.1	$7 \cdot 10^2$	$1.4696 \cdot 10^3$	$4.1602 \cdot 10^3$	220
Side	200	16.8	21.5	0.987	0.39	0.59	$4.4 \cdot 10^2$	$4.9639 \cdot 10^2$	$3.564 \cdot 10^2$	151

Table A.3: Girder characteristic properties.

A.3 Pylons

The pylons have not been fully designed, apart from the aesthetic design displayed in Figure A.5.



Figure A.5: Pylon design [Yip15].

There is no structural model for the pylons as yet and their weight and dimensions are conservatively assumed values. Other assumptions made for the pylon design are the following;

The pylon shape is assumed to be tubular, without gaps.

Each pylons' diameter is taken as half the diameter of the pontoon upon which it rests and the wall thickness is taken as 0.4 m for stiffness calculations.

The pylons are assumed to be stiff enough with respect to the other structural components to behave as a rigid components. To this end the same steel type is used for the pylons as for the bridge girders.

The pylon weight is 405.85 kN m $^{-1}$.

Table A.4 displays the steel characteristics used in the pylon design.

Steel Type	S460		
Young's modulus	E	200 · 10 ³	N mm ⁻²
Shear modulus	G	80 · 10 ³	N mm ⁻²
Yield stress	f_y	460	N mm ⁻²

Table A.4: Pylon steel properties.

The pylons and pontoons are numbered from 1 to 22, from the south to the north shore. Figure A.6 displays this numbering and the coordinate system used.

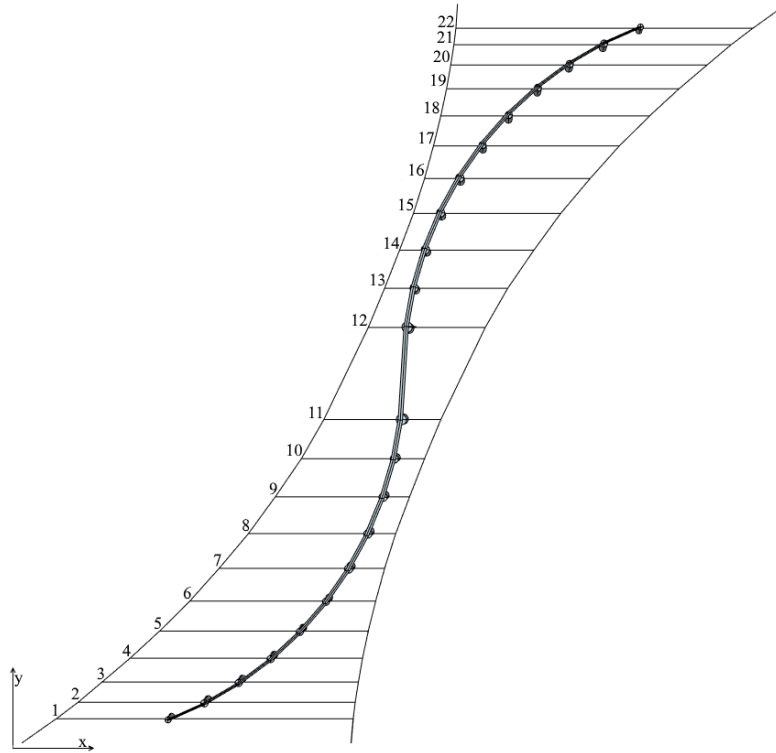


Figure A.6: Pylon and pontoon numbering.

Using the assumptions described earlier in this section, the properties used in the design and displayed in Table A.5 have been calculated. Equations A.1 and A.2 specify the expressions used for I_x , I_y and I_t , which are the moments of inertia around the major axes and the torsion constant, respectively. Since the bridge is point symmetric in the main span mid-point, the values for pylon 1 through 11 are given.

$$I_{x,y} = \frac{\pi}{4} (r_{outer}^4 r_{inner}^4) \quad (A.1)$$

In which;

$I_{x,y}$ is the moment of inertia about the x or y major axis

r_{outer} is the tube outer radius

r_{inner} is the tube inner radius

$$I_t = \frac{1}{3} \pi 2 r_{median} t^3 \quad (A.2)$$

In which;

I_t is the torsion constant

r_{median} is the radius to the median section of the tube wall

t is the tube wall thickness

Pylon	Height [m]	Diameter [m]	Weight [kN]	Area [m ²]	$I_{x,y}$ [m ⁴]	I_t [m ⁴]
1	4.19	15	1.70 · 10 ³	37.2	4.07 · 10 ³	1.98
2	15.31	18	6.21 · 10 ³	44.74	7.09 · 10 ³	2.39
3	26.39	18	10.71 · 10 ³	44.74	7.09 · 10 ³	2.39
4	36.32	18	14.74 · 10 ³	44.74	7.09 · 10 ³	2.39
5	45.11	18	18.31 · 10 ³	44.74	7.09 · 10 ³	2.39
6	52.74	18	21.40 · 10 ³	44.74	7.09 · 10 ³	2.39
7	59.23	21	24.04 · 10 ³	52.28	11.31 · 10 ³	2.79
8	64.57	21	26.21 · 10 ³	52.28	11.31 · 10 ³	2.79
9	68.77	21	27.91 · 10 ³	52.28	11.31 · 10 ³	2.79
10	71.82	21	29.15 · 10 ³	52.28	11.31 · 10 ³	2.79
11	73.72	26	29.92 · 10 ³	64.84	21.58 · 10 ³	3.46

Table A.5: Pylon properties.

A.4 Pontoons

As mentioned earlier, the bridge design incorporates 22 pontoons. The numbering is displayed in Figure A.6 in the previous section. The pontoon dimensions have been adapted from a previous study [Yip15], their mechanical properties are calculated in Subsection A.4.1. The pontoons are cylindrical in shape, like the tried offshore spar pontoon design. Figure A.7 displays the cross section of pontoon number 7 as an example of the pontoon design. In this cross section the internal ballast is shown as the striped area and the lateral cable connections are shown schematically.

The densities of the different pontoon components are shown in Table A.6.

$\rho_{concrete}$	2500	kg m ⁻³
$\rho_{ballast}$	2000	kg m ⁻³

Table A.6: Pontoon component densities.

The pontoon dimensions and coordinates are displayed in Table A.7. Since the bridge design is point symmetric in the main span midpoint, half the pontoons are shown. The coordinate system is specified in Figure A.6.

One more important factor in the bridge design is the local water depth at the pontoon locations. This is used in the calculation of wave forces on the pontoons. To this end, a linearised profile of the Sogne Fjord cross section has been assumed. This is depicted in Figure A.8.

The water depth per pontoon is determined by calculating its position along this profile using the pontoons y-coordinate. The results are displayed in Table A.8. Since the fjord depth profile is not symmetric, this value is displayed for all 22 pontoons.

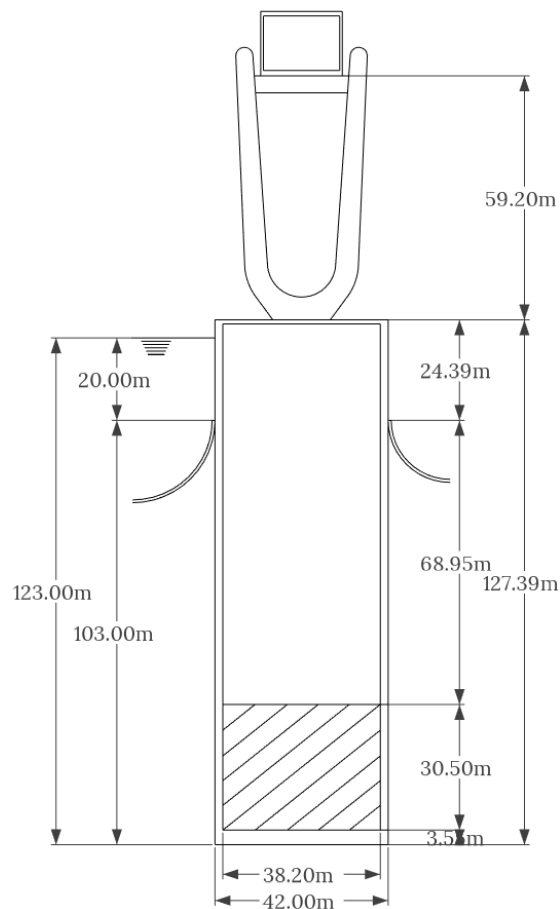


Figure A.7: Pontoon 7 cross section.

Number	Radius [m]	Length [m]	Draught [m]	Freeboard [m]	Thickness Top [m]	Thickness Side [m]	Thickness Bottom [m]	Height Ballast [m]	X- coordinate [m]	Y- coordinate [m]
1	15	77.42	-73.13	4.29	1	1.5	2.55	14.3	734.1	116.89
2	18	93.32	-88.8	4.52	1	1.7	2.86	19.5	915.96	199.86
3	18	104.44	-99.83	4.61	1	1.7	3.09	22.7	1087.9	301.85
4	18	115.18	-110.5	4.68	1	1.7	3.3	25.7	1247.95	421.63
5	18	124.15	-119.4	4.75	1	1.7	3.49	28.2	1394.27	557.84
6	18	134.31	-129.5	4.81	1	1.7	3.68	30.9	1525.18	708.91
7	21	114.16	-109.8	4.36	1	1.9	3.29	27.1	1639.18	873.13
8	21	127.39	-123	4.39	1	1.9	3.55	30.5	1734.96	1048.59
9	21	125.02	-120.6	4.42	1	1.9	3.5	30	1811.42	1233.29
10	21	137.53	-133.1	4.43	1	1.9	3.75	33.1	1867.69	1425.12
11	26	138.4	-133.5	4.9	1	2.23	3.76	35.1	1903.12	1621.86

Table A.7: Pontoon dimensions and coordinates.

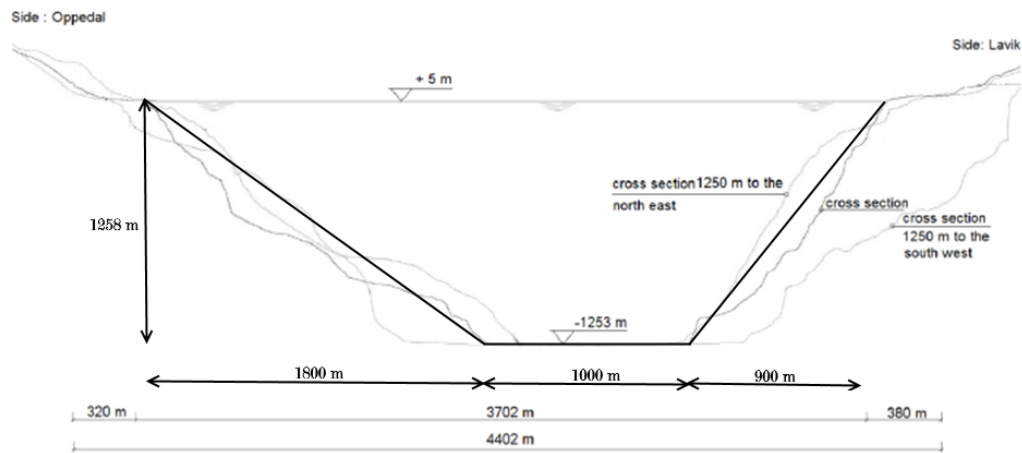


Figure A.8: Linearised cross section for pontoon water depth [Fje12].

Pontoon number	1	2	3	4	5	6	7	8	9	10	11
Water depth [m]	81.69	139.68	210.96	294.67	389.87	495.45	610.22	732.85	861.93	996.0	1133.5

Pontoon number	12	13	14	15	16	17	18	19	20	21	22
Water depth [m]	1258.0	1258.0	1258.0	1258.0	1213.85	1003.06	809.13	634.28	480.53	349.63	243.09

Table A.8: Water depth at each pontoon location.

A.4.1 Buoyancy and restoring moment

In this section the buoyancy force and restoring moment is calculated for the pontoons specified in the previous section. This leads to a mechanical model to be used in further analyses in this thesis.

To illustrate the method of calculation, the calculation is performed on pontoon number one. Figure A.9 displays the cross section and employed axis system for pontoon number one. Its dimensions are specified further in Table A.7 in section A.4. The dimensions and characteristics of the pylon and the girders connected to pontoon one are specified in sections A.3 and A.2.

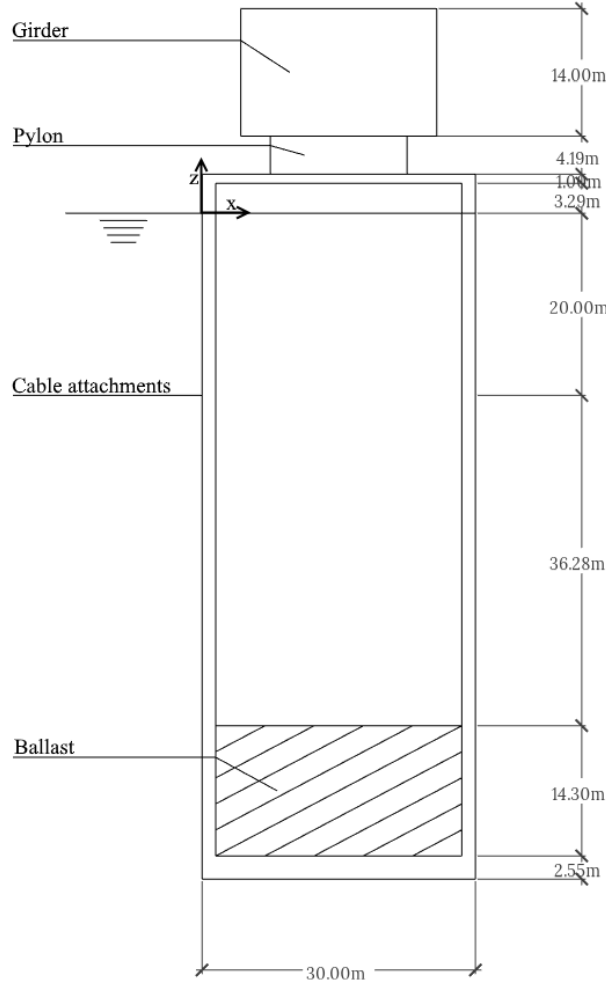


Figure A.9: Pontoon 1 cross section.

First, the buoyancy force is calculated according to Equation A.3.

$$F_{buoy} = \rho g \nabla \quad (\text{A.3})$$

In which;

F_{buoy} is the buoyancy force

ρ is the sea water mass density

g is the gravitational acceleration, to be taken as 9.81 m s^{-2}

∇ is the displaced volume of water, the pontoon volume under the water line

For pontoon number one this leads to a buoyancy force of $514.7 \cdot 10^3 \text{ kN}$. This is used later in the calculation.

Now the distribution of weight in the structure is examined. This is done by calculating the center of gravity. First, this is performed on the pylon and girder combination displayed in Figure A.10.

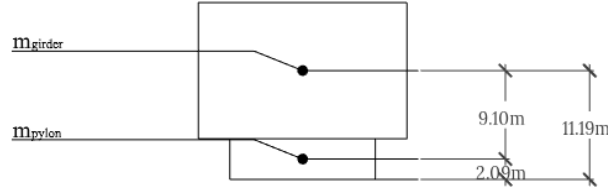


Figure A.10: Pontoon 1 pylon and girder centers of mass.

The calculation of the center of gravity is done using the expression in Equation A.4. This is done only in the vertical z -direction, due to the axial symmetry of the pontoons.

$$z_{CoG} = \frac{\sum m_i z_i}{\sum m_i} \quad (\text{A.4})$$

In which;

z_{CoG} is the z -coordinate of the center of gravity

m_i is the mass of element i

z_i is the z -coordinate of element i 's center of gravity

Performing the calculation for the girder and pylon leads to the combined center of gravity for the two elements displayed in Figure A.11. This figure also displays the locations of the centers of gravity of the other structural elements in the pontoon.

Recognizing that all the centers of gravity share the same horizontal coordinate, Equation A.4 is used to determine the center of gravity \underline{G} of the entire structure. Simultaneously the center of buoyancy \underline{B} is determined. This is the location through which the buoyancy force calculated earlier acts in positive z -direction. The center of buoyancy is defined as the center of the displaced volume ∇ . Finally, the metacenter \underline{M} of the structure is calculated. When the structure experiences a rotation through an angle of heel, the submerged volume ∇ changes and thus the center of buoyancy \underline{B} moves to new position. The metacenter \underline{M} , N_ϕ is the point where the work line of the buoyancy force in the undisturbed situation intersects the work line of the buoyancy force in the rotated situation. The expression for the calculation of the metacenter \underline{M} , N_ϕ position for symmetric, wall-sided structures is displayed in Equation A.5. From this equation it is apparent that for small angles of heel ϕ , the metacenter \underline{M} is different from the metacenter \underline{N}_ϕ when the angle of heel ϕ is larger. This is due to the $\tan \phi^2$ term.

$$\underline{BN}_\phi, \underline{BM} = \frac{I_T}{\nabla} \left(1 + \frac{1}{2} \tan^2 \phi \right) \quad (\text{A.5})$$

In which;

\underline{BN}_ϕ is the distance between center of buoyancy \underline{B} and the metacenter N_ϕ in case of a large heel angle ϕ

\underline{BM} is the distance between center of buoyancy \underline{B} and the metacenter \underline{M} in case of a small heel angle ϕ

I_T is the transverse moment of inertia of the section plane cut by the water surface about the axis of inclination according to Equation A.6

∇ is the displaced volume of water, the pontoon volume under the water line, which does not change for a symmetric structure

ϕ is the angle of heel

Equation A.6 displays the expression for the transverse moment of inertia of the pontoon section plane cut by the water line about the axis of rotation. This expression takes into account that the shape of the section plane cut by the water line changes from circular to elliptical with an increasing heel angle ϕ .

$$I_T = \frac{\pi}{4} r (\cos \phi r)^3 \quad (\text{A.6})$$

In which;

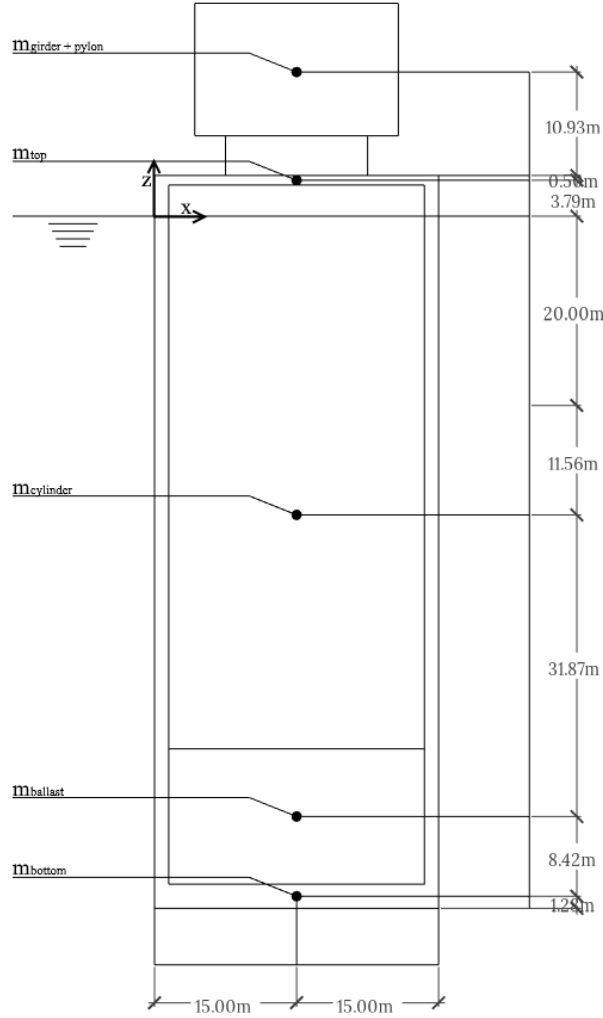


Figure A.11: Pontoon 1 centers of gravity.

I_T is the transverse moment of inertia

r is the pontoon radius

ϕ is the angle of heel

Figure A.12 displays \underline{B} , \underline{G} and \underline{M} calculated using Equation A.5 with $\phi = 0$. That the metacenter location is above the center of gravity shows that the pontoon is theoretically stable, it will right itself when small angles of heel ϕ are applied.

To determine the restoring moment M_{res} , a heel angle ϕ is applied to the pontoon. Figure A.13 displays the heeled situation. The restoring moment is the result of the move of the center of buoyancy \underline{B} to its new position in the heeled situation \underline{B}_ϕ and the lever arm about the center of gravity \underline{G} this creates. The restoring moment is calculated using the expressions in Equations A.7 and A.8.

$$M_{res} = \rho g \nabla \underline{GZ} \quad (\text{A.7})$$

In which;

M_{res} is the restoring moment

ρ is the mass density of the sea water

g is gravitational acceleration, to be taken as 9.81 m s^{-2}

∇ is the submerged volume

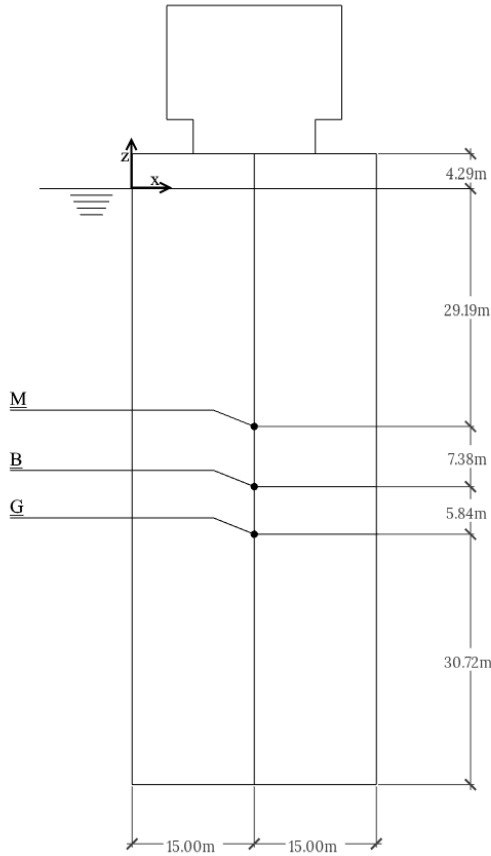


Figure A.12: Pontoon 1 center of gravity, center of buoyancy and metacenter.

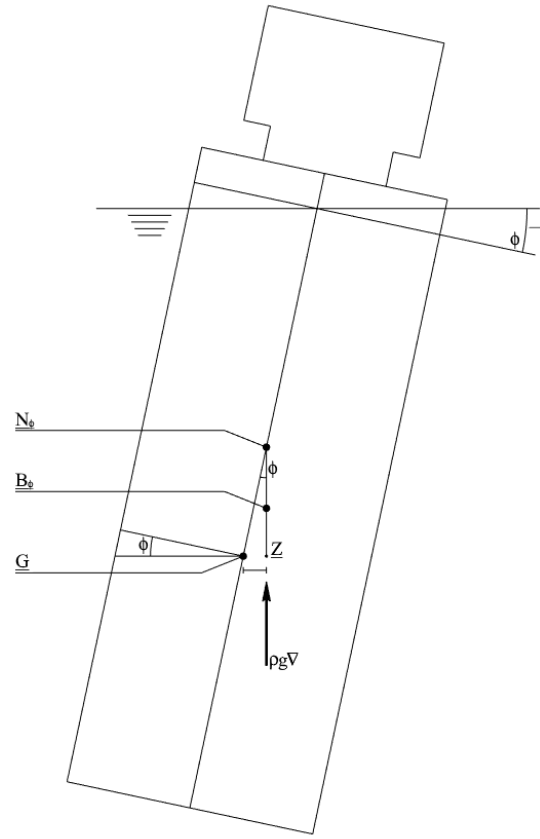


Figure A.13: Pontoon 1 center of gravity, center of buoyancy and metacenter in heeled situation.

\underline{GZ} is the restoring moment lever arm, according to Equation A.8.

$$\underline{GZ} = \underline{BN}_\phi + (\underline{B} - \underline{G}) \sin \phi \quad (\text{A.8})$$

In which;

\underline{GZ} is the restoring moment lever arm

\underline{BN}_ϕ is the distance between the undisturbed center of buoyancy \underline{B} and the metacenter \underline{N}_ϕ

\underline{B} is the location of the undisturbed center of buoyancy

\underline{G} is the location of the center of gravity of the structure

ϕ is the angle of heel

The result of the preceding calculation for pontoon 1 is displayed in Figure A.14. It should be noted that while the figure shows angles of heel between $-\pi$ rad and π rad, this expression is not accurate for such heel angles as they would suggest the pontoon is upside down. Furthermore, the expression does not take into account the change in shape of the section plane cut by the water line once the top corner of the pontoon gets submerged.

As is shown in Figure A.13, the heel prescribed at the water level is the same rotation the center of gravity experiences. The restoring moment in relation to the angle of rotation of the center of gravity can be expressed as a rotational stiffness of the structure about the center of gravity for rotation about the horizontal axes. The linear approximation to the restoring moment for small angles of heel displayed in Figure A.14 can be equated to the spring stiffness of a rotational spring acting in the center of gravity of the pontoon for rotation about the horizontal x- and y-axis. In the same manner the buoyancy force can be equated to the spring stiffness of a spring acting in the center of buoyancy of the pontoon, for

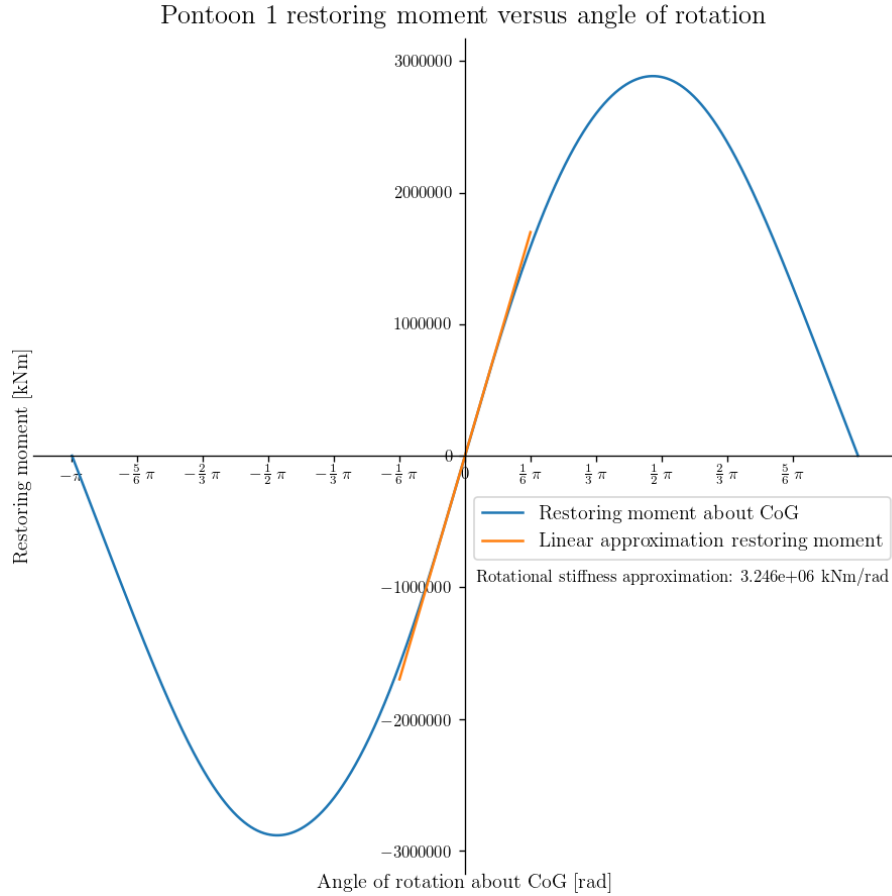


Figure A.14: Pontoon 1 restoring moment versus angle of heel.

translation in the vertical z -direction. This linearisation of the non-linear restoring moment caused by the buoyancy force is necessary for dynamic analysis and greatly simplifies static analysis. The calculation of the buoyancy stiffness, rotational stiffness and the center of buoyancy and gravity where the springs with this stiffness are applied is performed for all pontoons. The results of this calculation are displayed in Table A.9. Because the bridge is point symmetric in the main span mid-point, the values for the first 11 pontoons are shown.

The mechanical model incorporating these springs is displayed for pontoon 1 in Figure A.15.

Number	z-coordinate Center of gravity [m]	x-coordinate Center of gravity [m]	Rotational stiffness k_r [kN m rad ⁻¹]	z-coordinate Center of buoyancy [m]	x-coordinate Center of buoyancy[m]	Buoyancy stiffness k_{buoy} [kN m ⁻¹]
1	-42.16	15	$3.246 \cdot 10^6$	-36.56	15	7038.29
2	-54.0	18	$9.388 \cdot 10^6$	-44.4	18	10135.14
3	-60.96	18	$1.191 \cdot 10^7$	-49.91	18	10135.14
4	-67.73	18	$1.47 \cdot 10^7$	-55.25	18	10135.14
5	-73.36	18	$1.724 \cdot 10^7$	-59.7	18	10135.14
6	-79.88	18	$2.054 \cdot 10^7$	-64.75	18	10135.14
7	-68.03	21	$2.125 \cdot 10^7$	-54.9	21	13795.06
8	-76.99	21	$2.761 \cdot 10^7$	-61.5	21	13795.06
9	-75.08	21	$2.593 \cdot 10^7$	-60.3	21	13795.06
10	-83.0	21	$3.152 \cdot 10^7$	-66.55	21	13795.06
11	-80.83	26	$4.3 \cdot 10^7$	-66.75	26	21146.17

Table A.9: Pontoon dimensions and coordinates.

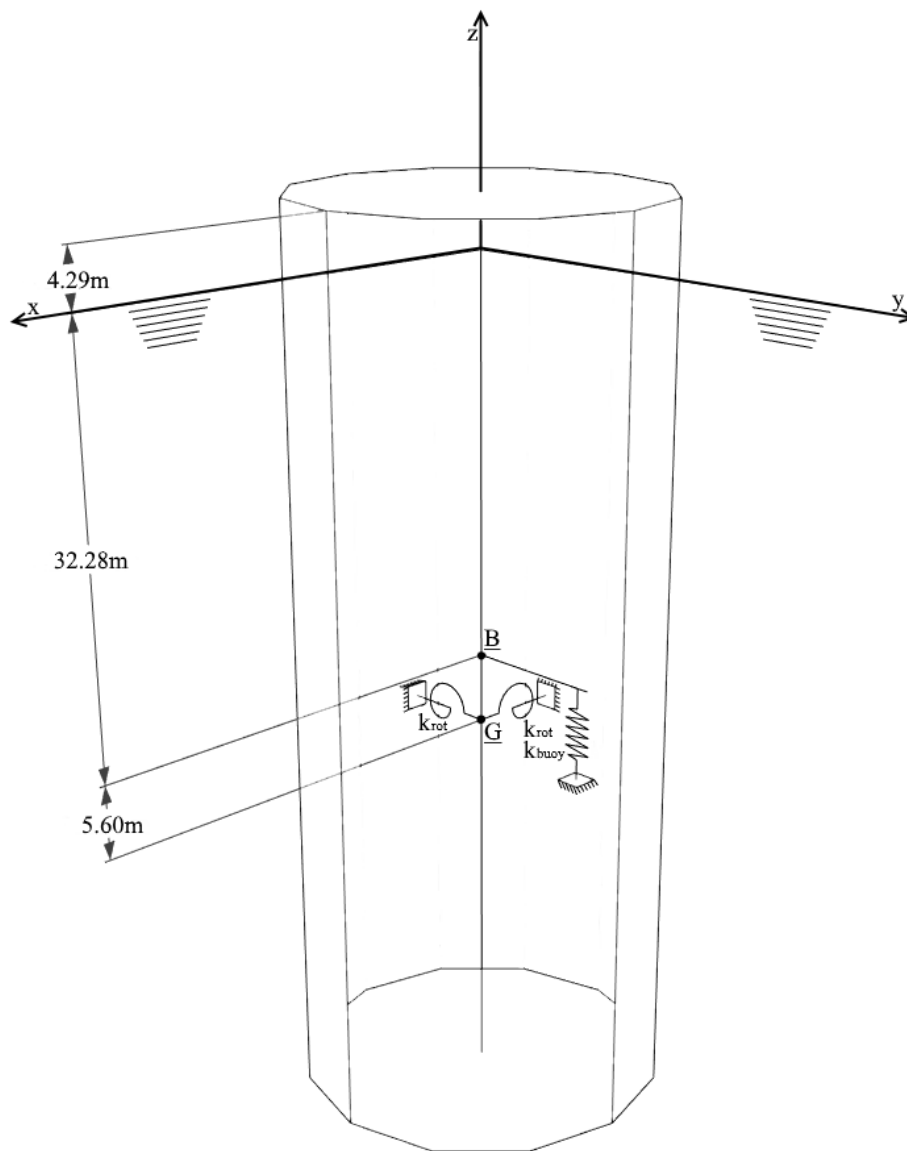


Figure A.15: Pontoon 1 mechanical model.

A.5 Cable System

The cable system is designed using two main cables anchored at the shores and lateral cables connecting each pontoon to the main cables. This leads to system containing a total of 46 cables. The cable characteristics can be found in Table A.10. Lateral cable lengths are displayed in Figure A.16 [Yip15]. The lateral cable lengths for the other half of the span are mirrored and the main cables have a total length of 4465 m. Internal cable geometry and layout has not been designed in any of the previous work performed on the bridge design. All that has been researched is the cable layout and steel cross section required per cable. Reference is made to appendix C for the detailed design of the main and lateral cables.

	Diameter [mm]	Material	Tensile strength [N mm ⁻²]	Modulus of elasticity [N mm ⁻²]	Mass den- sity in air [kg m ⁻²]
Main cables	1200	Y1860	1860	195000	7850
Lateral cables	350	Y1860	1860	195000	7850

Table A.10: Cable characteristics.

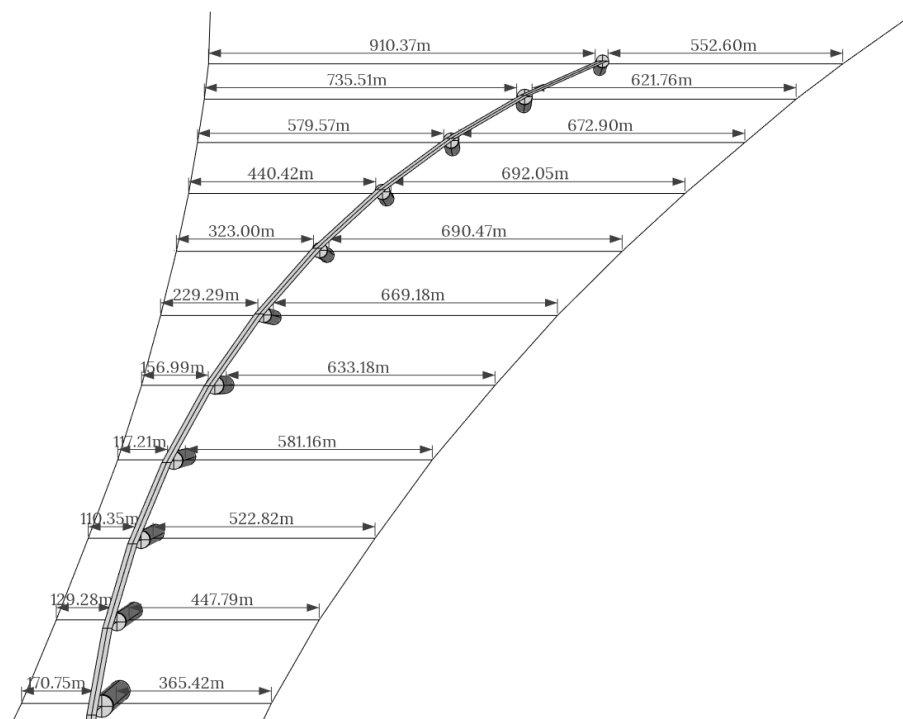


Figure A.16: Lateral cable lengths.

Appendix B

Loads

This appendix contains detailed information on the different loads on the bridge system. As a reference, Figure B.1 displays the location of the bridge.

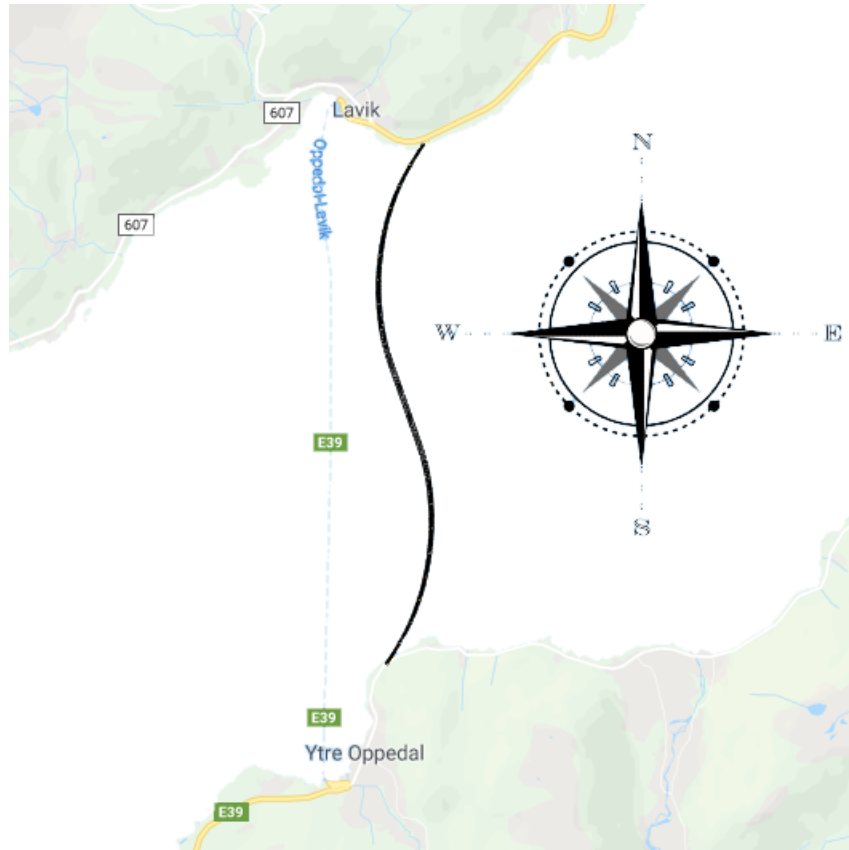


Figure B.1: Bridge location (Google Maps).

B.1 Wave loading

The waves considered at the bridge location are wind waves. Wind waves are measured at three locations in the fjord crossing: at the north shore, at the middle and at the south shore [al11]. The extreme values of the wind wave height, relative to the North, obtained from these measurements are displayed in Figure B.2.

The different wave characteristics are presented in Table B.1.

From these wave characteristics the applicable wave theory can be calculated. Figure B.3 displays the ranges of validity for the different wave theories. Table B.2 displays the measure of shallowness and steepness for the different measured wave regimes in $Ft s^{-2}$, as used in Figure B.3.

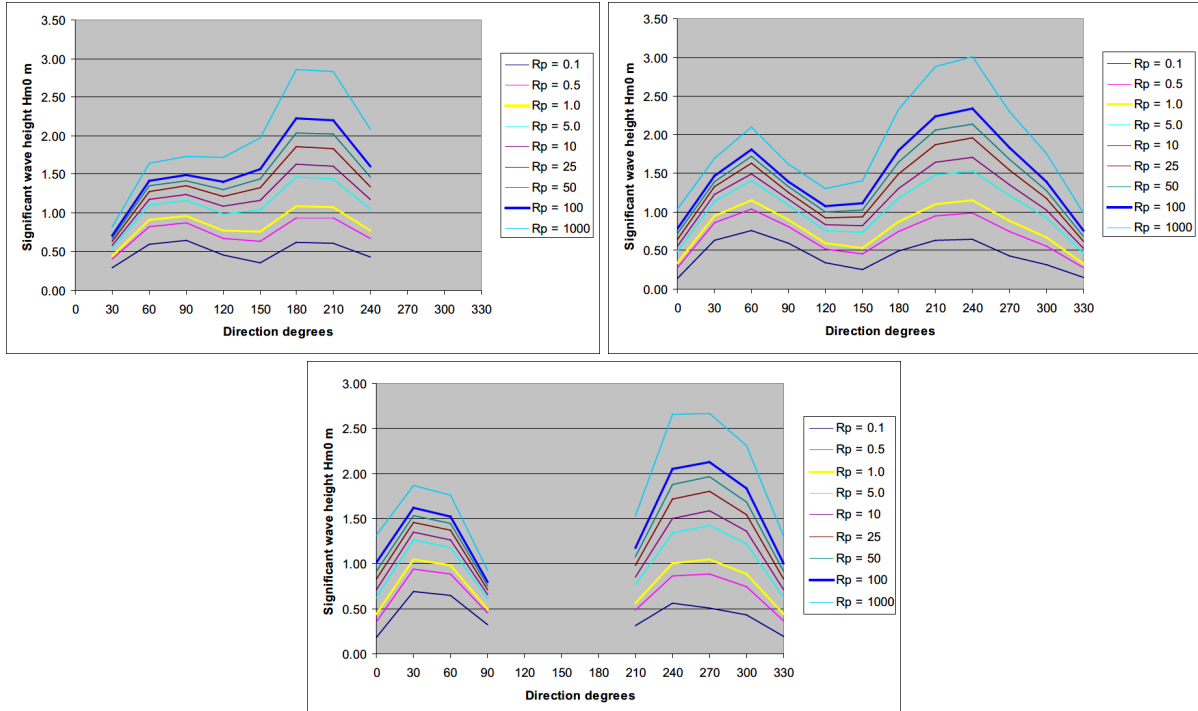


Figure B.2: Extreme values wind wave height per reference period vs. direction at respectively, the north shore, mid-fjord and the south shore [al11].

Parameter		Wind waves		
		North side	Mid-fjord	South side
Significant wave height	H_s [m]	2.22	2.34	2.13
Spectral top period	T_p [s]	4.6	4.8	4.8
Direction	[$^\circ$]	180	240	270
Maximum single wave height	H_{max} [m]	4.55	4.79	4.36
Wave length	λ [m]	33	36	36

Table B.1: Wave characteristics at the bridge location.

Wave	Shallowness characteristic $\left[\frac{d}{T_p^2}\right] [Ft s^{-2}]$	Steepness characteristic $\left[\frac{H_s}{T_p^2}\right] [Ft s^{-2}]$	Wave theory
Wind waves north side	186.059	0.3442	Third order Stokes
Wind waves mid-fjord	170.8771	0.3332	Third order Stokes
Wind waves south side	170.8771	0.3033	Third order Stokes

Table B.2: Wave steepness and shallowness characteristics.

For the loading of submerged structures by waves, the Morison equation is the most widely used expression to calculate the exerted force. The Morison equation does not, however, apply to large structures. Large structures have diameters that are larger than the wavelength divided by 6 ($D > \frac{\lambda}{6}$) [DNV10]. As can be seen in Tables B.1 and B.21, the wave length of the wind waves range between

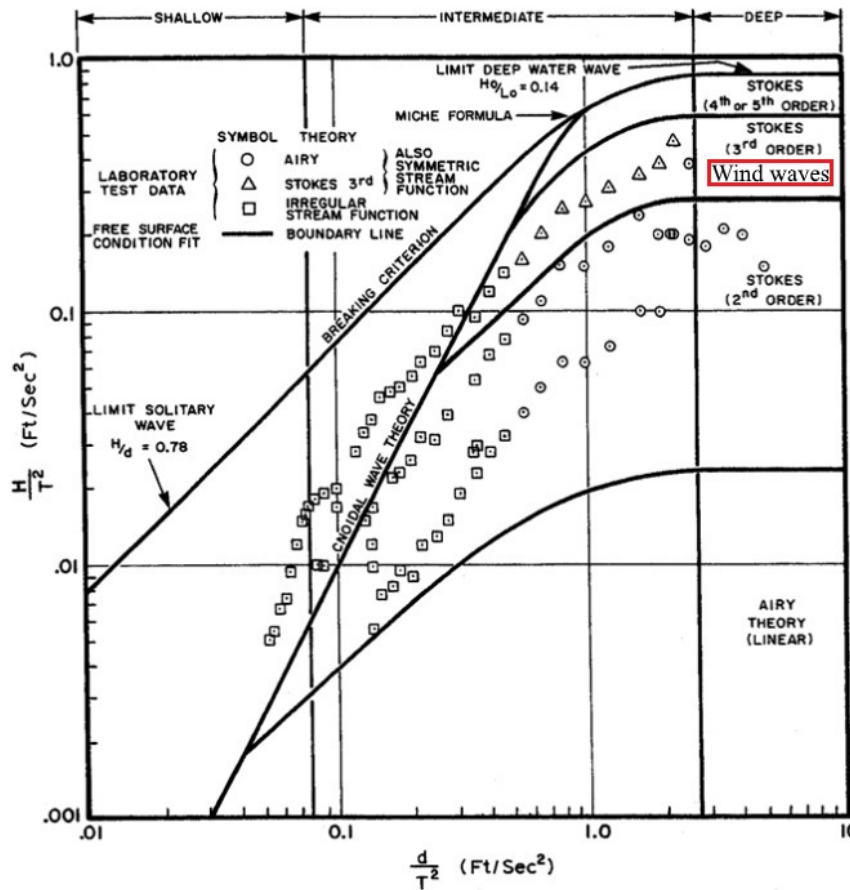


Figure B.3: Ranges of validity for various wave theories. The horizontal axis is a shallowness characteristic, the vertical axis is a deepness characteristic [DNV10] [Cha87]. The position of the occurring waves is marked with their name.

33-36 m and the pontoon diameters between 30-52 m. This is clearly outside the application range of the Morison Equation. To find the right theory model to calculate the wind wave loads on the pontoons the DNV-RP-C205 [DNV10] provides the figure displayed in Figure B.4. In this figure the ratios between significant waveheight H , the pontoon diameter D and the wavelength of the wave λ lead to a modelling 'region'.

In table B.3 the limits to these ratios for the different wave characteristics and pontoon dimensions are shown.

	Lower limit	Upper limit
$\frac{H}{D}$	0.04	0.08
$\frac{\pi D}{\lambda}$	2.6	4.9

Table B.3: Ratio limits of wave and pontoon characteristics.

Comparing the ratios from Table B.3 with Figure B.4 clearly shows that the pontoon dimensions and wave characteristics land in the 'Diffraction region'. This means that the incident wave field will be significantly deformed by the presence of the pontoons and the diffraction theory of wave scattering around the body can to be used. An analytical solution for a vertical cylinder is available, it is called the MacCamby Equation and shown in Equation B.1 [**maccamby-diffraction**]. This expression assumes that the incident waves are plane waves, which means that the wave height is constant perpendicular to the wave propagation direction. This is a conservative assumption and thus safe, since wave loading on a vertical cylinder is maximal when the incident waves are plane waves [Zhu93]. This expression assumes the incident waves are linear, or airy, waves. This means this expression may be used to roughly compute

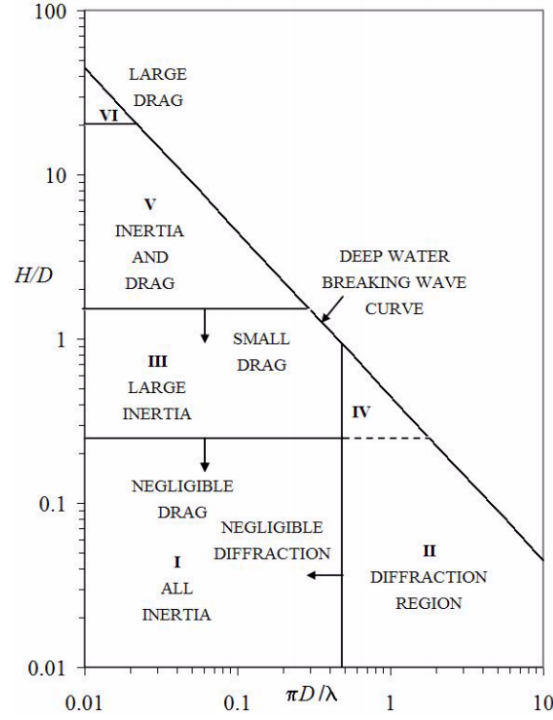


Figure B.4: Different wave force regimes [DNV10] [Cha87].

the wave loading by the 3rd order Stokes waves found in the critical wave conditions, since it leaves out higher order terms. Equation B.5 provides an expression for the load taking into account 2nd and higher order terms [maccamby-diffraction].

$$F_x = \frac{2 g H}{k} \frac{\cosh(k(d+z))}{\cosh(kd)} \frac{1}{\sqrt{J_1' \left(\frac{\pi D}{\lambda} \right)^2 + Y_1' \left(\frac{\pi D}{\lambda} \right)^2}} \cos(\omega t - \alpha) \quad (\text{B.1})$$

In which;

F_x is the x-component of the force on the cylinder per unit length in the z-direction, at depth z

g is the gravity acceleration, to be taken as 9.81 m s^{-2}

H is the wave height

k is the wave number according to Equation B.3

d is the water depth

z is the elevation below mean sea level

J_1' is the first derivate of the first-kind Bessel function of the first order

Y_1' is the first derivate of the second-kind Bessel function of the first order

D is the pontoon diameter

λ is the incident wave length

ω is the angular frequency of the wind wave, according to Equation B.4

α is a phase angle correction according to Equation B.2

Equation B.2 provides an expression for the phase angle correction.

$$\alpha = \arctan \frac{J_1' \left(\frac{\pi D}{\lambda} \right)}{Y_1' \left(\frac{\pi D}{\lambda} \right)} \quad (\text{B.2})$$

In which;

α is the phase angle correction

J_n' is the first derivative of the first-kind Bessel function of the first order

Y_n' is the first derivative of the second-kind Bessel function of the first order

D is the pontoon diameter

λ is the incident wave length

Equations B.3 and B.4 provide expressions for the wave number and the angular frequency, respectively.

$$k = \frac{2\pi}{\lambda} \quad (\text{B.3})$$

In which;

k is the wave number

λ is the wave length

$$\omega = \frac{2\pi}{T_p} \quad (\text{B.4})$$

In which;

ω is the angular frequency

T_p is the spectral top period

As mentioned earlier, Equation B.5 provides an expression for the force on a vertical cylinder per unit length in the z-direction including second order terms. In the formulation of this expression, the assumption has been made that the wave diffraction for large cylinders is the same as for small cylinders [**maccamby-diffraction**].

$$F_x = \frac{\rho g \pi D H}{2} \left(\frac{\cosh(k(d+z))}{\cosh(kd)} \frac{\pi D}{\lambda} \sin(\omega t) + \frac{\pi H}{\lambda} \left(\frac{3 \cosh(2k(d+z))}{4 \sinh^3(kd) \cosh(kd)} - \frac{1}{2 \sinh(2kd)} \right) \frac{2\pi D}{\lambda} \sin(2\omega t) \right) \quad (\text{B.5})$$

In which;

F_x is the x-component of the force on the cylinder per unit length in the z-direction, at depth z

g is the gravity acceleration, to be taken as 9.81 m s^{-2}

H is wave height

k is the wave number according to Equation B.3

d is the water depth

z is the elevation below mean sea level

D is the pontoon diameter

λ is the incident wave length

ω is the angular frequency of the wind wave, according to Equation B.4

Integrating the results of Equations B.1 and B.5 from the bottom of the pontoon to the water level provides the total load on the pontoon. To observe the difference in loading between the first order and second order MacCamby expressions and the loads calculated by the Morison expression shown in Equation B.6, the integrated total loads for pontoon one with the extreme wave case in the direction 180° relative to the North is plotted in Figure B.5.

$$q_N = \rho C_M A \dot{v} + \frac{1}{2} \rho C_D D v |v| \quad (\text{B.6})$$

In which;

q_N is the sectional load on the pontoon

ρ is the mean density of water, to be taken as 1015 kg m^{-3} [Cij18]

C_M is the effective inertia coefficient

A is the section area of the pontoon

\dot{v} is the horizontal particle acceleration, according to Equation B.7

C_D is the drag coefficient, to be taken as 1.0 [DNV10]

D is the diameter of the pontoon

v is horizontal particle velocity, according to Equation B.8

Equations B.7 and B.8 provide expressions for the horizontal particle acceleration and velocity according to the Stokes wave theory to be used in Equation B.6.

$$\dot{v} = \frac{2 \pi^2 H_s}{T_p^2} \frac{\cosh(k(z+d))}{\sinh(kd)} \sin \theta + \frac{3 \pi^2 H_s}{T_p^2} \frac{\pi H_s}{\lambda} \frac{\cosh(2k(z+d))}{\sinh(kd)^4} \sin(2\theta) \quad (\text{B.7})$$

In which;

v is horizontal particle acceleration

H_s is the significant wave height

T_p is the spectral top period

k is the wave number

z is the elevation below mean sea level

λ is the wave length

θ is equal to ωt

ω is the wave angular frequency

t is time

$$v = \frac{\pi H_s}{T_p} \frac{\cosh(k(z+d))}{\sinh(kd)} \cos \theta + \frac{3}{4} \frac{\pi H_s}{T_p} \frac{\pi H_s}{\lambda} \frac{\cosh(2k(z+d))}{\sinh(kd)^4} \cos(2\theta) \quad (\text{B.8})$$

In which;

v is horizontal particle velocity

H_s is the significant wave height

T_p is the spectral top period

k is the wave number

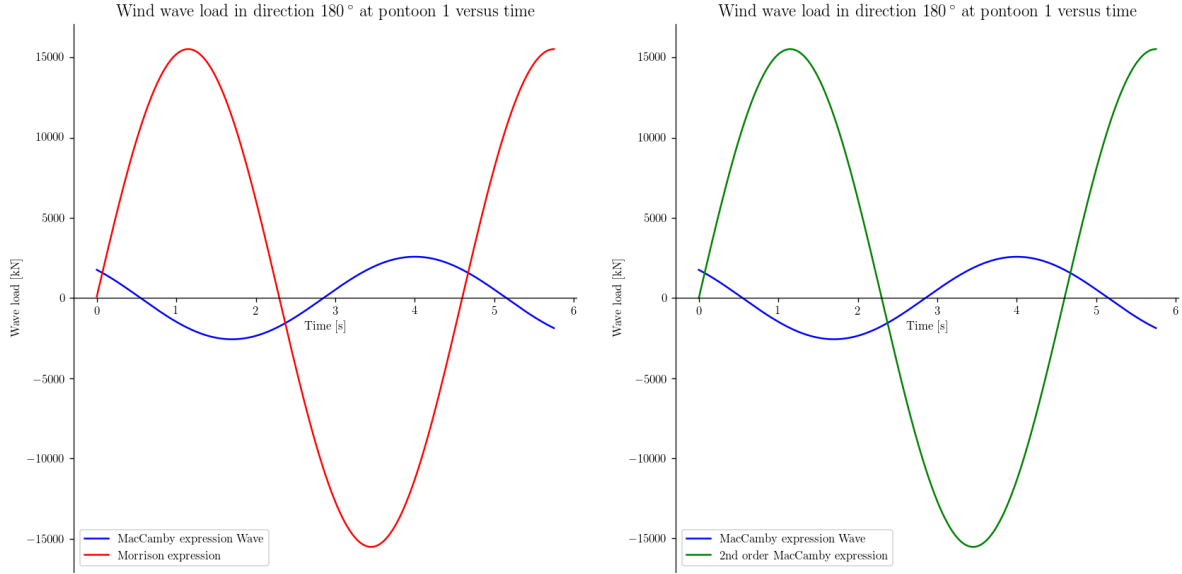


Figure B.5: Comparison of the first and second order MacCamby and Morison wave load calculation for extreme wave case 180° relative to the North for pontoon 1.

z is the elevation below mean sea level

ω is the wave angular frequency

The results displayed in Figure B.5 clearly show that the Morison equation produces wave loads of up to a factor six higher than the first order MacCamby expression. Furthermore, due to the assumption of small cylinders in the formulation of the second order MacCamby wave load expression, it turns into the Morison equation and is inapplicable for the combination of waves and pontoons in the bridge design.

Since most modelling software calculates wave loads using the Morison equation, it is of significant value to be able to model the actual load on the pontoons using a (scaled) form of the Morison equation. For this purpose a test wave is defined, with the same wave parameters as the observed wind wave, but the significant wave height which has been divided by a factor six, as this is the factor between the maximum loads observed in Figure B.5. The results of this test are shown in Figure B.6.

The result of this first test shows that 'scaling' the waves produces accurate results in terms of the maximum total load on the pontoons and thus Equation B.9 is obtained for the scaling factor.

$$s_{factor} = \frac{\max(F_{MacCamby})}{\max(F_{Morison})} \quad (B.9)$$

In which;

$\max(F_{MacCamby})$ is the maximum occurring load in a wave period according to the MacCamby expression

$\max(F_{Morison})$ is the maximum occurring load in a wave period according to the Morison expression

This scaling factor is then applied to the significant wave height H_s . Figure B.6 also displays a clear phase shift. This phase shift can be accounted for by shifting the result of the Morison expression for the test wave over a phase angle ϕ , as displayed in Figure B.7.

This phase shift ϕ is incorporated in the incident wave phase angle θ as expressed in Equations B.10 and B.11.

$$\phi = \phi_{time} \omega \quad (B.10)$$

In which;

ϕ is the phase shift in rad

ϕ_{time} is the phase shift in s

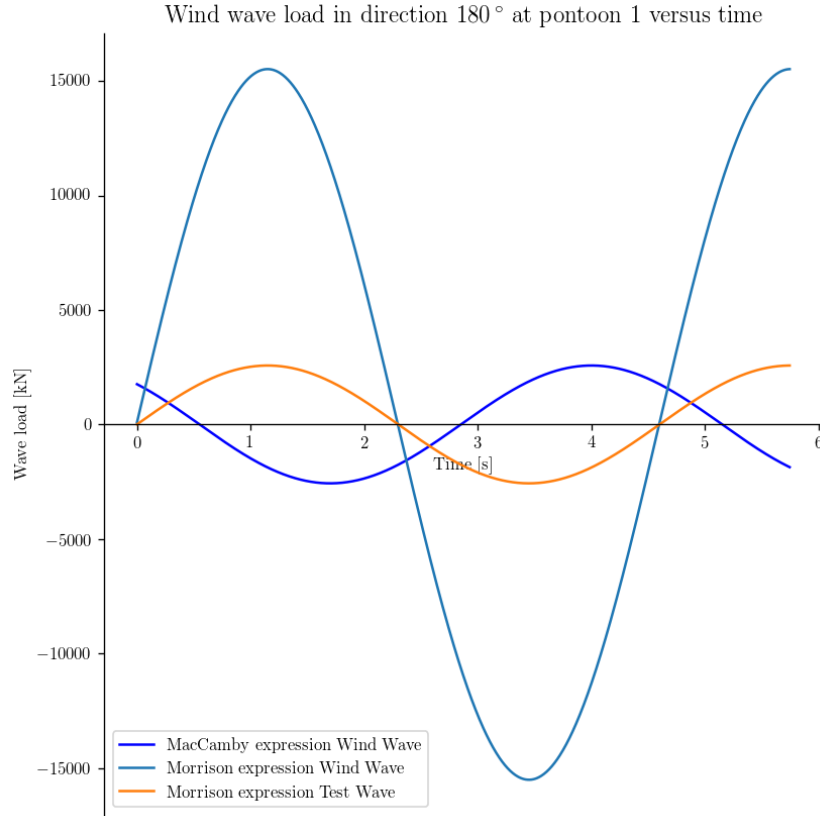


Figure B.6: Comparison of the wave load using the MacCamby and Morison expression for an observed wind wave and a scaled test wave

ω is the angular frequency according to Equation B.4

$$\theta = \omega t + \phi \quad (\text{B.11})$$

In which;

θ is the phase angle of the incident wave

ω is the angular frequency according to Equation B.4

ϕ is the phase shift according to Equation B.10

This method of scaling waves works well for waves on single pontoons. However, every combination of pontoon dimensions and wave characteristics leads to different scaling factors and phase shifts. This is displayed in Tables B.4 and B.5. Since the water local water depth at the pontoons is part of the calculations of the wave loads on the pontoons, it is expected that these values are not point symmetric in the bridge mid-point. Therefore, the scaling factors and phase shifts for all 22 pontoons have been calculated. From the results it has become clear that the local water depth has very little influence on these values and the scaling factors and phase shifts are equal for the same pontoon dimensions and wave conditions, regardless of local water depth. Therefore, only the results for the first 11 pontoons are displayed, since the bridge design is point symmetric in its mid-point. It is clear that there is quite a spread in both scaling factors and phase shifts for the different combinations of pontoons and wave conditions. This will provide a challenge in the modelling of the wave loads on the pontoons using computer software, since the wave conditions have to be scaled differently for the different pontoons. This would mean creating multiple wave conditions and in- or excluding pontoons from certain wave condition loading. This is not a common option in software packages. Another option is to model a wave using average values for the scaling and phase shift. Since the extremes are quite a bit apart, this would be a huge and unacceptable approximation of the actual conditions on the Sogne fjord.

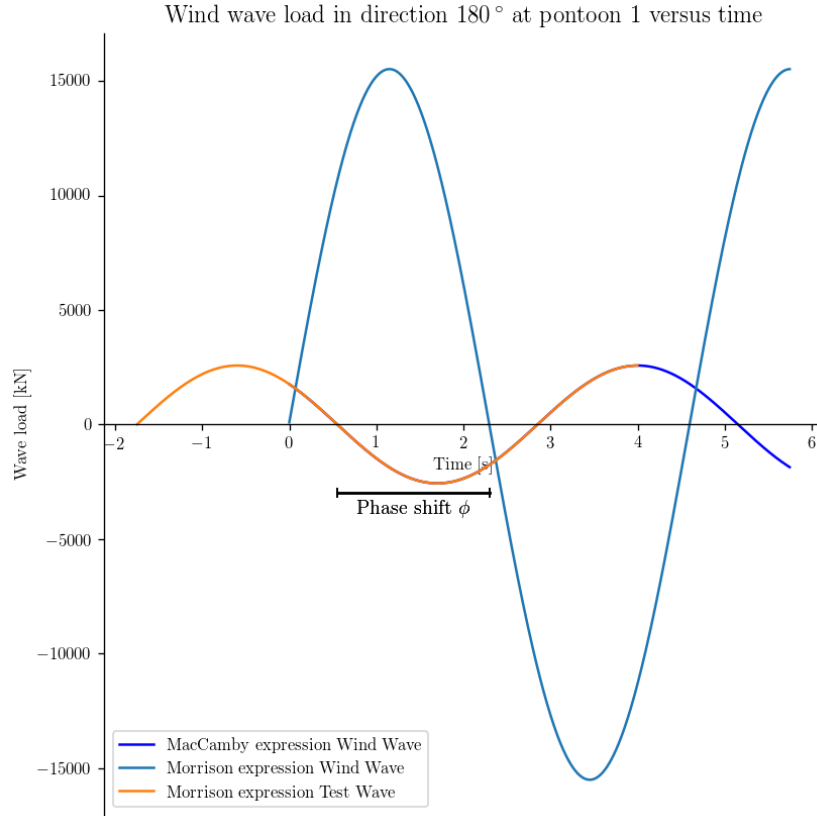


Figure B.7: Comparison of the wave load using the MacCamby and Morison expression for an observed wind wave and a scaled test wave, shifted to fit to the MacCamby expression

Pontoon number	Wind wave direction 180°	Wind wave direction 240°	Wind wave direction 270°
1	0.1658	0.1884	0.1884
2	0.1262	0.1435	0.1435
3	0.1262	0.1435	0.1435
4	0.1262	0.1435	0.1435
5	0.1262	0.1435	0.1435
6	0.1262	0.1435	0.1435
7	0.1001	0.1139	0.1139
8	0.1001	0.1139	0.1139
9	0.1001	0.1139	0.1139
10	0.1001	0.1139	0.1139
11	0.0727	0.0826	0.0826
Average	0.1154	0.1313	0.1313

Table B.4: Scaling factors for the different pontoon and wave combinations.

Another method to scale Morison wave loads to fit to the MacCamby expression is to modify the Morison equation to fit the total load of the MacCamby expression [Cha87]. The expression this produces is displayed in Equation B.12.

$$f_x = \rho C_M A \dot{v} \quad (\text{B.12})$$

In which;

Pontoon number	Wind wave direction 180°	Wind wave direction 240°	Wind wave direction 270°
1	-2.419	-2.1782	-2.1782
2	-2.9083	-2.6373	-2.6373
3	-2.9083	-2.6373	-2.6373
4	-2.9083	-2.6373	-2.6373
5	-2.9083	-2.6373	-2.6373
6	-2.9083	-2.6373	-2.6373
7	-0.4094	-3.119	-3.119
8	-0.4094	-3.119	-3.119
9	-0.4094	-3.119	-3.119
10	-0.4094	-3.119	-3.119
11	-1.2825	-0.8008	-0.8008
Average	-1.8073	-2.6038	-2.6038

Table B.5: Phase shifts for the different pontoon and wave combinations in [rad].

f_x is the x-component of the force on the cylinder per unit length in the z-direction, at elevation z

C_M is the effective inertia coefficient according to Equation B.13

A is the pontoon sectional area

\dot{v} is the water particle acceleration at an elevation z according to Equation B.7, with a phase shift $\phi = -\alpha + \frac{\pi}{2}$

The effective inertia coefficient is obtained using the expression shown in Equation B.13.

$$C_M = \frac{4}{\pi (k a)^2 \sqrt{J_1'(k a)^2 + Y_1'(k a)^2}} \quad (\text{B.13})$$

In which;

C_M is the effective inertia coefficient

k is the wave number according to Equation B.3

a is the pontoon radius

J_1' is the first derivative of the first-kind Bessel function of the first order

Y_1' is the first derivative of the second-kind Bessel function of the first order

Most software supports the option to specify the effective inertia and drag coefficient for structural elements per wave condition. This would mean setting the effective inertia coefficient C_M to the value calculated using Equation B.13 and the drag coefficient C_D to zero. The results of this modification are shown in Figures B.8 and B.9. Figure B.8 shows the Morison equation with the modified values of C_M and C_D implemented versus the MacCamby expression for pontoon number one under the wave condition with an angle of 180° relative to the North. Figure B.9 adds in the effect of the phase shift ϕ as described in Equation B.12.

From these figures it is clear that modifying the Morison expression according to Equation B.12 produces accurate results for the total load on the pontoons in comparison to the MacCamby expression. Since this method allows for the modification of the C_M and C_D values per pontoon per wave condition, this method is applicable in the software modelling of wave loads on the pontoons. The values of C_M per pontoon per wave condition are displayed in Table B.6. The results once again agree with the point-symmetric design of the bridge and thus the results for the first 11 pontoons are displayed.

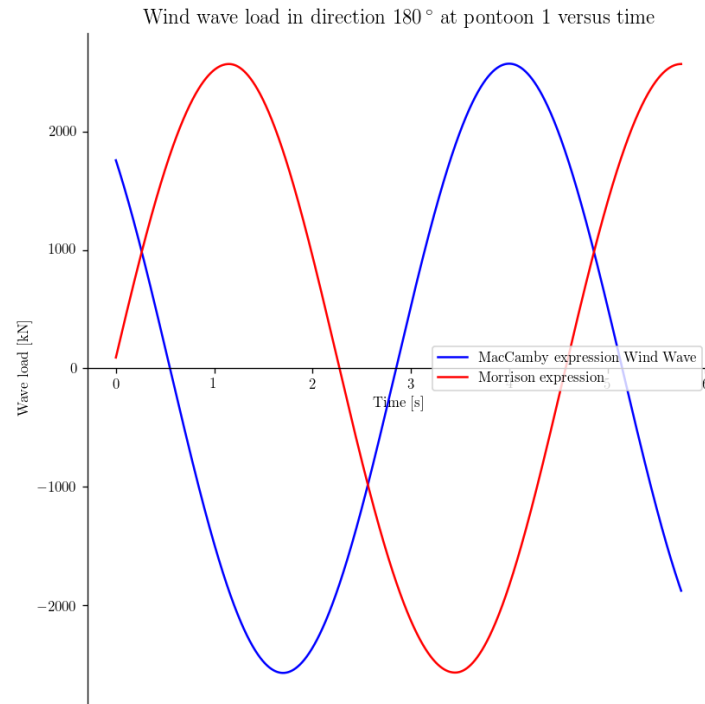


Figure B.8: Comparison of the wave load on pontoon one under the wave condition with an angle of 180° relative to the North using the MacCamby expression and Morison expression with modified C_M and C_D values.

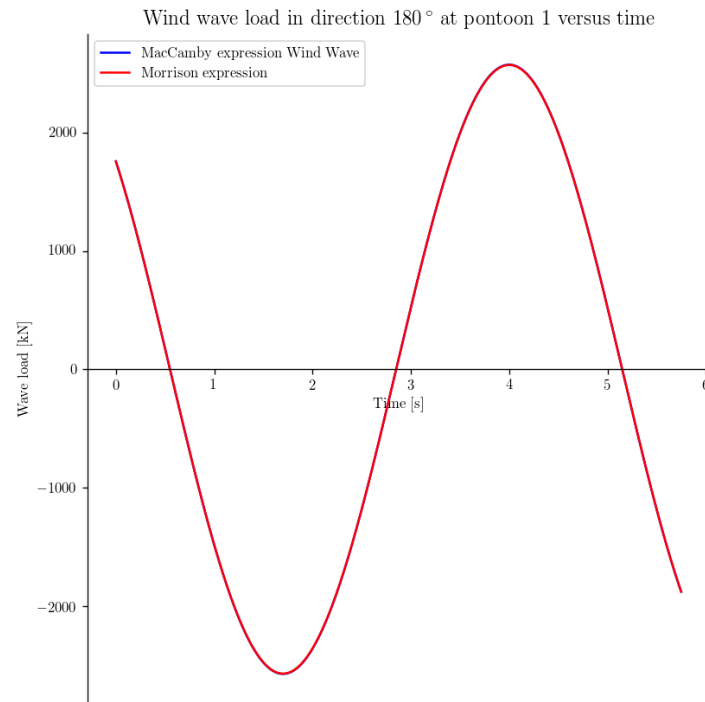


Figure B.9: Comparison of the wave load on pontoon one under the wave condition with an angle of 180° relative to the North using the MacCamby expression and Morison expression with modified C_M and C_D values and the phase shift ϕ

Pontoon number	Wind wave direction 180°	Wind wave direction 240°	Wind wave direction 270°
1	0.3312	0.3771	0.3771
2	0.2521	0.2872	0.2872
3	0.2521	0.2872	0.2872
4	0.2521	0.2872	0.2872
5	0.2521	0.2872	0.2872
6	0.2521	0.2872	0.2872
7	0.2	0.228	0.228
8	0.2	0.228	0.228
9	0.2	0.228	0.228
10	0.2	0.228	0.228
11	0.1451	0.1654	0.1654

Table B.6: C_M values per pontoon per wave condition.

B.2 Current loading

The current loading occurring at the bridge location is based on tests and calculations performed by SINTEF [al11]. The direction of the inward current in reality and translated to the bridge model used in this thesis is shown in Figure B.10.

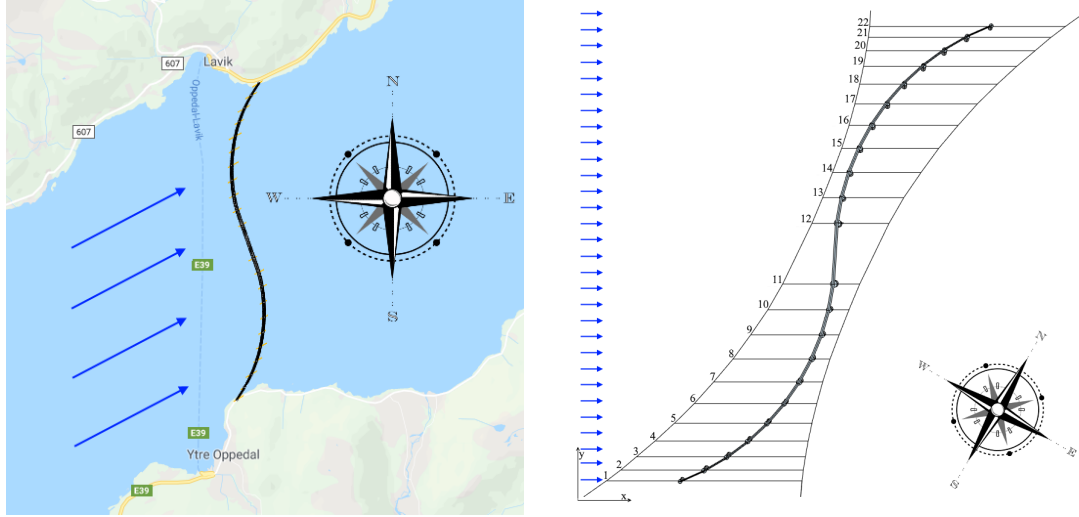


Figure B.10: Current flow direction in reality (left, Google Maps) and in the bridge model (right).

The values determined by SINTEF are depicted in Table B.7 and the power law current profile fit to the inward current data is depicted in Figure B.11. The power law current profile is calculated by fitting the provided measurements to Equation B.14 [DNV10] using a Python curve fitting regression tool.

Inwards - 60°		Outwards - 240°	
Depth	Velocity	Depth	Velocity
10 m	1.27 m s ⁻¹	10 m	1.06 m s ⁻¹
30 m	0.48 m s ⁻¹	30 m	0.55 m s ⁻¹
70 m	0.39 m s ⁻¹	70 m	0.44 m s ⁻¹

Table B.7: In- and outward current profile.

$$v_{c,tide}(z) = v_{c,tide}(0) \left(\frac{d+z}{d} \right)^\alpha \quad (\text{B.14})$$

In which;

$v_{c,tide}(z)$ is the current velocity at depth z

z is the depth

d is the local water depth

α is a scaling factor, to be fit to the provided data

For most analyses it is sufficient to compute the drag force the constant current applies to the different structural elements according to Equation B.15 and sum it with the other loads applied to the system. This method is used by SACS to accommodate current loading.

$$f_N(t) = \frac{1}{2} \rho C_D D v |v| \quad (\text{B.15})$$

In which;

$f_N(t)$ is the sectional force on a member

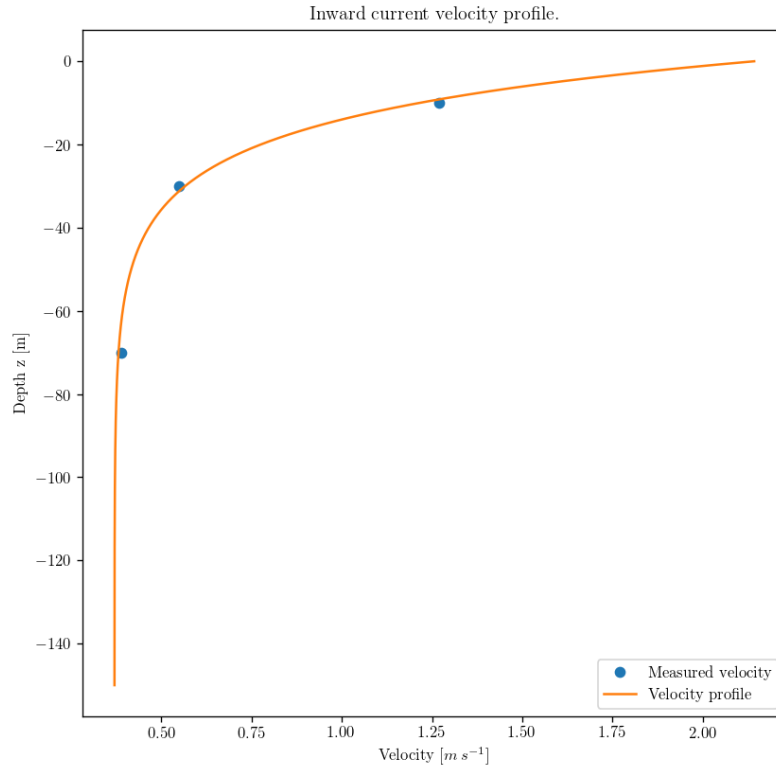


Figure B.11: Inward current velocity profile.

ρ is the water density

C_D is the coefficient of drag

D is the member diameter

v is the current velocity

Special care should be taken for the phenomenon of vortex induced vibrations, for which reference is made to appendix J.

B.3 Traffic loading

Static traffic loads have been a part of a previous study [Cij18]. The loads induced by traffic moving across the bridge are assumed to be much less significant than the wave and current loading found at the bridge location and is therefore not a part of the scope of this thesis.

B.4 Wind loading

Research into the dynamic loading applied to the bridge structure by wind forces has been set outside the scope of this thesis. A preliminary calculation of the wind loading based on the prevailing design codes for the bridge structure is given in this section.

The results of the calculation performed in this section are a preliminary, to be verified using wind tunnel tests and/or CFD calculations.

The wind loading is based on wind speeds with a return period of 100 years, the 10-minute and hourly mean wind velocity at a reference height of 10 m are shown in Table B.8.

Averaging period	Wind velocity [m s^{-1}]
10 min	35
1 h	32

Table B.8: Mean wind velocity at a reference height of 10 m at the bridge location [al11].

The direction of these mean wind speeds ranges from 180-240 deg relative to the North. The extreme wind speeds versus the direction relative to the North are displayed in Figure B.12 [al11].

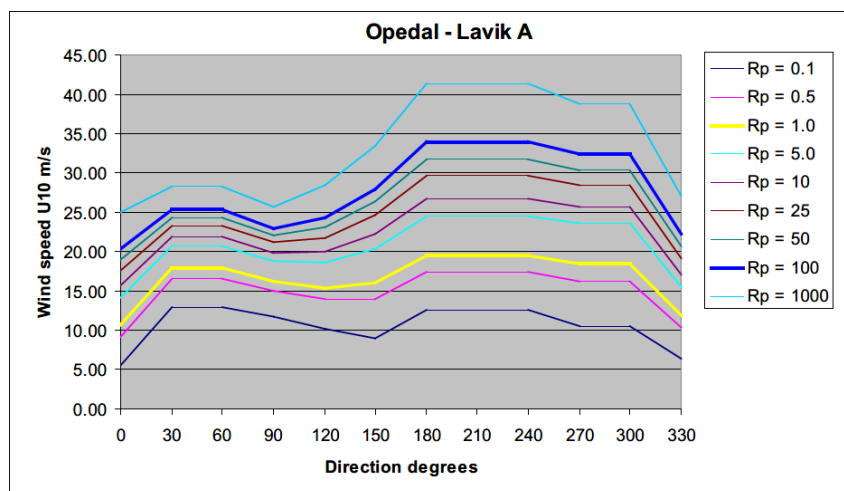


Figure B.12: Extreme wind speed values per reference period vs. direction at the bridge location.

The wind profile is extrapolated using the logarithmic function specified in DNV-RP-C205 [DNV10], since it coincides with the profile extrapolated using the function specified in EN 1991-1-4:2005+A1 [ECS10]. An example of this, and other, wind profiles is shown in Figure B.13.

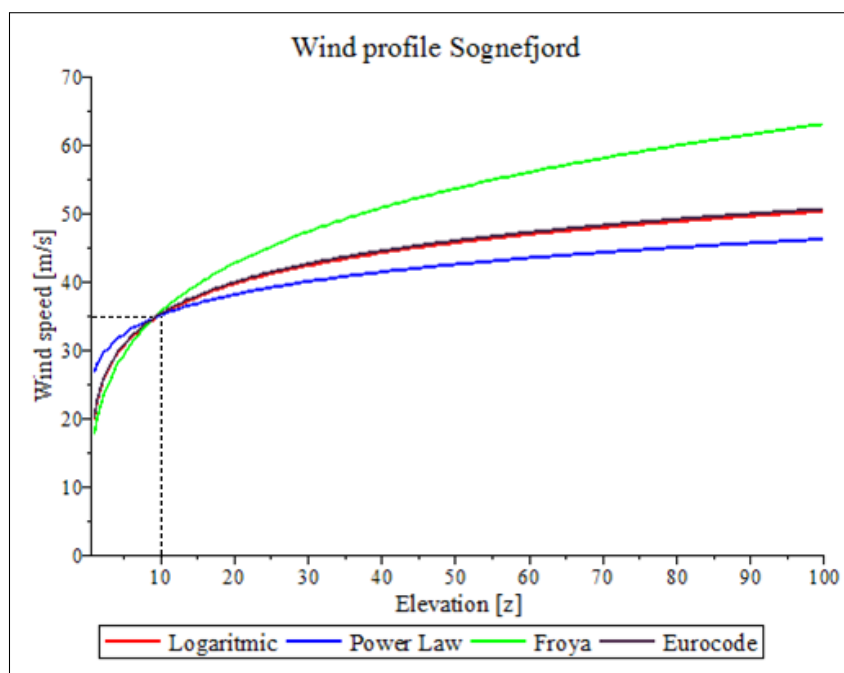


Figure B.13: Wind profiles extrapolated from the mean wind velocity at a height of 10 m at the bridge location.

The loads on the bridge deck, pylons and pontoons are calculated according to DNV-RP-C205 [DNV10] in the following subsections.

B.4.1 Wind load on bridge girder

The design for the bridge girder used in this section is found in section A.2. To calculate the static wind load on the bridge girders, Equation B.16 is provided.

$$F_W = C_e q S \phi \sin \alpha \quad (\text{B.16})$$

In which;

F_W is the wind force

C_e is the effective shape coefficient

q is the wind pressure according to Equation B.18

S is the projected area normal to the direction of the wind force

ϕ is the solidity ratio

α is the angle between the wind direction and the axis of the exposed member

First, the average solidity ratio of the truss structure is determined. It's definition is as taken from the code;

The solidity ratio ϕ is defined as the projected exposed solid area of the frame normal to the direction of the wind force divided by the area enclosed by the boundary of the frame normal to the direction of the wind force.

Since the internal chords in the truss girder are tubular, their area normal to wind force direction is the same for all directions. Some of the dimensional characteristics of the most recent girder design are shown in Table B.9 [Cij18]. In this table the main girder is the girder with the largest span, the intermediate girders span the spans next to the largest span and the side girders span the remaining spans. The girders are displayed in Figure B.14.

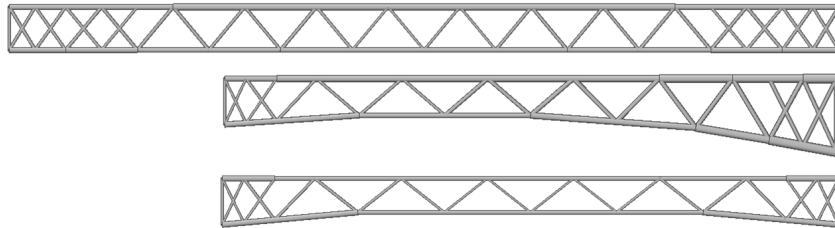


Figure B.14: The main, intermediate and side span girder designs [Cij18].

The total area per m is taken as the average height of the girders. The solid area per m is the diameter of the two main chords and the internal chord taken together. ϕ is calculated by dividing the solid area per m by the total area per m.

Girder	Main chord diameter [m]	Internal chord diameter [m]	Solid area [m ² m ⁻¹]	Total area [m ² m ⁻¹]	ϕ
Main	3	1.6	7.6	27	0.28
Intermediate	1.7	1.45	5.85	15	0.39
Side	1.4	0.6	3.4	13.4	0.25

Table B.9: Girder dimensions

The effective shape coefficient C_e is taken from Table 5-4 in DNV-RP-C205, this table is shown in Figure B.15.

To use the table, first the Reynolds number for the different member diameters must be computed. If the Reynolds number is bigger or smaller than $4.2 \cdot 10^5$, the the value of C_e is affected. Equation B.17 provides the calculation, the results are presented in Table B.10, in which the Reynolds numbers are

Table 5-4 Effective shape coefficient C_e for single frames			
Solidity ratio ϕ	Effective shape coefficient C_e		
	Flat-side members	Circular sections	
		$Re < 4.2 \times 10^5$	$Re \geq 4.2 \times 10^5$
0.10	1.9	1.2	0.7
0.20	1.8	1.2	0.8
0.30	1.7	1.2	0.8
0.40	1.7	1.1	0.8
0.50	1.6	1.1	0.8
0.75	1.6	1.5	1.4
1.00	2.0	2.0	2.0

Figure B.15: Effective shape coefficient for single frames [DNV10].

minimized by taking the smallest chord diameter and mean wind speed to see if they can be lower than $4.2 \cdot 10^5$.

$$R_e = \frac{D U_{T,z}}{\nu_a} \quad (\text{B.17})$$

In which;

R_e is the Reynolds number

D is the chord diameter

$U_{T,z}$ is the mean wind speed

ν_a is the kinematic viscosity of air, may be taken as $1.45 \cdot 10^{-5} \text{ m}^2 \text{ s}^{-1}$

		Reynolds numbers
Girder	Lowest chord diameter [m]	$U_{10,10} = 21 \text{ m s}^{-1}$
Main	1.6	$2.3 \cdot 10^6$
Intermediate	1.45	$2.1 \cdot 10^6$
Side	0.6	$8.7 \cdot 10^5$

Table B.10: Minimal Reynolds numbers for the different girders.

All Reynolds numbers are bigger than $4.2 \cdot 10^5$, so the value for C_e can be taken from Figure B.15 as 0.8 for all girders.

The wind pressure q can be calculated using Equation B.18.

$$q = \frac{1}{2} \rho_a U_{T,z}^2 \quad (\text{B.18})$$

In which;

q is the wind pressure

ρ_a is the mean mass density of air, to be taken as 1.226 kg m^{-3}

$U_{T,z}$ is the mean wind velocity averaged over an interval T at a height z above mean water level, according to Equation B.19

The mean wind velocity using a logarithmic wind profile can be calculated using Equation B.19.

$$U(z) = U(H) \cdot \left(1 + \frac{\ln\left(\frac{z}{H}\right)}{\ln\left(\frac{H}{z_0}\right)} \right) \quad (\text{B.19})$$

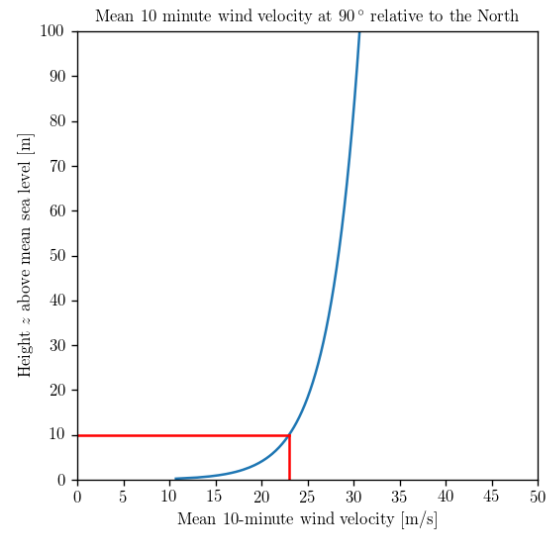
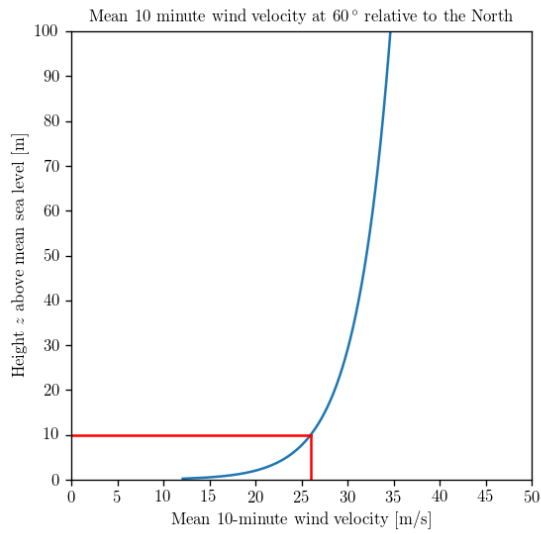
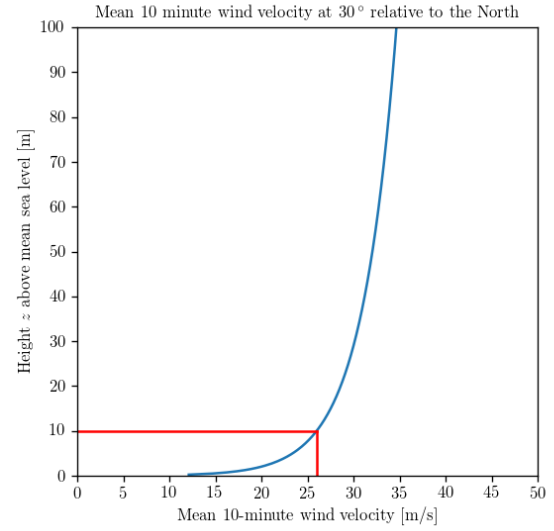
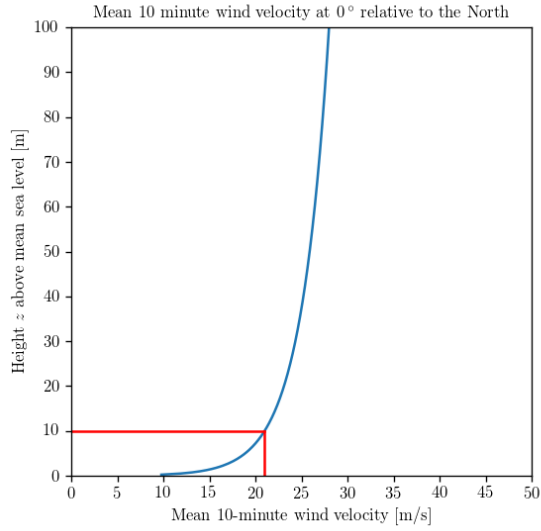
In which;

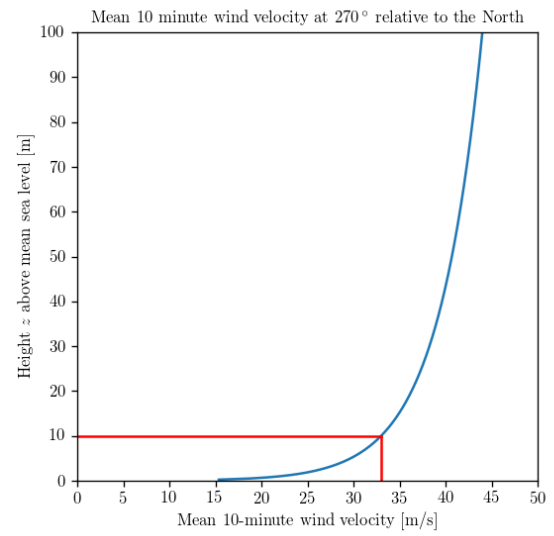
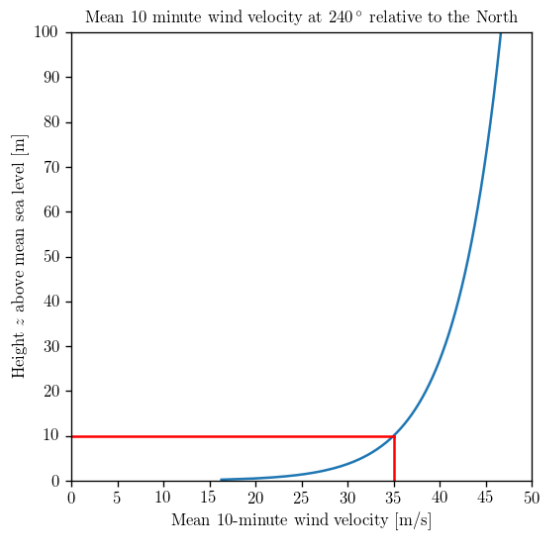
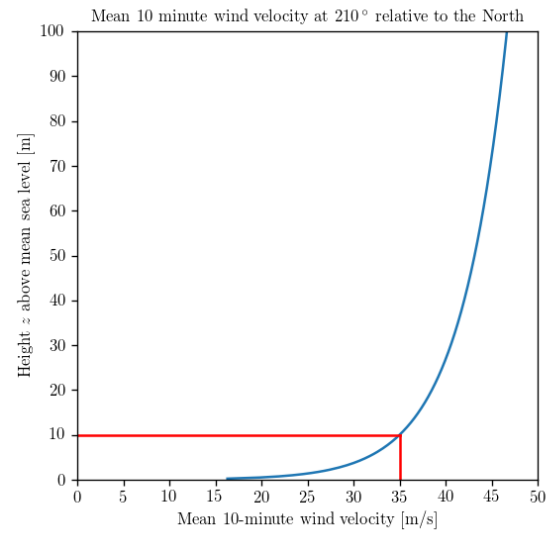
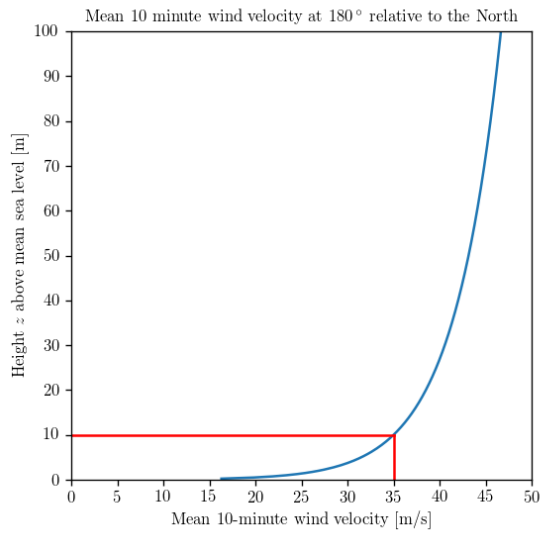
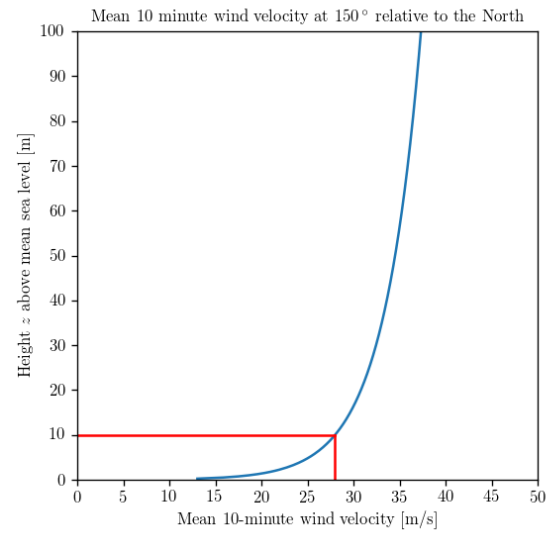
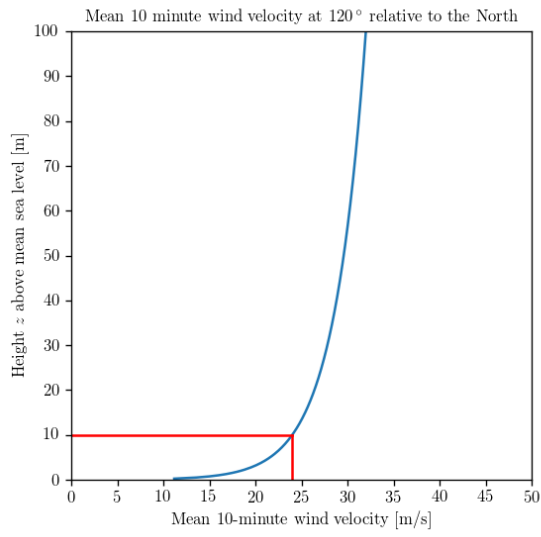
$U(z)$ is the mean wind speed at height z above mean water level

$U(H)$ is the mean wind speed at the reference height H above mean water level

z_0 is the terrain roughness parameter, taken as 0.01 [Cij18]

The logarithmic wind profiles per measurement direction depicted in Figure B.12 for the 10 min mean wind velocities are depicted in Table B.11.





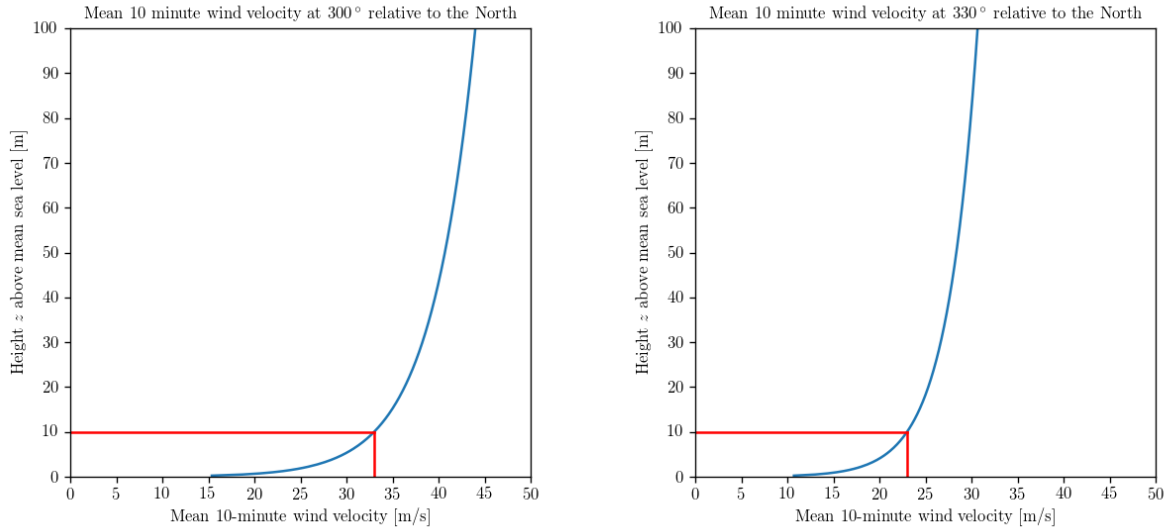


Table B.11: Mean wind velocity for the different wind directions.

To determine the values for S , q and α , needed to compute Equation B.16, the directions of the bridge girders relative to the north, their average height above mean sea level and their total side areas are needed. The girder numbering is shown in Figure B.17, their angles relative to the North, dimensions and ϕ -values are displayed in Table B.12. Since the bridge is symmetric, one half of the girders is displayed. Equation B.16 gives the wind load on the first horizontal side of the truss in the wind directions' path. To calculate the load on the second horizontal side, shielded by the first, Equation B.20 is provided.

$$F_{W,Shielded} = F_W \eta \quad (B.20)$$

In which;

F_W is the wind force

η is the shielding factor

The shielding factor η is determined using Table 5-1 in DNV-RP-C205, this table is shown in Figure B.16. To use this table, spacing ratio $\alpha_{spacing}$ and aerodynamic solidity ratio β need to be computed. Equation B.21 displays the calculation for β .

$$\beta_i = \phi_i a \quad (B.21)$$

In which;

β_i is aerodynamic solidity ratio for girder i

ϕ_i is the solidity ratio for girder i , see Tables B.9 and B.12

a is a constant, to be taken as 1.2 for circular sections in the subcritical range [DNV10]

The spacing ratio's description is as taken from the code;

The spacing ratio $\alpha_{spacing}$ is the distance, center to center, of the frames beams or girders divided by the least overall dimension of the frame measured at right angles to the direction of the wind force.

To compute the spacing ratio for the different wind directions, Equation B.22 is used.

$$\alpha_{spacing,i,j} = \frac{L_{ctc,i} \sin \alpha_{i,j}}{D_{chord}} \quad (B.22)$$

In which;

Table 5-1 The shielding factor η as function of spacing ratio α and aerodynamic solidity ratio β.								
β α	0.1	0.2	0.3	0.4	0.5	0.6	0.7	0.8
< 1.0	1.0	0.96	0.90	0.80	0.68	0.54	0.44	0.37
2.0	1.0	0.97	0.91	0.82	0.71	0.58	0.49	0.43
3.0	1.0	0.97	0.92	0.84	0.74	0.63	0.54	0.48
4.0	1.0	0.98	0.93	0.86	0.77	0.67	0.59	0.54
5.0	1.0	0.98	0.94	0.88	0.80	0.71	0.64	0.60
> 6.0	1.0	0.99	0.95	0.90	0.83	0.75	0.69	0.66

The *spacing ratio* α is the distance, centre to centre, of the frames, beams or girders divided by the least overall dimension of the frame, beam or girder measured at right angles to the direction of the wind. For triangular or rectangular framed structures diagonal to the wind, the spacing ratio should be calculated from the mean distance between the frames in the direction of the wind.

The *aerodynamic solidity ratio* is defined by $\beta = \phi a$ where

- ϕ = solidity ratio, see 5.3.2
- a = constant
 - = 1.6 for flat-sided members
 - = 1.2 for circular sections in subcritical range and for flat-sided members in conjunction with such circular sections
 - = 0.6 for circular sections in the supercritical range and for flat-sided members in conjunction with such circular sections.

Figure B.16: Shielding factor η as function of spacing ratio α and aerodynamic solidity ratio β [DNV10].

$\alpha_{spacing,i,j}$ is the spacing ratio of girder i under wind direction j

$L_{ctc,i}$ is the chord average c.t.c. distance for girder i

$\alpha_{i,j}$ is the angle between girder i and wind direction j , taken from Equation B.23

$D_{chord,i}$ is the chord diameter in girder i

Since the members used in the girders are tubular, the dimensions measured at angles to the wind direction do not change. Table B.12 includes the average center to center distances of chords in the girders and chord diameters.

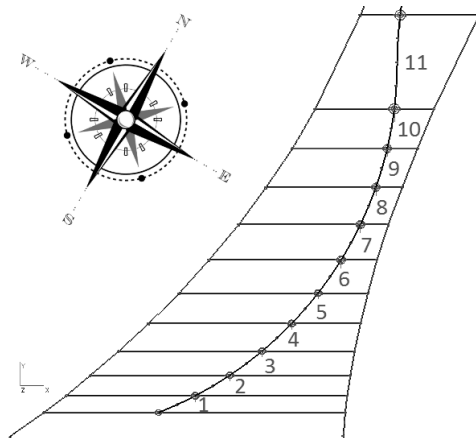


Figure B.17: Girder numbering.

To compute α and S , to be used in Equation B.16, Equations B.23 and B.24 are used.

$$\alpha_{i,j} = \gamma_i - \theta_j \quad (\text{B.23})$$

In which;

$\alpha_{i,j}$ is the angle between girder i and wind direction j

Girder number	Angle relative to the North [°]	Average height above MSL [m]	Area [m ²]	ϕ	Average c.t.c distance chords [m]	Chord diameter [m]
1	35	5.44	2680	0.25	14	0.6
2	30	17.08	2680	0.25	14	0.6
3	25	28.25	2680	0.25	14	0.6
4	15	38.26	2680	0.25	14	0.6
5	10	47.11	2680	0.25	14	0.6
6	5	54.80	2680	0.25	14	0.6
7	-5	60.66	2680	0.25	14	0.6
8	-10	66.03	2680	0.25	14	0.6
9	-15	70.25	2680	0.25	14	0.6
10	-20	73.32	3000	0.39	14	1.45
11	-25	75.44	12420	0.28	20	1.6

Table B.12: Girder angles relative to the North, dimensions and values for ϕ .

γ_i is the angle of girder i relative to the north

θ_j is the angle of wind direction j relative to the north

$$S_{i,j} = A_i \sin \alpha_{i,j} \quad (\text{B.24})$$

In which;

$S_{i,j}$ is the projected area of girder i normal to the direction of wind force j

A_i is area of girder i

$\alpha_{i,j}$ is the angle between girder i and wind direction j

The total load per girder per wind direction can be computed, taking into account all of the above, using Equation B.25.

$$FW_{tot,i,j} = FW_{i,j} + FW_{shielded,i,j} \quad (\text{B.25})$$

In which;

$FW_{tot,i,j}$ is the total wind load on girder i in the wind direction j

$FW_{i,j}$ is the wind load on the first horizontal side of girder i in the wind direction j

$FW_{shielded,i,j}$ is the wind load on the second horizontal side of girder i in the wind direction j

Tables B.13, B.14, B.15, B.16, B.17, B.18, B.19 and B.20 show the intermediate results and the resulting loads on the bridge girders per wind direction.

The calculation results clearly show that the static wind loading on the bridge girders is maximal when the wind direction is at around 240°-270° relative to the North.

Girder/ Wind direction	1	2	3	4	5	6	7	8	9	10	11
0°	225.6	313.5	357.7	385.5	405.0	419.8	430.0	438.2	444.4	448.7	451.7
30°	345.8	480.5	548.4	591.0	620.9	643.5	659.1	671.7	681.3	687.7	692.4
60°	345.8	480.5	548.4	591.0	620.9	643.5	659.1	671.7	681.3	687.7	692.4
90°	270.6	376.0	429.1	462.5	485.8	503.5	515.8	525.6	533.1	538.2	541.8
120°	294.6	409.4	467.2	503.6	529.0	548.3	561.6	572.4	580.5	586.0	590.0
150°	401.0	557.3	636.0	685.4	720.0	746.3	764.4	779.0	790.1	797.6	803.0
180°	626.6	870.7	993.7	1070.9	1125.1	1166.1	1194.4	1217.2	1234.6	1246.3	1254.8
210°	626.6	870.7	993.7	1070.9	1125.1	1166.1	1194.4	1217.2	1234.6	1246.3	1254.8
240°	626.6	870.7	993.7	1070.9	1125.1	1166.1	1194.4	1217.2	1234.6	1246.3	1254.8
270°	557.0	774.1	883.4	952.0	1000.2	1036.6	1061.8	1082.1	1097.5	1107.9	1115.4
300°	557.0	774.1	883.4	952.0	1000.2	1036.6	1061.8	1082.1	1097.5	1107.9	1115.4
330°	270.6	376.0	429.1	462.5	485.8	503.5	515.8	525.6	533.1	538.2	541.8

Table B.13: Wind pressure per wind direction per girder in kN m^{-2} .

Girder/ Wind direction	1	2	3	4	5	6	7	8	9	10	11
0°	35°	30°	25°	15°	10°	5°	5°	10°	15°	20°	25°
30°	5°	0°	5°	15°	20°	25°	35°	40°	45°	50°	55°
60°	25°	30°	35°	45°	50°	55°	65°	70°	75°	80°	85°
90°	55°	60°	65°	75°	80°	85°	95°	100°	105°	110°	115°
120°	85°	90°	95°	105°	110°	115°	125°	130°	135°	140°	145°
150°	115°	120°	125°	135°	140°	145°	155°	160°	165°	170°	175°
180°	145°	150°	155°	165°	170°	175°	185°	190°	195°	200°	205°
210°	175°	180°	185°	195°	200°	205°	215°	220°	225°	230°	235°
240°	205°	210°	215°	225°	230°	235°	245°	250°	255°	260°	265°
270°	235°	240°	245°	255°	260°	265°	275°	280°	285°	290°	295°
300°	265°	270°	275°	285°	290°	295°	305°	310°	315°	320°	325°
330°	295°	300°	305°	315°	320°	325°	335°	340°	345°	350°	355°

Table B.14: Angle alpha between wind direction and girder per wind direction per girder.

Girder/ Wind direction	1	2	3	4	5	6	7	8	9	10	11
0°	1537.2	1340.0	1132.6	693.6	465.4	233.6	233.6	465.4	693.6	1026.1	5248.9
30°	233.6	0.0	233.6	693.6	916.6	1132.6	1537.2	1722.7	1895.0	2298.1	10173.9
60°	1132.6	1340.0	1537.2	1895.0	2053.0	2195.3	2428.9	2518.4	2588.7	2954.4	12372.7
90°	2195.3	2321.0	2428.9	2588.7	2639.3	2669.8	2669.8	2639.3	2588.7	2819.1	11256.3
120°	2669.8	2680.0	2669.8	2588.7	2518.4	2428.9	2195.3	2053.0	1895.0	1928.4	7123.8
150°	2428.9	2321.0	2195.3	1895.0	1722.7	1537.2	1132.6	916.6	693.6	520.9	1082.5
180°	1537.2	1340.0	1132.6	693.6	465.4	233.6	233.6	465.4	693.6	1026.1	5248.9
210°	233.6	0.0	233.6	693.6	916.6	1132.6	1537.2	1722.7	1895.0	2298.1	10173.9
240°	1132.6	1340.0	1537.2	1895.0	2053.0	2195.3	2428.9	2518.4	2588.7	2954.4	12372.7
270°	2195.3	2321.0	2428.9	2588.7	2639.3	2669.8	2669.8	2639.3	2588.7	2819.1	11256.3
300°	2669.8	2680.0	2669.8	2588.7	2518.4	2428.9	2195.3	2053.0	1895.0	1928.4	7123.8
330°	2428.9	2321.0	2195.3	1895.0	1722.7	1537.2	1132.6	916.6	693.6	520.9	1082.5

Table B.15: Projected area S per wind direction per girder in m.

Girder/ Wind direction	1	2	3	4	5	6	7	8	9	10	11	Total
0°	39.8	42.0	34.2	13.8	6.6	1.7	1.8	7.1	16.0	49.1	224.4	436.5
30°	1.4	0.0	2.2	21.2	38.9	61.6	116.2	148.8	182.6	377.8	1292.6	2243.3
60°	33.1	64.4	96.7	158.4	195.3	231.4	290.2	317.9	340.7	624.3	1911.7	4264.2
90°	97.3	151.2	188.9	231.3	252.6	267.8	274.4	273.2	266.6	444.8	1238.2	3686.4
120°	156.7	219.4	248.5	251.8	250.4	241.4	202.0	180.0	155.6	226.6	540.0	2672.5
150°	176.6	224.0	228.7	183.7	159.5	131.6	73.2	48.8	28.4	22.5	17.0	1293.9
180°	110.5	116.7	95.1	38.4	18.2	4.8	4.9	19.7	44.3	136.4	623.5	1212.5
210°	2.6	0.0	4.0	38.4	70.5	111.6	210.6	269.6	330.9	684.5	2342.4	4065.2
240°	60.0	116.7	175.2	287.0	353.9	419.4	525.9	576.1	617.4	1131.3	3464.3	7727.2
270°	200.3	311.2	388.9	476.1	519.9	551.4	564.8	562.5	548.9	915.7	2549.0	7588.7
300°	296.3	414.9	469.9	476.1	473.4	456.4	381.9	340.4	294.1	428.5	1020.9	5052.7
330°	119.1	151.2	154.3	123.9	107.6	88.8	49.4	33.0	19.1	15.2	11.4	873.1

Table B.16: Wind load on the first frame of the girders per wind direction per girder in kN.

Girder/ Wind direction	1	2	3	4	5	6	7	8	9	10	11
0°	1.0	1.0	1.0	1.0	0.9	0.9	0.9	0.9	1.0	0.7	0.9
30°	0.9	0.9	0.9	1.0	1.0	1.0	1.0	1.0	1.0	0.8	1.0
60°	1.0	1.0	1.0	1.0	1.0	1.0	1.0	1.0	1.0	0.8	1.0
90°	1.0	1.0	1.0	1.0	1.0	1.0	1.0	1.0	1.0	0.8	1.0
120°	1.0	1.0	1.0	1.0	1.0	1.0	1.0	1.0	1.0	0.8	1.0
150°	1.0	1.0	1.0	1.0	1.0	1.0	1.0	1.0	1.0	0.7	0.9
180°	1.0	1.0	1.0	1.0	0.9	0.9	0.9	0.9	1.0	0.7	0.9
210°	0.9	0.9	0.9	1.0	1.0	1.0	1.0	1.0	1.0	0.8	1.0
240°	1.0	1.0	1.0	1.0	1.0	1.0	1.0	1.0	1.0	0.8	1.0
270°	1.0	1.0	1.0	1.0	1.0	1.0	1.0	1.0	1.0	0.8	1.0
300°	1.0	1.0	1.0	1.0	1.0	1.0	1.0	1.0	1.0	0.8	1.0
330°	1.0	1.0	1.0	1.0	1.0	1.0	1.0	1.0	1.0	0.7	0.9

Table B.17: Shield factor η per wind direction per girder in kN.

Girder/ Wind direction	1	2	3	4	5	6	7	8	9	10	11	Total
0°	37.8	39.9	32.5	13.2	6.1	1.6	1.6	6.6	15.2	36.4	211.0	401.7
30°	1.3	0.0	2.0	20.2	37.0	58.5	110.4	141.3	173.4	313.5	1228.0	2085.7
60°	31.4	61.2	91.9	150.5	185.5	219.9	275.7	302.0	323.7	518.2	1816.1	3976.0
90°	92.4	143.6	179.5	219.7	239.9	254.5	260.6	259.6	253.3	369.2	1176.3	3448.6
120°	148.9	208.5	236.1	239.2	237.9	229.3	191.9	171.0	147.8	188.1	513.0	2511.7
150°	167.7	212.8	217.3	174.5	151.5	125.0	69.5	46.4	27.0	16.0	15.4	1223.2
180°	105.0	110.8	90.4	36.5	16.9	4.3	4.4	18.3	42.1	101.0	586.1	1115.8
210°	2.3	0.0	3.7	36.5	67.0	106.0	200.1	256.1	314.3	568.2	2225.3	3779.5
240°	57.0	110.8	166.5	272.7	336.2	398.4	499.6	547.3	586.5	939.0	3291.1	7205.1
270°	190.3	295.6	369.5	452.3	493.9	523.8	536.6	534.4	521.4	760.0	2421.6	7099.4
300°	281.5	394.2	446.4	452.3	449.7	433.6	362.8	323.3	279.4	355.6	969.9	4748.7
330°	113.2	143.6	146.6	117.7	102.2	84.4	46.9	31.3	18.2	10.8	10.4	825.3

Table B.18: Wind load on the second frame of the girders per wind direction per girder in kN.

Girder/ Wind direction	1	2	3	4	5	6	7	8	9	10	11	Total
0°	193.6	245.7	250.9	201.5	174.9	144.4	80.3	53.6	31.1	21.6	18.2	1415.8
30°	118.9	125.6	102.4	41.4	19.4	5.0	5.1	21.0	47.7	131.0	667.5	1285
60°	2.7	0.0	4.3	41.4	75.9	120.1	226.6	290.1	356.0	691.3	2520.6	4329
90°	50.5	98.2	147.6	241.7	298.0	353.2	442.8	485.1	519.9	894.0	2917.2	6448.2
120°	206.6	320.9	401.1	491.1	536.2	568.7	582.5	580.2	566.1	886.3	2629.1	7768.8
150°	416.0	582.4	659.6	668.4	664.6	640.7	536.1	477.8	412.9	564.5	1433.3	7056.3
180°	537.9	682.6	696.9	559.7	485.9	401.0	223.0	148.8	86.4	60.2	50.6	3933
210°	215.4	227.5	185.5	75.0	35.1	9.1	9.3	38.0	86.4	237.4	1209.6	2328.3
240°	4.9	0.0	7.7	75.0	137.6	217.7	410.7	525.7	645.2	1252.7	4567.6	7844.8
270°	104.0	202.3	303.8	497.5	613.4	727.0	911.6	998.7	1070.3	1840.5	6005.4	13274.5
300°	390.6	606.8	758.4	928.4	1013.9	1075.2	1101.4	1096.9	1070.3	1675.7	4970.6	14688.2
330°	280.7	393.0	445.1	451.0	448.4	432.3	361.7	322.4	278.6	380.9	967.1	4761.2

Table B.19: Total wind load per wind direction per girder in kN.

Girder/ Wind direction	1	2	3	4	5	6	7	8	9	10	11
0°	0.1	0.1	0.0	0.0	0.0	0.0	0.0	0.0	0.0	0.0	0.1
30°	0.0	0.0	0.0	0.0	0.1	0.1	0.2	0.2	0.3	0.3	0.4
60°	0.0	0.1	0.1	0.2	0.3	0.3	0.4	0.5	0.5	0.5	0.5
90°	0.1	0.2	0.3	0.3	0.4	0.4	0.4	0.4	0.4	0.4	0.4
120°	0.2	0.3	0.4	0.4	0.4	0.4	0.3	0.3	0.2	0.2	0.2
150°	0.3	0.3	0.3	0.3	0.2	0.2	0.1	0.1	0.0	0.0	0.0
180°	0.2	0.2	0.1	0.1	0.0	0.0	0.0	0.0	0.1	0.1	0.2
210°	0.0	0.0	0.0	0.1	0.1	0.2	0.3	0.4	0.5	0.5	0.7
240°	0.1	0.2	0.2	0.4	0.5	0.6	0.8	0.8	0.9	0.9	1.0
270°	0.3	0.4	0.6	0.7	0.8	0.8	0.8	0.8	0.8	0.7	0.7
300°	0.4	0.6	0.7	0.7	0.7	0.7	0.6	0.5	0.4	0.3	0.3
330°	0.2	0.2	0.2	0.2	0.2	0.1	0.1	0.0	0.0	0.0	0.0

Table B.20: Distributed wind load per wind direction per girder in kN m^{-2} .

B.4.2 Wind load on bridge pylons and pontoons

The pylon and pontoon design used in this section is specified in sections A.3 and A.4.

Equation B.26 is a modified version of Equation B.16 which is used to compute the static wind loads on the pylons and pontoons.

$$F_W = C_e q S \sin \alpha \quad (\text{B.26})$$

In which;

F_W is the wind force

C_e is the effective shape coefficient, taken from Figure B.15 as being 0.7, since the solidity ratio ϕ of the pylons and pontoons is below 0.1

q is the wind pressure according to Equation B.18, using $U_{T,z}$ taken as the average value over the height of the pylon or pontoon

S is the projected area normal to the direction of the wind force, in this case to be taken as the pylon diameter D multiplied with its height above mean sea level z

α is the angle between the wind direction and the axis of the exposed member, which is taken as 90° for every wind direction due to the tubular shape of the pylons

The pylon and pontoon numbering is shown in Figure B.18. Their dimensions are shown in B.21 [Cij18]. Since the bridge is symmetric, only half the pylons and pontoons are displayed.

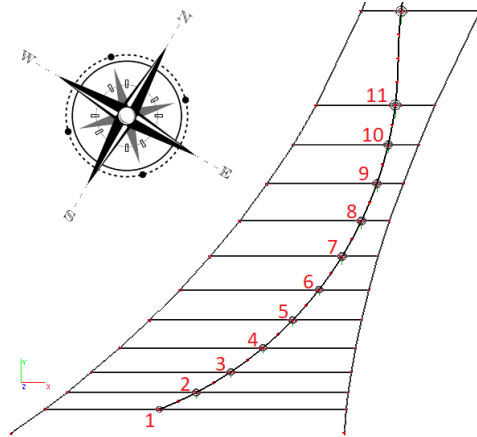


Figure B.18: Pylon and pontoon numbering.

The results of performing the calculation in Equation B.26 are displayed in Tables B.22, ??, B.24 and B.25.

As is expected, the wind load on the pylons and pontoons is maximal in the directions where the 10 min mean wind speed is measured to be maximal. This is due to the assumed tubular shape of both pylons and pontoons, due to which the exposed area of both does not change with a changing wind direction.

Number	Pylon height [m]	Pylon diameter [m]	Pontoon height above MSL [m]	Pontoon diameter [m]
1	0	15	4.29	30
2	11.64	18	4.52	36
3	22.81	18	4.61	36
4	32.82	18	4.68	36
5	41.67	18	4.75	36
6	49.36	18	4.81	36
7	55.22	21	4.36	42
8	60.59	21	4.39	42
9	64.81	21	4.42	42
10	67.88	21	4.43	42
11	70	26	4.90	52

Table B.21: Pylon and pontoon dimensions.

Pylon/ Wind direction	1	2	3	4	5	6	7	8	9	10	11	Total
0°	0.0	25.9	68.3	112.1	154.1	192.1	259.4	292.3	318.8	338.5	435.7	2197.2
30°	0.0	39.8	104.7	171.8	236.2	294.4	397.7	448.0	488.6	518.9	667.9	3368.1
60°	0.0	39.8	104.7	171.8	236.2	294.4	397.7	448.0	488.6	518.9	667.9	3368.1
90°	0.0	31.1	81.9	134.5	184.8	230.4	311.2	350.6	382.4	406.0	522.6	2635.7
120°	0.0	33.9	89.2	146.4	201.3	250.9	338.9	381.8	416.4	442.1	569.1	2869.9
150°	0.0	46.1	121.4	199.3	273.9	341.5	461.2	519.6	566.7	601.8	774.6	3906.2
180°	0.0	72.0	189.8	311.4	428.0	533.6	720.7	811.9	885.5	940.3	1210.3	6103.4
210°	0.0	72.0	189.8	311.4	428.0	533.6	720.7	811.9	885.5	940.3	1210.3	6103.4
240°	0.0	72.0	189.8	311.4	428.0	533.6	720.7	811.9	885.5	940.3	1210.3	6103.4
270°	0.0	64.0	168.7	276.8	380.5	474.3	640.7	721.8	787.2	835.9	1075.9	5425.8
300°	0.0	64.0	168.7	276.8	380.5	474.3	640.7	721.8	787.2	835.9	1075.9	5425.8
330°	0.0	31.1	81.9	134.5	184.8	230.4	311.2	350.6	382.4	406.0	522.6	2635.7

Table B.22: Total wind load per wind direction per pylon in kN.

Pylon/ Wind direction	1	2	3	4	5	6	7	8	9	10	11
0°	0.0	0.1	0.2	0.2	0.2	0.2	0.2	0.2	0.2	0.2	0.2
30°	0.0	0.2	0.3	0.3	0.3	0.3	0.3	0.4	0.4	0.4	0.4
60°	0.0	0.2	0.3	0.3	0.3	0.3	0.3	0.4	0.4	0.4	0.4
90°	0.0	0.2	0.2	0.2	0.2	0.3	0.3	0.3	0.3	0.3	0.3
120°	0.0	0.2	0.2	0.2	0.3	0.3	0.3	0.3	0.3	0.3	0.3
150°	0.0	0.2	0.3	0.3	0.4	0.4	0.4	0.4	0.4	0.4	0.4
180°	0.0	0.3	0.5	0.5	0.6	0.6	0.6	0.6	0.6	0.7	0.7
210°	0.0	0.3	0.5	0.5	0.6	0.6	0.6	0.6	0.6	0.7	0.7
240°	0.0	0.3	0.5	0.5	0.6	0.6	0.6	0.6	0.6	0.7	0.7
270°	0.0	0.3	0.4	0.5	0.5	0.5	0.6	0.6	0.6	0.6	0.6
300°	0.0	0.3	0.4	0.5	0.5	0.5	0.6	0.6	0.6	0.6	0.6
330°	0.0	0.2	0.2	0.2	0.2	0.3	0.3	0.3	0.3	0.3	0.3

Table B.23: Distributed wind load per wind direction per pylon in kN m^{-2} .

Pontoon/ Wind direction	1	2	3	4	5	6	7	8	9	10	11	0
0°	7.2	9.7	9.9	10.7	10.8	11.0	10.2	11.0	11.1	11.1	17.0	119.6
30°	11.0	14.9	15.2	16.4	16.6	16.8	15.7	16.9	17.0	17.0	26.1	183.4
60°	11.0	14.9	15.2	16.4	16.6	16.8	15.7	16.9	17.0	17.0	26.1	183.4
90°	8.6	11.6	11.9	12.8	13.0	13.2	12.2	13.2	13.3	13.3	20.4	143.5
120°	9.4	12.7	12.9	13.9	14.1	14.3	13.3	14.4	14.5	14.5	22.2	156.3
150°	12.8	17.2	17.6	19.0	19.2	19.5	18.2	19.6	19.7	19.7	30.2	212.7
180°	19.9	27.0	27.5	29.6	30.1	30.4	28.4	30.6	30.8	30.8	47.3	332.3
210°	19.9	27.0	27.5	29.6	30.1	30.4	28.4	30.6	30.8	30.8	47.3	332.3
240°	19.9	27.0	27.5	29.6	30.1	30.4	28.4	30.6	30.8	30.8	47.3	332.3
270°	17.7	24.0	24.4	26.3	26.7	27.1	25.2	27.2	27.3	27.4	42.0	295.4
300°	17.7	24.0	24.4	26.3	26.7	27.1	25.2	27.2	27.3	27.4	42.0	295.4
330°	8.6	11.6	11.9	12.8	13.0	13.2	12.2	13.2	13.3	13.3	20.4	143.5

Table B.24: Total wind load per wind direction per pontoon in kN.

Pontoon/ Wind direction	1	2	3	4	5	6	7	8	9	10	11
0°	0.1	0.1	0.1	0.1	0.1	0.1	0.1	0.1	0.1	0.1	0.1
30°	0.1	0.1	0.1	0.1	0.1	0.1	0.1	0.1	0.1	0.1	0.1
60°	0.1	0.1	0.1	0.1	0.1	0.1	0.1	0.1	0.1	0.1	0.1
90°	0.1	0.1	0.1	0.1	0.1	0.1	0.1	0.1	0.1	0.1	0.1
120°	0.1	0.1	0.1	0.1	0.1	0.1	0.1	0.1	0.1	0.1	0.1
150°	0.1	0.1	0.1	0.1	0.1	0.1	0.1	0.1	0.1	0.1	0.1
180°	0.2	0.2	0.2	0.2	0.2	0.2	0.2	0.2	0.2	0.2	0.2
210°	0.2	0.2	0.2	0.2	0.2	0.2	0.2	0.2	0.2	0.2	0.2
240°	0.2	0.2	0.2	0.2	0.2	0.2	0.2	0.2	0.2	0.2	0.2
270°	0.1	0.2	0.2	0.2	0.2	0.2	0.1	0.2	0.2	0.2	0.2
300°	0.1	0.2	0.2	0.2	0.2	0.2	0.1	0.2	0.2	0.2	0.2
330°	0.1	0.1	0.1	0.1	0.1	0.1	0.1	0.1	0.1	0.1	0.1

Table B.25: Distributed wind load per wind direction per pontoon in kN m^{-2} .

B.5 Load cases

This section shows the load cases considered in this thesis. These load cases are combinations of the waves specified in section B.1 and the current specified in section B.2.

Loadcase	Wave direction - height - wavelength	Current direction
1	180° - 4.55 m - 33 m	Inwards
2	180° - 4.55 m - 33 m	Outwards
3	240° - 4.79 m - 36 m	Inwards
4	240° - 4.79 m - 36 m	Outwards
5	270° - 4.36 m - 36 m	Inwards
6	270° - 4.36 m - 36 m	Outwards

Table B.26: Wave load cases.

Another load case is the inward current for the research into vortex induced vibrations caused by this current. Reference is made to appendix J.

Appendix C

Cable design

This chapter shows the design considerations and choices made in the more detailed design of the main and lateral cable cross sections. The choice of material has been made in earlier work, reference is made to section A.5 [Yip15]. The chosen material is steel, thus the cables are steel wire ropes, as steel cables are generally named [Fey07].

C.1 Cross section type

There are many different types of steel wire ropes with different application areas. The main types of wire rope are displayed in Figure C.1. They are differentiated due to their properties in multiple areas, such as corrosion protection, fatigue characteristics and effective Young's Modulus [Fey07]. All of these factors contribute to the choice of the wire rope design.

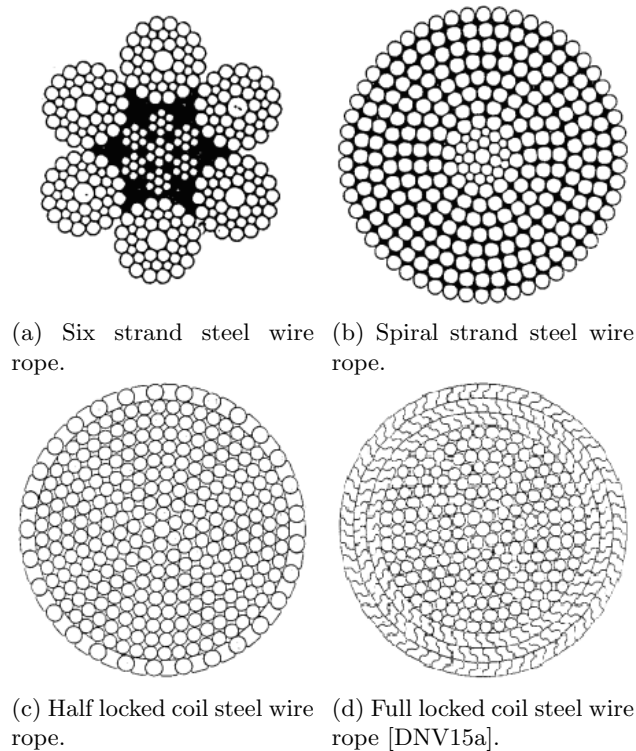


Figure C.1: Basic steel wire rope types

The choice of wire rope is heavily influenced by the guidelines set in DNVGL-OS-E304 Offshore mooring steel wire ropes [DNV15a]. The recommendation for any type of long-term mooring is to use the spiral strand, half locked- or full locked coil type of wire rope. This is due to these rope layouts preventing sea water and other contaminants from entering the rope and 'locking in' the lubrication agent

used [DNV15a]. Further specification of this guideline is given in DNVGL-OS-E301 Position mooring [DNV15b], which gives the guidelines shown in Table C.1.

Field design life [years]	Possibilities for replacement of wire rope segments	
	Yes	No
< 8	A/B/C	A/B/C
8 – 15	A/B/C	A/B
> 15	A/B	A
A	Half locked coil/full locked coil/spiral rope with plastic sheathing.	
B	Half locked coil/full locked coil/spiral rope without plastic sheathing.	
C	Six strand rope.	

Table C.1: Choice of steel wire rope construction [DNV15b].

The field design life of the cable mooring system is above 15 years, with a large preference for not having to replace wire rope segments. According to Table C.1, this leads to a rope construction with plastic sheathing and eliminates the six strand rope as a design option. The next criterion to consider is the fatigue characteristics of the rope. Figure C.2 displays design fatigue curves for different mooring lines, also including two types of mooring chains.

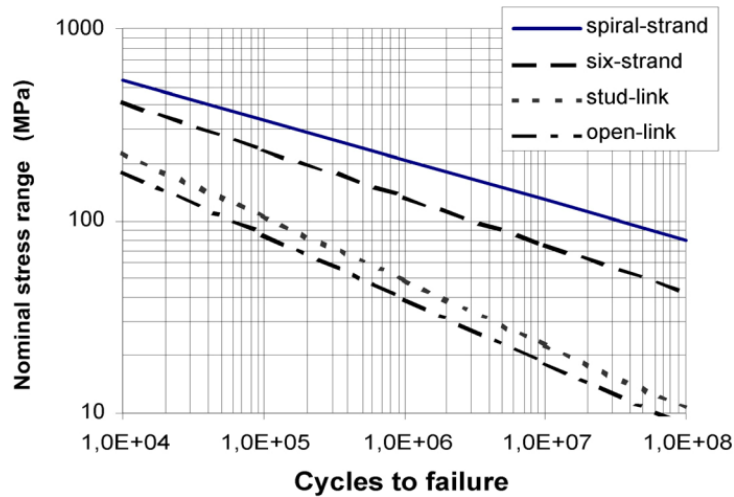


Figure C.2: Fatigue design S-N curves for different mooring line types [DNV15b].

From Figure C.2, it is clear that for fatigue loading the spiral strand rope has the best design characteristics.

These considerations lead to the choice of spiral strand wire rope with a plastic sheathing for environmental protection. This choice may be changed to half- or full locked coil rope if required without much difficulty at a later stage, as the calculation of rope characteristics are not very different for these types [Fey07]. The plastic sheathing is disregarded in the calculation of mechanical properties, as its contribution is expected to be insignificant.

C.2 Cross section design

In previous work performed on the bridge design, the steel cross section of the cables has been determined. This cross section is displayed in Table C.2 and reference is made to section A.5.

This cross section is needed to ensure the stresses in the cable remain at or under the values calculated in the previous work. However, due to the fact that each layer of strands in the rope has to be 'complete' (it can't miss strands in the layer [Fey07]), the total steel cross section of the rope will be higher than the one calculated in this earlier work. To ensure that the new steel cross sectional area is as close as possible to the one calculated earlier, a rope cross section optimization tool has been written in Python. This tool calculates the optimal strand- and rope layout based on the minimum and maximum steel wire

	Diameter [mm]	Steel area [mm ²]
Main cables	1200	1131 · 10 ³
Lateral cables	350	96.2 · 10 ³

Table C.2: Cable steel cross section.

sizes to minimize the 'extra' rope steel sectional area. The calculation is based on a spiral stranded rope and spiral stranded strands with 6 extra strands or wires per consecutive layer and a single strand or wire core. The effect of a larger or smaller strand or wire core has not been researched and may be the subject of more research.

The minimum and maximum wire size to be used in steel wire rope for a certain design tensile strength grade is given in EN 10264-1:2002 Steel wire and wire products - steel wire for ropes [ECS02]. For the design tensile strength of 1860 N mm⁻² the wire diameter range is 0.20 mm to 5 mm [ECS02].

These values for the minimum and maximum wire diameter are fed to the tool with steps of 0.1 mm in between for both the main and lateral cables. The resulting cross sections are displayed in Figures C.3 and C.4 and their characteristic values in Tables C.3 and C.4.

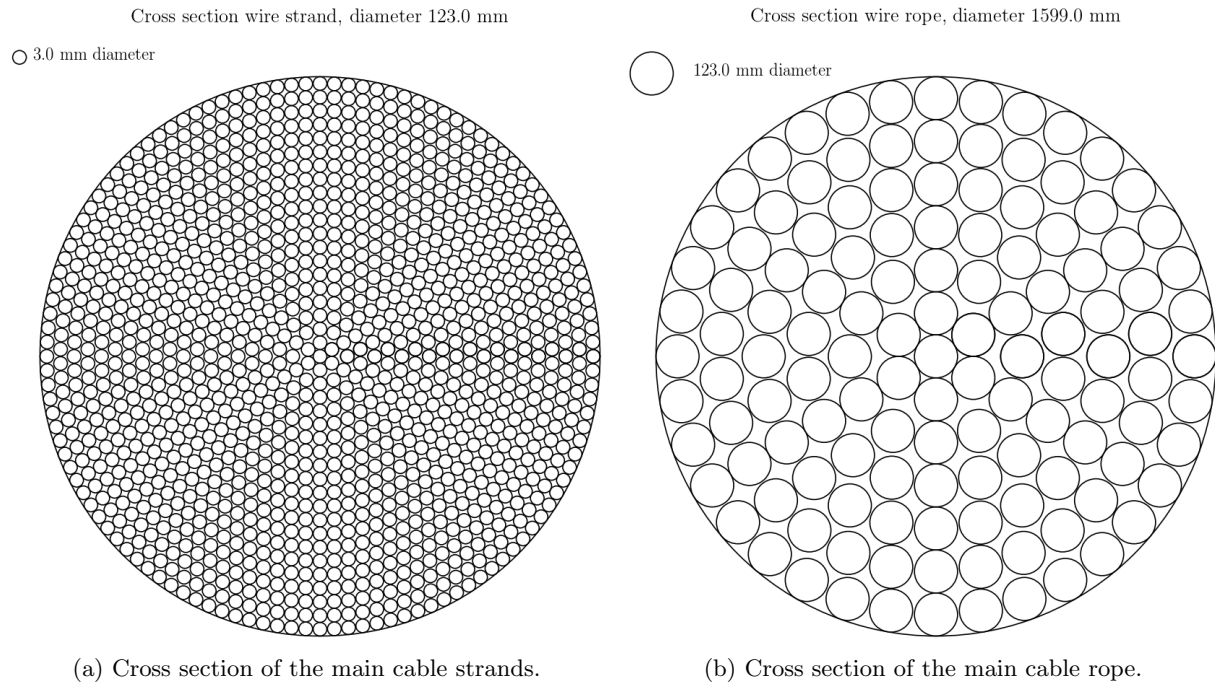


Figure C.3: Cross sections of the main cable strands and total rope

	Layers	Strands/wires	Diameter [mm]	Steel area [mm ²]
Main cable rope	6	127	1599	1132.01 · 10 ³
Main cable strand	20	1261	123	8.913 · 10 ³

Table C.3: Main cable wire rope properties.

	Layers	Strands/wires	Diameter [mm]	Steel area [mm ²]
Lateral cable rope	5	91	465.3	96.3 · 10 ³
Lateral cable strand	4	61	42.3	1.058 · 10 ³

Table C.4: Lateral cable wire rope properties.

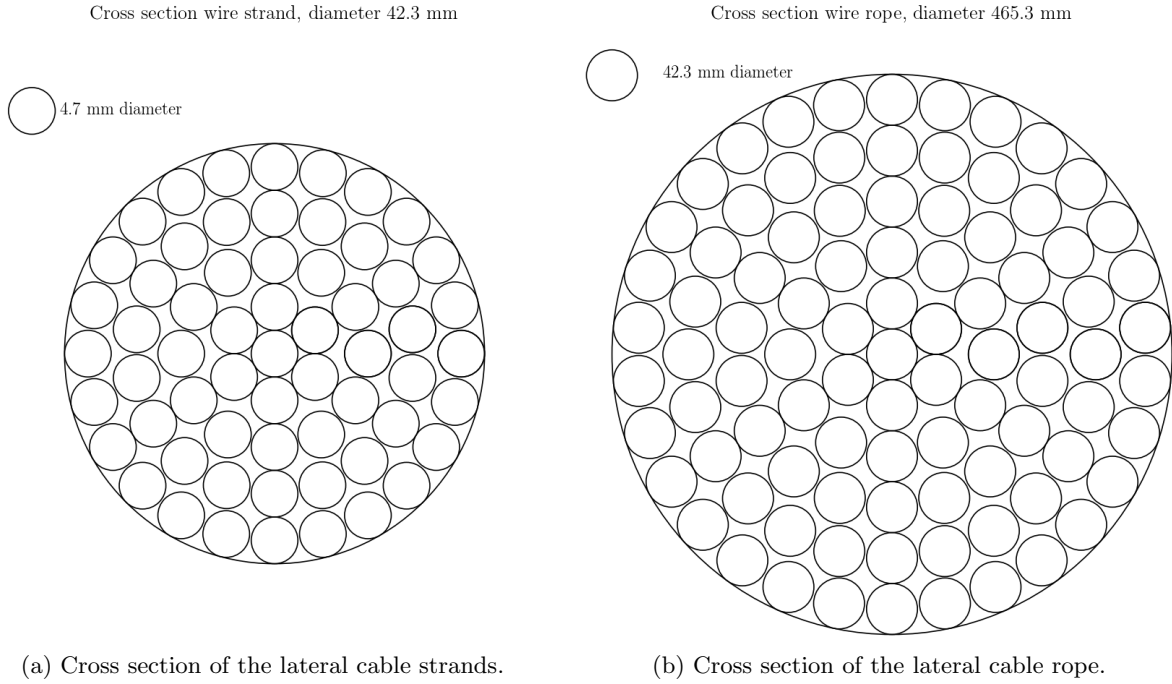


Figure C.4: Cross sections of the lateral cable strands and total rope

C.3 Elasticity module

An important factor in wire rope properties is the lay angle of the rope, which is the angle under which the wires or strands are twisted around the core. The lay angle influences the elasticity module of the rope, which is different from the steel's Young's Modulus for the entire rope or strand. The difference the lay angle makes on a rope's elasticity module is shown in Figure C.5, in which the elasticity module multiplied by a unit area of 1 mm^2 of the main cable strand determined in section C.2 is plotted versus different lay angles. The expression to calculate this elasticity module is shown in Equation C.1.

$$E_S = \frac{1}{A} \sum_{i=0}^n \frac{z_i \cos^3 \alpha_i}{1 + \nu \sin^2 \alpha_i} E_i A_i \quad (\text{C.1})$$

In which;

E_S is the rope or strand elasticity module

A is the steel sectional area

n is the number of layers of wires or strands

z_i is the number of wires or strands in the layer

α_i is the lay angle of the layer

ν is Poisson's ratio

E_i is the elasticity module of the layer

A_i is the wire or strand sectional area in the layer

As is shown in Figure C.5, as the lay angle increases, the elasticity module of the entire rope decreases. This leads to a larger extension of the wire rope under the same loading and due to higher deformability of the cross section under a lower tensile force, potentially more wire wear due to inter-wire friction. The advantage of the lay angle is to 'lock in' the rope lubricant, which has the greatest positive effect on the rope endurance under cyclical loading [Fey07]. The lay angle also has an influence on the wire rope's variable bending stiffness, which is addressed in section C.4.

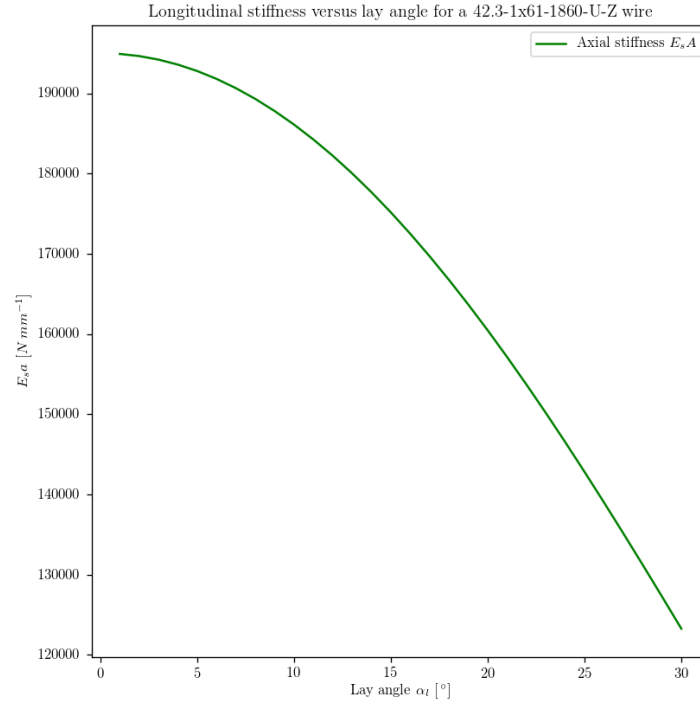


Figure C.5: Longitudinal stiffness of the lateral cable strand design versus lay angle per mm^2 .

C.4 Bending stiffness

Wire rope bending stiffness is variable, depending upon the curvature of the rope [Pap97]. The method of determining the variable bending stiffness used in this thesis is based on work done by Papaillou. As a caveat it must be mentioned that his work is based on transmission line conductors, which are much smaller than the cables considered in this thesis. His work does consider multi-layered conductors, which makes it suitable for the many-layered cables used in this bridge design.

The bending stiffness is variable due to the wires 'sticking' together to form a solid beam under low curvature and 'slipping' apart as the curvature of the rope increases. This means that there is a critical slip curvature where wires pass from the slip to the stick state. The expression for the critical slip curvature is shown in Equation C.2.

$$\kappa_i(\varphi_n) = \frac{(Z_{T,i} + S_i)(e^{\mu \sin \beta \varphi_n} - 1)}{A_i E_i r_i \sin \phi_n \cos^2 \beta} \quad (\text{C.2})$$

In which;

κ_i is the critical slip curvature of the wire

φ_n is the wire helix angle, according to Figure C.6

$Z_{T,i}$ is the tensile force in the wire according to Equation C.3

S_i , this term considers the contribution of the tensile forces in the layers 'above' this layer to the tensile force $Z_{T,i}$ of this layer, according to Equation C.4

μ is the wire rope friction coefficient, typically taken as 0.5 [Pap97]

β is the lay angle of the wire

A_i is the wire or strand sectional area

E_i is the wire or strand elasticity modulus

r_i is radius of the wire layer according to Figure C.6

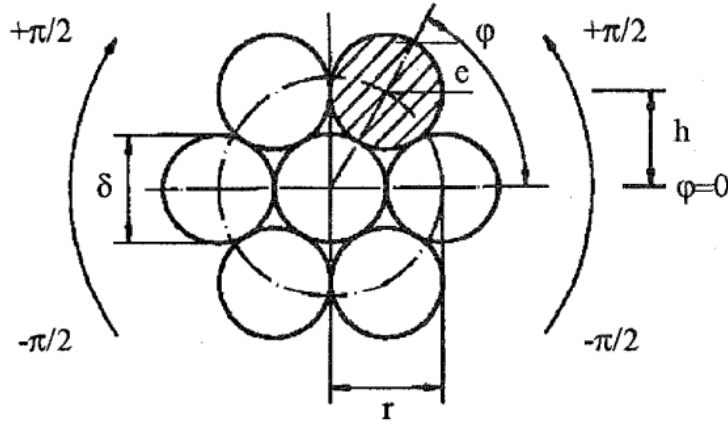


Figure C.6: Helix angle and layer radius definition [Pap97].

The definition of the wire or strand helix angle and layer radius is depicted in Figure C.6. The helix angle is a value between $-\pi/2$ and $\pi/2$.

The expression for the tensile force in a single wire is given in Equation C.3.

$$Z_{T,i} = \frac{E_i A_i \cos^2 \beta}{\sum_{\text{all wires}} E_i A_i \cos^3 \beta} T \quad (\text{C.3})$$

In which;

$Z_{T,i}$ is the tensile force in a single wire

E_i is the wire or strand elasticity modulus

A_i is the wire or strand sectional area

β is the lay angle of the wire or strand

T is the tensile force acting on the rope

The expression for the term that incorporates the influence of the tensile forces in the 'higher' layers to the tensile force of the present layer is given in Equation C.4.

$$S_i = \sum_{j=i+1}^n 2 Z_{T,j} \quad (\text{C.4})$$

In which;

S_i , this term considers the contribution of the tensile forces in the layers 'above' this layer to the tensile force $Z_{T,i}$ of this layer

n is the number of layers of wires or strands in the rope

$Z_{T,j}$ is the tensile force in a single wire

The variable bending stiffness is defined by Equation C.6. Equations C.7, C.8, C.9 and C.10 define the bending stiffness of the wire rope wires or strands in their different stick or slipped states.

$$0 < \kappa \leq \kappa_{slip,a} : EI(\kappa) = EI_{max} \quad (\text{C.5})$$

$$\kappa_{slip,i} \leq \kappa \leq \kappa_{slip,i-1} : EI_i(\kappa) = EI_{min,i} + \sum_{j=1}^{i-1} EI_{stick,j} + \sum_{j=i}^a EI_{slip,j} \quad (\text{C.6})$$

In which;

κ is the curvature of the rope

κ_{slip} is the critical slip curvature

a is the total number of wires or strands

EI_{max} is the maximal bending stiffness of the rope according to equation C.7

$EI_{min,i}$ is the minimum bending stiffness of a wire or strand according to Equation C.8

$EI_{stick,j}$ is the sticking bending stiffness of a wire or strand according to Equation C.9

EI_{slip} is the slipped bending stiffness of a wire or strand according to Equation C.10

$$EI_{max} = \sum_{i=0}^a EI_{min,i} + EI_{stick,i} \quad (C.7)$$

In which;

EI_{max} is the maximal bending stiffness of the rope

a is the total number of wires or strands

$EI_{min,i}$ is the minimum bending stiffness of a wire or strand according to Equation C.8

$EI_{stick,i}$ is the sticking bending stiffness of a wire or strand according to Equation C.9

$$EI_{min,i} = E_i \frac{\pi \delta_i^4}{64} \cos \beta \quad (C.8)$$

In which;

$EI_{min,i}$ is the minimal bending stiffness of a wire or strand

E_i is the elasticity modulus of the wire or strand

δ is the wire or strand diameter

β is the wire or strand lay angle

$$EI_{stick,i} = E_i A_i (r_i \sin \varphi_n)^2 \cos^3 \beta \quad (C.9)$$

In which;

$EI_{stick,i}$ is the stick bending stiffness of a wire or strand

E_i is the elasticity modulus of the wire or strand

A_i is the sectional area of the wire or strand

r_i is the layer radius of the wire or strand according to Figure C.6

φ_n is the wire or strand helix angle according to Figure C.6

β is the wire or strand lay angle

$$EI_{slip,i} = \frac{(Z_{slip,i}(\varphi_n) r_i \sin \varphi_n \cos \beta)}{\kappa} \quad (C.10)$$

In which;

$EI_{slip,i}$ is the slipped bending stiffness of a wire or strand

$Z_{slip,i}$ is the maximum possible friction force in a wire or strand after they have slipped according to Equation C.11

φ_n is the wire or strand helix angle according to Figure C.6

r_i is the layer radius of the wire or strand according to Figure C.6

β is the wire or strand lay angle

κ is the rope curvature

$$Z_{slip,i}(\varphi) = (Z_{T,i} + S_i) (e^{\mu \sin \beta \varphi} - 1) \quad (C.11)$$

In which;

$Z_{slip,i}(\varphi)$ is the maximal possible friction force in a wire or strand after they have slipped

$Z_{T,i}$ is the tensile force in a single wire according to Equation C.3

S_i , this term considers the contribution of the tensile forces in the layers 'above' this layer to the tensile force $Z_{T,i}$ of this layer, according to Equation C.4

μ is the wire rope friction coefficient, typically taken as 0.5 [Pap97]

β is the lay angle of the wire

φ_n is the wire or strand helix angle according to Figure C.6

Using these expressions the variable bending stiffness of the wire ropes designed in section C.2 can be plotted, and the influence of the strand and rope lay angle on the bending stiffness can be examined. Figure C.7 displays the main cable bending stiffness versus its curvature with different strand lay angles. The lay angle used for the wires in the strand in this figure is 2° and the rope tension is set at 829 000 kN, which is the maximum value found for the cable tension in earlier work [Yip15].

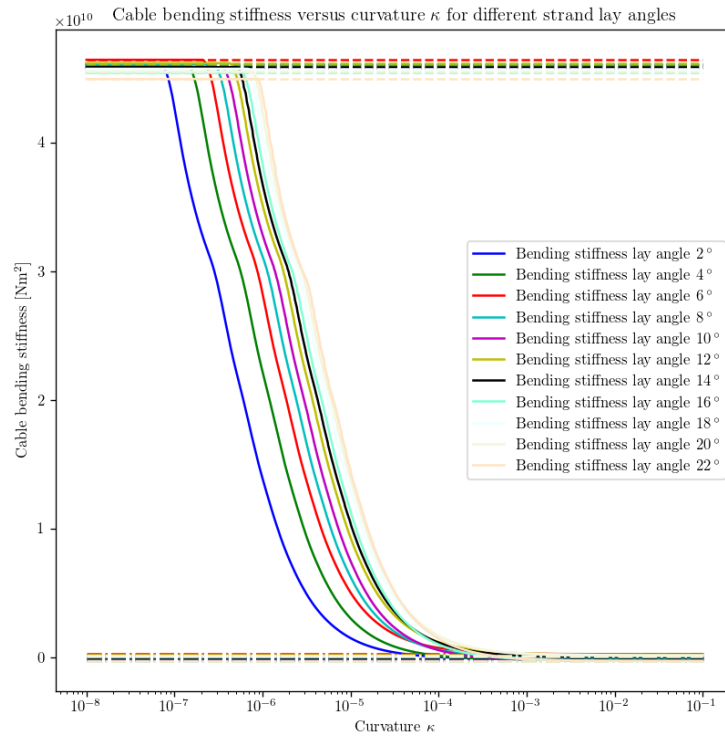


Figure C.7: Main cable wire rope bending stiffness versus curvature for different strand lay angles, lay angle wires in strands is 2° and rope tension is 829 000 kN.

Figure C.7 clearly shows the influence of the strand lay angle on the variable bending stiffness. The main difference is visible near the minimal bending stiffness, where for the lower lay angles the minimal bending stiffness is reached at a lower curvature value. The minimum- and maximum bending stiffness are maximal when the strand lay angle is 6° . They are minimal at the higher strand lay angle of 22° .

The influence of the lay angle of the wires in the rope strands is examined by performing the same calculation with a lay angle of the wires in the rope strands of 22° . The results are displayed in Figure C.8.

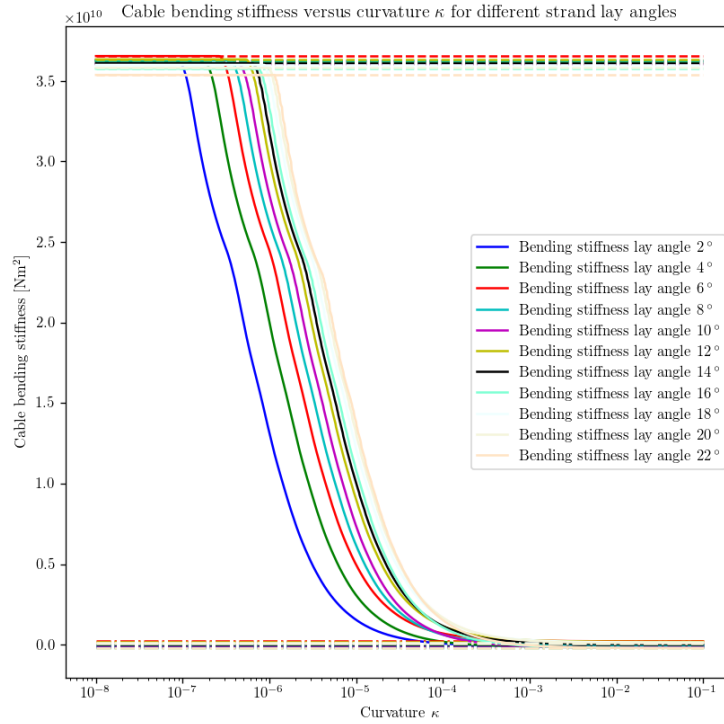


Figure C.8: Main cable wire rope bending stiffness versus curvature for different strand lay angles, lay angle wires in strands is 22° and rope tension is 829 000 kN.

The difference between the lower and higher lay angle of the wires in the strand is mainly visible in the maximal bending stiffness, which is approximately 10^{10} N m² lower across all strand lay angles. This is due to the lower elasticity modulus for the strands with the higher wire lay angles. Apart from lowering both the maximum- and minimum bending stiffness, there is no difference in the shape or the curvature at which the minimum- or maximum bending stiffness are achieved.

The same calculation has been performed for wire lay angles in the strands between 2° and 22°. The results are as to be expected, the variation of the minimum- and maximum bending stiffness versus change in lay angle follow the shape of the plot shown in Figure C.5. Which is unsurprising, since the elasticity modulus has a direct influence on the minimum- and maximum wire bending stiffness, as is shown in Equations C.8 and C.9. The shape of the plots is largely unchanged, due to the fact that the changing elasticity modulus has no effect on the slipped wire bending stiffness.

Another influence to examine is the effect of the rope tension on the bending stiffness-curvature relation. The previous calculations were performed under the maximum occurring rope tension of 829 000 kN. A new calculation is now performed with the minimum main cable tensile force of 530 000 kN to examine the effect the rope tension has on the wire rope stiffness behaviour. This is displayed in Figure C.9, in which a wire lay angle of 2° is used in the strands.

Comparing Figure C.9 to C.7, one is hard pressed to find a difference. This is due to the fact that the minimum and maximum bending stiffness remain unchanged. If one looks closely, it is visible that the minimum tension is attained at a slightly lower curvature value. It can be concluded that this huge change in cable tension has had a minimal effect on the cable bending stiffness.

The same four analyses as performed for the main cable are performed for the lateral cable and displayed in Figures C.10, C.11, C.12 and C.13. These results confirm the conclusions of the tests performed with the main cable wire rope and show that these conclusions hold for these rope and strand layouts and rope tensile loads.

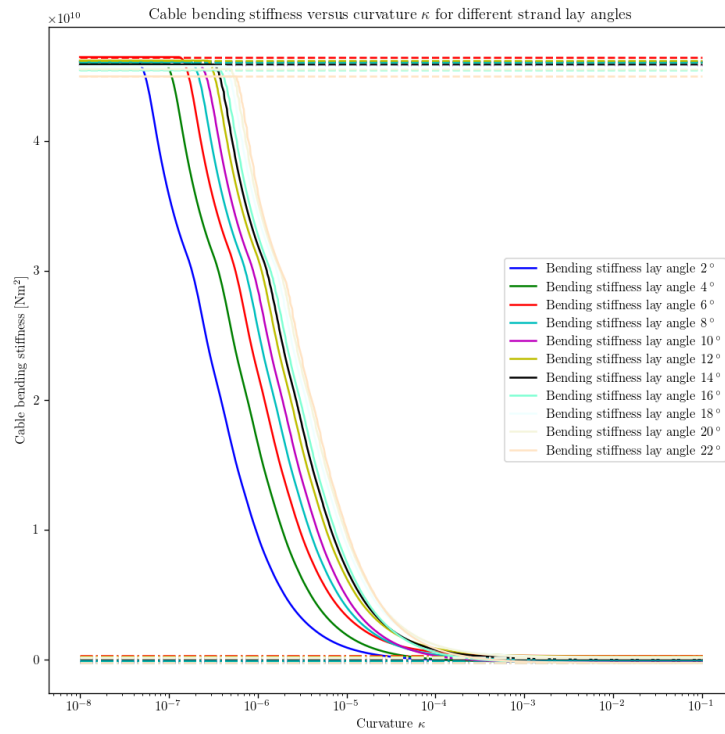


Figure C.9: Main cable wire rope bending stiffness versus curvature for different strand lay angles, lay angle wires in strands is 2° and rope tension is 530 000 kN.

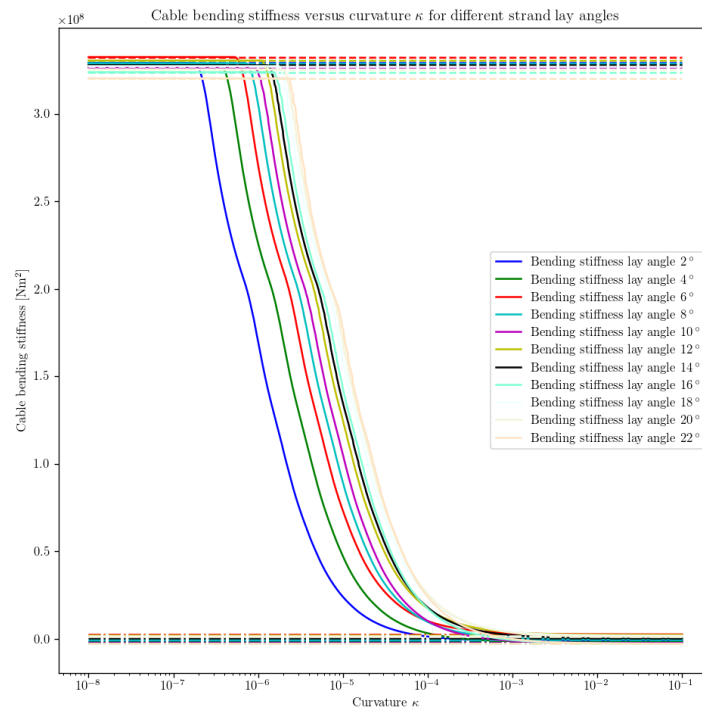


Figure C.10: Lateral cable wire rope bending stiffness versus curvature for different strand lay angles, lay angle wires in strands is 2° and rope tension is 52 146 kN.

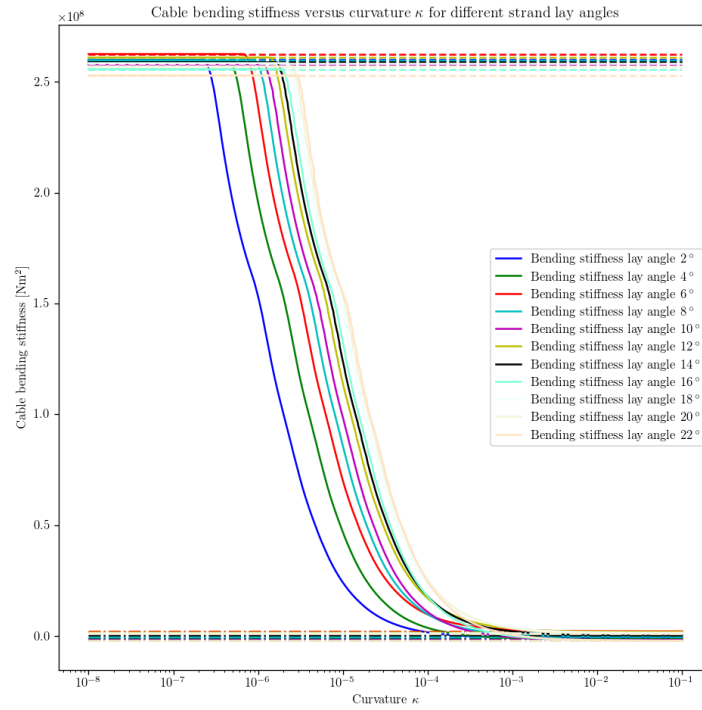


Figure C.11: Lateral cable wire rope bending stiffness versus curvature for different strand lay angles, lay angle wires in strands is 22° and rope tension is 52 146 kN.

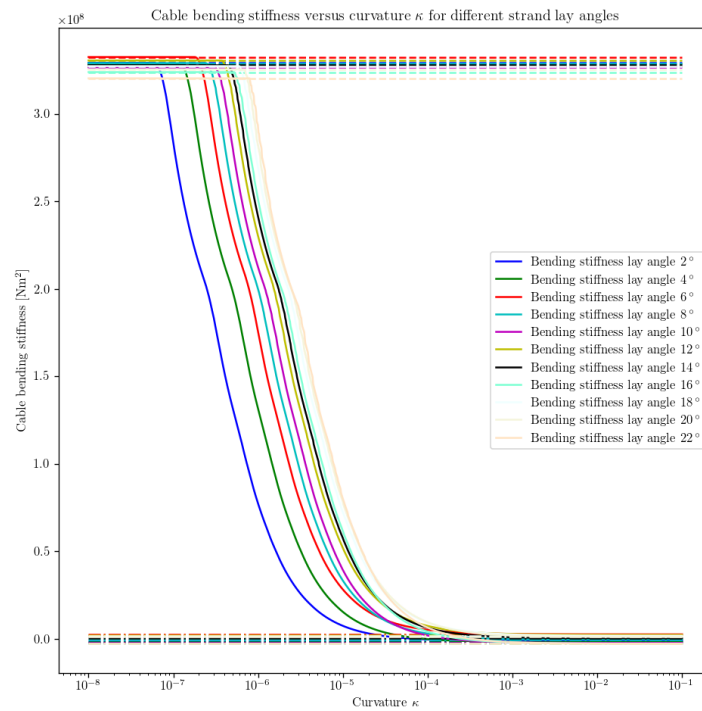


Figure C.12: Lateral cable wire rope bending stiffness versus curvature for different strand lay angles, lay angle wires in strands is 2° and rope tension is 17 702 kN.

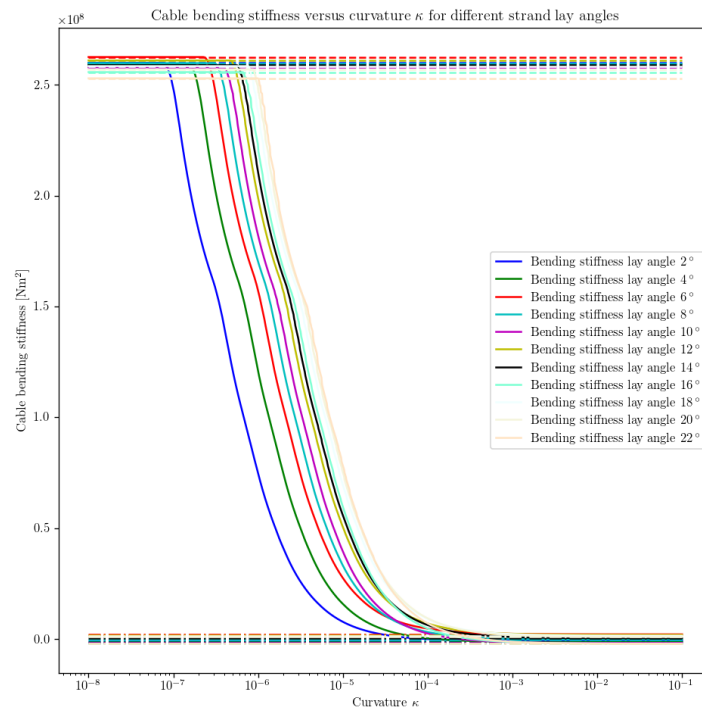


Figure C.13: Lateral cable wire rope bending stiffness versus curvature for different strand lay angles, lay angle wires in strands is 22° and rope tension is 17 702 kN.

C.5 Conclusion

As a result of the calculations performed in this appendix the final design for the main and lateral cables can be determined. The desired properties of the rope should lead to a long fatigue life, low extension under tensile stress, good environmental protection and high hysteretic damping.

Both a long fatigue life and low tensile extension are achieved by choosing low lay angles for these axially loaded stay cables. The environmental protection should mainly be achieved by the plastic sheathing added to the cross section. However, by giving both the strands and the wires in the strands a small lay angle, the containment of the rope lubricating agent in all rope parts will be improved, improving the fatigue life of the rope [Fey07]. Hysteretic damping is mentioned here for the first time. It is the damping of cable motions due to inter-wire friction and pure material damping in the wires themselves. It can be modelled by taking the cable's non-linear bending stiffness as a function of its curvature into account during dynamic analysis. From previous studies it has been found that when loaded under its own weight, most cable segment curvatures fall between 10^{-3} to 10^{-5} . Thus to maximize hysteretic damping, a lay angle should be chosen that maximizes the stiffness change in this curvature range. As the damping is achieved mainly through inter-wire friction, this will most likely be detrimental to the fatigue life of the cable.

Taking these considerations into account and balancing the different advantages and disadvantages has led to the main and lateral cable properties displayed in Table C.5 and the cross sections as depicted in section C.2 in Figures C.3 and C.4. The lay angle of the wires in the cable strands is kept at a low 2° , as this lay angle has a large influence on the elasticity modulus of the cable as a whole and thus the cable extension under axial loading. The cable strands' lay angle is slightly higher at 6° as this allows for a better 'lock in' of lubricating agent in the ropes. At 6° the change in bending stiffness in the regarded curvature range is already quite significant, while further increases in lay angle yield smaller increases in the variability of the bending stiffness. It is expected that these values for the lay angles provide a good balance between fatigue life on the one hand and damping on the other hand. The bending stiffness versus curvature for the main and lateral cables is shown in Figures C.14 and C.14.

Once again, it should be noted that the method used to obtain the cable bending stiffness characteristics was not developed for or tested with cables of the size implemented here. A recommendation to be made is to test the veracity of this method for cables of the sizes used in this design.

	Material	Type	Wire lay angle	Wire diameter [mm]	Wire layers	Strand lay angle	Strand diameter [mm]	Strand layers
Main cable	Y1860	Spiral rope	2°	3.0	20	6°	123	6
Lateral cable	Y1860	Spiral rope	2°	4.7	4	6°	42.3	5

Table C.5: Cable wire rope properties.

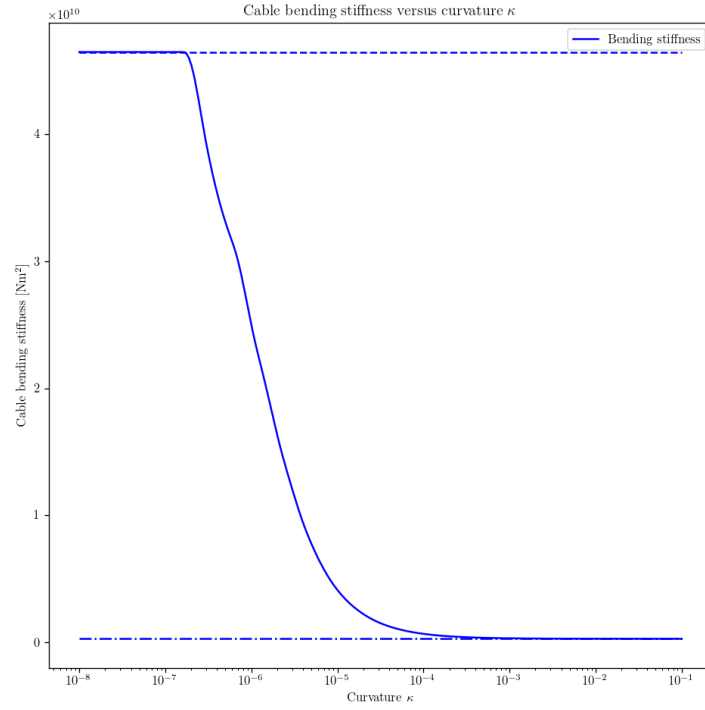


Figure C.14: Main cable bending stiffness versus curvature.

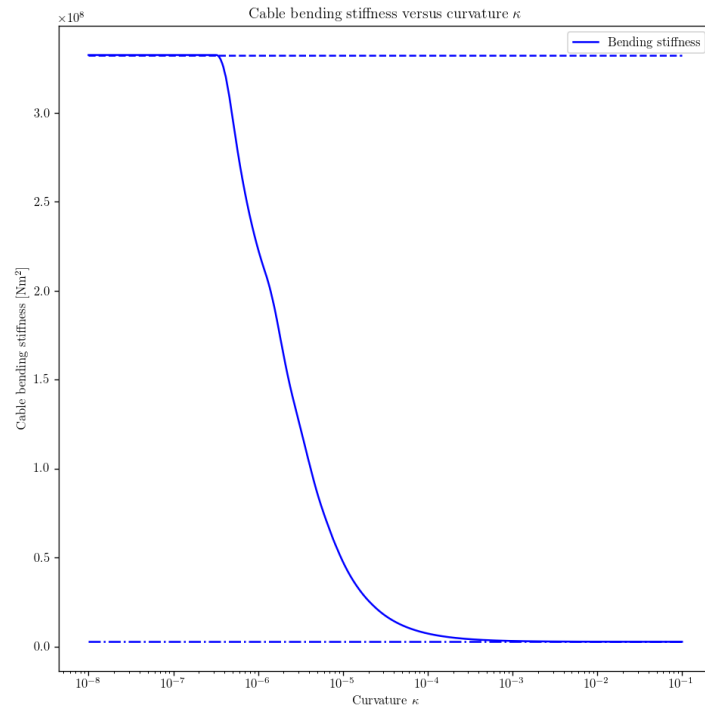


Figure C.15: Lateral cable bending stiffness versus curvature.

Appendix D

Cable damping

This chapter outlines the calculation of the internal damping of the cables in the bridge model.

D.1 Hysteretic damping

As mentioned in section C.5, hysteretic damping is the internal structural damping of the cable motion. This is mainly caused by friction between the strands and wires in the cables and only a negligible contribution is made by damping in the wire material itself [Spa13].

Hysteretic damping is caused by the dissipation of energy due to inter-wire friction as the cables deform under loading. This can be visualised using a force-displacement hysteresis curve. An example of a wire rope hysteresis curve is depicted in Figure D.1. In this Figure, the load sequence is depicted with numbers 1 – 4. In this load sequence, the load path during unloading is different than during loading, creating the shaded area in the Figure. The area contained in this load path is the energy extracted from the motion by the internal hysteretic damping during this load cycle.

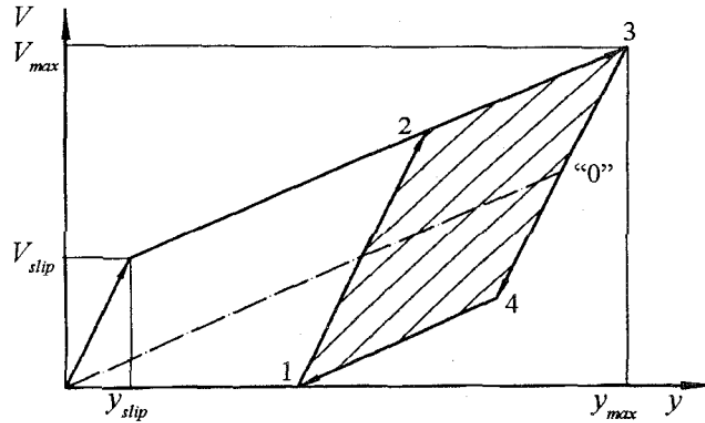


Figure D.1: An example force-deflection hysteresis curve [Pap97].

A method to model the effect of this hysteretic damping due to inter-wire friction is to model the cable with a variable bending stiffness, dependant upon the curvature and tension of the cable [Pap97]. For each analysis step, the bending stiffness is updated, reflecting the state of the cable.

D.2 Modelling cable damping

As mentioned in section D.1, in the method used in this thesis to model cable hysteretic damping, the bending stiffness of the cable is to be updated during analysis based on the curvature and tension of the cable. Little to no Finite Element software packages provide options to implement this and SACS is no exception. The SACS software does, however, allow for the structural damping to be entered as a percentage of critical damping for all modes of the structural model (also known as a structural damping factor). The critical damping is the damping value for which the approach of the system to its

zero amplitude (equilibrium position) from a displaced situation is the quickest. If the damping value is higher, the approach takes longer. If it is lower, it reaches the zero amplitude faster, but subsequently oscillates around it. The damping factor for the entire bridge system is expected to be much lower than the critical damping. The methodology to transform the hysteretic damping model from the non-linear bending stiffness to a percentage of critical damping (or damping factor) is described in this section and subsections.

D.2.1 Overview

The path to transform the variable bending stiffness in a cable cross section into a structural damping factor for the entire bridge model is quite extensive, this section provides an overview of the steps taken. The work-flow for the iterations is depicted visually in Figure D.2.

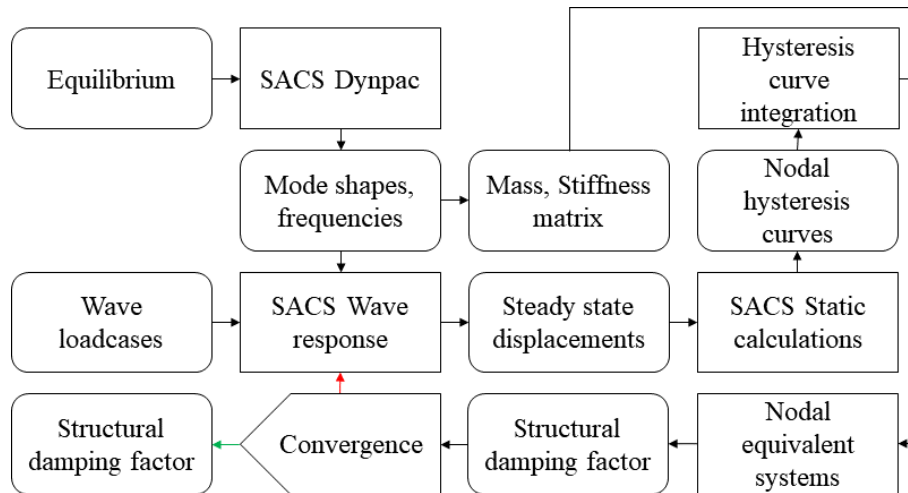


Figure D.2: Work-flow for structural damping iterations.

Use the variable cable bending stiffness to create an equilibrium situation (in terms of displacement u_0 , bending stiffness EI_0 and tension T_0) of the bridge model loaded by its self-weight through iterative non-linear FEM analysis as described in appendix F.

Taking the bridge model in this equilibrium situation, calculate mode shapes, mode frequencies and mass M and stiffness K_0 matrices using the Dynpac module of the SACS software package.

Use the SACS wave response program to pre-calculate the steady state response of the model without damping and with constant cable bending stiffness EI_0 , calculated previously, to the different wave load cases as described in section G.6.

Create a set of linear analyses in which the model is deformed according to the steady state displacements calculated earlier, time-stepping the model through the displacement to obtain hysteresis curves per node. The cable bending stiffness EI is updated per time step.

These hysteresis curves are integrated to calculate the dissipated energy per node during the steady state excitation.

Per node, per degree of freedom, simple mass-spring-dashpot systems are used as equivalent systems. The spring stiffness k is determined from the global stiffness matrix K_0 . The viscous damping is to be determined.

Hysteretic damping factors μ are determined per degree of freedom per node by equating the dissipated energy in the hysteretic curves to the dissipated energy in the equivalent system.

An energy consistent structural damping factor for the entire system is determined from the nodal damping factors.

The following subsections address the different parts of the methodology outlined here.

D.2.2 Equilibrium

The first step is to determine the equilibrium situation of the entire bridge model when loaded by its self weight. A short summary of the proceedings is given here, for more detail reference is made to appendix F. To find the equilibrium situation, in terms of displacement and cable bending stiffness and tension, an iterative procedure using the FEM package Scia Engineer is performed. This procedure starts with a non-linear analysis in Scia using the maximum cable stiffness as calculated in section C.4. Then, reading out the cable tension and displaced position, the cable bending stiffness is recalculated and updated before performing another non-linear analysis. This iteration is repeated until convergence in terms of displacement is reached.

D.2.3 Mode shapes

The next step is to take the resulting tension and displacement data from the equilibrium situation and create a SACS model incorporating this data. Using the SACS Dynpac module, the mode shapes, mode frequencies, stiffness-, and mass matrix are calculated. This step is performed in SACS due to the possibility to automatically take into account fluid added mass in determining these properties of the model.

D.2.4 Undamped steady state solution

Taking the results of the modal analysis, the SACS Wave Response program is run for the different wave load cases outlined in section B.5 with the structural damping factor set to zero for the first iteration, and following iterations set to the resulting structural damping factor calculated in the previous iteration. As described in section H.2, the Wave Response program calculates the steady state response of the structure to these load cases.

D.2.5 Pre-set displacement

The calculated steady state displacements are applied to the model as pre-set displacement per time step using SACS. For each time step, a new cable bending stiffness EI is calculated and applied per cable section. The analysis performed is a linear calculation, with each node receiving a pre-set displacement per time step.

The energy dissipated in the steady state movement per node per degree of freedom $\Delta E_{n,dof}$ is calculated by integrating the area contained in the hysteresis curve created by the resulting forces per node per degree of freedom and the displacements per node per degree of freedom. The method used to integrate the hysteresis curves is detailed in section D.2.6. An example of a hysteresis curve produced using the pre-set displacements is shown in Figure D.3.

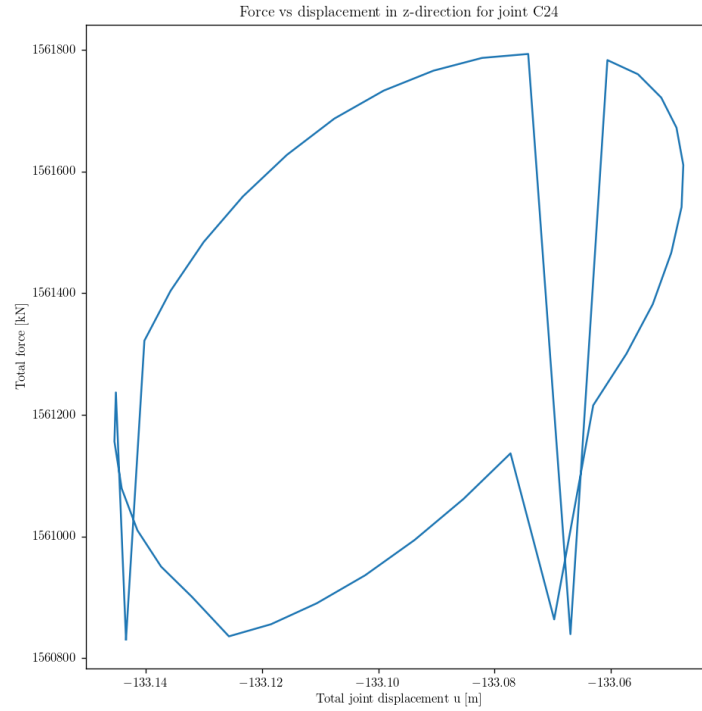


Figure D.3: Force-deflection hysteresis curve for joint C24 in the z-direction.

D.2.6 Integration

This section deals with the integration of the hysteresis curves produced using a linear analysis with pre-set displacements in SACS. Examples of hysteresis curves produced using this method are shown in Figures D.3 and D.4.

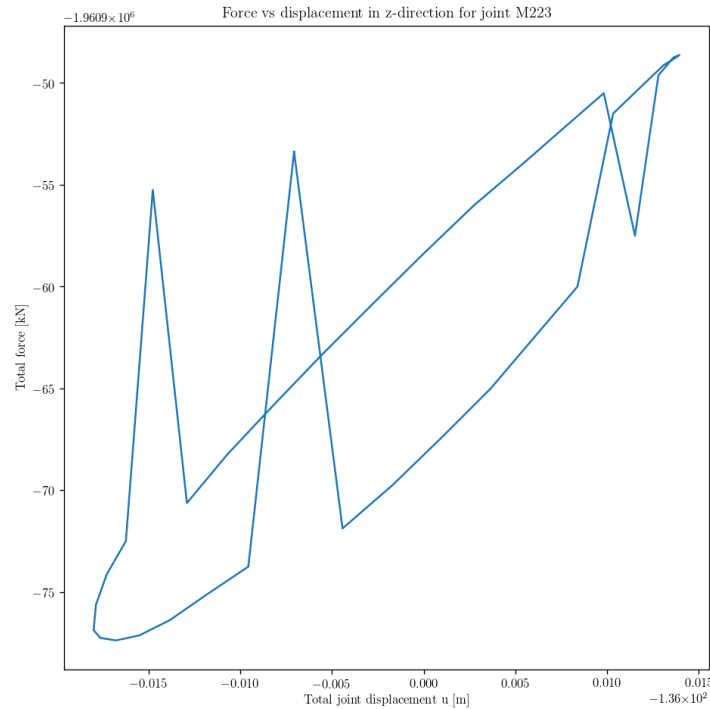


Figure D.4: Force-deflection hysteresis curve for joint M223 in the z-direction.

As is seen in these figures, the hysteresis curve are very jumpy and contain large peaks caused by

outlying values. These outlying values are caused in part by the bridge geometry and relative displacement and partly by numerical errors in the linear SACS analysis. When multiple data points are the cause of one these peaks it is most likely due to the geometry and relative displacement of the cable at the node location. However, when a peak is caused by single outlying data point which is not in accordance with the surrounding data, it is likely caused by a numerical error. To mitigate the influence of these single outlying values on the integrated area, a corner-cutting algorithm is employed to smooth the curve surface and reduce single peaks. The corner-cutting algorithm chosen to perform this task is Chaikin's Corner Cutting Algorithm [Cha74]. This algorithm iteratively refines a collection of data points to smooth the curve area. Using this refining algorithm with proportions 0.6 : 0.4 and 3 iterations yields the refinement shown in Figures D.5 and D.6. These proportions are tested to yield a large 'protection' against outlying values, while the refinement limit of three iterations provides a good balance between 'smoothness' and computation time.

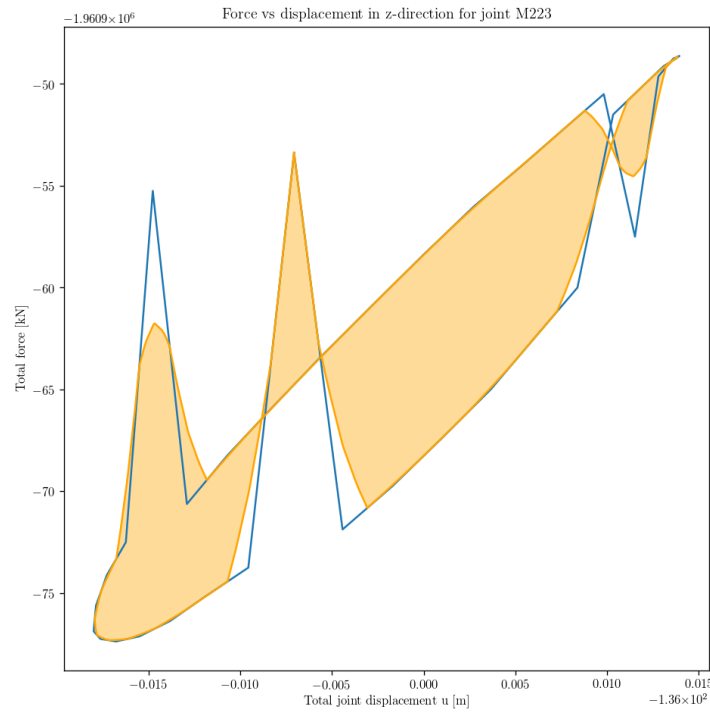


Figure D.5: Force-deflection hysteresis curve for joint M223 in the z-direction, refined using Chaikin's Corner Cutting Algorithm with 3 iterations and 0.6 : 0.4 proportions.

As can be seen in Figure D.5, some peaks are not 'cut' by the algorithm. This is due to the fact that although these peaks appear to be single outliers, they are in fact comprised of multiple data points.

Another example of Chaikin's Corner Cutting Algorithm in action is displayed in Figure D.6. In this figure the peaks are caused by single outliers and the corner cutting algorithm decreases their influence on the total area in the hysteresis curve.

After processing the data to smooth out numerical errors, the curves can be integrated to obtain the total dissipated energy per steady state movement per node per degree of freedom.

To integrate the area contained in the hysteresis curves, Green's Theorem is used [Rie51]. This Theorem links the area bounded by a closed curve to the path integral following its border. The expression for Green's Theorem is found in Equation D.1.

$$A = \iint_D dA = \frac{1}{2} \oint_C (-y dx + x dy) \quad (D.1)$$

In which;

A is the area bounded by curve C

C is the curve bounding area A

The integration procedure expressed in Equation D.1 is performed for every degree of freedom of each node in the bridge system.

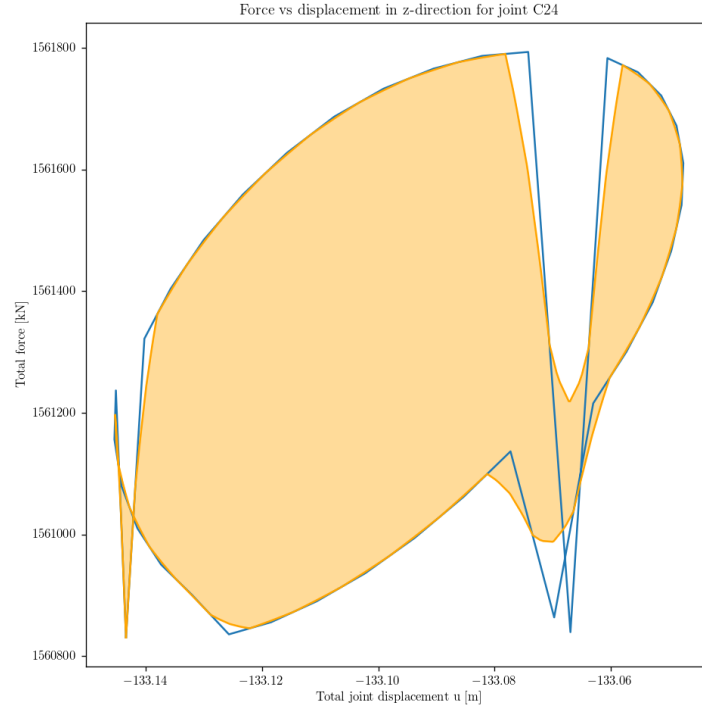


Figure D.6: Force-deflection hysteresis curve for joint C24 in the z-direction, refined using Chaikin's Corner Cutting Algorithm with 3 iterations and 0.6 : 0.4 proportions.

D.2.7 Equivalent systems

Per node, per degree of freedom, equivalent systems must be set up to equate the dissipated energy in the steady state movement to the energy dissipated in the equivalent system. The equivalent systems are simple mass-spring-dashpot systems, as is depicted in Figure D.7.

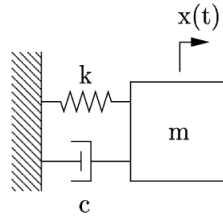


Figure D.7: A mass-spring-dashpot system.

The spring stiffness used in the equivalent systems is taken from the global bridge system stiffness matrix. The values relating the displacement in the x-, y-, or z-degree of freedom one a node to a force in the same degree of freedom on the node are used.

The expression for the energy dissipated in this system at resonance is given in Equation D.2 and the expression for the equivalent damping factor μ_{eq} is then achieved by a simple operation on this expression and given in Equation D.3 [Adh13].

$$\Delta W = 2 \pi k \mu x_{max}^2 \quad (D.2)$$

In which;

ΔW is the dissipated energy per cycle

k is the spring stiffness

μ is the damping factor as percentage of critical damping according to Equation D.3

x_{max} is the absolute maximum amplitude

$$\mu_{eq} = \frac{\Delta W}{2 \pi k x_{max}^2} \quad (D.3)$$

The equivalent damping factor per node per degree of freedom is calculated by inserting the energy dissipation obtained through the integration of the hysteresis curves into Equation D.3.

D.2.8 Structural damping factor

After obtaining the equivalent damping factors per node per degree of freedom, a final operation is required to obtain the total structural damping factor.

This operation is detailed in Equations D.4 and D.5. This operation leads to an energy-consistent structural damping factor for the steady state motion across all modes [al96].

$$\zeta = \frac{1}{2} \frac{\sum_{m=1}^{n_{hysteretic}} \mu^{(m)} E_{max}^{(m)}}{\sum_{m=1}^{n_{hysteretic}} E_{max}^{(m)}} \quad (D.4)$$

In which;

ζ is the structural damping factor

$n_{hysteretic}$ is the number of hysteretic systems in the model

$\mu^{(m)}$ is the hysteretic damping factor for hysteretic system m

$E_{max}^{(m)}$ is the maximum potential energy in the steady state movement for hysteretic system m according to Equation D.5

$$E_{max}^{(k)} = \frac{1}{2} k^{(k)} u_{max}^{(k)2} \quad (D.5)$$

In which;

$E_{max}^{(k)}$ is the maximum potential energy in the steady state movement for hysteretic system k

$k^{(k)}$ is the spring stiffness of hysteretic system k

$u_{max}^{(k)}$ is the absolute maximum displacement of hysteretic system k in the steady state movement

D.3 Results

This section displays and discusses the results obtained using the methodology outlined in section D.2. First it is necessary to explain that the structural damping factor has been calculated for the six load cases outlined in section B.5. Each of these load cases correspond to a critical wave (with aligned direction) together with in- or outgoing current. Each two load cases thus represent the same wave loading, in which only the current has changed direction. The calculated structural damping factors are displayed in Table D.1.

Load case	Undamped ζ	Iteration 1 ζ	Iteration 2 ζ	Iteration 3 ζ
1	1.894 %	0.912 %	1.644 %	1.624 %
2	1.850 %	0.878 %	1.768 %	1.776 %
3	7.145 %	5.568 %	5.403 %	
4	6.958 %	5.365 %	5.612 %	
5	2.377 %	2.347 %		
6	2.347 %	2.337 %		

Table D.1: Structural damping factors per load case.

D.4 Conclusions

As can be seen in the results, the structural damping factor is highly dependant upon the wave excitation and almost insensitive to the change in current loading. That the damping factors are the same for the in- and outgoing current cases coupled to the same wave loading also provides a simple sanity check for the entire damping calculation, because it is expected that these values match closely. It is clear that when the wave loading remains the same, the damping factor remains mostly the same. As the wave loading changes and excites more modes of vibration of the structure, the structural damping increases. This is expected, since the source of the structural damping is the friction between the strands and wires in the steel cables. If the steel cables move less, there is less friction and the damping is less.

The solution is quick to converge, which makes this method quite effective to obtain a structural damping factor for all modes of vibration quickly.

It is also clear that for every loading scenario, a recalculation of the cable structural damping is necessary to obtain the structural damping as applicable for that specific load case.

A point of attention is the fact that the results obtained from this analysis have to be verified and potentially modified after experiments with steel cables whose properties approach the cables used in this design.

Appendix E

Waves steady state displacement

This appendix contains the steady state displacement analysis performed in this study. The goal of this analysis as presented in this appendix is to determine the motion of the bridge deck due the wave loads on the bridge system. First the theory behind steady state analysis is presented. Then the set-up of the analysis as it is performed in this thesis is described. After which the results and conclusions that can be drawn from the analysis are presented.

E.1 Theory

The steady state displacement of a structure under an unchanging known harmonic load is the movement of the structure after a sufficient amount of time has passed and the structure vibrates at the same frequency as the load, albeit possibly with a phase shift. For the calculation of said response, first the system's eigenmodes and corresponding modal frequencies need to be determined, for this operation reference is made to section H.1. Following this, the system's equation of motion (Equation E.1) can be transformed into the modal form by substituting the expression in Equation E.2. This expression states that the sum of all modal responses can be combined to into the actual response of the structure, which assumes that all degrees of freedom within a modal response move using the same time function. After some operations this leads to the expression for the modal equation of motion shown in Equation E.3.

$$M \ddot{u} + C \dot{u} + K u = F(t) \quad (\text{E.1})$$

In which;

u is the system displacement

M is the system mass matrix

C is the system damping matrix

K is the system stiffness matrix

$F(t)$ is the forcing function

$$u(t) = \sum_{i=1}^n \hat{x}_i u_i(t) \quad (\text{E.2})$$

In which;

$u(t)$ is the system response

n is the number of system eigenmodes

\hat{x}_i is the eigenvector (mode shape) of mode i

$u_i(t)$ is the modal response of mode i

$$\ddot{u}_i + 2 \xi_i \omega_i \dot{u}_i + \omega_i^2 u_i = \frac{F^*(t)}{m_{ii}^*}, \quad (i = 1 \dots n) \quad (\text{E.3})$$

In which;

u_i is the modal displacement for mode i

ξ_i is the modal damping factor for mode i

ω_i is the modal eigenfrequency for mode i

$F^*(t)$ is generalized force for mode i

m_{ii}^* is the entry in the modal damping matrix for mode i

n is the number of modes in the system

For the steady state solution it is assumed that the influence of the initial conditions on the structure response have 'died out' and that just the system response to the forcing function is left, thus that sufficient time has passed for just the particular solutions to the system of equations presented in Equation E.3 to be present in the modal response functions. To obtain the particular solutions, the Duhamel integral (Equation E.4) is utilized in combination with the unit impulse response function shown in Equation E.5, which leads to the expression for the particular solutions depicted in Equation E.6.

$$u_i(t) = \int_{\tau=0}^t F^*(\tau) g_i(t - \tau) d\tau, \quad (i = 1 \dots n) \quad (\text{E.4})$$

In which;

u_i is the particular solution for the modal displacement for mode i

$F^*(\tau)$ is generalized force for mode i

$g_i(t - \tau)$ is the modal unit impulse response function as expressed in Equation E.5

$$g_i(t) = \frac{1}{m_{ii}^* \omega_i \sqrt{1 - \xi_i^2}} \exp -\xi_i \omega_i t \sin \left(\omega_i \sqrt{1 - \xi_i^2} t \right), \quad (i = 1 \dots n) \quad (\text{E.5})$$

In which;

$g_i(t)$ is the modal unit impulse response function

m_{ii}^* is the entry in the modal damping matrix for mode i

ω_i is the modal eigenfrequency for mode i

ξ_i is the modal damping factor for mode i

$$u_i(t) = \int_{\tau=0}^t \frac{F^*(\tau)}{m_{ii}^* \omega_i \sqrt{1 - \xi_i^2}} \exp -\xi_i \omega_i t \sin \left(\omega_i \sqrt{1 - \xi_i^2} t \right) d\tau, \quad (i = 1 \dots n) \quad (\text{E.6})$$

In which;

u_i is the particular solution for the modal displacement for mode i

$F^*(\tau)$ is generalized force for mode i

m_{ii}^* is the entry in the modal damping matrix for mode i

ω_i is the modal eigenfrequency for mode i

ξ_i is the modal damping factor for mode i

This method of calculating the steady state response assumes a linear system, which, due to the non-linear nature of the cables, the bridge model in this thesis is not. Therefore, employing this calculation method is an approximation.

section H.2 describes the implementation of this calculation method in the SACS wave response module, with particular emphasis on the calculation of the hydrodynamical loading.

E.2 Set-up

The steady state analysis presented here is performed for the six critical wave load cases defined in section B.5 and shown in Table E.1.

Loadcase	Wave direction - height - wavelength	Current direction
1	180° - 4.55 m - 33 m	Inwards
2	180° - 4.55 m - 33 m	Outwards
3	240° - 4.79 m - 36 m	Inwards
4	240° - 4.79 m - 36 m	Outwards
5	270° - 4.36 m - 36 m	Inwards
6	270° - 4.36 m - 36 m	Outwards

Table E.1: Wave load cases.

For the calculation of the structural damping factor used for all modes of vibration, reference is made to appendix D. The damping factors per loadcase are shown in Table E.2.

Load case	ζ
1	1.624 %
2	1.776 %
3	5.403 %
4	5.612 %
5	2.347 %
6	2.337 %

Table E.2: Structural damping factors per load case.

The serviceability limits of note for this analysis for the bridge deck motion are shown in Table E.3. Table E.4 shows the maximum displacement amplitudes allowed for the bridge decks.

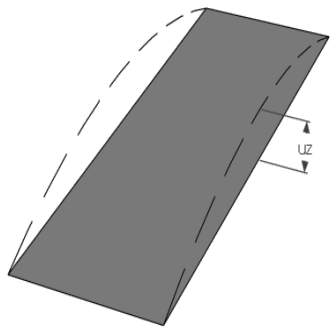
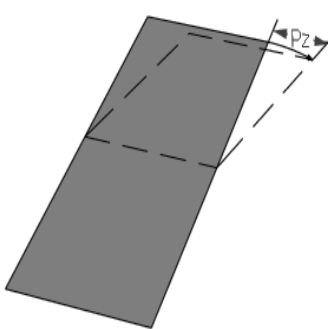
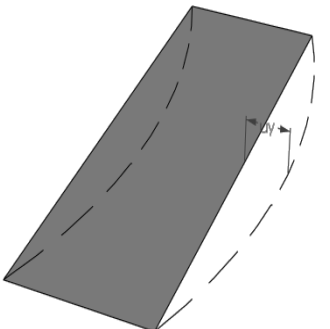
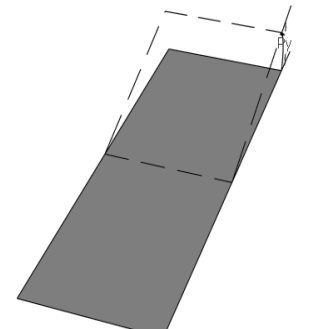
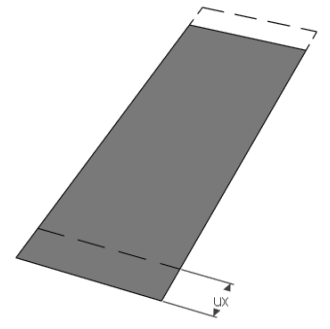
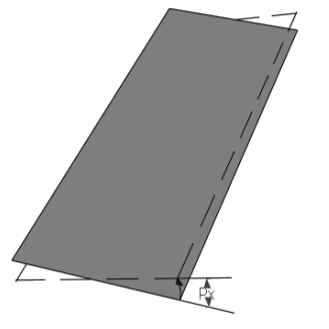
Vertical deformation		Lateral plane rotation	
			
$u_z \leq L/200 \text{ m}$	$a_z \leq 0.7 \text{ m s}^{-2}$	$\phi_z \leq 0.060 \text{ rad}$	$\zeta_z \leq 0.050 \text{ rad s}^{-2}$
Lateral deformation		Cross section plane rotation	
			
$u_y \leq L/200 \text{ m}$	$a_y \leq 0.5 \text{ m s}^{-2}$	$\phi_y \leq 0.044 \text{ rad}$	$\zeta_y \leq 0.107 \text{ rad s}^{-2}$
Longitudinal deformation		Vertical section plane rotation	
			
Not considered	$a_x \leq 0.5 \text{ m s}^{-2}$	Not considered	

Table E.3: Bridge deck deformation serviceability limits.

Deck number	Length [m]	Maximum displacement [m]
1 to 11 and 13 to 23	200	1
12	465	2.325

Table E.4: Maximum allowed deck displacements.

E.3 Results

This section contains the results of this analysis. First the calculated amplitudes of displacement for the cable nodes are depicted in Figure E.1. Next the calculated total displacement amplitudes and maximum accelerations for the bridge deck nodes are depicted in Figures E.2 and E.3. Figures E.4, E.5, E.6 and E.7 show the calculated maximum rotations and angular accelerations for the bridge decks.

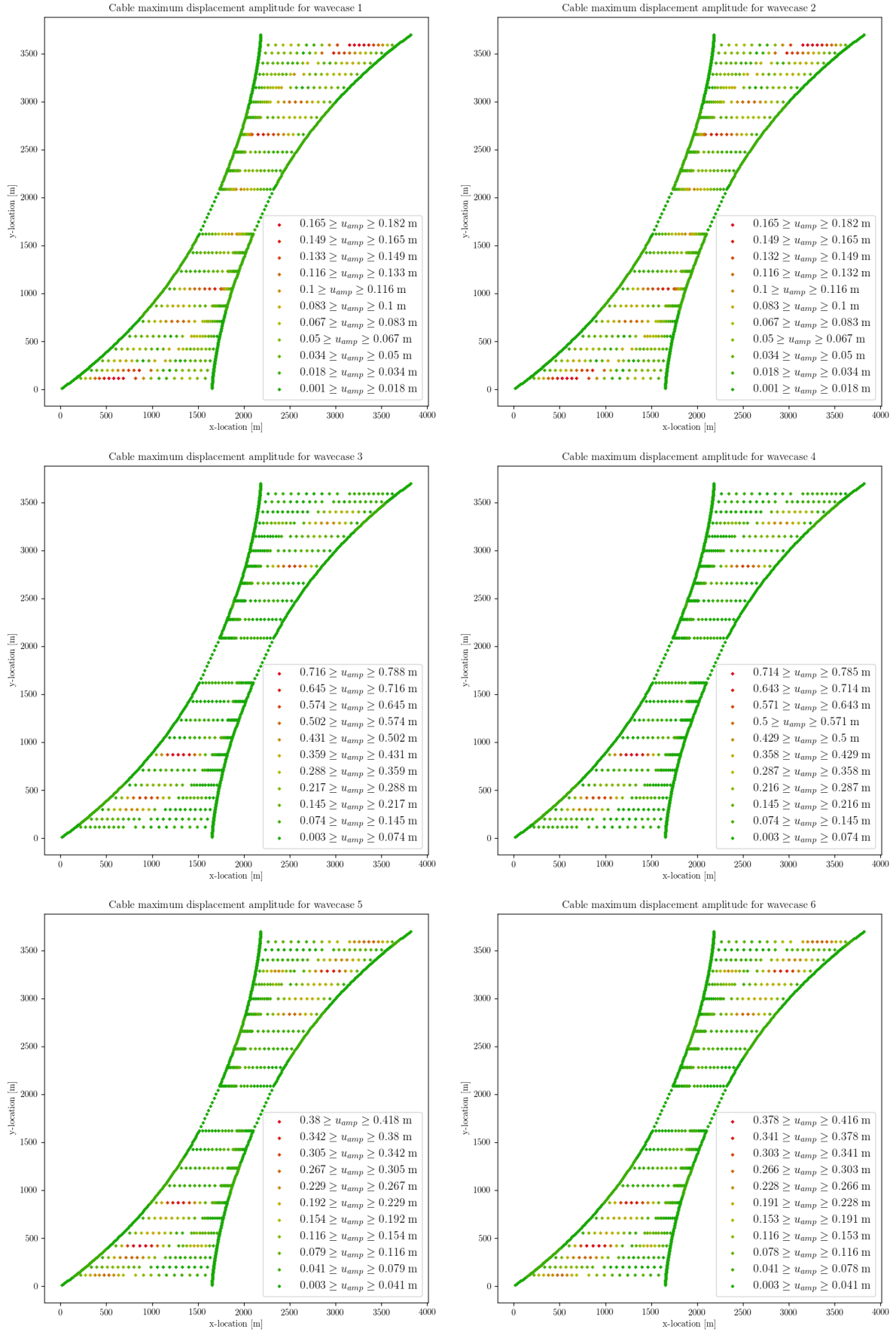


Figure E.1: Cable node displacement amplitude values for the different load cases.

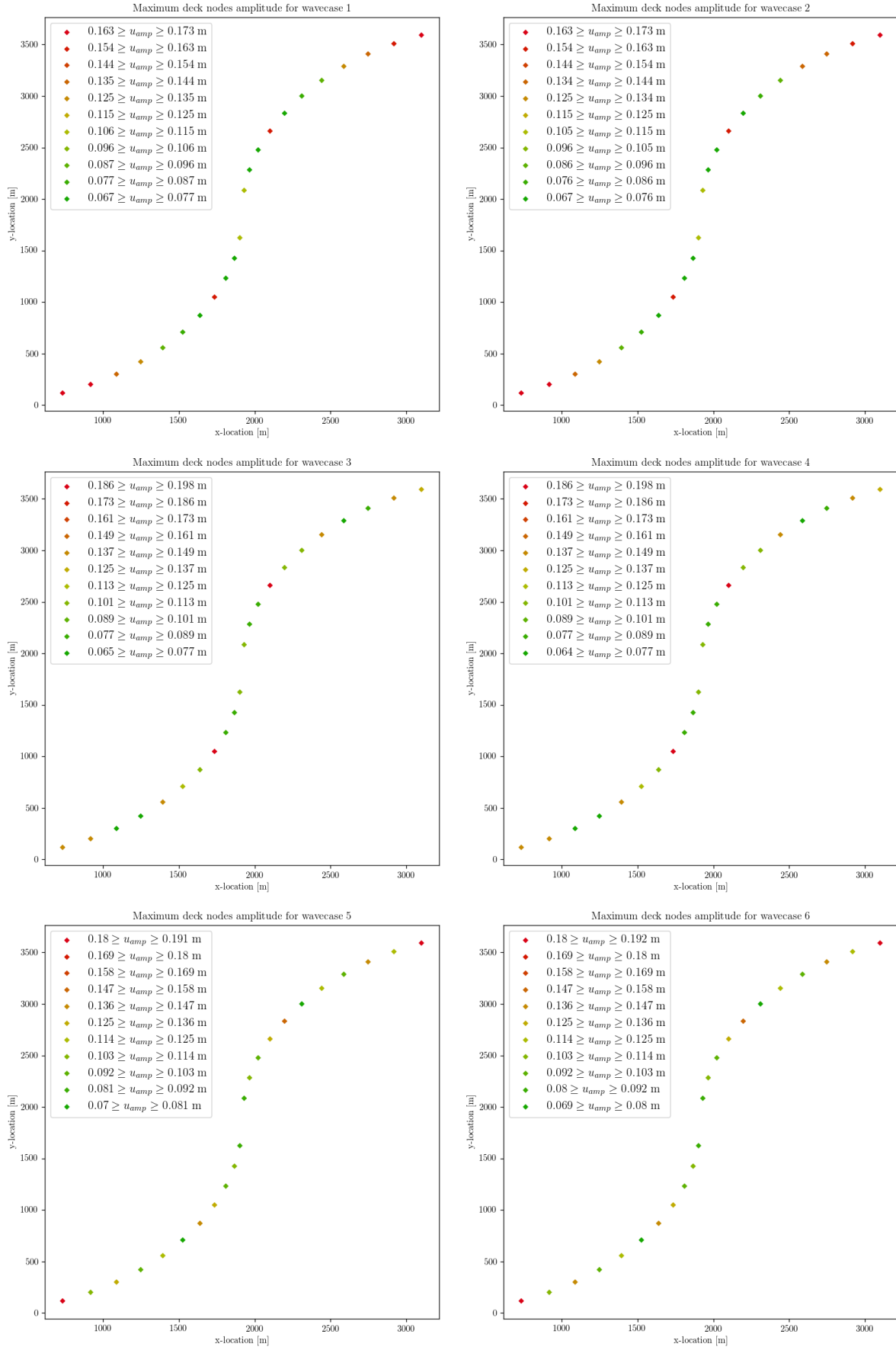


Figure E.2: Bridge deck node displacement amplitude values for the different load cases.



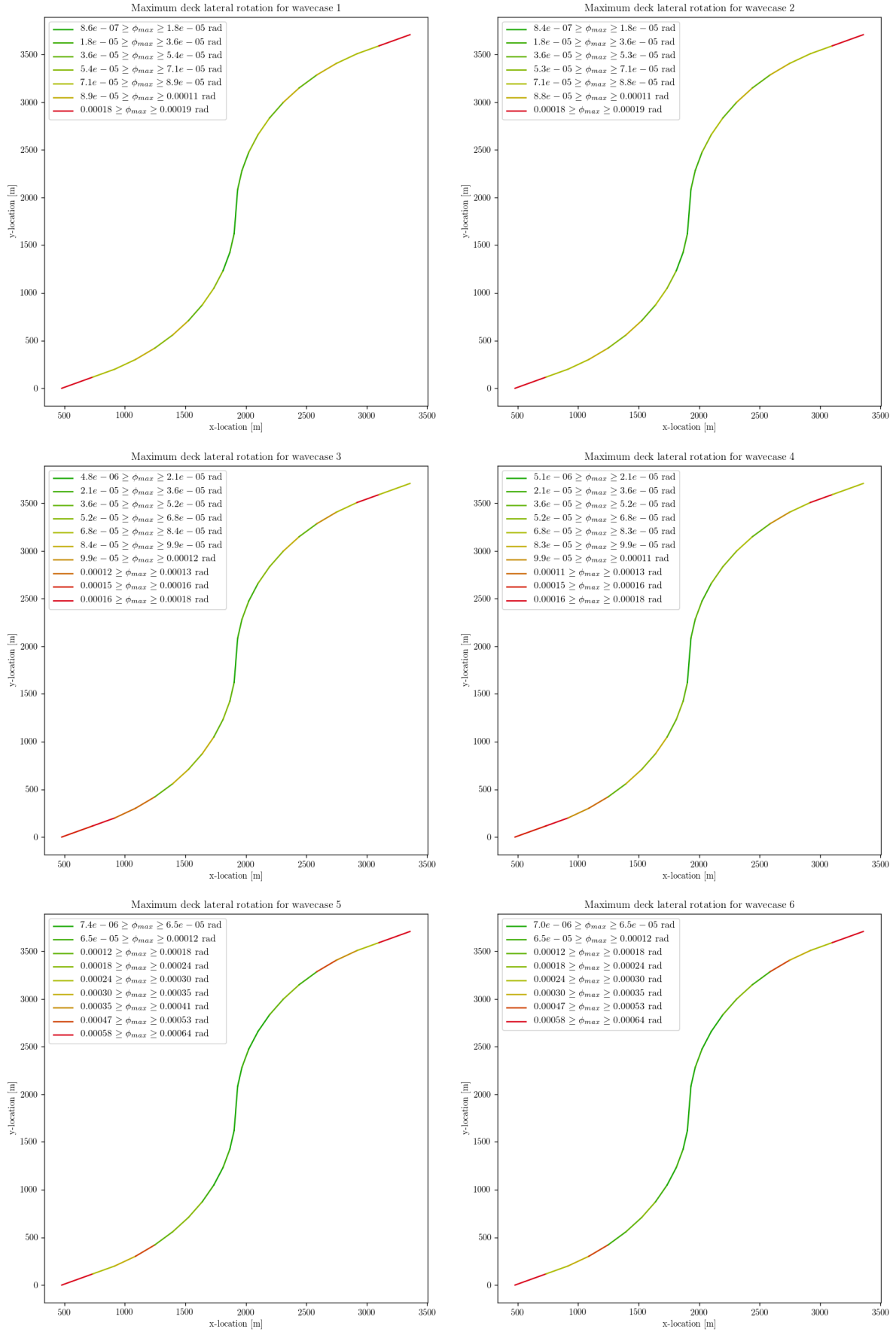


Figure E.4: Bridge deck maximum lateral rotation values for the different load cases.

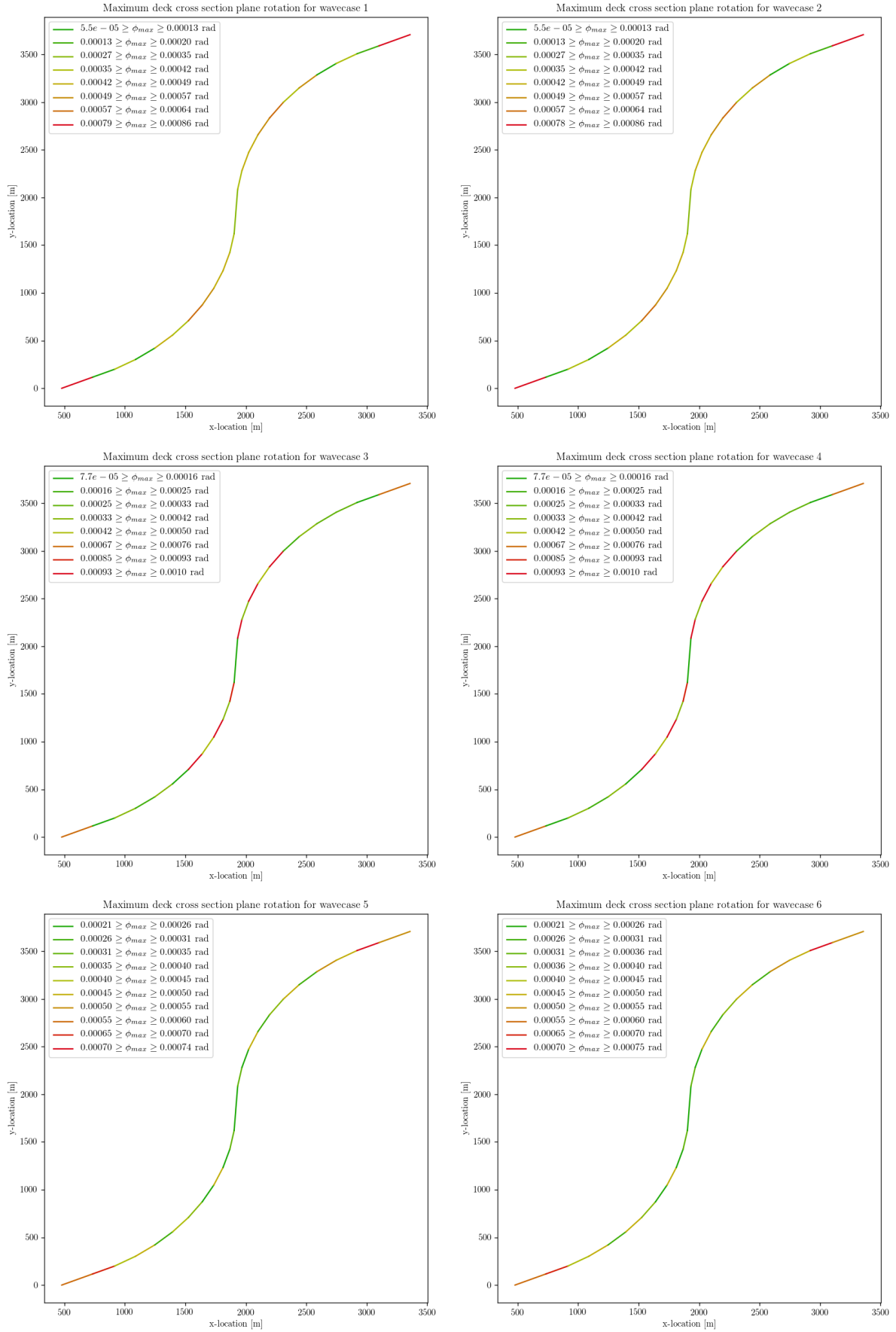


Figure E.5: Bridge deck maximum cross section plane rotation values for the different load cases.

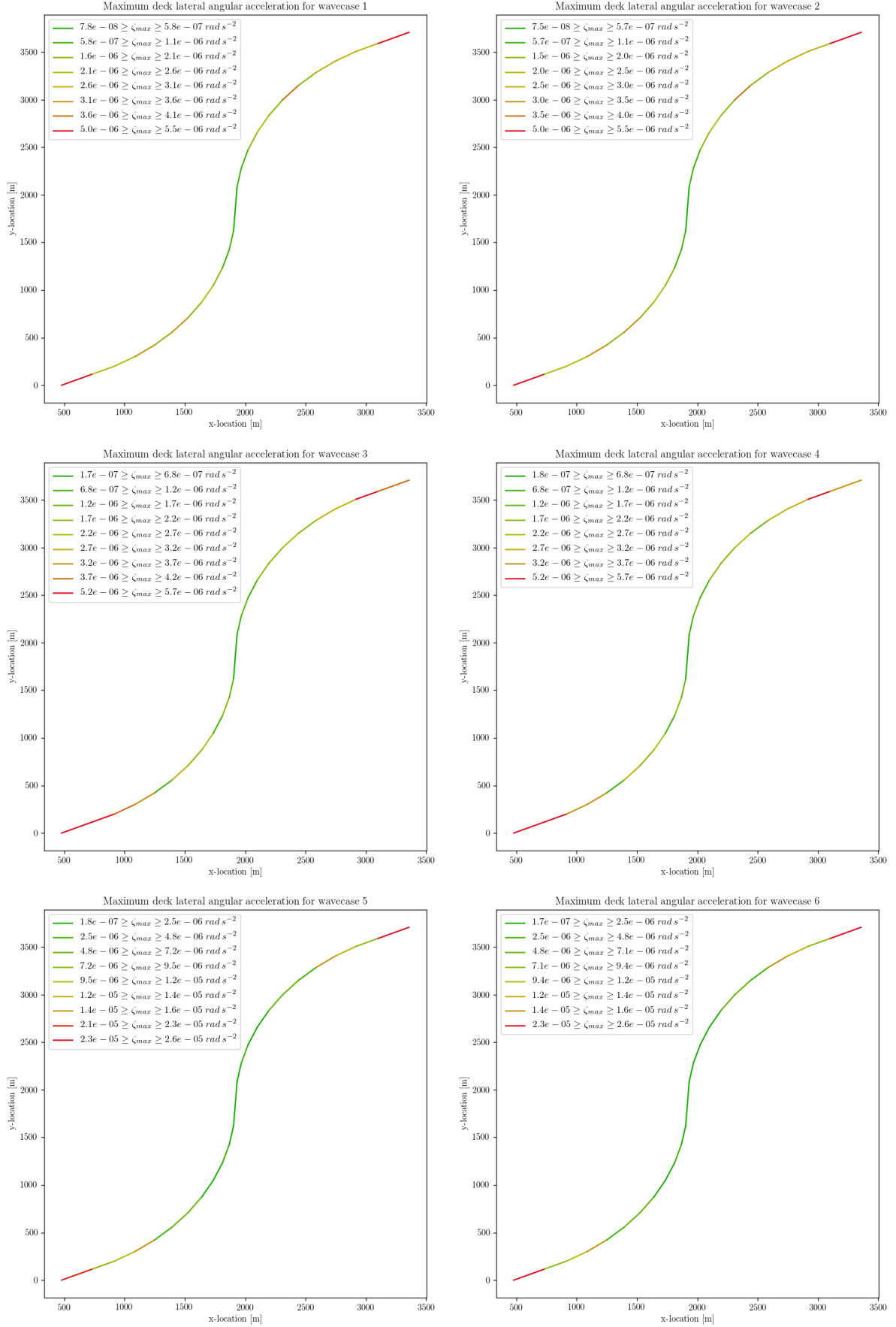


Figure E.6: Bridge deck maximum lateral angular acceleration values for the different load cases.

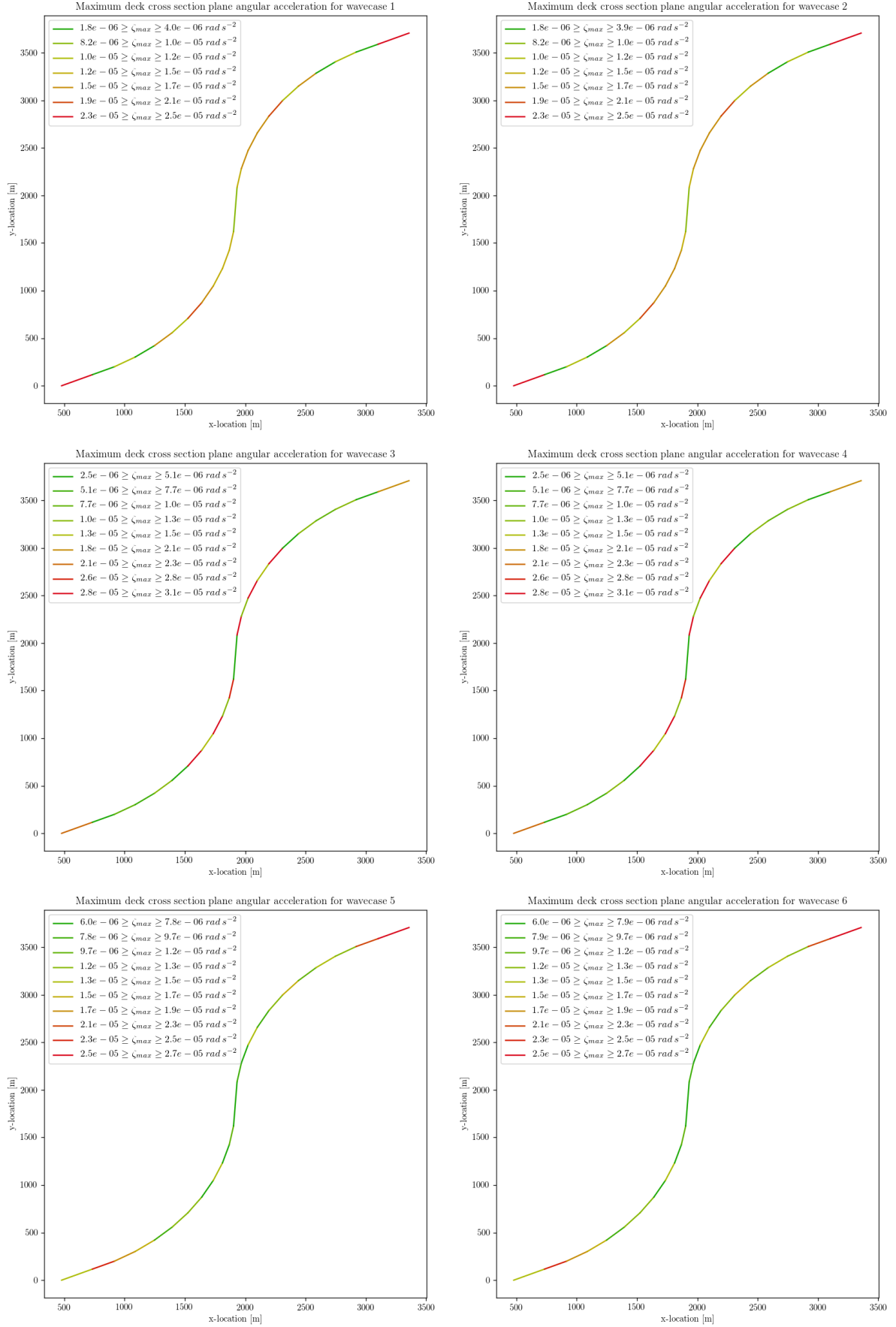


Figure E.7: Bridge deck maximum cross section plane angular acceleration values for the different load cases.

E.4 Conclusions

The conclusions to be drawn from this analysis are clear. The serviceability limit states for the bridge deck given in Table E.3 aren't broken during any of the steady state analyses. Therefore, it is concluded that, since the wave cases considered are extreme wave cases, bridge deck motion due to wave excitation will not break the serviceability limits.

Appendix F

Nonlinear analysis

This appendix describes the non-linear analysis performed with the Scia Engineer software package to obtain the model deformation, cable tension and bending stiffness when loaded with its own self-weight.

F.1 Nonlinear analysis

The Scia Engineer software package contains a non-linear solver, which can solve large deflection non-linear models. This is done using a Newton-Rhapson solver to iterate to equilibrium per load step.

In cable model adopted for this thesis, the cable bending stiffness changes as the curvature of cables change. This is not a common option for finite element software packages, and Scia Engineer is no exception. To accommodate the changing bending stiffness as the cables flex and their curvature changes, a non-linear solver (called Sciapython) is created which adds an additional iteration step in terms of the cable element bending stiffness to the calculation. The work-flow for this program is shown in Figure F.1. The program utilizes the "ESA_XML.exe" tool provided by the creators of Scia Engineer to interact with the Scia solvers.

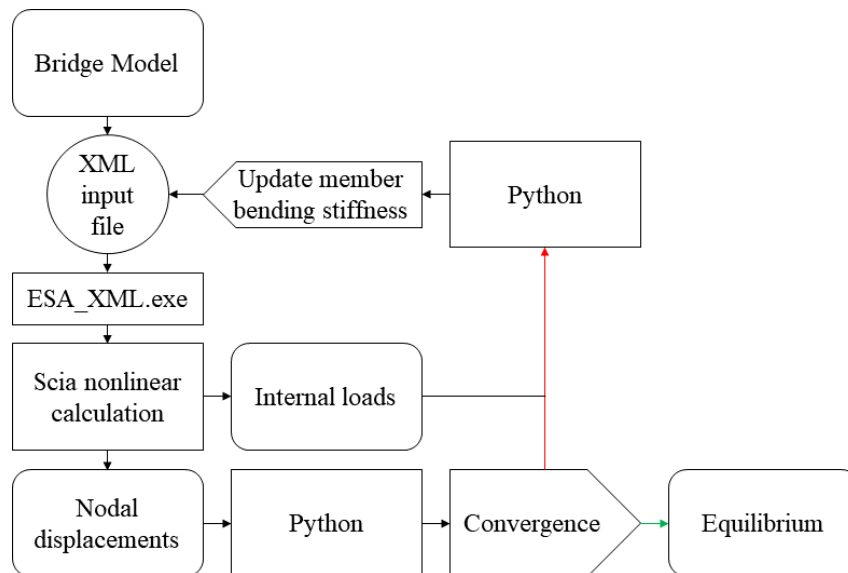


Figure F.1: Sciapython solver work-flow.

The steps in the solver process are the following;

First the bridge model is created, with a set level for the bending stiffness of all main and lateral cables.

From this model an xml input file is created, which is converted to a Scia model by the "ESA_XML" tool.

With different commands passed to the "ESA_XML", the nonlinear calculation is prepared and performed by Scia. The Scia Engineer non-linear solver is run with the options specified in Table F.1.

The output results of the calculation are split in a displacement file and an internal load file.

Convergence is calculated by Sciapython based on the nodal displacements. The convergence norm is $u_n - u_{n-1} \leq \frac{u_{n-1}}{100}$, or a convergence norm of 0.01.s

If the solution converges the solver stops here.

If it doesn't, Sciapython calculates the cable bending stiffness per cable segment according to the method described in appendix C using the expression for the curvature shown in Equation F.1 [Bel99].

The updated cable bending stiffness is exported to the XML input file and the iteration loop restarts.

Solver type	Direct
Average elements per member	10
Geometrical non-linearity	3rd order, large displacement
Calculation method	Newton-Rhapson
Number of load increments	50
Maximum iterations	100
Solver precision ratio	1
Solver robustness ratio	1
Initial stress	Yes
Initial stress from load case	Self-weight

Table F.1: Solver options.

$$\kappa_{BC} = \frac{\kappa_B + \kappa_C}{2} \quad (\text{F.1})$$

In which;

κ_{BC} is the curvature of the element from Node B to Node C

κ_B is curvature at node B, according to Equation F.2

κ_C is curvature at node C, according to Equation F.2

$$\kappa_N = \frac{\sqrt{(MN + NO + MC)(NO + MO - MN)(MO + MN - NO)(MN + NO - MO)}}{4(MN \cdot NO \cdot MO)} \quad (\text{F.2})$$

In which;

κ_N is the curvature at node N

M is the (x,y,z) location of node M, which is connected to node N

N is the (x,y,z) location of node N, which is connected to both node M and N

O is the (x,y,z) location of node O, which is connected to node N

MN is the distance from node M to N

NO is the distance from node N to O

MO is the distance from node M to O

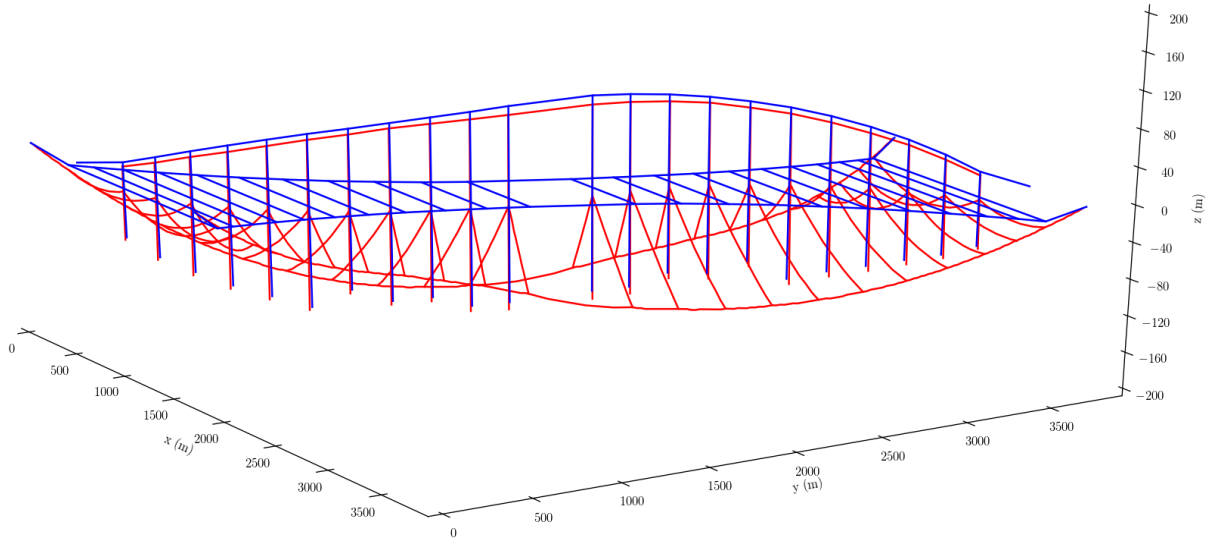


Figure F.2: Isometric view of the undeformed (blue) and deformed (red) equilibrium shape as calculated by the Sciapthon solver.

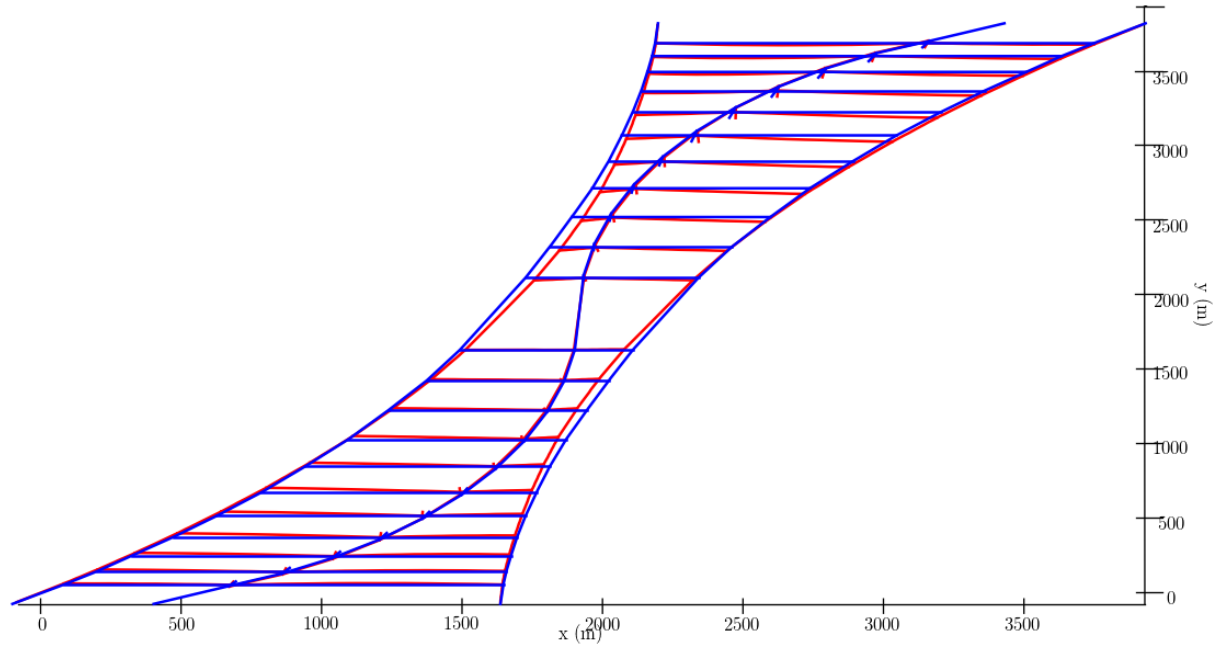


Figure F.3: Top view of the undeformed (blue) and deformed (red) equilibrium shape as calculated by the Sciapthon solver.

The results of the solver calculation are displayed visually in Figures F.2, F.3 and F.4.

Due to the large number of nodes used in this calculation, there are many resulting deflections. To give an indication of the deflection of the cables, the displacements of the connection nodes between main and lateral cables of the same number depicted in Figure F.5 are shown in Table F.2.

The largest vertical deflections occur at nodes C17 and C28, with approximately -115 m. The largest deflections in the x-direction occur at joints C18 and C27, with -31.83 m and 31.83 m, respectively. The largest y-deflections are relatively small, compared to the z- and x-directions, with 10.06 m and -10.06 m occurring at joints C11 and C34. The point symmetric design of the bridge is reflected in the displacement results, with each joint having a 'twin' with the same, or opposite displacement. The largest axial tensions occur in the main cables, at the four supports. The axial load in the cables reaches $931\,541$ kN in main cable no. 46 and similar values, though lower, at the other three main cable supports.

The results of the solver calculation are incorporated in the SACS model used in the subsequent dynamic analyses in the following parameters;

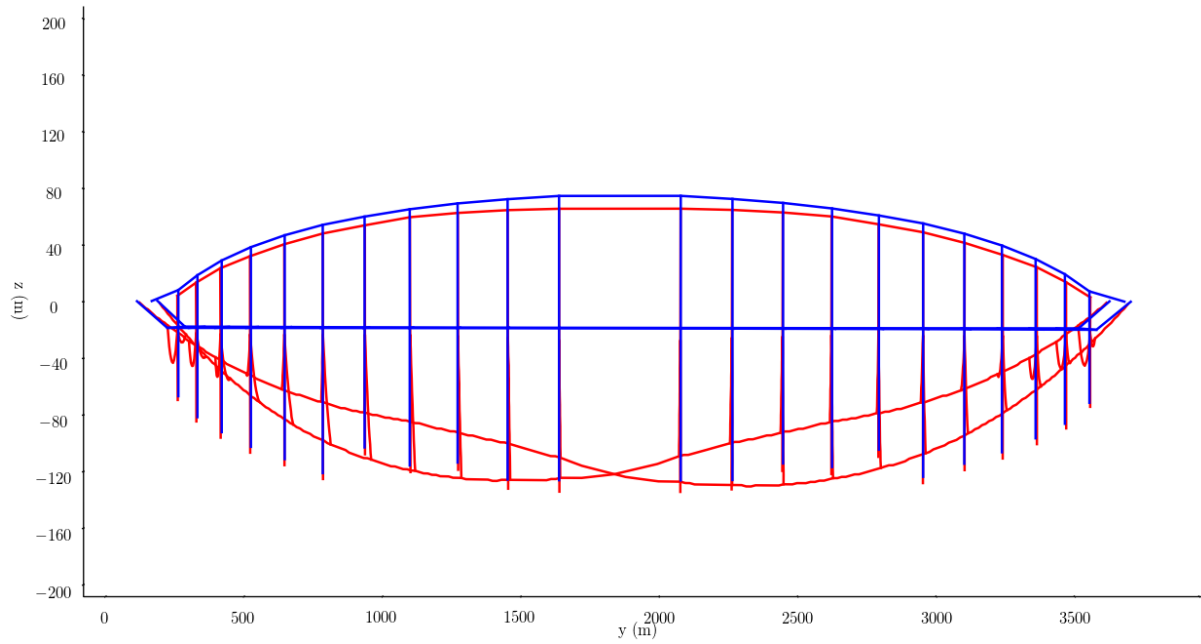


Figure F.4: Side view of the undeformed (blue) and deformed (red) equilibrium shape as calculated by the Sciapthon solver.

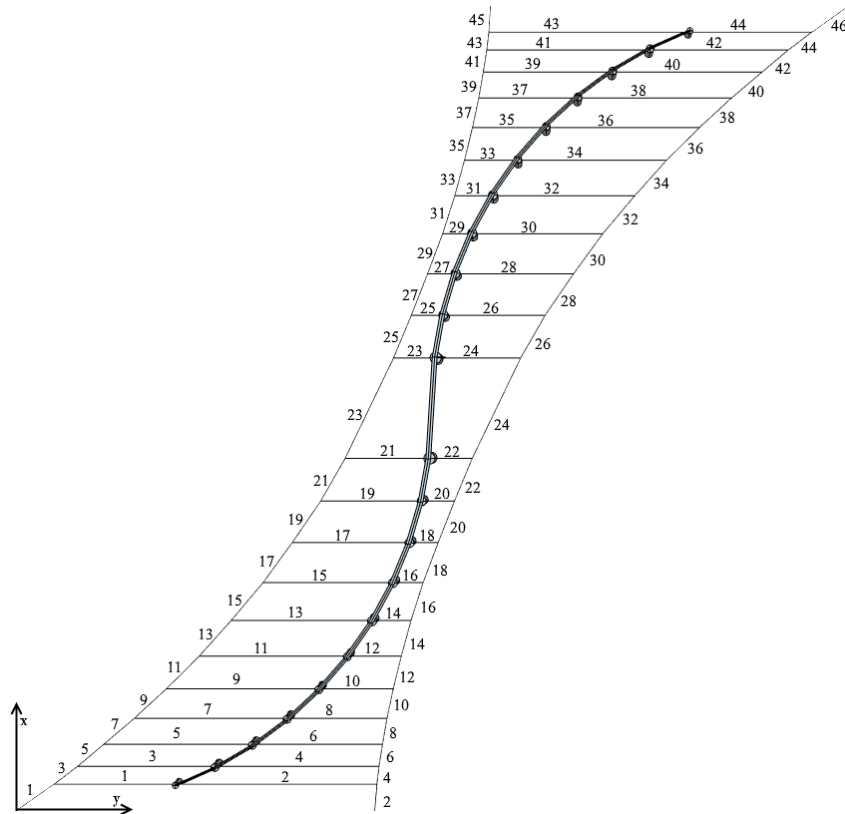


Figure F.5: Main and lateral cable numbers.

The axial tension, which is incorporated as a pre-stressing load on the beam elements which represent the cables segments.

The calculated curvature and tension dependant bending stiffness, which is input as a section property per cable segment.

Node name	X-deflection [m]	Y-deflection [m]	Z-deflection [m]
C1	-3.09277	4.45428	-6.8637
C2	-2.84115	0.7169	1.40486
C3	-4.76871	5.96832	-23.30378
C4	-4.77616	0.35867	-10.01821
C5	-4.53812	5.18554	-40.76301
C6	-7.06488	0.21667	-22.35835
C7	-6.78496	7.54098	-58.80405
C8	-9.14932	0.25039	-34.66561
C9	-8.03332	8.96732	-75.59014
C10	-12.8866	0.87943	-46.11637
C11	-8.72953	10.06431	-90.18508
C12	-17.76454	2.09385	-55.96377
C13	-6.14194	8.34692	-101.73449
C14	-21.89583	3.43509	-63.82604
C15	-4.39451	7.69608	-109.75209
C16	-27.45579	5.50739	-70.12377
C17	-0.27525	5.47719	-114.71929
C18	-31.8274	7.48778	-78.13269
C19	2.09816	4.71613	-115.6574
C20	-31.72164	7.87766	-86.31981
C21	8.09088	1.94853	-113.9699
C22	-25.26808	5.45433	-96.54096
C23	25.26929	-5.45554	-96.54489
C24	-8.09006	-1.94943	-113.9644
C25	31.72262	-7.87883	-86.32282
C26	-2.09708	-4.71717	-115.65239
C27	31.82815	-7.4889	-78.13471
C28	0.27733	-5.47889	-114.71469
C29	27.45685	-5.50865	-70.12454
C30	4.39699	-7.69802	-109.74859
C31	21.89834	-3.43683	-63.82471
C32	6.14588	-8.35002	-101.7319
C33	17.76774	-2.0958	-55.96134
C34	8.73316	-10.06695	-90.18398
C35	12.89111	-0.88167	-46.11347
C36	8.03776	-8.97062	-75.58995
C37	9.15252	-0.25236	-34.66304
C38	6.78816	-7.54281	-58.80474
C39	7.06309	-0.21778	-22.35654
C40	4.53938	-5.18512	-40.76388
C41	4.7677	-0.3588	-10.01716
C42	4.76106	-5.95735	-23.30419
C43	2.82343	-0.71524	1.39957
C44	3.07149	-4.42567	-6.86579

Table F.2: Displacement of lateral and main cable connections.

F.2 Linear analysis

The cable bending stiffness and tension calculated using the SciaPython program are exported to SACS to be used in the linear dynamic calculations. To prove that the results using this method comply with the results calculated by SciaPython, a static calculation is performed using the SACS linear solver and the results are compared to the non-linear results computed using SciaPython.

The results are compared using the Mean Squared Displacement Percentage error metric presented in Equation F.3 [MGB74].

$$MSDP(u, \hat{u}, \bar{u}) = 1 - \frac{(MSD(u, \hat{u}))}{(MSD(u, \bar{u}))} \quad (\text{F.3})$$

In which;

$MSDP$ is the error metric, which is smaller than 1 and maximal when it is 1

u is the vector containing the true displacements

\hat{u} is the vector containing the displacement to test

\bar{u} is the vector containing the undeformed structure

$MSD(y, \hat{y})$ is the Mean Squared Displacement according to Equation F.4

$$MSD(y, \hat{y}) = \frac{1}{n_{samples}} \sum_{i=0}^{n_{samples}-1} (y_i - \hat{y}_i)^2 \quad (\text{F.4})$$

In which;

$MSD(y, \hat{y})$ is the average squared displacement

y is the vector containing the true displacement

\hat{y} is the vector containing the displacement to test

The results from the test with this error metric for the displacements in the three degrees of freedom are shown in Table F.3.

	X	Y	Z
MSDP	0.8681	0.9353	0.9858

Table F.3: Results for the MSDP in comparing the non-linear displacement calculated by the SciaPython program to the linear displacement calculated by SACS.

It is clear that the linear analysis displays some differences in comparison to the non-linear analysis, mainly in the horizontal plane. In the vertical plane the two methods produce very similar results. To analyse the magnitude of the errors in the three directions, the maximum absolute errors between the non-linear and linear results are displayed in Table F.4.

	X	Y	Z
Absolute error	3.015 m	0.949 m	1.304 m

Table F.4: Absolute errors comparing the non-linear displacement calculated by the SciaPython program to the linear displacement calculated by SACS.

These results show that although the error metric points to an error close to 14 % for for instance the x-displacement results, the absolute error is still extremely small compared to the model dimensions.

Taking into account the absolute maximum error values calculated for the displacement directions, the error scores for the full set of nodal displacements are deemed to be acceptable. Especially taking the scale of the model into consideration.

Appendix G

SACS modelling

This appendix includes the assumptions and design choices made for the full bridge model in the finite element software SACS. It also includes analytical verification of the dynamic response of parts of the model.

G.1 Cables

In this section the assumptions made when modelling cables in SACS are defined and as verification a static analysis and an eigenfrequency analysis for a simple cable model are performed.

The cable model used in the bridge design are defined further in Appendices C, F and D. In SACS, the cables are modelled as tensioned Euler Bernoulli beam elements. The bending stiffness is determined per cable element according to the calculations specified in the Appendices mentioned earlier. The shear area modifier is set set to 0.9, which is a common value for cable elements [a10].

The characteristics of the steel used in the cables is depicted in in Table G.1.

Modulus of elasticity E	$195\,000\text{ N mm}^{-2}$
Shear modulus G	$80\,000\text{ N mm}^{-2}$
Yield strength f_y	1860 N mm^{-2}
Density ρ in air	7850 kg m^{-3}

Table G.1: Y1860 steel characteristics.

G.1.1 Verification of the SACS cable model

For the verification of the SACS cable model, different cable properties have been adopted than the ones calculated in Appendices C, F and D. The cable model to be checked has the characteristics displayed in Table G.3 and the steel and element properties displayed in Tables G.1 and G.2.

Torsional moment of inertia	10^{-5} mm^4
Moment of inertia about the local Y-axis	10^{-5} mm^4
Moment of inertia about the local X-axis	10^{-5} mm^4
Shear area modifier for tubular sections	0.9

Table G.2: Test cable moments of inertia.

Length	50 m
Diameter	150 mm
Cable tension	1000 kN

Table G.3: Test cable model characteristics.

G.1.1.1 Static analysis

The value of 1000 kN for the cable tension has been chosen by using Equation G.1 [Sim11] to plot the relation between the cable sag at midspan and the tension shown in G.1 and choosing a reasonable deflection and tension.

$$w = \frac{T}{\mu} \left(\cosh \frac{\mu l}{2T} - \cosh \left(\frac{\mu}{T} \left(\frac{l}{2} - x \right) \right) \right) \quad (\text{G.1})$$

In which;

w is the cable deflection

T is the cable tension

μ is the cable weight

l is the cable length

x is the coordinate along the cable span

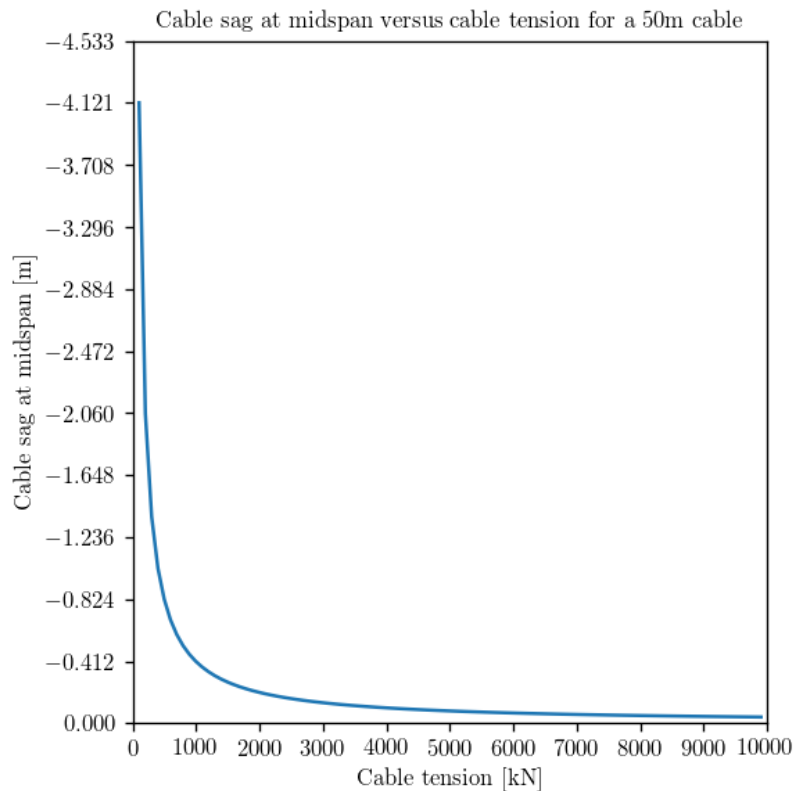


Figure G.1: The relation between cable sag at midspan and cable tension for a 50 m cable loaded by its own weight.

The cable deflection at midspan according to Equation G.1 is 0.425 m for the cable defined in this section. The deflection of the entire cable plotted along its length is shown in Figure G.2.

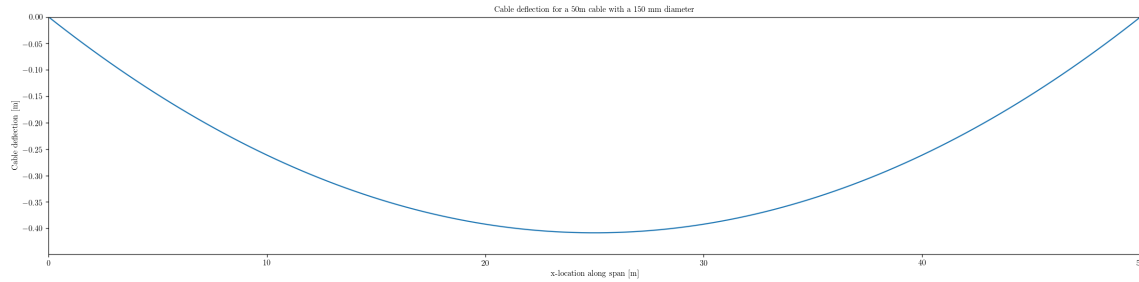


Figure G.2: Cable deflection along its length, loaded by self weight.

This cable model is modelled in SACS using the parameters described previously. The cable span is divided into four sections, by using four equally spaced nodes. The end nodes are fixed in all translational degrees of freedom and free to rotate. The members connecting the nodes are loaded with the cable self weight. The result of a linear static calculation of this model is shown in Figure G.3.

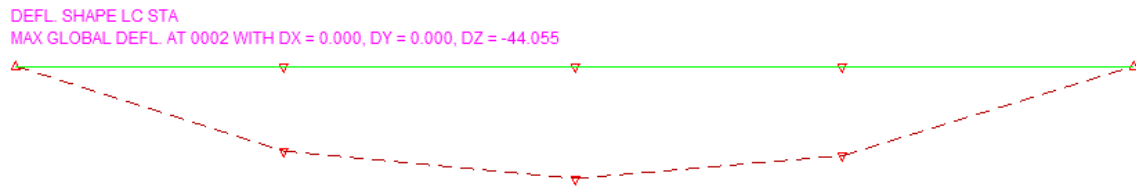


Figure G.3: Cable deflection along its length, loaded by self weight using 4 nodes in a linear static SACS analysis. Max deflection is -0.44 m.

This result shows that the SACS analysis produces a similar result compared to the analytical solution. The slight difference in results is mainly caused by the non linear nature of cable action. This result can be seen as a first 'guess' of the final cable shape, after which the new values for the cable tension and deflection are to be fed into a new linear analysis until the solution converges on the analytical solution. In the analytical solution provided the final cable shape is known to be a catenary - a computer program needs to iteratively work towards this shape. Since SACS does not provide a non-linear solver capable of dealing with low stiffness elements, this analysis can't be performed. To look at the influence of an increase in 'resolution', meaning an increase in the amount of cables segments in the span, the results of a linear static analysis of a twenty node SACS model is shown in Figure G.4.



Figure G.4: Cable deflection along its length, loaded by self weight using 20 nodes in a linear static SACS analysis. Max deflection is -0.38 m.

This result shows that a higher resolution leads to a more 'smooth' cable shape. It also shows that it does not favourably influence the accuracy of the results in a linear static analysis. This further reinforces the fact that more iterations are needed to converge on the analytical result.

Since the aim of this study is to look into dynamic behaviour, the linear analysis is deemed suitable enough.

G.1.1.2 Eigenfrequency analysis

To validate the suitability of SACS for dynamical analysis, an eigenfrequency analysis is performed on the previously defined test cable using both SACS and an analytical solution.

First the analytical solution is presented, starting with the equation of motion and boundary conditions of the model, shown in Equation G.2.

$$\rho A \frac{\partial^2 w}{\partial t^2} - T \frac{\partial^2 w}{\partial x^2} = 0 \quad (\text{G.2})$$

With boundary conditions;

$$w(0, t) = 0$$

$$w(50, t) = 0$$

In which;

$w(x, t)$ is the cable deflection

ρ is the cable density

A is the cable cross sectional area

T is the cable tension

The solution to this differential equation can be found by splitting the problem in a spatial and temporal part, as shown in Equation G.3.

$$w(x, t) = w(x) \sin(\omega t + \phi) \quad (\text{G.3})$$

Substituting this in the equation of motion from Equation G.2 leads to Equation G.4.

$$-\rho A \omega^2 \sin(\omega t + \phi) w(x) - T \sin(\omega t + \phi) w''(x) = 0 \quad (\text{G.4})$$

Since the time function can't be equal to zero for all t , the other factor should be equal to zero, as shown in G.5.

$$w''(x) + \frac{\rho A \omega^2}{T} w(x) = 0 \quad (\text{G.5})$$

Solving this differential equation with the boundary conditions specified in G.2 leads to the expression for the eigenfrequencies of the cable shown in Equation G.6.

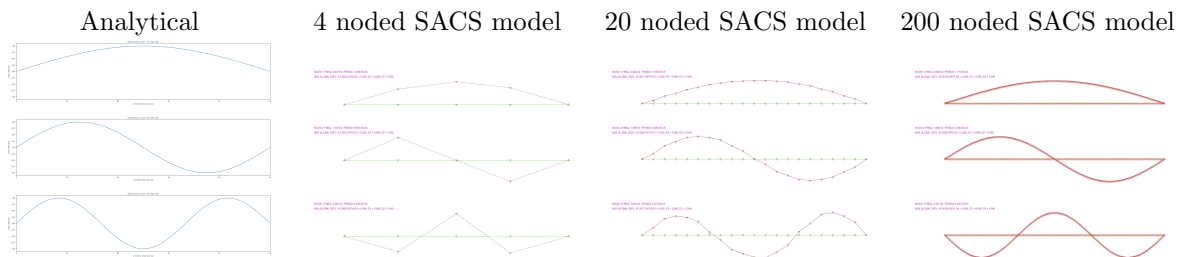
$$\omega_n = \sqrt{\frac{T}{\rho A}} \frac{k \pi}{L}, \quad (k = 1, 2, \dots \infty) \quad (\text{G.6})$$

In which;

L is the cable length

For the eigenfrequency analysis in SACS, the two previously defined models and one model using two hundred nodes are used. The modal mass matrix is built using the consistent method and the vertical displacements are considered for dynamical analysis.

Using Equation G.6 and the three SACS models, the first ten eigenfrequencies of the cable are calculated and shown in Table G.5. The four node SACS model only has three degrees of freedom to be considered for this analysis and thus only produces three eigenfrequencies and modal shapes. The results clearly validate the solution provided by SACS to be in the same range as the analytical results. It also shows that when the nodes do not coincide with the maxima and zero-points (also called nodes) of the modal shape, the solution tends to have a higher error. This can also be seen in the modal shapes, which are displayed in Table G.4.



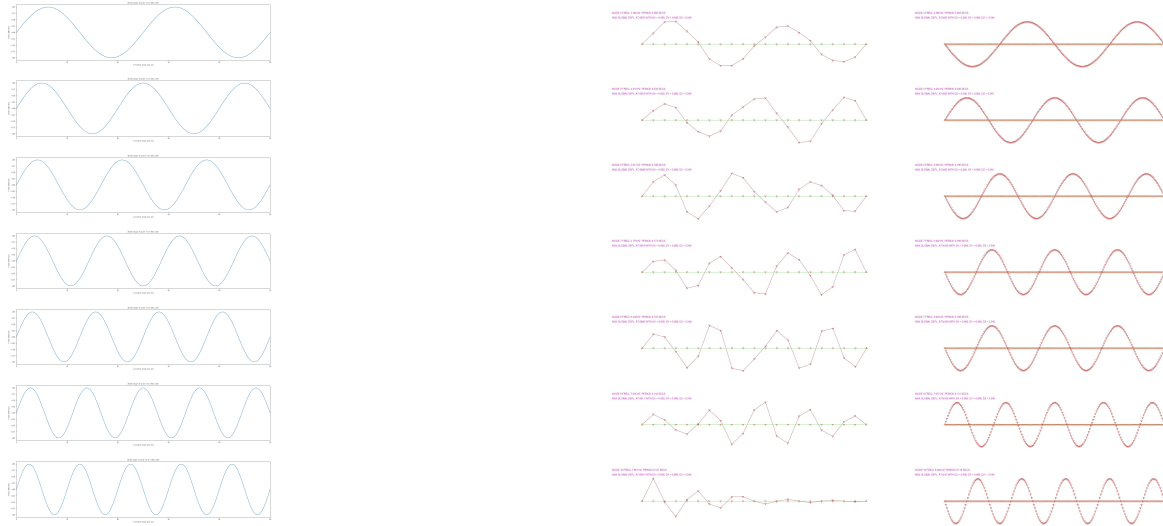


Table G.4: First ten modal shapes of the cable model.

If the resolution of the cable is chosen high enough, the margin of error for the results drop significantly, becoming nearly non-existent. This shows the importance of performing resolution studies during the design modelling. It also shows that SACS is a suitable software package for dynamic cable analysis.

Number	Analytical	SACS 4 nodes	SACS 20 nodes	SACS 200 nodes
1	0.849 Hz	0.827 Hz	0.902 Hz	0.849 Hz
2	1.698 Hz	1.530 Hz	1.698 Hz	1.698 Hz
3	2.547 Hz	2.000 Hz	2.663 Hz	2.547 Hz
4	3.396 Hz		3.384 Hz	3.396 Hz
5	4.245 Hz		4.310 Hz	4.245 Hz
6	5.094 Hz		5.017 Hz	5.093 Hz
7	5.943 Hz		5.779 Hz	5.942 Hz
8	6.792 Hz		6.438 Hz	6.789 Hz
9	7.641 Hz		7.035 Hz	7.637 Hz
10	8.490 Hz		7.851 Hz	8.484 Hz

Table G.5: Test cable model eigenfrequencies.

G.2 Pontoons

In this section the assumptions and design choices made modelling the pontoons in SACS are described and verified. The pontoon parameters and mechanical model are defined in detail in section A.4.

The pontoons are modelled as stiff tubular Euler-Bernoulli beam elements to examine their rigid body movements, Table G.6 shows the chosen parameters in SACS.

Modulus of elasticity E	$2\,000\,000\text{ N mm}^{-2}$
Shear Modulus G	$2\,000\,000\text{ N mm}^{-2}$
Yield strength f_y	2500 N mm^{-2}

Table G.6: Modelled pontoon parameters.

To validate the pontoon model in SACS, an eigenfrequency analysis is performed for pontoon number seven. Figure G.5 shows a section cut and related mechanical model for pontoon number seven.

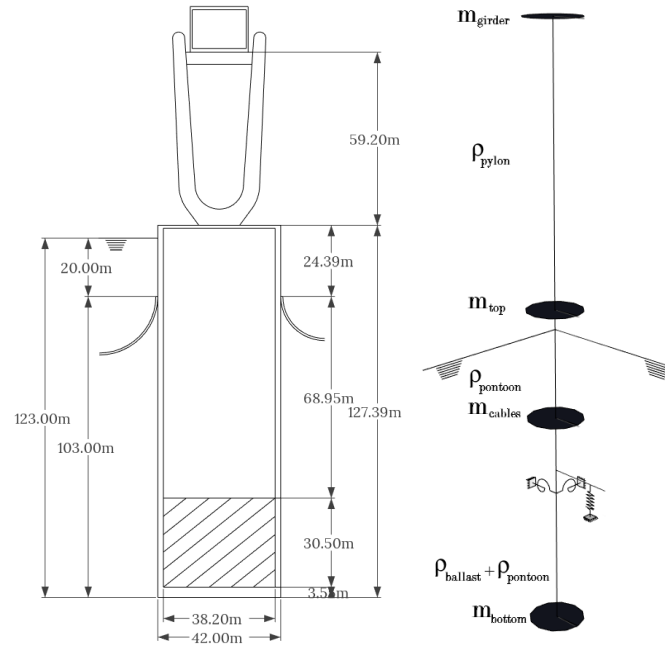


Figure G.5: section cut and mechanical model for pontoon number seven [Yip15].

The bridge girder resting on the pontoon and the lateral cables hanging from the center of rotation of the system are modelled as point masses at their respective locations. The pylon weight, pontoon cylinder weight, ballast weight and the pontoon top and bottom weights are modelled as distributed loads along their respective length. The masses, distributed weights and values for the spring stiffness used for pontoon seven are displayed in Table G.7.

Pontoon number		7	
Rotational stiffness	$k_{rotational}$	21250	$\cdot 10^3 \text{ kN m rad}^{-1}$
Buoyancy stiffness	k_{buoy}	13795	kN m^{-1}
Mass girder	m_{girder}	3078.5	$\cdot 10^3 \text{ kg}$
Mass cables in air	m_{cables}	1800.7	$\cdot 10^3 \text{ kg}$
Mass pylon	ρ_{pylon}	38.9	$\cdot 10^3 \text{ kg m}^{-1}$
Mass top pontoon	ρ_{top}	3463.6	$\cdot 10^3 \text{ kg m}^{-1}$
Mass cylinder pontoon in air	$\rho_{cylinder}$	598.4	$\cdot 10^3 \text{ kg m}^{-1}$
Mass ballast in air	$\rho_{ballast}$	2292.2	$\cdot 10^3 \text{ kg m}^{-1}$
Mass bottom pontoon in air	ρ_{bottom}	3463.6	$\cdot 10^3 \text{ kg m}^{-1}$

Table G.7: Characteristic masses and stiffness pontoon seven.

G.2.1 Static analysis

Static analysis is foregone for the pontoons. Since all loads modelled in the proposed model are in the z -direction and have no eccentricity to the rotation center, the analysis boils down to dividing the total mass by the buoyancy stiffness. The buoyancy stiffness and total mass is verified in the eigenfrequency analysis, so there is no need to perform an additional validation.

G.2.2 Eigenfrequency analysis

To simplify the calculation, the verification is performed in two decoupled degrees of freedom, rotation around the center of rotation and translation in the z -direction. Figure G.6 displays the two degrees of freedom. Damping is disregarded for this benchmark analysis. It will change the results significantly.

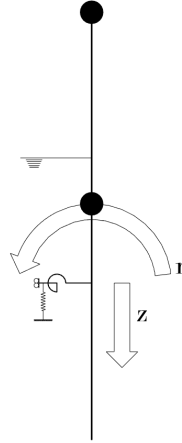


Figure G.6: Degrees of freedom for the pontoon model.

The expressions for the two equations of motion are displayed in Equations G.7 and G.8.

$$m_{tot} \ddot{z} + k_{buoy} z = 0 \quad (G.7)$$

In which;

m_{tot} is the summed mass of the pontoon, according to Table G.7

k_{buoy} is the buoyancy spring stiffness, according to Table G.7

$$J \ddot{r} + k_{rot} r = 0 \quad (G.8)$$

In which;

J is the pontoon's mass moment of inertia around the rotation center, according to Equation G.9

k_{rot} is the rotational spring stiffness, according to Table G.7

The pontoon's mass moment of inertia is calculated using the expression in Equation G.9.

$$J = \int \rho z^2 dz \quad (G.9)$$

In which;

J is the pontoon's mass moment of inertia around the rotation center

ρ is the distributed weight along the pontoon's z-axis

z is the distance from the rotation center along the z-axis

The equations of motion belong to simple undamped mass spring systems and the eigenfrequencies can be found directly. The expressions for the two eigenfrequencies related to the two degrees of freedom are displayed in Equations G.10 and G.11.

$$\omega_r = \sqrt{\frac{k_r}{J}} \frac{1}{2\pi} \quad (G.10)$$

In which;

ω_r is the eigenfrequency related to the pontoon rotation r in Hz

k_r is the rotational spring stiffness, according to Table G.7

J is the pontoon's mass moment of inertia around the rotation center

$$\omega_z = \sqrt{\frac{k_z}{m_{tot}}} \frac{1}{2\pi} \quad (G.11)$$

In which;

ω_z is the eigenfrequency related to the pontoon displacement z in Hz

k_z is the buoyancy spring stiffness, according to Table G.7

m_{tot} is the summed mass of the pontoon, according to Table G.7

The pontoon and pylon are modelled in SACS as Euler Bernoulli beams with internal stiffness parameters according to Table A.9. The masses are modelled as point and distributed loads in the vertical direction on the beam element. The beam is supported by a hinged support at the metacenter with rotational and translational stiffness according to Table G.7. The Dynpac dynamic analysis tool provided by SACS converts the loads in the z -direction into a consistent mass matrix and performs the eigenfrequency analysis for the two degrees of freedom. Table G.8 displays the results of the analytical calculation and SACS analysis for pontoon number seven. The SACS results are presented visually in Figure G.7.

Pontoon number 7				
Analytical results				
Mass moment of inertia	J	302907659.8	$\cdot 10^3$	kg m^2
Summed mass	m_{tot}	152228.3	$\cdot 10^3$	kg
Eigenfrequency translation	ω_z	0.0479		Hz
Eigenfrequency rotation	ω_r	0.0297		Hz
SACS results				
Eigenfrequency translation	ω_z	0.049		Hz
Eigenfrequency rotation	ω_r	0.029		Hz

Table G.8: Eigenfrequency analysis results for pontoon number seven.

The results presented in Table G.8 clearly validate the results generated by SACS for the rigid body motion of the pontoons. The minute differences can be explained by rounding differences in load input and numerical errors.

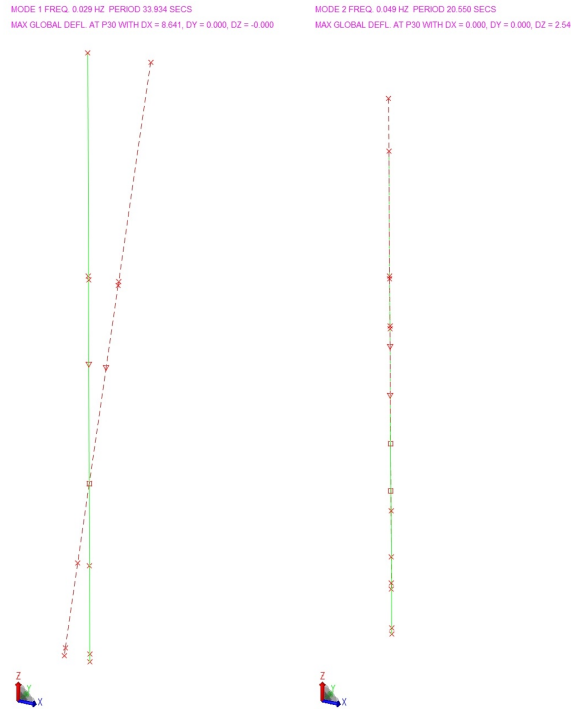


Figure G.7: Rigid body modes and eigenfrequencies calculated by SACS for pontoon number seven.

G.3 Pylons

This section describes the manner in which the pylons detailed in section A.3 are modelled in SACS. The pylons are modelled as Euler-Bernoulli tubular sections in SACS. Their section properties are set as manual input.

G.4 Girders

This section describes the design and modelling choices made for modelling the bridge girders in SACS. The design and characteristic properties of the bridge girders modelled in this section can be found in appendix A. The bridge girders are modelled in SACS as prismatic rectangular beam elements. The beam characteristics such as its area, shear area and moments of inertia are set manually, according to the girder properties. An example of these characteristics for the main girder beam is displayed in Table G.9. For detailed static analysis of the bridge girder reference is made to W. Cijssouw. “A

Height	Z	27	m
Width	Y	21.5	m
Cross sectional area	A	4.342	m ²
Shear area in Y-direction	$A_{shear,y}$	1.7	m ²
Shear area in Z-direction	$A_{shear,z}$	2.6	m ²
Torsional moment of inertia	I_t	1300	m ⁴
Moment of inertia about Y-axis	I_y	299.45	m ⁴
Moment of inertia about Z-axis	I_z	112.45	m ⁴
Self weight	G	408	kN m ⁻¹

Table G.9: Main girder beam characteristics.

continuous superstructure for the Sognefjord bridge”. Delft University of Technology, 2018. Since the bridge girders are very stiff in comparison to the other structural elements present in the bridge design (mainly the cables), they can be assumed to be near rigid bodies. Their internal dynamic behaviour is not investigated further in this thesis.

G.5 Bridge model

This section describes the modelling of the entire bridge in SACS. The previous sections have described the modelling of the different structural components of the bridge design. This section outlines the total model and the manner in which these components fit in this model.

G.5.1 Dimensions and axis system

This subsection describes the model dimensions and the axis system used. The bridge model is contained in a 3835.17 m by 3707.52 m area horizontally. The highest point is at 78.66 m. Figure G.8 gives an overview of the model. The axis system used has its origin at the left endpoint of the main cable on the left. The z-axis origin coincides with the water level. The fjord floor is modelled at an elevation of −1200 m below mean sea level and thus the z-axis origin.

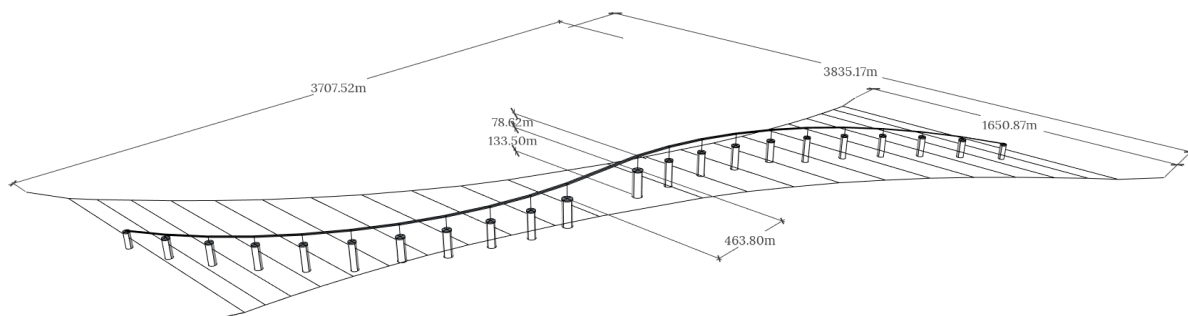


Figure G.8: Overview of the total model.

G.5.2 Component coordinates

In this section the locations of the different structural components are shown. Figure G.9 displays the x- and y-coordinates of the connections between the main and lateral cables. The main and lateral cables are modelled at an elevation of -20 m below mean sea level. The main cables are supported at their top and bottom endpoints. From the main cable support to the first connection with a lateral cable the main cable is modelled with a linear sag.

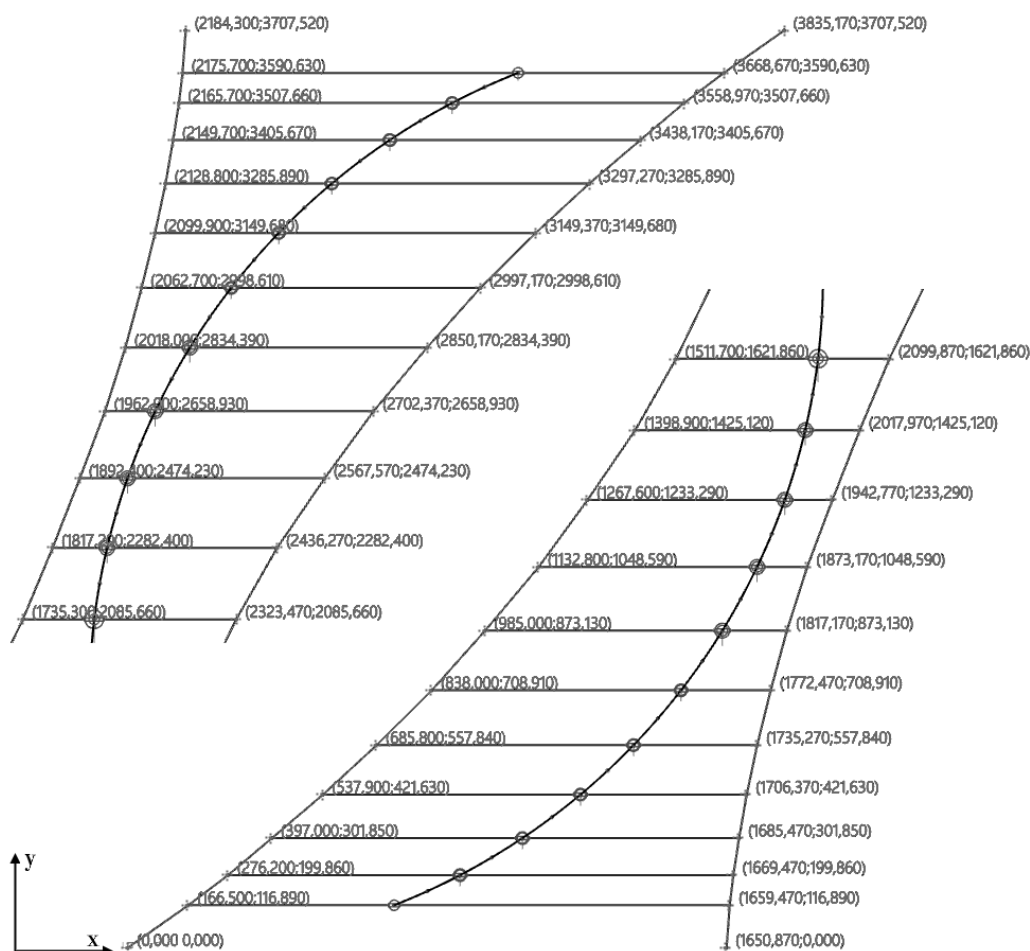


Figure G.9: Coordinates of the main and lateral cable connections.

Table G.10 displays the x- and y-coordinates of the pontoons. The pontoon numbering is shown in Figure G.10.

The elevation of the tops of the pylons above mean sea level and thus their z-coordinate is displayed in Table G.11. The pylons share x- and y-coordinates with the pontoon they are placed on. The bridge girders are modelled connecting the tops of the pylons.

Pontoon number	1	2	3	4	5	6	7	8	9	10	11
X-coordinate [m]	734.1	915.96	1087.9	1247.95	1394.27	1525.18	1639.18	1734.96	1811.42	1867.69	1903.12
Y-coordinate [m]	116.89	199.86	301.85	421.63	557.84	708.91	873.13	1048.59	1233.29	1425.12	1621.86

Pontoon number	12	13	14	15	16	17	18	19	20	21	22
X-coordinate [m]	1932.05	1967.48	2023.75	2100.21	2195.99	2309.99	2440.9	2587.22	2747.27	2919.21	3101.07
Y-coordinate [m]	2085.66	2282.4	2474.22	2658.92	2834.39	2998.6	3149.68	3285.89	3405.66	3507.63	3590.63

Table G.10: Pontoon coordinates.

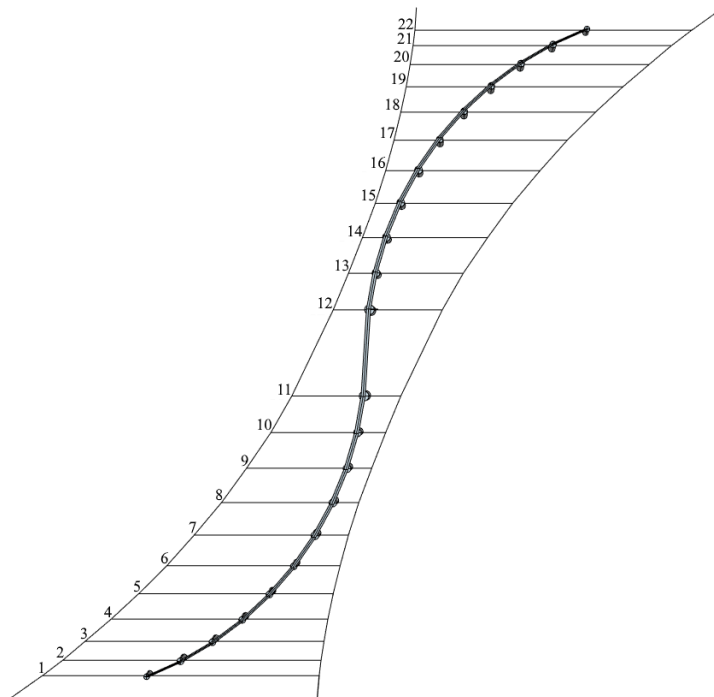


Figure G.10: Pontoon numbering.

Pontoon number	1	2	3	4	5	6	7	8	9	10	11
Pylon elevation [m]	8.48	19.83	31.0	41.0	49.86	57.55	63.59	68.96	73.19	76.25	78.62

Pontoon number	12	13	14	15	16	17	18	19	20	21	22
Pylon elevation [m]	78.62	76.25	73.19	68.96	63.59	57.55	49.86	41.0	31.0	19.83	7.37

Table G.11: Pylon top elevation.

G.5.3 Connections

This subsection describes the location and nature of the different connections between the structural elements in the model.

The main cables are restrained at both ends. These supports are modelled as rigid supports, allowing no rotations or translations to portray a cable cast in concrete or secured in some form of clamp. The

connection between the main and lateral cables are modelled as rigid connections. This is done because the connection will involve a clamp or other form of rigid connection.

The lateral cables are connected to the pontoons at an elevation of -20 m below mean sea level. This connection is modelled as a rigid connection as well, for the connection to the pontoons will involve some form of clamp.

In the structural model, there is no distinct connection between the pontoon and pylons. The connection present between them is rigid.

In the current bridge design, the entire bridge girder is a continuous girder, resting on hinged supports in axial and horizontal normal directions. Axial rotation around the pylon vertical axis is prevented by the support conditions. As such, This rotational degree of freedom is set to be fixed, while the others are free. All translational degrees of freedom between the pylon and girders are fixed. For a mechanical model of the pylon to girder connections reference is made to section A.2.

G.5.4 Full model

This section describes the construction method and depict the complete bridge model built in SACS.

G.5.4.1 SACS Input file

The model is built in SACS using a SACS input file. An example of a sportion of a SACS input file is shown in Figure G.11.

In this part of the input file, the model options are set on the OPTIONS line. This line is currently set to make the model use metric units and export a joint displacement report, an internal load report, a member forces and moments report and a joint reaction report in static analysis.

The SECT lines input the different member section types and their geometric characteristics to be used in the model. The previous sections of this thesis provide an accurate description of the member section characteristics used in the SACS bridge model.

Figure G.12 shows the following part of the input file, detailing the member groups to be assigned to the members in the model. The GRUP lines assigns member sections to member groups and assigns shear and elasticity moduli. It also assigns shear and elasticity moduli, member group densities and member group shear areas.

In Figure G.13 lines creating members are shown. The MEMB lines displayed create the members of which pontoon number 22, the first section of one of the main cables and main-, intermediate- and side-span girders are comprised. The lines display the two joints which are connected by the member, the member group to which the member is to be assigned and the member end fixities. These fixities describe the member support conditions at the two member ends for the six degrees of freedom. The order of the degrees of freedom is as follows: displacement x - displacement y - displacement z - rotation x - rotation y - rotation z. The value 0 means the end release of the member is fixed for this degree of freedom. The value 1 means the member end release is free in this degree of freedom. The depicted lines for the side-span girders and pylon show the girder support conditions. The member line can also assign a local density and diameter for members, this is visible in the member lines representing pontoon 22.

```

SECT
SECT PYL1      TUB6.48+53.4600+821.58+1121.58+11 2600.040.00
SECT PYL2      TUB5.23+52.7900+811.31+1111.31+11 2100.040.00
SECT PYL3      TUB4.47+52.3900+87.090+117.090+11 1800.040.00
SECT PYL4      TUB3.72+51.9800+84.070+114.070+11 1500.040.00
SECT PONT1     TUB2.12+76.039+105.772+125.772+12 5200.0223.0
SECT PONT2     TUB1.39+73.017+102.582+122.582+12 4200.0190.0
SECT PONT3     TUB1.02+71.852+101.450+121.450+12 3600.0170.0
SECT PONT4     TUB7.07+61.060+107.375+117.375+11 3000.0150.0
SECT MAINCAB   TUB1.13+42.0405+7 2.409+7 2.409+7 120.0059.90
SECT LATCABL   TUB962.11147580.0171760.8171760.8 35.00017.40
SECT GIRDMN    PRI4.34+41.299+112.995+101.125+10 2700.0      2150.01.7+42.6+4
SECT GIRDSI    PRI9870.04.400+104.964+103.564+10 1680.0      2150.03.9+35.9+3
SECT GIRDIN    PRI1.88+47.000+101.497+114.160+10 1680.0      2150.07.6+31.1+4

```

Figure G.11: SECT lines detailing section properties in the SACS input file.

```

GRUP PY1 PYL1          20.0020.0046.00 1      1.001.00          0.6380
GRUP PY2 PYL2          20.0020.0046.00 1      1.001.00          0.7913
GRUP PY3 PYL3          20.0020.0046.00 1      1.001.00          0.9246
GRUP PY4 PYL4          20.0020.0046.00 1      1.001.00          1.1121
GRUP P01 PONT1         20.0020.0046.00 1      1.001.00
GRUP P02 PONT2         20.0020.0046.00 1      1.001.00
GRUP P03 PONT3         20.0020.0046.00 1      1.001.00
GRUP P04 PONT4         20.0020.0046.00 1      1.001.00
GRUP CAL LATCABL       T19.298.000186.0 1      1.001.00      0.900 7.8500
GRUP CAM MAINCAB       T19.358.000186.0 1      1.001.00      0.900 7.8500
GRUP GRM GIRDMN        21.508.077 46.0 1      1.001.00          9.5829
GRUP GRI GIRDIN        21.508.077 46.0 1      1.001.00          11.928
GRUP GRS GIRDSI        21.508.077 46.0 1      1.001.00          15.595

```

Figure G.12: Member group lines in a SACS input file.

For the main cable a MEMB2 line is added, in which the member tension is assigned in kN. The final 0.9 value inputs the shear area modifier for a cable, as mentioned in chapter G.1.

```

MEMBER P210P211 PY4    000110000000
MEMBER P211P212 P04          N          2.5    3000.
MEMBER P212P213 P04          N          0.475  3000.
MEMBER P213P214 P04          N          0.475  3000.
MEMBER P214P215 P04          N          0.475  3000.
MEMBER P215P216 P04          N          0.475  3000.
MEMBER P216P217 P04          N          2.095  3000.
MEMBER P217P218 P04          N          2.5    3000.
MEMBER M0 M1 A O          000000000000          0.9
MEMB2 931165.
MEMBER G0 P0 GRS          000000000000
MEMBER P0 P10 GRS         000000000000
MEMBER P10 P20 GRS        000000000000
MEMBER P20 P30 GRS        000000000000
MEMBER P30 P40 GRS        000000000000

```

Figure G.13: Member lines in a SACS input file.

Figure G.14 displays the lines creating the joints for pontoon number 22 and a section of one of the main cables. The joints names are the first input on these lines, followed by the integer values of their x-, y- and z-coordinates in m. The next three values are the decimal values of the joint location. The final input is the joint fixity. The order for the joints fixity is the following: displacement x - displacement y - displacement z - rotation x - rotation y - rotation z. A 2 or 0 value means the degree of freedom is not fixed, the 2 value instructs SACS to consider this degree of freedom in dynamic analysis. A 1 value fixes the degree of freedom for this particular joint, or, when the joint line is followed by a line ending with ELASTI, assigns the stiffness specified on the ELASTI line to this degree of freedom. The displayed portion of the input file instructs the program to consider the top of pontoon number 22's pylon for dynamic analysis. It also instructs SACS to fix the first node of the main cable to the shore and to consider its joints for dynamic analysis. Finally, it creates the rotational stiffness and buoyancy stiffness of the pontoon in the joint located at the pontoon center of buoyancy and center of rotation.

Figure G.15 displays the LOAD input lines assigning a unit distributed load of 1 kN to the submerged part of pontoon 21, in the x-direction. This load line is called by the dynamic response program to model the distributed current load calculated using Ansys Fluent. Reference is made to appendix J. The lines start with the direction in which the load is acting, which in this case is the global direction X. Next the member on which the load acts is set. Then the length from the start of the member until the start of the load is input in m, if applicable. After this the starting value for the load, which in this case acts in the positive x-direction, is prescribed in kN. Next the length along the member on which the load acts is applied in m, if applicable. If this is not set explicitly, the load will act until the end of the member. Following this the end value of the load is input in kN. The GLOB UNIF specify that the load inputs


```

JOINT P210  3101.  3590.    7.   07.   63.   37.  222000
JOINT P211  3101.  3590.    4.   07.   63.   29.
JOINT P212  3101.  3590.    3.   07.   63.   29.
JOINT P213  3101.  3590.   -20.   07.   63.      222000
JOINT P214  3101.  3590.   -36.   07.   63.   -56.  001000
JOINT P214          7038.29                      ELASTI
JOINT P215  3101.  3590.   -42.   07.   63.   -16.  000110
JOINT P215          3.246+63.246+6      0.1 ELASTI
JOINT P216  3101.  3590.   -56.   07.   63.   -28.
JOINT P217  3101.  3590.   -70.   07.   63.   -58.
JOINT P218  3101.  3590.   -73.   07.   63.   -13.
JOINT M0      0.    0.    0.                      111111
JOINT M1     15.   10.   -1. 13.636 62.636-81.818 222000
JOINT M2     30.   21.   -3. 27.272 25.272-63.636 222000
JOINT M3     45.   31.   -5. 40.909 87.909-45.454 222000
JOINT M4     60.   42.   -7. 54.545 50.545-27.272 222000

```

Figure G.14: Joint lines in a SACS input file.

are in the global coordinate system and contain distributed loads.

```

LOADCNP21X
LOAD X P202P203  3.52  1.0          1.0          GLOB UNIF
LOAD X P203P204  0.0   1.0          1.0          GLOB UNIF
LOAD X P204P205  0.0   1.0          1.0          GLOB UNIF
LOAD X P205P206  0.0   1.0          1.0          GLOB UNIF
LOAD X P206P207  0.0   1.0          1.0          GLOB UNIF
LOAD X P207P208  0.0   1.0          1.0          GLOB UNIF

```

Figure G.15: Load lines in a SACS input file.

G.5.4.2 Graphical presentation

The input file described in the previous subsection produces the visual model in SACS depicted in Figures G.16 and G.17. As can be seen in these Figures, the resolution chosen for the cable segments is 4.

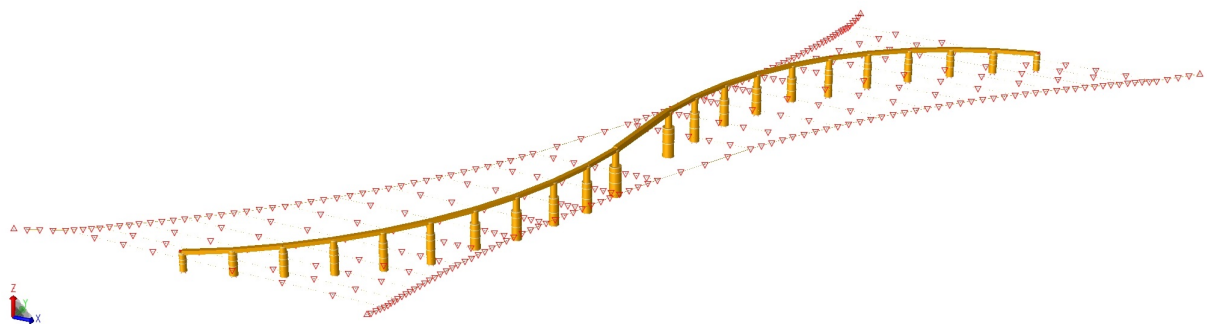


Figure G.16: Visual presentation of the bridge model in SACS.

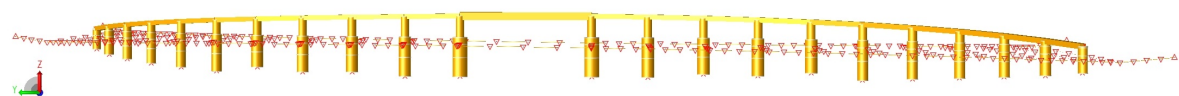


Figure G.17: Side view of the bridge model in SACS.

G.6 Waves and current

This section describes the modelling of waves as they are described in section B.1 in appendix B. It also provides verification of the loads generated by SACS with the theory presented in section B.1. As a quick reference, the wave properties described in appendix B are shown in Table G.12.

Parameter		Wind waves		
		North side	Mid-fjord	South side
Significant wave height	H_s [m]	2.22	2.34	2.13
Spectral top period	T_p [s]	4.6	4.8	4.8
Direction	[°]	180	240	270
Maximum single wave height	H_{max} [m]	4.55	4.79	4.36
Wave length	λ [m]	33	36	36
Wave theory		Stokes 3 rd	Stokes 3 rd	Stokes 3 rd

Table G.12: Wave characteristics at the bridge location.

G.6.1 Modelling

SACS employs a separate module to calculate wave loads, called SeaState. The Seastate module accept an input file in a similar style as the SACS input file and is usually (in offshore situations) the location where the loading is added to the model.

```
LOADCNI180
CURR
CURR      1183.    0.39    90.
CURR      1228.    0.48    90.
CURR      1248.    1.27    90.
MEMOV  P2  P3                                0.330.33
MEMOV  P3  P4                                0.330.33
MEMOV  P4  P5                                0.330.33
MEMOV  P5  P6                                0.330.33
:
:
WAVE
WAVE      STOK  4.55          4.6          210.      D      0.  10.0  36AL
DEAD
DEAD      -Z
END
```

Figure G.18: Different inputs in a Seastate load case.

Figure G.18 displays the load case with an inward current and the critical wave case in the direction with an angle of 180° relative to the North. The first lines, marked 'CURR', input the current velocity profile. This is done from the bottom up, with the first values representing the elevation above the ocean floor (or mudline). The second value is the current velocity in m s^{-1} and the third the angle relative to the y-axis. The following lines, marked 'MEMOV' provide the opportunity to locally override member properties for this single load case. This is an important feature for this study, since it allows to locally override the pontoon C_M , or coefficient of inertia, values for the different waves to be used by SeaState in the Morison equation. Reference is made to section B.1. In this case, the coefficient of inertia for both the local member y- and x-direction is set to 0.33. Then the line marked 'WAVE' inputs the wave into SeaState. The first value, tells SeaState which wave theory should be used. In this case SeaState should

employ the 5th order Stokes theory. The second value inputs the significant wave height H_s and the third the wave period T_p . The following value tells the program in which direction, measured in degrees relative to the y-axis, the wave propagates. The 'D' value tells the program that the next two values are input in degrees of angular motion. The '0.' value tells SeaState to start the wave at its 0° and the last values tells it to model the loading in 36 increments of 10° out of the 360° that make up one wave period and to output loads at all increments. Finally, the lines marked 'DEAD' tell SeaState to include the dead weight of all structural elements in the load case. The 'DEAD' option calculates the member weight based on the densities and section properties defined in the SACS input file. The dead calculation also takes into account buoyancy effects for all members which aren't marked as 'flooded' and thus displace water, leading to upward loads.

G.6.2 Verification

To verify the wave and current loads on the pontoons, two calculations are performed. Both are performed modelling loads on pontoon 1, which is fixed at the top and bottom for the purposes of this calculation. The SACS input file detailing this situation is shown in Figure G.19.

```

OPTIONS      MN      SD      1 1      PTPT      PT  PTPTPTMXPT
SECT
SECT PONT4      TUB7.07+61.060+107.375+117.375+11 3000.0150.0
GRUP
GRUP P04 PONT4      3000.      20.0020.0046.00 1      1.001.00
MEMBER
MEMBER P1  P2  P04      N      2.5  3000.
MEMBER P2  P3  P04      N      0.475 3000.
MEMBER P3  P4  P04      N      0.475 3000.
MEMBER P4  P5  P04      N      0.475 3000.
MEMBER P5  P6  P04      N      0.475 3000.
MEMBER P6  P7  P04      N      2.095 3000.
MEMBER P7  P8  P04      N      2.5  3000.
JOINT
JOINT P1      734.  116.  4.  1.  89.  29. 111111
JOINT P2      734.  116.  3.  1.  89.  29.
JOINT P3      734.  116. -20. 1.  89.
JOINT P4      734.  116. -36. 1.  89. -56.
JOINT P5      734.  116. -42. 1.  89. -16.
JOINT P6      734.  116. -56. 1.  89. -28.
JOINT P7      734.  116. -70. 1.  89. -58.
JOINT P8      734.  116. -73. 1.  89. -13. 111111
END

```

Figure G.19: Pontoon 1 input model for the wave and current load verification.

This pontoon is then loaded using Seastate. First with the wave case with an angle of 180° relative to the North, the SeaState input detailing this load is shown in Figure G.20.

The result of this analysis is a collection of 72 wave load cases, in which distributed loads are modelled on the pontoon. This is displayed visually in Figure G.21 for step 15 out of 72, along with the distributed load calculated using the method detailed in section B.1. As is visible in the figure, the shape of the distributed loading agrees with the theoretical calculation. To determine if the loading values agree, the distributed load calculated by SACS in the x- and y-direction is transformed into a load in the wave direction, as in the theoretical calculation. Then both are integrated along the vertical axis to determine the total load on the pontoon. The results of this integration is shown in Figure G.22 for a single wave period.

As can be seen in Figure G.22, the results are relatively similar, though there are remarkable differences. One of the causes is that the theoretical calculation is performed using the 2nd order Stokes theoretical application, as opposed to the 5th order SACS employs, for the velocity and acceleration terms, leading to a slightly different wave shape. The wave shape in the 5th order specification is more defined and thus more accurate, although the difference is small considering the large water depth at the

```

LDOPT      NF+Z    1.015      -1258.    1258.GLOBMN
FILE B
LOAD
LOADCNI180
WAVE
WAVE      STOK    4.55          4.6          210.      D      0.    5.0  72AL
MEMOV     P2     P3                                0.330.33
MEMOV     P3     P4                                0.330.33
MEMOV     P4     P5                                0.330.33
MEMOV     P5     P6                                0.330.33
MEMOV     P6     P7                                0.330.33
MEMOV     P7     P8                                0.330.33
END

```

Figure G.20: SeaState input file for the wave case with an angle of 180° relative to the North, loading pontoon 1.

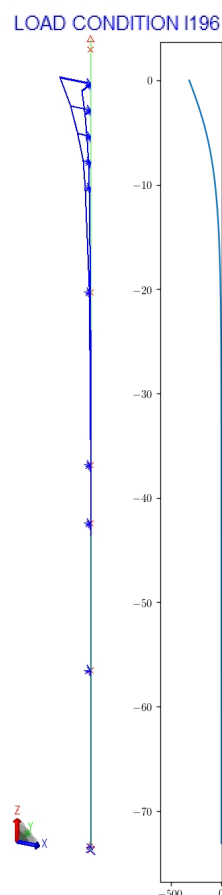


Figure G.21: Distributed load calculated by SACS in the x- and y-direction along with the distributed load from the theoretical calculation.

bridge location. Thus this does not explain all differences, and the most likely explanation for the difference is that SeaState modifies the surface elevation while the wave loads the pontoon, thus increasing and decreasing the loaded area on the pontoon, leading to differences in load shape and amplitude and a much more accurate representation of reality. On the whole, this calculation verifies the wave loading on members calculated by SeaState.

For the current loading, the same SACS model is used, with pontoon 1 restrained at the top and bottom. The inward current profile is applied, as specified in Table G.13.

The inward current is applied in the SeaState input file as shown in Figure G.23.

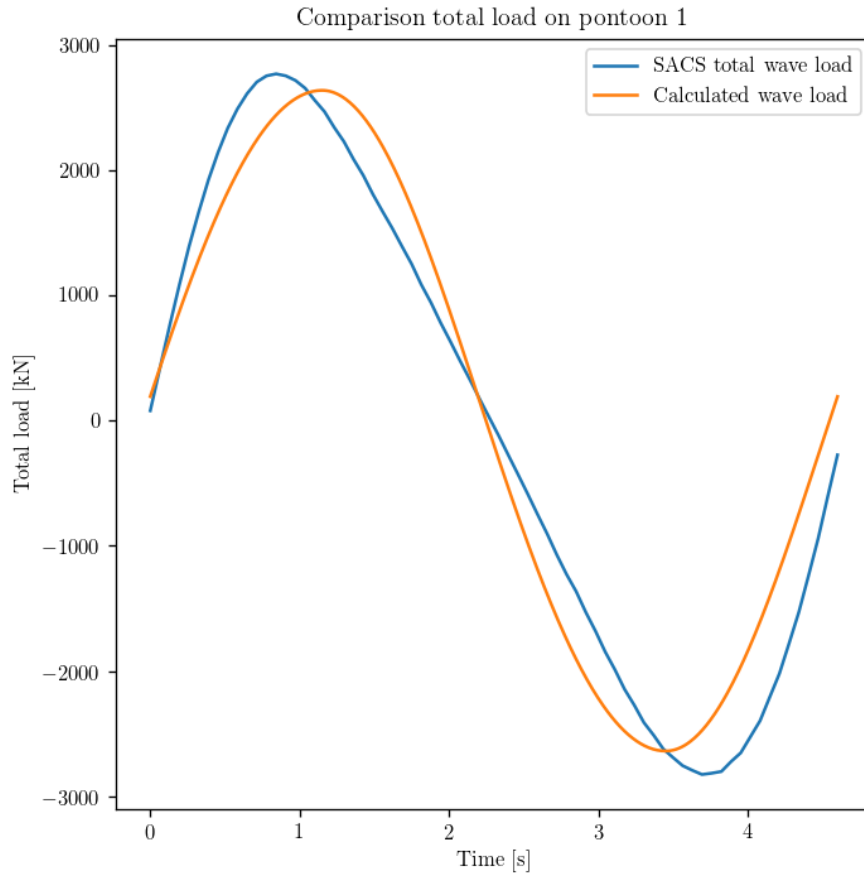


Figure G.22: Distributed load calculated by SACS in the x- and y-direction along with the distributed load from the theoretical calculation.

Inwards - 60°	
Depth	Velocity
10 m	1.27 m s ⁻¹
30 m	0.48 m s ⁻¹
70 m	0.39 m s ⁻¹

Table G.13: Inward current profile.

```

LDOPT      NF+Z    1.015      -1258.    1258.GLOBMN
FILE B
LOAD
LOADCNCURI
CURR
CURR      1183.    0.39      0.
CURR      1228.    0.48      0.
CURR      1248.    1.27      0.
END

```

Figure G.23: SeaState input file for the inward current case.

The resulting shape of the distributed current load on pontoon 1, calculated by SACS and using the theory presented in section B.2 is shown in Figure G.24. It is visible that the shape of both loads are very similar, although SeaState linearises between the calculated distributed loads instead of between current velocities, resulting in straight lines in the distributed load profile.

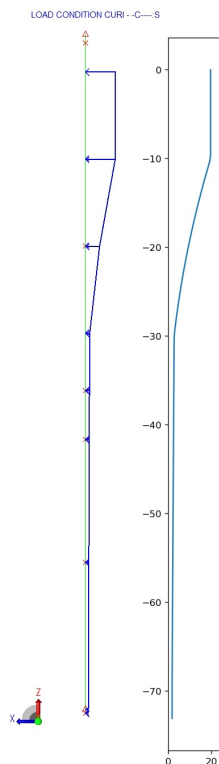


Figure G.24: Distributed current load calculated by SACS along with the distributed load from the theoretical calculation.

The calculated values of both methods are compared in Figure G.25. The comparison clearly verifies the values calculated by SeaState with the values calculated according to the theory.

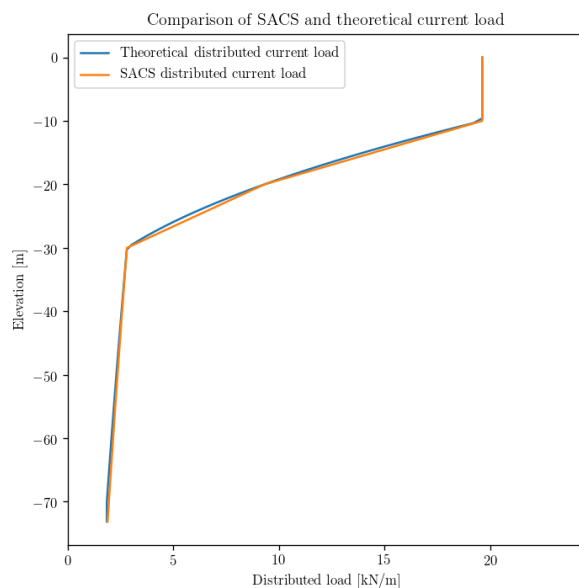


Figure G.25: Distributed current load calculated by SACS along with the distributed load from the theoretical calculation.

Appendix H

SACS dynamic analysis

This appendix contains information and insights into the methods employed by the SACS software package for different dynamic analyses.

H.1 Eigenfrequency analysis

Eigenfrequency, or modal, analysis calculates a structures eigen- or natural frequencies of vibration and shape the structure takes once vibrating in this frequency. This section shows how the Dynpac tool in the SACS software package performs this analysis and which design choices were made in relation to this analysis for this study. It is performed in Dynpac by first calculating the structural stiffness matrix through a static calculation of the model. Then this stiffness matrix is reduced, the mass matrix is generated and reduced, too and finally the eigenfrequencies and modal shapes, or eigenvectors, are calculated for the master degrees of freedom and expanded for the slave degrees of freedom. SACS allows the user to set master degrees of freedom and slave degrees of freedom manually. This is done in the SACS input file, where per joint the user can set a degree of freedom to be retained for dynamic analysis (become a master dof). This is displayed in Figure H.1, where the top and cable joint of pontoon 22 are assigned translational master degrees of freedom, as well all main- and lateral cable joints (except for the support joints, such as 'M0'). The reason not all free degrees of freedom in the model are assigned a master degree of freedom is due the fact that Dynpac can only allow up to 3000 master degrees of freedom in a single model. Therefore it has been chosen to retain the tops of the pontoon pylons and cable joints as master joints, since the pontoons only need two master joints to display their rigid body motion and there is no need for more. The cable joints translational degrees of freedom are all assigned master status, because, as evidenced by the verification calculation in section G.1.1.2, the more joints with master degrees of freedom used in a cable model, the closer the resulting mode shapes and frequencies come to the theoretical results and therefore, presumably, reality.

JOINT P210	3101.	3590.	7.	07.	63.	37.	222000
JOINT P211	3101.	3590.	4.	07.	63.	29.	
JOINT P212	3101.	3590.	3.	07.	63.	29.	
JOINT P213	3101.	3590.	-20.	07.	63.		222000
:							
JOINT M0	0.	0.	0.			111111	
JOINT M1	15.	10.	-1.	13.636	62.636-81.818	222000	
JOINT M2	30.	21.	-3.	27.272	25.272-63.636	222000	
:							
JOINT L0	682.	116.	-20.	5.	89.		222000
JOINT L1	630.	116.	-20.	9.	89.		222000
JOINT L2	579.	116.	-20.	3.	89.		222000

Figure H.1: Joint lines with translational master degrees of freedom assigned.

H.1.1 Stiffness matrix reduction

Once the structural stiffness matrix is known, a Guyan reduction is performed to reduce the structural stiffness matrix [HH88]. This reduction uses the definition of slave degrees of freedom, that no external forces are directly applied to them, to reduce the number of equations that need to be solved. By performing this reduction, the relation between the applied force and relating displacement is also reduced to only forces applied to master dofs, stiffness matrix entries related to master dofs and displacements of master degrees of freedom. After this system of equations has been solved, the slave degrees of freedom can be calculated from the results obtained for the master degrees of freedom.

H.1.2 Mass matrix generation

Dynpac can generate a mass matrix based on two methods; the lumped mass method and the consistent mass method. The lumped mass method concentrates the mass calculated by integration along the element axis at the joints, creating a fully diagonal mass matrix. This method is quicker than the consistent mass method, but it is not recommended in cases where for instance fluid added mass is added to a slender element. This is because the element mass for a slender element including fluid added mass is not the same in each direction, since there is additional fluid mass acting normal to the element. Since the bridge design includes many slender elements immersed in fluid, such as all cables used for the cable system, it has been decided not to use the lumped mass approach. Therefore the mass matrix generation is performed using the consistent mass approach, which is implemented in Dynpac by first integrating the expression for the kinetic energy along the element axis. Then the resulting expression for the kinetic energy is differentiated first with respect to the element joint degree of freedom velocities and then with respect to time, resulting in an expression of Force. This resulting expression contains the consistent mass matrix, and the joint degree of freedom accelerations. The consistent mass matrix contains off-diagonal elements, coupling all degrees of freedom. Once the mass matrix has been generated, it is reduced using a Guyan reduction, just as the stiffness matrix.

H.1.3 Result calculation

The reduced system of equations created by the Guyan reductions is then solved for the eigenfrequencies and mode shapes using a QR algorithm, which employs QR decomposition and to solve for the eigenvalues (eigenfrequencies) and eigenvectors (mode shapes) [Apo09]. The results are then expanded to obtain results for the slave degrees of freedom, to facilitate the calculation of modal reactions and modal internal loads.

H.2 Steady state analysis

Steady state analysis is the analysis of a structure under a constant periodic load. In this analysis it is assumed that the frequency of vibration of the structure and the frequency of the periodic load align after a sufficient time span. SACS can calculate steady responses using two different program modules; the dynamic response module for general periodic vibrations and the wave response module, which specifically calculates wave generated steady state vibrations. The steady state analysis performed in this thesis is the analysis of the six critical load cases defined in section B.5, comprised of critical wave- and in- or outgoing current loading. Therefore the wave response program is used for this analysis.

The wave response program calculates the steady state response by first assuming that an infinite train of the periodic wave has passed and the system vibrates in the same frequency as the wave. Since the structure is immersed in fluid, it is subjected to hydrodynamic forcing, both by the wave on the structure- and by the fluid displaced by the displaced structure due to wave forcing. This calculation is highly non-linear, as the force the wave exerts on the structure is dependant upon the displacement and velocity of the structure, as is the displacement and velocity of the structure dependant upon both the wave forcing and the fluid reaction on the displacing structure. Therefore the wave response program employs an iterative procedure to calculate the hydrodynamic forcing (which includes any hydrodynamic damping). The procedure starts by assuming the structure is at rest and generating the distributed wave loading for one full cycle of the wave in load steps using the Morison equation. The equivalent joint forces are calculated using static equilibrium. These equivalent joint forces are transformed into modal generalized forces by multiplying them with the modal eigenvectors. Then each mode is considered individually and the generalized force is decomposed into Fourier components, which are sinusoidal functions with varying

phase angles. The amount of Fourier components is determined by setting the Fourier series convergence tolerance, which is a percentage root mean squared error over the full range of outputs. After this the modal response is calculated per Fourier component, which is then linearly combined into a total modal response. By summing the response of all modes, the motion of the entire structure is calculated. Then this motion is combined with the wave case and fluid the structure is immersed in to calculate a new set of distributed wave loads per wave step and the iterative procedure restarts. The process is ended when the generalized forces of the present- and previous load step are within the specified tolerance.

The tolerance for the generalized forces are set as a percentage root mean squared error and is set to 1 % in this thesis.

Because the wave response program takes into account the hydrodynamic forcing due to displacing structure, there is no need for a separate calculation of the fluid damping on the structure.

H.3 Time history analysis

In time history analysis any type of forcing can be applied to a structure, after which a time history of the structure response is calculated. Time history analyses are applied in this thesis in the vortex induced vibration analysis, for which reference is made to appendix J. Time history analysis is possible in SACS, using either the dynamic response or the wave response module. The dynamic response module accepts any time history input loading, while the wave response module works exclusively with wave time histories. In this study non-wave loading is applied to the pontoons in the time history analyses, therefore the dynamic response program is used.

The force time history can be applied in a Dynamic Response input file, of which an example is shown in Figure H.2.

```
DROPT VIBR 500 +Z-1200.
SDAMP      4.300
FDAMP PCNL
LOAD
FVIB  THIS LINE NFD          LN  JTD
```

Figure H.2: Example dynamic response input file.

In this file the 'SDAMP' line sets the structural damping factor to 4.3 % of the critical damping across all modes of vibration. The 'FDAMP' line set to 'PCNL' informs the module that it has to calculate the non-linear fluid damping based on the structure motion, which is described in more detail in section H.2.

The dynamic response program operates by first transforming the force time history input by the user and if applicable, the fluid response, into modal generalized forces by multiplying them with the modal eigenvectors. The input is interpolated to make sure the generalized force is continuous throughout the complete time history. This is needed, since the solution calculation utilizes a variable time stepping integration procedure to speed up computation and maintain error control throughout the solution.

Figure H.3 shows an example of a portion of time history input in a Dynamic Response input file. In this example, the time history is set in terms of the distributed loads 'P1X' and 'P1Y' set in the SACS input file (for more on this, see section G.5.4.1) and timesteps of 7.4 s.

```
:
:
LOADC  P1X0.00015.4755
LOADC  P1Y0.000-0.1384
LOADC  P1X7.40766.0743
LOADC  P1Y7.4070.45331
:
:
```

Figure H.3: Example portion of a force time history input.

Appendix I

Pontoon decoupling

This appendix contains the calculations and analyses performed to determine the stiffness and potential frequency dependence of the coupling springs used to model the constraints the rest of the bridge structure imposes upon the pontoons. These coupling springs are to be used in part of the vortex induced vibration analysis, for which reference is made to appendix J. Figure I.1 contains a mechanical model of a pontoon with attached coupling springs. A model such as this allows an analysis to be performed on a single pontoon, without neglecting the influence the rest of the bridge structure has on the analysis performed. In the model displayed, the pontoon is expected to behave as a rigid body. Therefore, the coupling springs only have to be attached in one location on the pontoon, as the rest of the pontoon body will move rigidly with respect to this location. This means that the movement of any point on the pontoon can be calculated from the movement of the point where the coupling springs attach. The location where the springs are modelled are chosen to be at the water level.

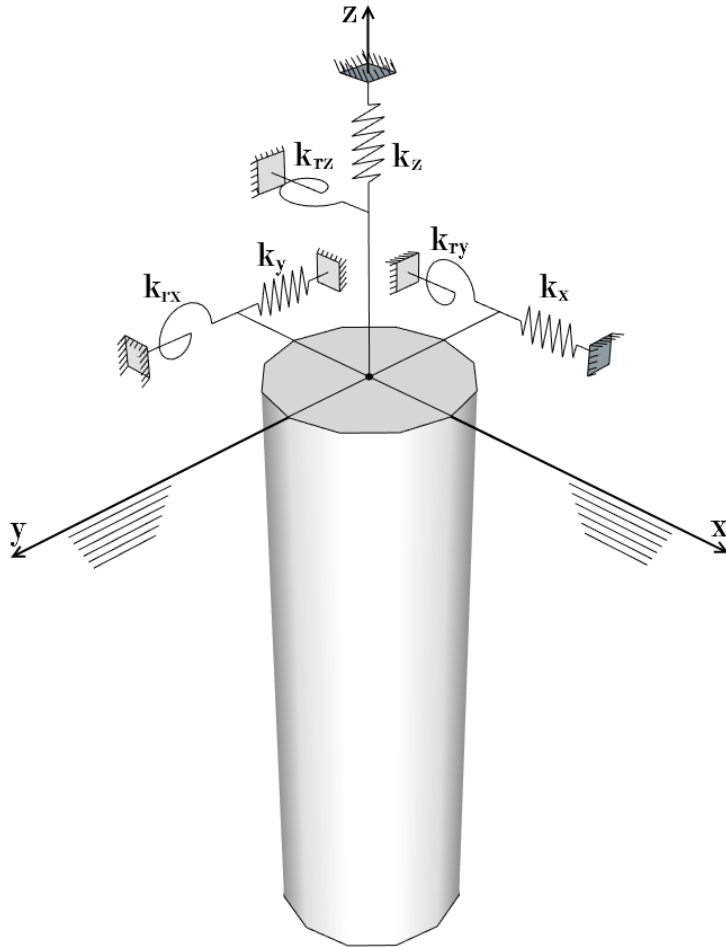


Figure I.1: Mechanical model decoupled pontoon.

I.1 Methodology

The methodology to determine the static- and frequency dependent stiffness of the coupling springs is described in this section and an overview is depicted in Figure I.2.

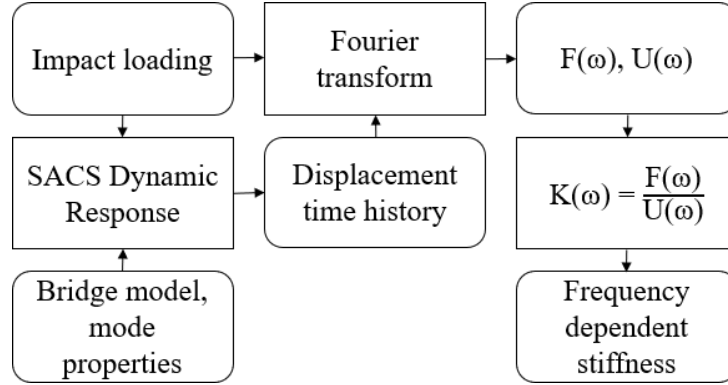


Figure I.2: Workflow to determine the decoupling spring stiffness.

The starting point is the static equilibrium situation of the bridge, with the properties as calculated in appendix F. Then, using the Dynpac module of the SACS software package, for which reference is made to section H.1, the mode shapes and eigenfrequencies are calculated. Next, each degree of freedom for which we are calculating the stiffness is loaded with a numerical impact force, for which the properties are shown in Table I.1 and a visual presentation can be found in Figures I.3. As can be seen in Figure I.1, the numerical impacts modelled create a load amplitude that is the same across all frequencies that may be excited. This means that the energy distribution of the load is the same across all frequencies, which, in theory, should lead to a frequency response spectrum in which the modal frequencies are clearly visible.

Degrees of freedom	Loading	Duration
u_x, u_y, u_z	$100 \cdot 10^3$ kN	1 s
r_x, r_y, r_z	$1 \cdot 10^6$ kN m	1 s

Table I.1: Impact load and moment properties.

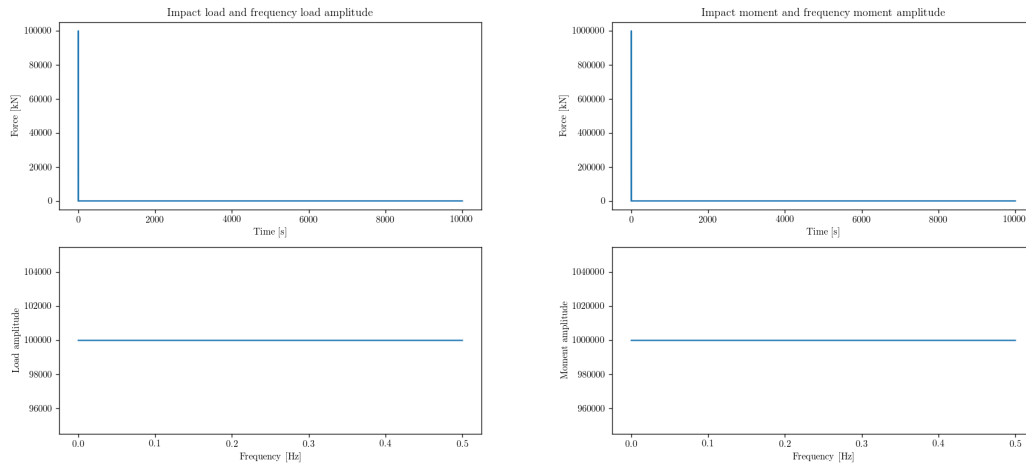


Figure I.3: Impact load (left) and moment (right) plotted in time (top) and their amplitude versus frequency (bottom).

Afer this, the Dynamic Response module is used to calculate the displacement time history response

over a period of 10 000 s. For more information on this calculation module, reference is made to section H.3.

Both the displacement time history and the impact load are transformed to the frequency domain using the Fast Fourier Transform algorithm, which is a numerical implementation of the Fourier transform [CT65]. This yields a collection of complex numbers, which are the Fourier components of the signal at the corresponding frequency. Taking the absolute value of the Fourier components leads to the amplitude of the signal at the corresponding frequency. This is shown visually in Figure I.3, in which the absolute value of the Fourier components versus frequency is plotted in the lower two graphs. This step yields the amplitude frequency response of both the exciting load, $F(\omega)$, and the resulting displacement, $U(\omega)$ for each degree of freedom.

Subsequently, the frequency dependant stiffness is calculated for each of the six impact loads and degrees of freedom according to Equation I.1, leading to a frequency dependent stiffness matrix as shown in Equation I.2. A visual representation of the frequency dependent stiffness matrix is given in Figure I.4.

$$K_{i,j}(\omega) = \frac{F_j(\omega)}{U_i(\omega)} \quad (\text{I.1})$$

In which;

$K_{i,j}(\omega)$ is the frequency dependent stiffness at frequency ω and degree of freedom i due to a load at degree of freedom j

$F_j(\omega)$ is load amplitude at frequency ω and degree of freedom j

$U_i(\omega)$ is displacement amplitude at frequency ω and degree of freedom i

$$K(\omega) = \begin{bmatrix} K_{1,1}(\omega) & K_{1,2}(\omega) & K_{1,3}(\omega) & \dots & K_{1,6}(\omega) \\ K_{2,1}(\omega) & K_{2,2}(\omega) & K_{2,3}(\omega) & \dots & K_{2,6}(\omega) \\ \vdots & \vdots & \vdots & \ddots & \vdots \\ K_{6,1}(\omega) & K_{6,2}(\omega) & K_{6,3}(\omega) & \dots & K_{6,6}(\omega) \end{bmatrix} \quad (\text{I.2})$$

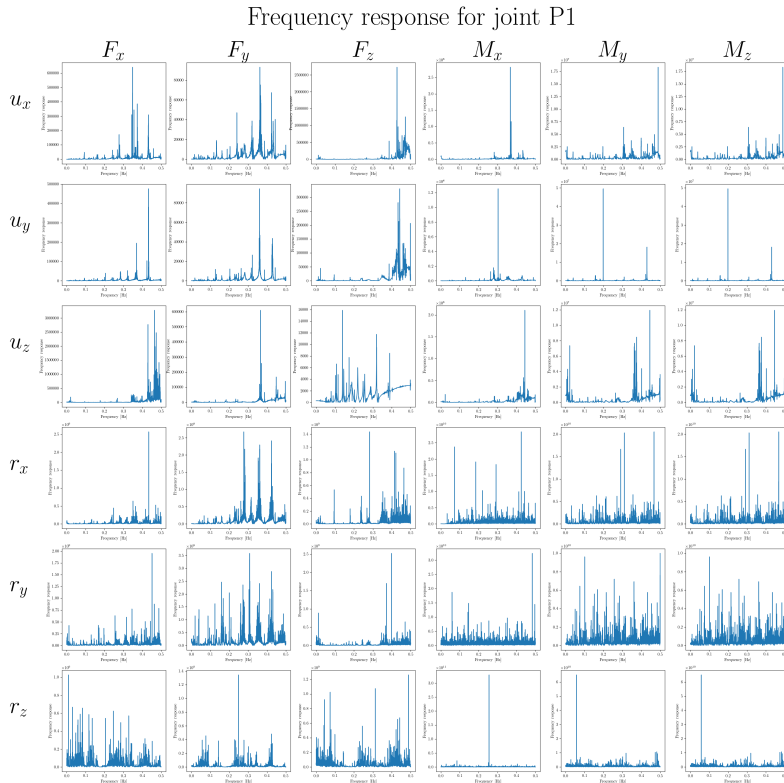


Figure I.4: Visual representation of the frequency dependent stiffness matrix for joint P1.

I.2 Results

The results of this analysis clearly show the modal eigenfrequencies of the bridge model returning in the displacement amplitude response and the frequency dependent stiffness. To illustrate this, Figure I.5 displays the load amplitude versus frequency, the displacement amplitude versus frequency and the resulting frequency dependent stiffness for joint 'P1' degree of freedom u_x loaded by an impact load at that same degree of freedom. This result illustrates that the bridge structure has a very high stiffness when responding to loads at frequencies away from its own modal eigenfrequencies- and a very low stiffness in response to loads at its modal eigenfrequencies. This is visible because the impact load provides the same energy to all frequencies and the response varies across the frequencies.

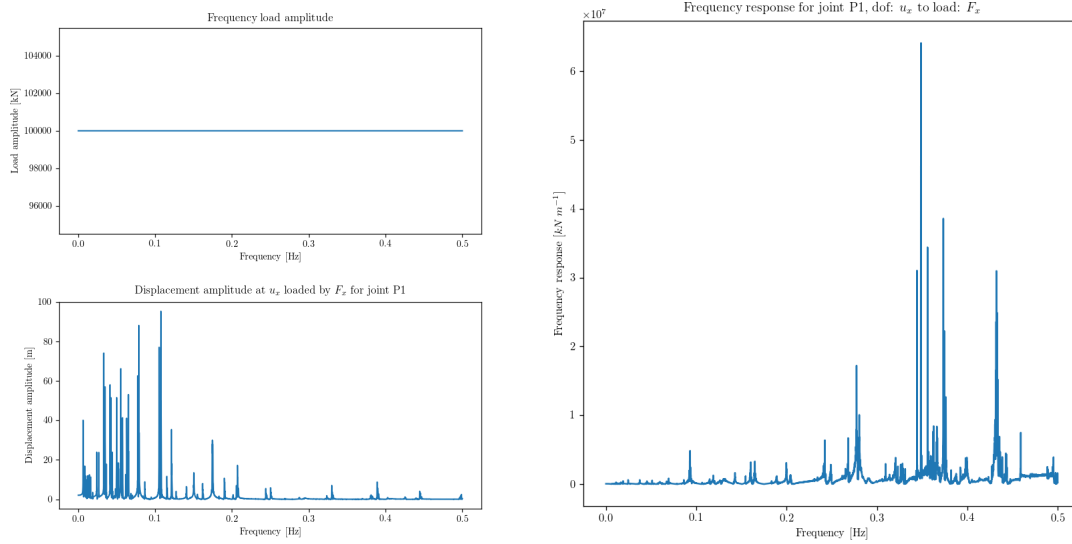


Figure I.5: Impact load amplitude (top left) and displacement amplitude (bottom left) versus frequency and frequency dependant stiffness (right) for joint 'P1' dof u_x .

I.3 Significance

The results obtained from this analysis in terms of the frequency dependent stiffness can be used as spring stiffness for the pontoon coupling springs. In case the choice is made to only take into account the static stiffness, and thus leave out the frequency dependent portion, the value found at a frequency of 0 Hz can be used, as this is the static stiffness. To use these results to model the frequency dependence of the structures' reaction as well, additional operations are necessary.

The results of this calculation have been used in a trial run of a coupled vortex induced vibrations analysis. Details can be found in section J.3.6.

Appendix J

Vortex induced vibrations

This chapter describes the vortex induced vibration analysis performed in this thesis. It starts with a short description of the phenomenon of vortex induced vibrations, after which an overview of the follow research method is shown. Then the research itself, results and conclusions are presented.

J.1 Theory

The theory behind the phenomenon of vortex induced vibrations is described here. As a current flows past an object, vortex shedding takes place in the area behind the object, in terms of the flow direction. For a circular object, vortices are formed on both left and right side of the cylinder, when looking along the flow direction, and they are shed one side after the other. The frequency with which this occurs is the shedding frequency. The shedding of vortices causes the fluid to flow faster along one side of the cylinder, creating a large cross-flow force on one side than on the other. This is called a cross-flow lift force. Figure J.1 depicts vortex shedding by showing a contour plot of the magnitude of the velocity of the flow past a cylindrical object. In areas where vortices are found, the magnitude of the velocity is low (coloured in blue). The areas with a high magnitude of velocity are coloured in red. It is visible that there is an inequality in the velocity magnitude between the sides of the cylinder and the contact area of this higher velocity zone with the cylinder. This inequality causes the cross-flow forcing.

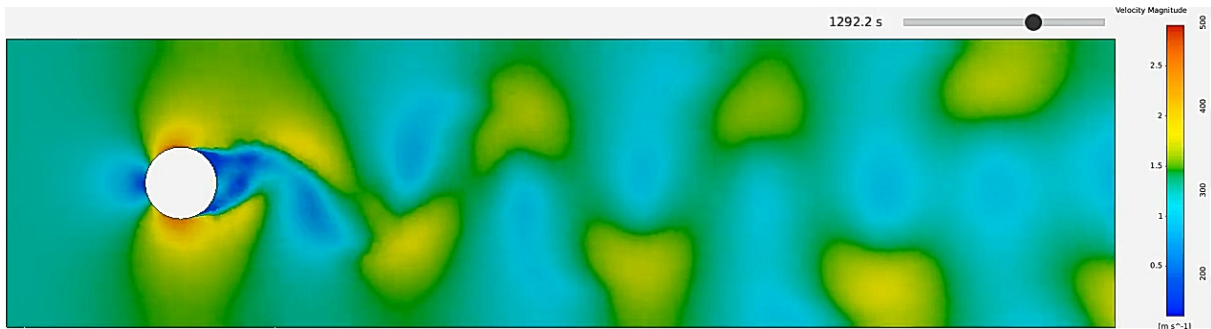


Figure J.1: Magnitude of fluid flow velocity around a cylinder.

Vortex induced vibrations are caused by the cross-flow forcing and tend to be problematic when the frequency of the cross-flow loading are around modal eigenfrequencies of the loaded structure. The range of frequencies for which the shedding frequency can be considered too close to the modal eigenfrequencies is larger than is usual in structural dynamics. This is because the fluid flow past the object is influenced by the motion of the object, therefore the vortex shedding frequency is often shifted closer to the structures frequency of vibration. Since structures tend to vibrate in their modal eigenfrequencies, this leads to a wide range of vortex shedding frequencies shifting to modal eigenfrequencies, causing larger structural excitation. In this thesis, the fluid flow around the pontoons, including vortices, is modelled using the Ansys Fluent program. This program utilizes computational fluid dynamics to calculate fluid flow. More information on the theory behind the functioning of this software is found in section J.1.1.

J.1.1 Ansys Fluent turbulent flow modelling

This subsection deals with the theory behind the modelling of fluid flow by the Ansys Fluent program.

J.1.1.1 Constitutive equations

Ansys Fluent models fluent flows based on the conservation of mass and momentum, according to the Navier-Stokes equations, shown in Equations J.1 and J.2.

$$\nabla \cdot (\rho \vec{v}) = S_m \quad (\text{J.1})$$

In which;

ρ is the fluid mass density

\vec{v} is the fluid velocity

S_m is the constant mass of the observed volume

$$\frac{\partial}{\partial t} (\rho \vec{v}) + \nabla \cdot (\rho \vec{v} \vec{v}) = -\nabla p + \nabla \cdot (\bar{\bar{\tau}}) + \rho \vec{g} + \vec{F} \quad (\text{J.2})$$

In which;

ρ is the fluid mass density

\vec{v} is the fluid velocity

p is the fluid static pressure

$\bar{\bar{\tau}}$ is the fluid stress tensor according to Equation J.3

$\rho \vec{g}$ are the gravitational forces

\vec{F} are external forces on the fluid body

$$\bar{\bar{\tau}} = \mu \left((\nabla \vec{v} + \nabla \vec{v}^T) - \frac{2}{3} \nabla \cdot \vec{v} I \right) \quad (\text{J.3})$$

In which;

$\bar{\bar{\tau}}$ is the fluid stress tensor

μ is the molecular viscosity

\vec{v} is the fluid velocity

I is the unit identity tensor

For modelling turbulent flows, different models are available with ranges of validity for different flow- and structure models and a higher- or lower accuracy in different regions of the models. For this thesis, the choice was made to model the fluid flow using the two-transport-equation k- ω model with shear stress transport. This model allows for an accurate near-wall treatment and high accuracy boundary layer simulations and switches to a different transport equation for fluid flow further from boundaries [Men94]. Since the goal of the analysis is to determine the cross-flow force exerted on the pontoon walls, high modelling accuracy in this area of the model is needed and this model fits the needs of the research. The k- ω -SST model used in this thesis makes use of Reynold's averaging, in which the (exact) solution variables in the Navier-Stokes equations are decomposed into mean (time-averaged) and fluctuating components. This is shown for velocity components in Equation J.4. This is also performed for the fluid pressure and other scalar quantities, as shown in Equation J.5.

$$u_i = \bar{u}_i + u'_i, \quad i = 1, 2, 3 \quad (\text{J.4})$$

In which;

u_i are the fluid velocity components

\bar{u}_i are the mean fluid velocity components

u'_i are the fluctuating fluid velocity components

$$\phi = \bar{\phi} + \phi' \quad (\text{J.5})$$

In which;

ϕ is the fluid pressure, or a different scalar quantity

$\bar{\phi}$ is the mean fluid pressure, or different scalar quantity

ϕ' is the fluctuating fluid pressure, or different scalar quantity

Substituting these into Equations J.1 and J.2 yields the expressions shown in Equations J.6 and J.7. These expressions are the Reynolds-averaged-Navier-Stokes (RANS) equations and include additional terms that represent the effects of turbulence, the Reynold's stresses. These Reynold's stresses, $(-\rho u'_i u'_j)$ must be modelled for the expressions to be closed.

$$\frac{\partial}{\partial x_i} (\rho \bar{u}_i) = 0 \quad (\text{J.6})$$

In which;

$\frac{\partial}{\partial x_i}$ is the partial derivative in direction x_i

\bar{u}_i is the mean (time-averaged) fluid velocity component in direction x_i

$$\frac{\partial}{\partial t} (\rho \bar{u}_i) + \frac{\partial}{\partial x_j} (\rho \bar{u}_i \bar{u}_j) = -\frac{\partial p}{\partial x_i} + \frac{\partial}{\partial x_j} \left(\mu \left(\frac{\partial \bar{u}_i}{\partial x_j} + \frac{\partial \bar{u}_j}{\partial x_i} - \frac{2}{3} \delta_{ij} \frac{\partial \bar{u}_l}{\partial x_l} \right) \right) + \frac{\partial}{\partial x_j} (-\rho u'_i u'_j) \quad (\text{J.7})$$

In which;

ρ is the fluid mass density

$\frac{\partial}{\partial x_i}$ is the partial derivative in direction x_i

\bar{u}_i is the mean (time-averaged) fluid velocity component in direction x_i

p is the fluid static pressure

μ is the molecular viscosity

u'_i is the fluctuation fluid velocity component in direction x_i

To model the turbulent fluid flows the k- ω -SST model rewrites and appends the RANS-equations into an expression for the transport of the fluid's turbulent kinetic energy and one for the specific turbulent dissipation rate. These expression are shown in Equations J.8 and J.9.

$$\frac{D\rho k}{Dt} = \tau_{ij} \frac{\partial u_i}{\partial x_j} - \beta^* \rho \omega k + \frac{\partial}{\partial x_j} \left((\mu + \sigma_k \mu_t) \frac{\partial k}{\partial x_j} \right) \quad (\text{J.8})$$

In which;

$\frac{D}{Dt}$ is the Lagrangian derivative: $\partial/\partial t + u_i \partial/\partial x_i$

ρ is the fluid mass density

k is the fluid's turbulent kinetic energy

τ_{ij} is the turbulent stress tensor, $-\rho u'_i u'_j$, according to Equation J.10

u_i is the mean (time-averaged) fluid velocity component in direction x_i

β^* is a closure coefficient

ω is the specific turbulent dissipation rate

μ is the molecular viscosity of the fluid

σ_k is a diffusion constant

μ_t is the turbulent eddy viscosity, according to Equation J.11

$$\frac{D\rho\omega}{Dt} = \frac{\gamma}{\nu_t} \tau_{ij} \frac{\partial u_i}{\partial x_j} - \beta^* \rho \omega^2 + \frac{\partial}{\partial x_j} \left((\mu + \sigma_\omega \mu_t) \frac{\partial \omega}{\partial x_j} \right) + 2\rho(1 - F_1) \sigma_{\omega 2} \frac{1}{\omega} \frac{\partial k}{\partial x_j} \frac{\partial \omega}{\partial x_j} \quad (\text{J.9})$$

In which;

$\frac{D}{Dt}$ is the Lagrangian derivative: $\partial/\partial t + u_i \partial/\partial x_i$

ρ is the fluid mass density

ω is the specific turbulent dissipation rate

γ is a closure coefficient

ν_t is the kinematic turbulent eddy viscosity, according to Equation J.11

τ_{ij} is the turbulent stress tensor, $-\rho u'_i u'_j$, according to Equation J.10

u_i is the mean (time-averaged) fluid velocity component in direction x_i

β^* is a closure coefficient

μ is the molecular viscosity

σ_ω is a diffusion constant

μ_t is the turbulent eddy viscosity, according to Equation J.11

F_1 is a blending function

$\sigma_{\omega 2}$ is a diffusion constant

k is the fluid's turbulent kinetic energy

$$\tau_{ij} = \mu_t \left(\frac{\partial u_i}{\partial x_j} + \frac{\partial u_j}{\partial x_i} - \frac{2}{3} \frac{\partial u_k}{\partial x_k} \delta_{ij} \right) - \frac{2}{3} \rho k \delta_{ij} \quad (\text{J.10})$$

In which;

τ_{ij} is the turbulent stress tensor, $-\rho u'_i u'_j$

μ_t is the turbulent eddy viscosity, according to Equation J.11

u_i is the mean (time-averaged) fluid velocity component in direction x_i

δ_{ij} is the Kronecker delta

ρ is the fluid mass density

k is the fluid's turbulent kinetic energy

$$\nu_t = \frac{\mu_t}{\rho} = \frac{k}{\omega} \quad (\text{J.11})$$

In which;

ν_t is the kinematic turbulent eddy viscosity

μ_t is the turbulent eddy viscosity

ρ is the fluid mass density

k is the fluid's turbulent kinetic energy

ω is the specific turbulent dissipation rate

These equations provide a closed-form solution to model turbulent fluid flows.

J.1.1.2 Boundary conditions

The pontoon wall is modelled as a no-slip wall boundary. To incorporate this in Ansys Fluent, the software takes the following boundary conditions into account. The distance from a boundary or interface is often indicated using the y -variable in literature and this convention will be used here as well.

$$\hat{u}_i = 0, \quad k = 0 \quad \text{at } y = 0 \quad (\text{J.12})$$

In which;

\hat{u}_i is fluid velocity component in direction x_i , relative to the velocity of the boundary in direction x_i

k is the fluid's turbulent kinetic energy

$$\omega = 10 \frac{6\nu}{\beta_1 (\Delta y)^2} \quad (\text{J.13})$$

In which;

ω is the specific turbulent dissipation rate

ν is the fluid's kinematic viscosity

β_1 is a closure coefficient

Δy is the distance to the next point away from the wall

J.1.1.3 Moving boundaries in Fluent

There are multiple methods to implement moving boundaries in Fluent. First, a short description of each method is given.

The first method is called dynamic meshing. This method moves the boundary 'through' the mesh and re-meshes and deforms the mesh to accommodate this motion. This method allows the investigation of fluid behaviour between multiple boundaries in different states of movement and creates a visual representation of the movement of the boundary. Figure J.2 shows an example mesh of a pontoon in a fluid volume in un-deformed (left) and deformed (right) state, when the dynamic meshing method is used. To illustrate the effect of dynamic meshing, Figure J.3 uses colour-coding to show the (approximate) cell mesh velocity caused by the re-meshing on the left and the fluid velocity relative to the pontoon boundary on the right. One of the advantages of this method, is that it is possible to assign dynamic properties to the moving boundary, allowing for the immediate calculation of motion of the object and resulting disturbance in fluid flow. Due to the nature of the dynamic mesh, it immediately creates an animation of the corresponding pontoon motion and fluid flow.

The second method is called the sliding mesh method. This method moves the entire mesh together with the boundary that is moved. Figure J.4 shows this visually. For the case studied in this thesis, this approach is not correct. This is because the entire fluid volume is given a velocity, moving with the pontoon. Because of this, the relative velocity of the volume in relation to the pontoon is zero, causing the calculated load on the pontoon to be the same as for a stationary pontoon. This is shown visually in Figure J.5, which uses colour-coding to show the mesh velocity on the left and the fluid velocity relative to the pontoon boundary on the right.

The third method, the one used in this thesis, assigns motion to a boundary relative to the surrounding fluid volume, without disturbing the mesh. This method will be called the 'boundary condition' method in this text. The method is shown visually in Figure J.6, in which it is clearly shown that the mesh is undisturbed. To illustrate the similarity in the effective physical models created using this method and the dynamic meshing method, Figure J.7 uses colour-coding to show the mesh velocity and fluid velocity relative to the pontoon boundary for the boundary condition method. It is clear that in physical reality, the methods are equivalent.

On the basis of these descriptions, it is clear that the sliding mesh method can't be used for the calculation of the loads on the pontoon. The dynamic meshing method with coupling springs and dynamic characteristics seems like the best option to calculate pontoon motion due to the fluid loading. However, this method is very demanding in terms of computation power. The computer available for these calculations is the author's laptop computer, which is not very well suited to the task. To illustrate

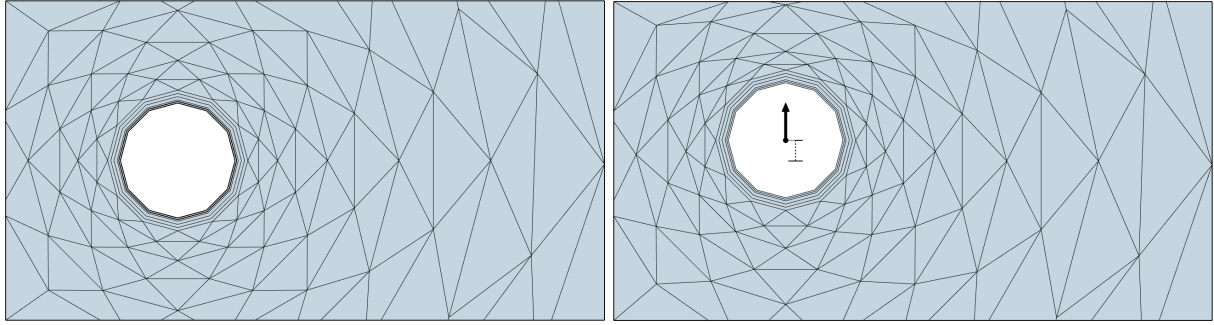


Figure J.2: Undeformed and deformed mesh using the dynamic meshing method.

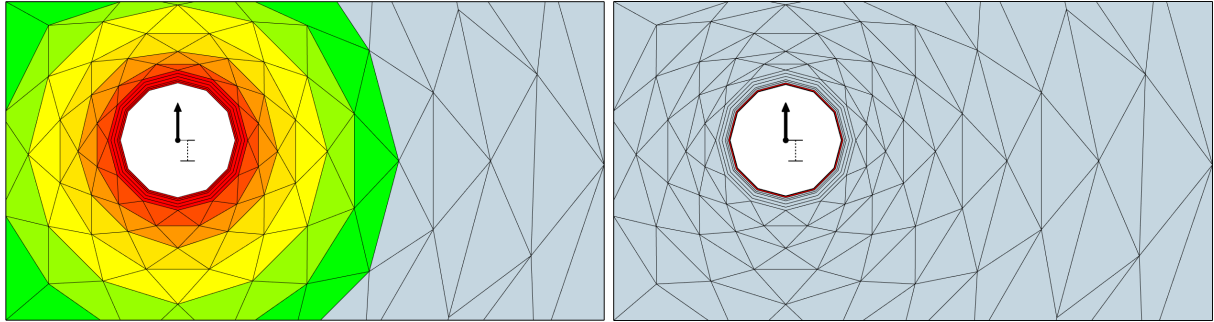


Figure J.3: Mesh velocity (left) and fluid velocity relative to the pontoon boundary (right), shown using colour-coding for the dynamic mesh method.

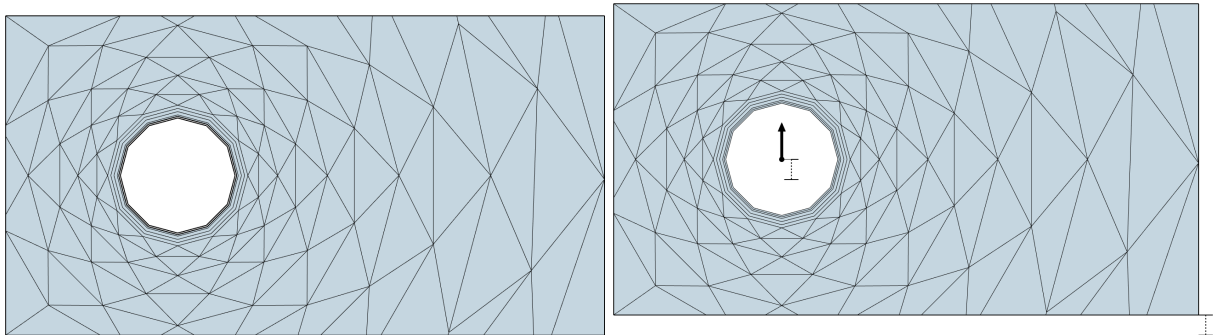


Figure J.4: Undeformed and deformed mesh using the sliding meshing method.

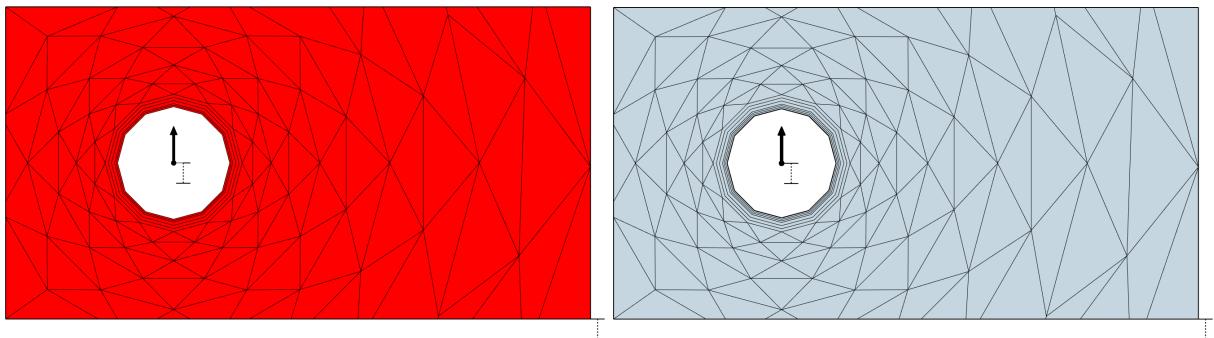


Figure J.5: Mesh velocity (left) and fluid velocity relative to the pontoon boundary (right), shown using colour-coding for the sliding mesh method.

the, one test calculation in which the mesh was too rough and the chosen time-step too large to produce useful results, took 24 hours for one modelled hour.

Calculating the fluid loading on stationary pontoons or pontoons with a given velocity is faster, taking about 2 and a half hours to calculate one modelled hour.

As Figures J.3 and J.7 show, the dynamic meshing method and boundary condition method produce

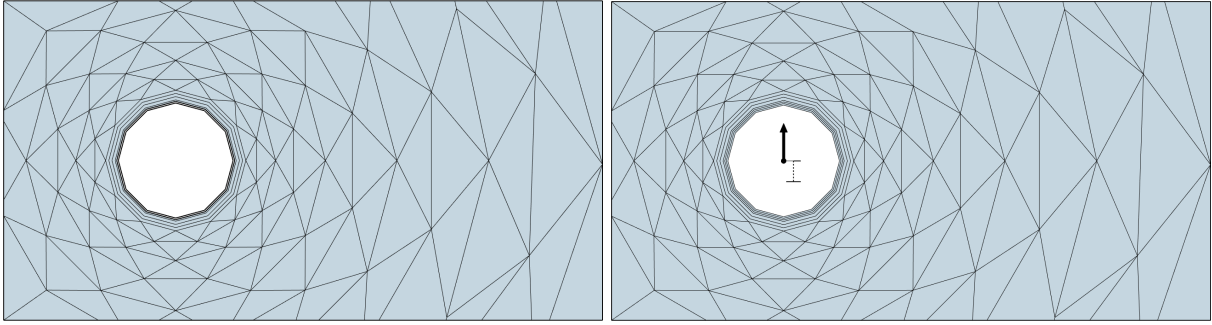


Figure J.6: Stationary pontoon (left) and pontoon in motion (right).

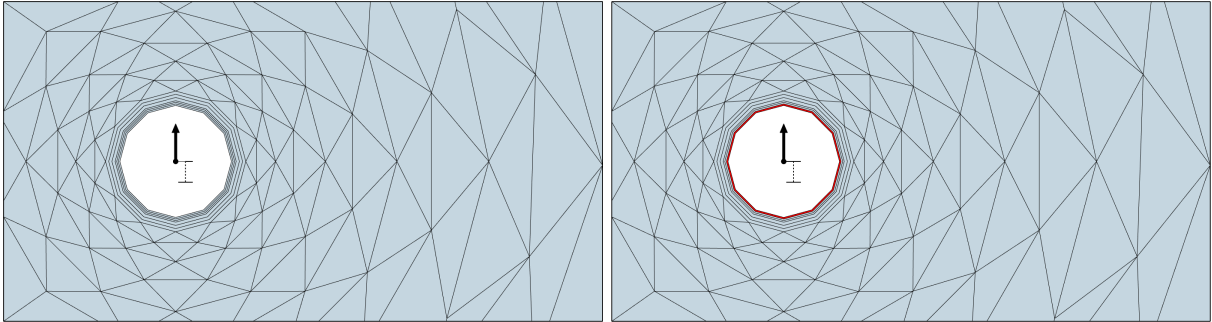


Figure J.7: Mesh velocity (left) and fluid velocity relative to the pontoon boundary (right), shown using colour-coding for the boundary condition method.

physically similar results. This coupled to the fact that the $k-\omega$ -SST model calculates the boundary conditions and thus the flow around these boundaries in the same manner for both methods leads to the conclusion that they are equivalent.

Therefore the choice is made to perform the coupling calculations using two separate programs. The fluid loading is calculated in Fluent, the resulting motion is calculated using SACS and re-implemented in Fluent through a pontoon wall velocity boundary condition.

J.2 Methodology

This section outlines the methodology and different analyses performed to investigate vortex induced vibrations in the bridge system. The fluid flow analyses are carried out using the program Ansys Fluent and all structural calculations are performed using SACS. The steps taken in the process are the following;

First the pontoon modal eigenfrequencies are calculated from the model calculated in appendix F using the method described in section H.1.

Next a 'semi-2D' analysis is performed on stationary pontoon models and the resulting cross-flow loading frequencies are compared to the pontoon modal eigenfrequencies. This is detailed further in section J.3.2.

After this, the influence of pontoon spacing relative to the flow direction on the loading is investigated, as a pontoon being in the wake region where vortices are shed by preceding pontoons may influence the loading on that pontoon. More on this can be found in section J.3.3.

If the preceding analyses indicate sensitivity to vortex induced vibrations, a 3D analysis is performed on stationary pontoon models for a more realistic calculation of the cross-flow loading frequencies. These are then compared to the modal eigenfrequencies of the bridge model, too. This analysis can be found in section J.3.4.

To verify the calculation model calculating the loads on four representative pontoons out of the twenty-two, a verification calculation is performed for pontoons with matching diameters and different draughts. This analysis is found in section J.3.5.

If the system is deemed sensitive to vortex induced vibrations based on the preceding analysis, a coupled analysis is performed. In this coupled analysis the influence of the pontoon motion on the fluid flow is taken into account, leading to a more accurate depiction of reality and a calculation of the bridge motion due to vortex induced vibrations. The performed analysis can be found in section J.3.7. A trial analysis using a different method is found in section J.3.6.

A verification calculation of the model to calculate vortex induced vibrations introduced in this thesis (the Fluent-SACS model) is performed using a wake oscillator model based on the work by Ogink and Metrikine (2010) [OM10]. The verification is performed for the motion of a single pontoon, pontoon 11, in just the cross-flow direction. The theory behind this model and the detailed set-up of this analysis is found in section J.3.8.

If all analyses show that vortex induced vibrations will be a problem for the bridge design, possible solutions to the problem are presented. This can be found in section J.3.9

J.3 Research and results

This section contains the set-up, results and conclusions of the analyses performed in the vortex induced vibration study. First some properties of the analysis set-up that are the same for all analyses, unless specified otherwise, are presented.

J.3.1 Shared parameters

The parameters described in this section are the same for all analyses, unless specified otherwise. The inward current velocity profile, detailed in section B.2 is chosen to be used in all analyses as the velocities observed in the inward current are higher than in the outward current. The velocity profile and the truncated version of this profile used in 3D analyses are shown in Figure J.8. Table J.1 displays the values for- and the depth of measurement of the inward current velocity. Figure J.9 shows the inward current direction in reality and the translation to the bridge model used in this thesis.

The parameters used with the $k-\omega$ -SST model are displayed in Table J.2, for more information on the theory behind this model, reference is made to section J.1.1.1.

All simulations run are transient simulations with over a length of, unless specified otherwise, of 3600 s, with a time-step fixed at 6 s and a maximum of 40 iterations per time step.

The solution method utilized by the Fluent program, the spatial discretization method and order for the different fluid flow variables and the transient formulation are displayed in Table J.3.

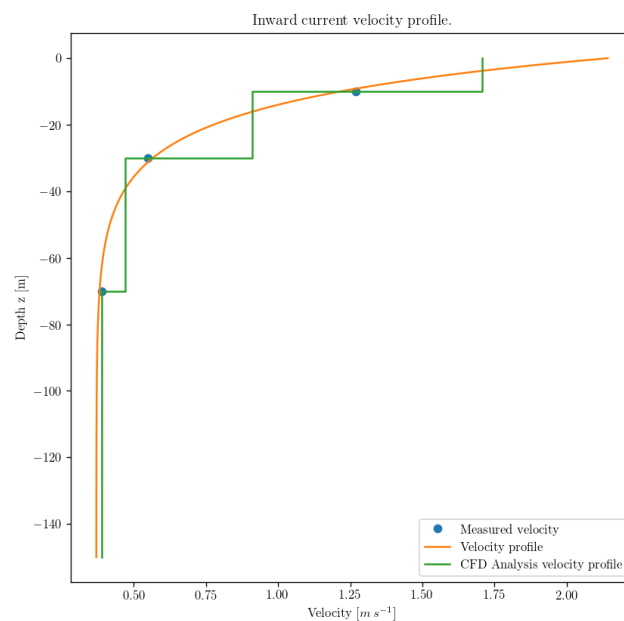


Figure J.8: Measured values of inward current velocity, the power law profile fitted to these values and the truncated profile used in 3D VIV analyses.

Inwards - 60°	
Depth	Velocity
10 m	1.27 m s ⁻¹
30 m	0.48 m s ⁻¹
70 m	0.39 m s ⁻¹

Table J.1: Inward current measured values.

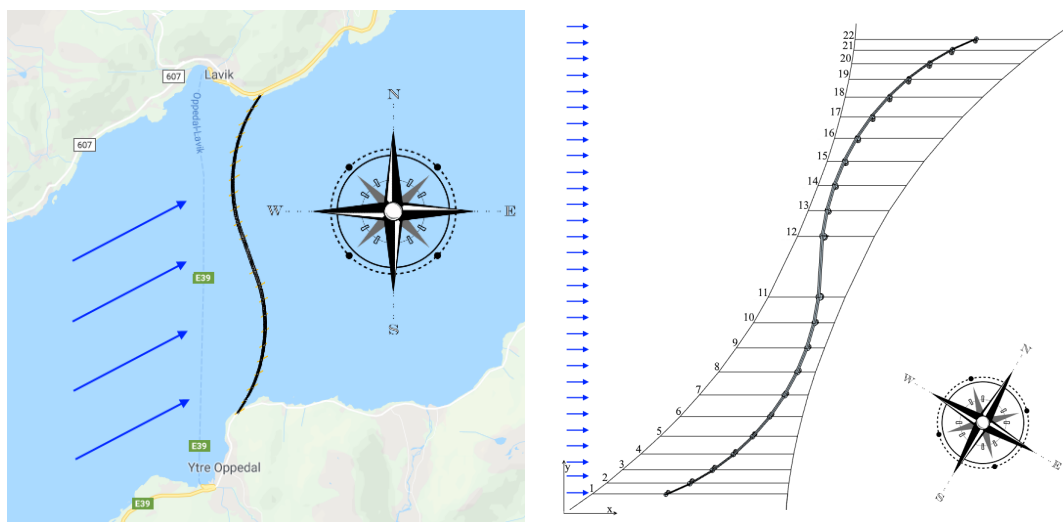


Figure J.9: Current flow direction in reality (left, Google Maps) and in the bridge model (right).

The solution controls used in Ansys Fluent are shown in Table J.4 and the convergence criteria are shown in Table J.5.

For an in-depth description of the pontoons, reference is made to section A.4. The important pontoon

Parameter	Value
α_{∞}^*	1
α_{∞}	0.52
β_{∞}^*	0.09
a_1	0.31
$\beta_{i,inner}$	0.075
$\beta_{i,outer}$	0.0828
TKE inner Prandtl number	1.176
TKE outer Prandtl number	1
SDR inner Prandtl number	2
SDR outer Prandtl number	1.168
Production limiter clip factor	10

Table J.2: Parameters used with the k- ω SST model turbulent flow model.

Parameter	Value
Pressure-velocity coupling	Coupled scheme

Spatial discretization	
Gradient	Least squares cell based
Pressure	Second order
Momentum	Second order upwind
Turbulent kinetic energy	Second order upwind
Specific dissipation rate	Second order upwind
TKE inner Prandtl number	1.176
TKE outer Prandtl number	1
SDR inner Prandtl number	2
SDR outer Prandtl number	1.168

Transient formulation	Second order implicit
-----------------------	-----------------------

Table J.3: Solution method, spatial discretization and transient formulation used in the analyses with Ansys Fluent.

properties for the vortex induced vibration research are shown in Table J.6, since the bridge model is point rotationally symmetric in the bridges center, only the first eleven pontoons are displayed. The roughness height of the concrete pontoons is taken 0.001 m [CGZ14]. Figure J.10 shows the diameters of the pontoons in the bridge model.

Parameter	Value
Flow courant number	200

Explicit relaxation factors	
Pressure	1
Momentum	1

Under-relaxation factors	
Density	1
Body forces	1
Turbulent kinetic energy	0.8
Specific dissipation rate	0.8
Turbulent viscosity	1

Table J.4: Solution controls used in the Ansys Fluent program.

Parameter	Value
Continuity	0.001
x-velocity	0.001
y-velocity	0.001
z-velocity	0.001
k	0.001
ω	0.001

Table J.5: Convergence criteria used in the Ansys Fluent program.

Pontoon number	Diameter [m]	Depth [m]
1	30	-73.13
2	36	-88.80
3	36	-99.83
4	36	-110.5
5	36	-119.4
6	36	-129.5
7	42	-109.8
8	42	-123.0
9	42	-120.6
10	42	-133.1
11	52	-133.5

Table J.6: Pontoon diameter and depth.

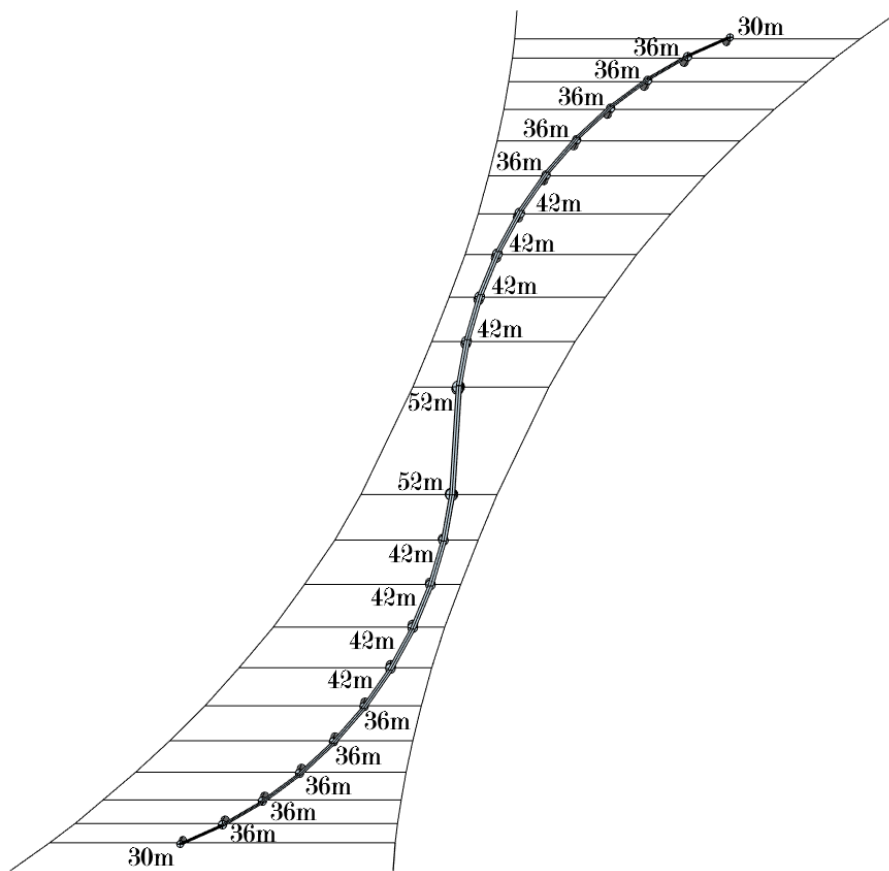


Figure J.10: Pontoon diameter displayed in the bridge model.

J.3.2 'Semi-2D' analysis

The 'semi-2D' analysis is an analysis in which the flow of a fluid layer of unit height 1 m is modelled around a stationary cylinder with the same modelled height. The main advantage of this analysis is the size reduction of the modelled volume and thus a much shorter computation time. Therefore, a quick indication of the cross-flow loading frequency can be made to compare to the pontoon modal eigenfrequencies.

J.3.2.1 Set-up

Since a flow volume with a height of 1 m is used, the fluid velocity is taken as constant across the height of the volume. The value chosen for the velocity is 1.27 m s^{-1} , or the measured value at a depth of 10 m below the water surface. The analysis is performed for the four different pontoon diameters present in the model, as shown in Table J.6 and Figure J.10.

An example of the mesh used in these analyses is shown in Figure J.11 and the mesh parameters used to generate the meshes are shown in Table J.7.

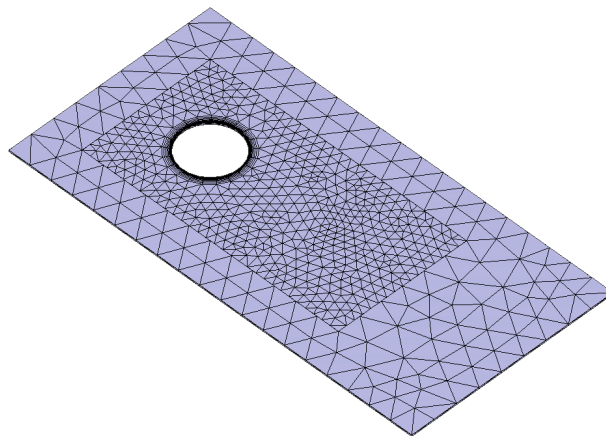


Figure J.11: Mesh for the 2D analysis of a 36m diameter pontoon.

Parameter	Value
Element shape	Tetrahedrons

Boundary layer	
Define by	First layer thickness
First layer thickness	0.1 m
Maximum layers	14
Growth rate	1.2

Size controls inner volume	
Max element face size	8 m

Size controls outer volume	
Max element face size	18 m

Table J.7: Mesh parameters used for the 2D mesh.

J.3.2.2 Results

The results are in terms of the cross-flow force, examples of the output cross flow loading are shown in Figures J.12 and J.13.

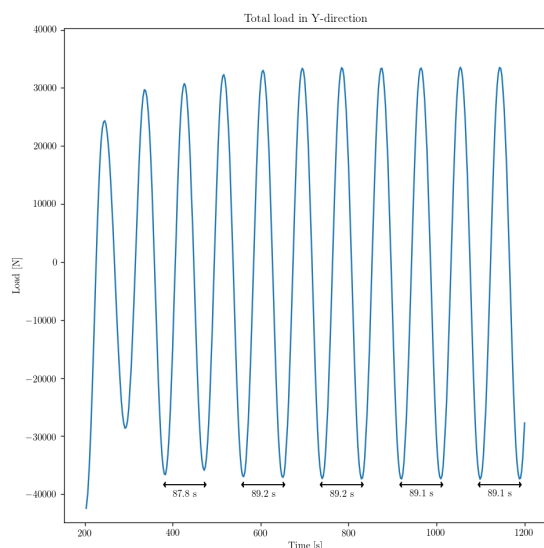


Figure J.12: Resulting cross flow loading for a 36m diameter pontoon shown from 200 s to 1200 s.

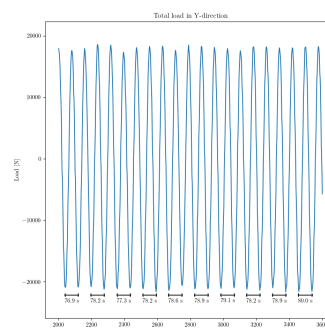


Figure J.13: Resulting cross flow loading for a 30m diameter pontoon shown from 2000 s to 3600 s.

Table J.8 shows the first two modal eigenperiods for the first 11 pontoons and the load period results calculated with Fluent. The loading periods close to one of the two first eigenperiods of the corresponding pontoon are shown in bold. It should be noted that some loading periods also correspond to eigenperiods of other pontoons - which may cause problems since the pontoons are connected through the bridge deck.

Pontoon number	Diameter	First eigenperiod [s]	Second eigenperiod [s]	"Semi-2D" VIV load period [s]
1	30 m	79.167	57.187	78.9
2	36 m	96.987	59.388	89.1
3	36 m	110.123	67.436	89.1
4	36 m	122.226	75.277	89.1
5	36 m	125.271	83.525	89.1
6	36 m	128.881	89.194	89.1
7	42 m	130.616	89.712	104.0
8	42 m	131.444	92.492	104.0
9	42 m	133.908	96.640	104.0
10	42 m	132.461	100.173	104.0
11	52 m	137.071	106.649	136.6

Table J.8: Pontoon eigenfrequencies and "Semi-2D" VIV load periods.

J.3.2.3 Conclusions

The results clearly show that the load periods for a pontoon in a flow with velocity 1.27 ms^{-1} are near one of the two eigenperiods of four pontoons. Since this flow velocity is found in the inward current velocity profile, there is at least part of the pontoon loaded at the frequency displayed in the Table J.8 and it can be stated that the pontoons appear sensitive to vortex induced vibrations. It may also be that other load periods are too close to the pontoon eigenperiods due to the pontoon fluid interaction described in section J.1, but that is not certain until a coupled analysis is performed.

J.3.3 Wake effect influence

The 'wake effect' is the influence the 'wake' of a pontoon 'in front', in terms of the fluid flow direction, of a pontoon has on the loading the current applies to that pontoon. To investigate this influence, a 'semi-2D' analysis is set up with a fluid flow volume height of 1 m in which multiple pontoons are modelled spaced at the same distance as in the complete model. The output cross-flow loading is compared to the 'semi-2D' analysis for a single pontoon of the same diameter. Figure J.14 displays the area investigated in this analysis and Figure J.15 displays the model used for the analysis.

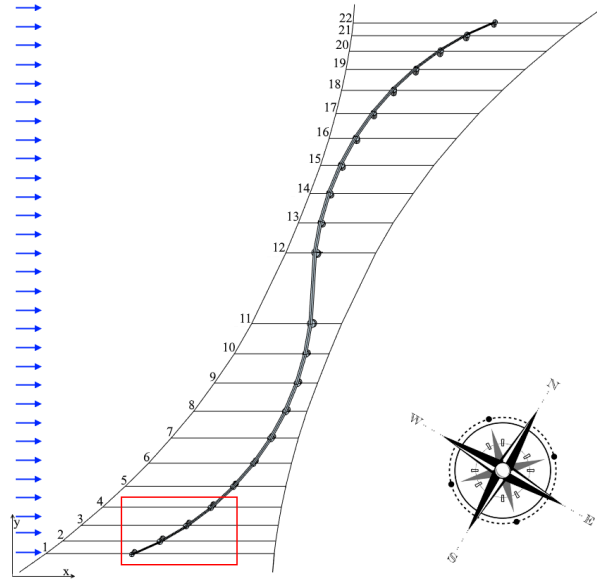


Figure J.14: The red box indicates the model area investigated for wake effects.

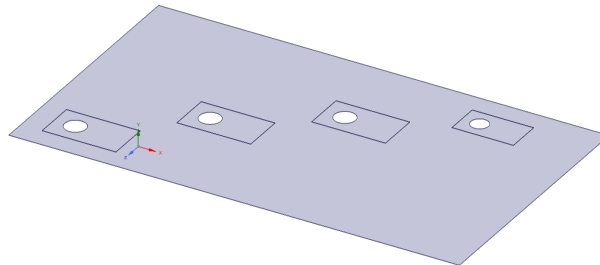


Figure J.15: Model used for the wake effects analysis. The bottom pontoon has a 30m diameter, the others a 36m diameter.

J.3.3.1 Set-up

Table J.9 displays the meshing properties used for the wake effects analysis and Figure J.16 displays the mesh visually. The pontoons are loaded by the 1.27 m s^{-1} current measured at a depth of 10 m, which is constant across the flow volume height.

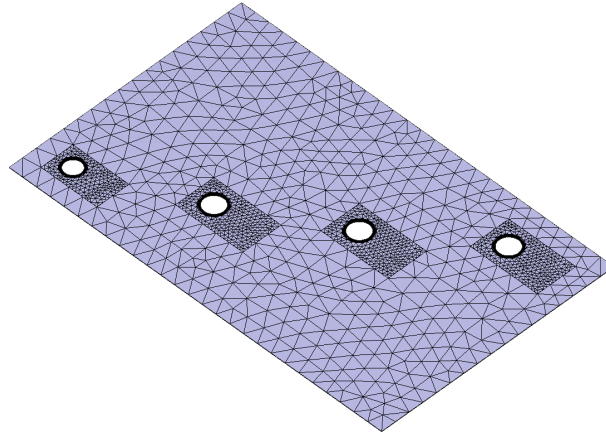


Figure J.16: Mesh used in the wake effect analysis.

Parameter	Value
Element shape	Tetrahedrons

Boundary layer	
Define by	First layer thickness
First layer thickness	0.1 m
Maximum layers	14
Growth rate	1.2

Size controls inner volume	
Max element face size	6 m

Size controls outer volume	
Max element face size	26 m

Table J.9: Mesh parameters used for the wake effect analysis.

J.3.3.2 Results

A first visual inspection of the results is depicted in Figures J.17. These figures show the magnitude of the flow velocity at two moments in the transient simulation. In both these Figures it is visible that part of the wake of the pontoons in 'front' of the others interacts with the flow field around these pontoons.

To quantify the interaction visible in the earlier figures, results in terms of the cross-flow loading from the 'semi-2D' single pontoon analysis are compared to the results obtained in this analysis. Figure J.18 displays the results of a 'semi-2D' analysis on a single 36 m diameter pontoon and the result obtained in this analysis for the second pontoon.

The results for all pontoons are displayed in Tables J.10, J.11 and J.12. As is expected, both the load period and load amplitude for the first pontoon in line remains unchanged. Both values due, however, change for the other pontoons in the analysis.

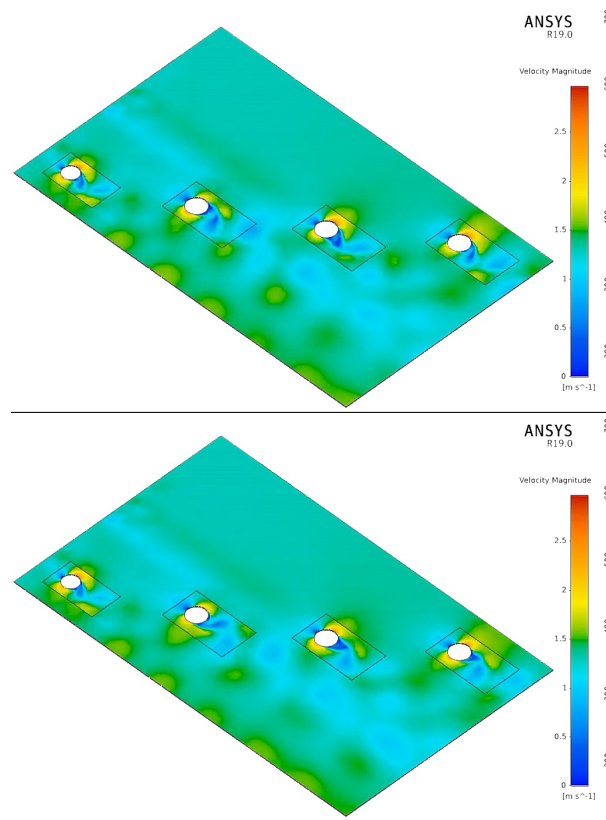


Figure J.17: Flow velocity magnitude at two time points in the wake effect analysis.

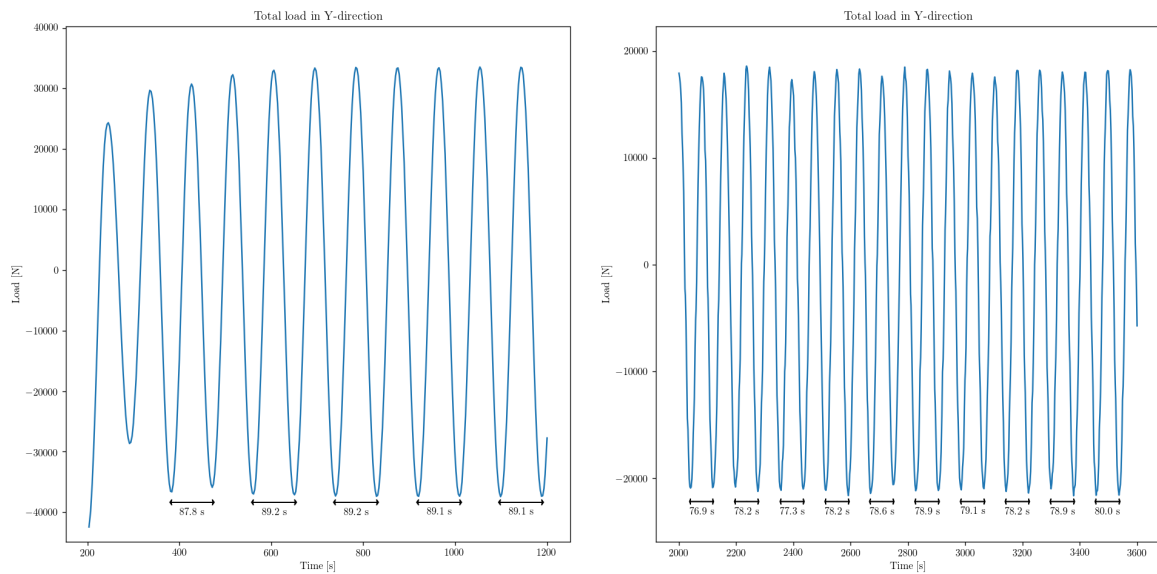


Figure J.18: Cross flow load for a single 36 m diameter pontoon (left) and the cross flow load for the second pontoon with the same diameter from the wake effect analysis (right).

Pontoon number	Diameter	"Semi-2D" VIV load period [s]	Wake effect load period [s]	Percentage difference
1	30 m	78.9	78.9	0 %
2	36 m	89.1	103.2	15.8 %
3	36 m	89.1	103.4	16.0 %
4	36 m	89.1	102.8	15.4 %

Table J.10: Change in VIV load periods due to wake effects.

Pontoon number	Diameter	"Semi-2D" VIV load amplitude [kN]	Wake effect load amplitude [kN]	Percentage difference
1	30 m	36	36	0 %
2	36 m	64	56	14.3 %
3	36 m	64	60	6.2 %
4	36 m	64	58	10.3 %

Table J.11: Change in VIV load amplitudes due to wake effects.

Pontoon number	Diameter	First eigenperiod [s]	Second eigenperiod [s]	"Wake effect load period [s]
1	30 m	79.167	57.187	78.9
2	36 m	96.987	59.388	103.2
3	36 m	110.123	67.436	103.4
4	36 m	122.226	75.277	102.8

Table J.12: Pontoon eigenperiods and "Semi-2D" VIV load periods due to wake effects.

J.3.3.3 Conclusions

Based on both the visual representation in terms of the flow velocity magnitude and the resulting calculated loads there is a wake effect present in the part of the model analysed. The wake effect provides, on average, a -10% decrease in the cross-flow load amplitude for pontoons effected by the wake of preceding pontoon. This is a positive effect. The average increase of about 15% of the load period is not necessarily a positive effect since it moves the load frequency away from the second eigenperiods of the pontoons, which are between 59.4 s and 75.3 s , but towards the first eigenperiods of the pontoons, which are between 97 s and 122.2 s . Therefore the results of this analysis should be taken as is, an on average -10% decrease in cross-flow loading and a 15% increase in cross-flow load periods.

J.3.4 3D analysis

The 'semi-2D' analysis performed in section J.3.2 showed that the pontoons show sensitivity to vortex induced vibrations. Therefore a more detailed, full 3D analysis of stationary pontoons in 3D flow is performed to see if the sensitivity can also be observed in a model closer to reality. Figure J.19 gives a visual representation of a 3D model used to calculate the cross-flow loading in Fluent.

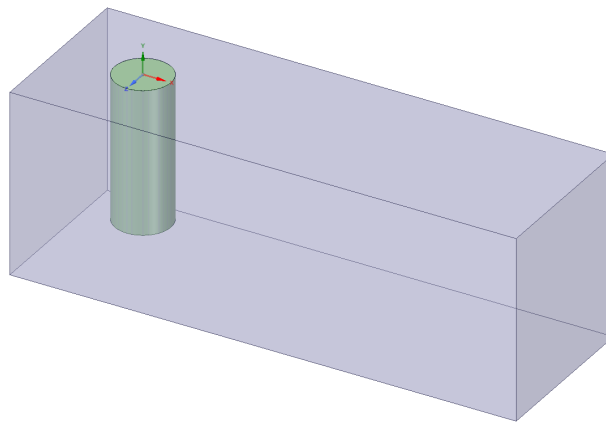


Figure J.19: 3D Model for a 52 m diameter pontoon in a 3D fluid volume.

J.3.4.1 Set-up

The 3D analyses are performed for four pontoons out of the twenty-two, their properties are displayed in Table J.13. This is done because 3D flow calculations take a long time and only performing the calculation for four pontoons saves time. The only relevant variable different between the pontoons chosen and other pontoons of the same diameter is the draught to which the pontoons reach under the water level. The assumption is made that dividing the total cross-flow load on pontoons by their length under water and applying this distributed load to the pontoons is, still, an accurate representation of reality. This assumption is put to the test in section J.3.5.

Pontoon number	Diameter	Draught [m]	First eigenperiod [s]	Second eigenperiod [s]
1	30 m	73.13	79.167	57.187
6	36 m	129.5	128.881	89.194
10	42 m	133.1	132.461	100.173
11	52 m	133.5	137.071	106.649

Table J.13: Characteristics of pontoons used for the 3D analysis.

The current profile used for the 3D analysis is depicted in Figure J.20, in which the measured values, power law curve fit and truncated velocity profile are shown on the right and the representation of the truncated velocity for the flow volume in Fluent using vectors is shown on the left.

The current profile is programmed into the Fluent calculation using User Defined Functions (UDF) programmed in C++. They can be compiled using Microsoft Visual Studio and added to Fluent. One

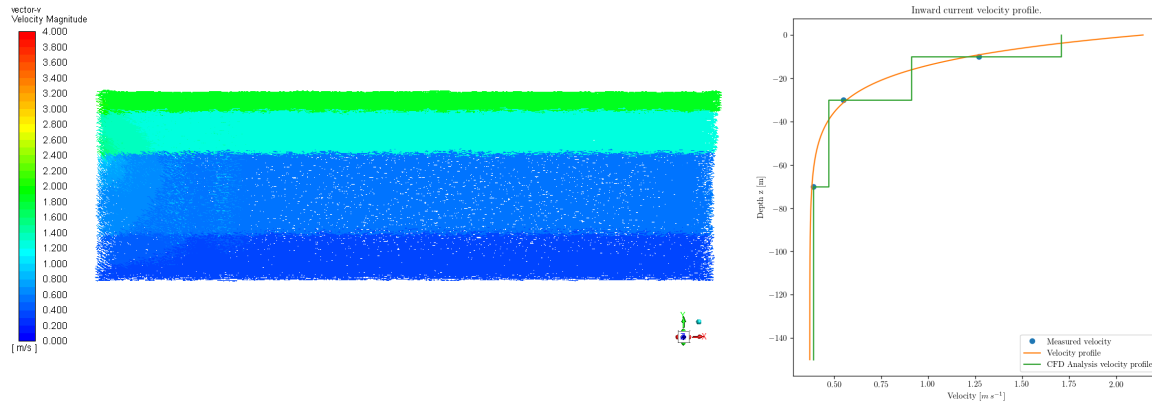


Figure J.20: Velocity vector representation of the 3D current profile for the flow volume in Fluent (left) and the measured values, power law curve and truncated profile (right).

of the functions defines the velocity at the fluid flow inlet, the code for this function is shown in Figure J.21. The input into Fluent is shown in Figure J.22

```
#include "udf.h"

DEFINE_PROFILE(inlet_x_velocity, thread, position)
{
    real x[ND_ND]; /* this will hold the position vector */
    real y, v_in;
    face_t f;
    real h[3] = {-10, -30, -70}; /* inlet height in m */
    real v[4] = {1.84, 1.27, 0.55, 0.39};

    begin_f_loop(f, thread)
    {
        F_CENTROID(x, f, thread);
        y = x[1]; /* y coordinate */
        v_in = (y > h[0]) ? v[0] : (y > h[1]) ? v[1] : (y > h[2]) ? v[2] : v[3];
        F_PROFILE(f, thread, position) = v_in;
    }
    end_f_loop(f, thread)
}
```

Figure J.21: User Defined Function to define the velocity conditions for the fluid volume inlet in Fluent.

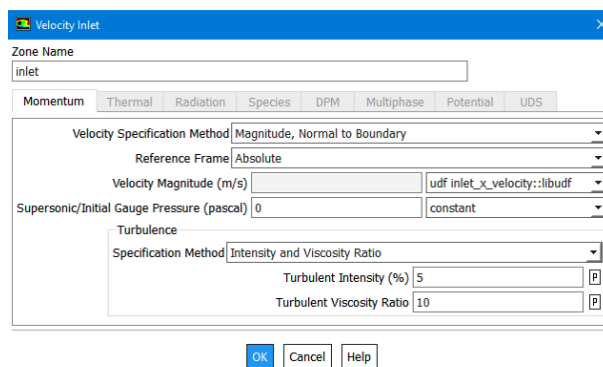


Figure J.22: Setting the inlet velocity profile to the UDF defined in Figure J.21.

The other UDF defines an initial condition in which the fluid flow for the entire volume is set. This function is shown in Figure J.23. The input into Fluent is shown in Figure J.24.

```
#include "udf.h"

DEFINE_INIT(velocity,d)
{
    cell_t c;
    Thread *t;
    real x[ND_ND];
    real y;

    real v_p;

    real h[3] = {-10, -30, -70}; /* inlet height in m */
    real v[4] = {1.84, 1.27, 0.55, 0.39};
    /* loop over all cell threads in the domain */
    thread_loop_c(t,d)
    {
        /* loop over all cells */
        begin_c_loop_all(c,t)
        {
            C_CENTROID(x,c,t);
            y = x[1]; /* y coordinate */

            v_p = (y > h[0]) ? v[0] : (y > h[1]) ? v[1] : (y > h[2]) ? v[2] :
                v[3];

            C_U(c,t) = v_p;
        }
        end_c_loop_all(c,t)
    }
}
```

Figure J.23: User Defined Function to define the initial velocity conditions for the fluid volume in Fluent.

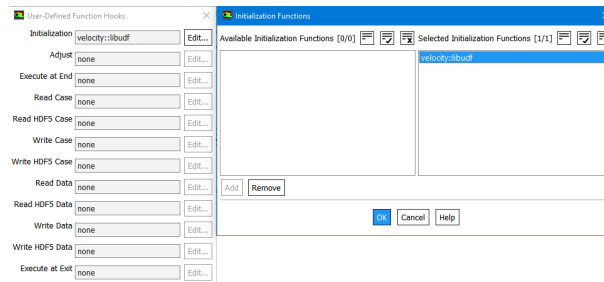


Figure J.24: Setting the initial velocity profile to the UDF defined in Figure J.23.

A visual depiction of the mesh used for Pontoon number 1, with properties as shown in Table J.13, is given in Figure J.25. The mesh parameters used for these analyses are shown in Table J.14.

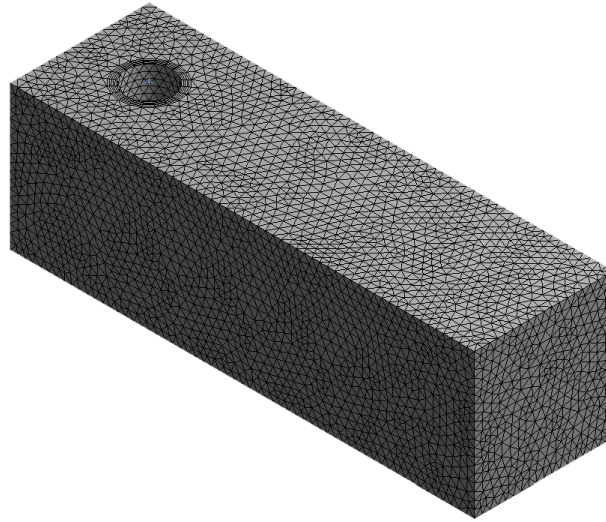


Figure J.25: Mesh for pontoon 1.

Parameter	Value
Element shape	Tetrahedrons

Boundary layer	
Define by	Smooth transition
Transition ratio	0.21
Maximum layers	7
Growth rate	1.05

Size controls Pontoon 1	
Max element face size	5 m
Size controls Pontoon 6, 10, 11	
Max element face size	6 m

Table J.14: Mesh parameters used for the 3D analysis.

J.3.4.2 Results

The resulting velocity magnitude for Pontoon 11 at 2880s into the simulation is depicted in Figure J.26 in a vector representation for the entire flow volume. The pontoon itself is visible in top left, with its low velocity wake trailing behind. In the bottom right the higher velocity region is shown across the height of the flow volume. In this area it is visible that the frequency of vortex shedding is different across the pontoon height, as fast-flowing region is in different cross-flow positions across the height of the flow volume. This will lead to different frequencies being visible in the time plot of the total cross-flow force.

Figure J.27 depicts the total force on Pontoon 11 during the 3D analysis. It is obvious that multiple frequencies cross-flow loading are present. To visualize the energy content per frequency and determine the primary frequency of cross-flow loading, spectra are created using the FFT algorithm [CT65]. This is depicted in Figure J.28.

Using the spectra the primary frequencies of cross-flow loading can be determined. These are shown in Table J.15.

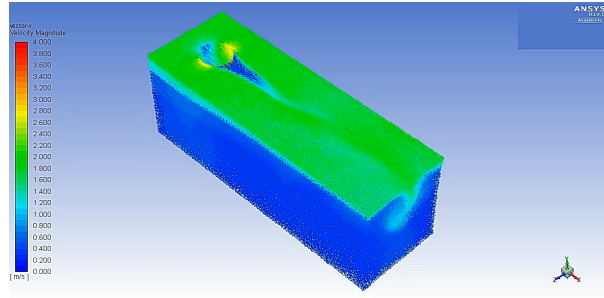


Figure J.26: Pontoon 11 velocity magnitude vector representation at 2880 s into the transient 3D analysis.

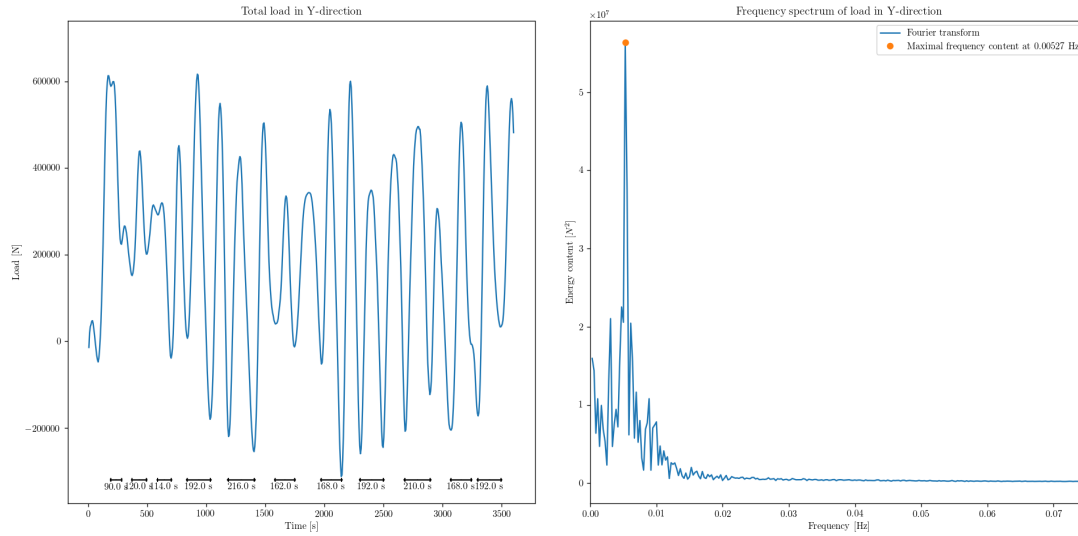


Figure J.27: Pontoon 11 total cross-flow load Figure J.28: Spectrum of the cross-flow load at plotted against time. pontoon 11.

Pontoon number	Diameter	First eigenperiod [s]	Second eigenperiod [s]	3D VIV main loading period [s]
1	30 m	79.167	57.187	142.9
6	36 m	128.881	89.194	166.7
10	42 m	132.461	100.173	200.4
11	52 m	137.071	106.649	189.8

Table J.15: Pontoon eigenfrequencies and 3D VIV load periods.

J.3.4.3 Conclusions

At first sight the results of the 3D analysis seem to indicate that the pontoons are less sensitive to vortex induced vibrations than may have been expected from the results of the 'semi-2D' analysis. The primary cross-flow loading periods have moved quite a bit away from the corresponding pontoons first two eigenperiods. However, it must be stated that not all energy transferred from the current to the cross-flow loading is transferred in the primary loading frequency. There are peaks at other frequencies which may correspond to other modal eigenfrequencies of the pontoons. This is shown in Figure J.29.

The main indication that these results only show a larger sensitivity to vortex induced vibrations is given when the eigenfrequencies of the entire bridge structure are taken into account. The first ten eigenfrequencies and periods of the entire bridge structure are depicted in Table J.16.

When comparing the first eigenfrequency of the entire bridge to the main loading periods calculated in this analysis it becomes obvious that the main loading period for pontoon 6 coincides with the bridge structure's first eigenperiod. Under the assumption that the cross-flow loading for different pontoon lengths does not change significantly, this means that ten out of the twenty-two pontoons will be subject

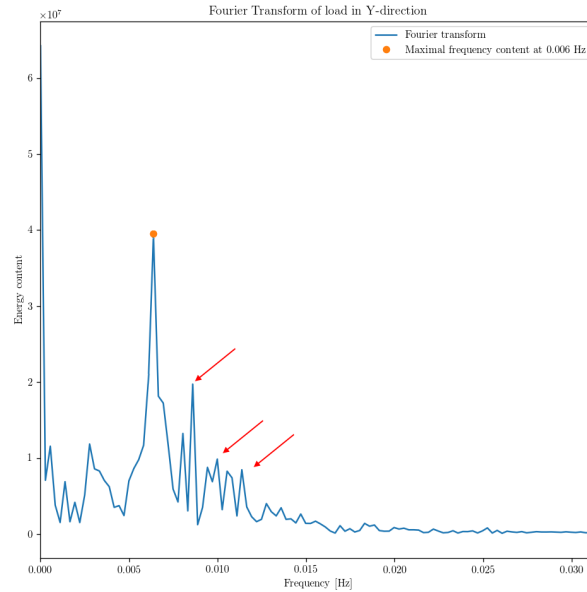


Figure J.29: Pontoon 6 spectrum of cross-flow loading. with additional peaks indicated

Mode number	Eigenfrequency [Hz]	Eigenperiod [s]
1	0.006231	160.5
2	0.008432	118.6
3	0.008974	111.4
4	0.009476	105.5
5	0.009677	103.3
6	0.009933	100.7
7	0.010019	99.8
8	0.010107	98.9
9	0.010318	96.9
10	0.010321	96.9

Table J.16: Bridge system eigenfrequencies of the first ten modes.

to loading at the structure's first eigenfrequency. This indicates a very high sensitivity to vortex induced vibrations due to the current as present at the bridge location. Furthermore, as a coupled analysis may show, the range of load frequencies which are shifted to a frequency closer to eigenfrequencies of the bridge structure may be large enough to 'capture' even more of the load frequencies found.

J.3.5 3D draught comparison

This analysis is performed to put the assumption that dividing the total cross-flow load on pontoons by their length under water and applying this distributed load to the pontoons is an accurate representation of reality to the test. The analysis is performed by comparing the results of a 3D analysis for two pontoons of the same diameter and different draughts.

J.3.5.1 Set-up

The pontoons used for this analysis are shown in Table J.17.

The flow velocity profile used is the same as used in the 3D analysis in section J.3.4. The mesh parameters used for both analyses are depicted in Table J.18.

Pontoon number	Diameter	Draught [m]	First eigenperiod [s]	Second eigenperiod [s]
2	36 m	88.80	96.99	59.39
6	36 m	129.5	128.881	89.194

Table J.17: Characteristics of pontoons used for the 3D analysis.

Parameter	Value
Element shape	Tetrahedrons
Boundary layer	
Define by	Smooth transition
Transition ratio	0.21
Maximum layers	7
Growth rate	1.05
Size controls	
Max element face size	6 m

Table J.18: Mesh parameters used for the draught comparison 3D analysis.

J.3.5.2 Results

The results in terms of the total cross-flow force plotted against time are depicted in Figures J.30 and J.31.

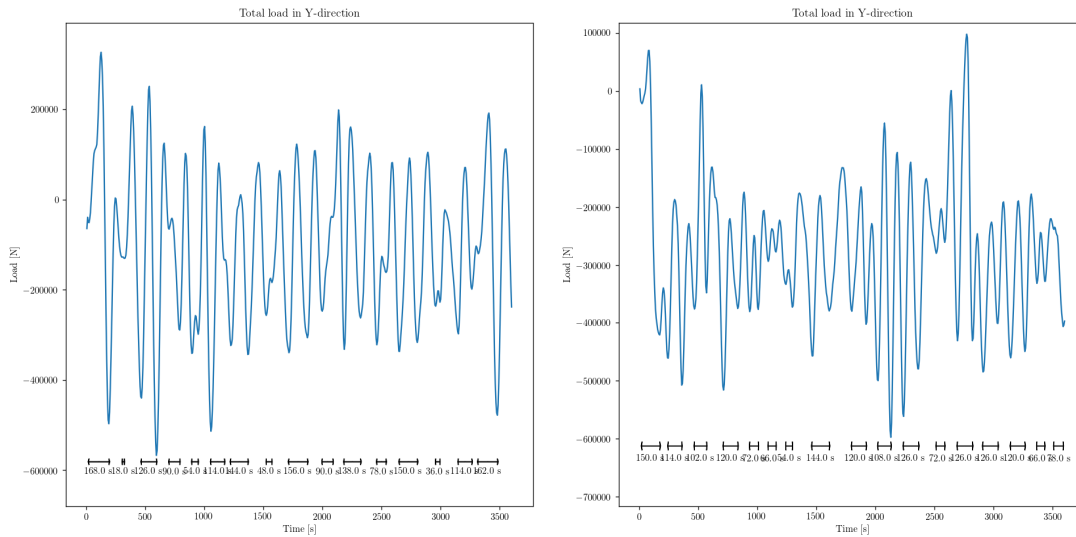


Figure J.30: Pontoon 6 total cross-flow load plotted against time. Figure J.31: Pontoon 2 total cross-flow load plotted against time.

To directly compare the total cross-flow time histories is futile, therefore the frequency spectra of both loads are plotted together to compare them. This is shown in Figure J.32, in which load 1 corresponds to pontoon 6 and load 2 to pontoon 2. Table J.19 shows different error scores for larger data sets as used for the comparison of the spectra.

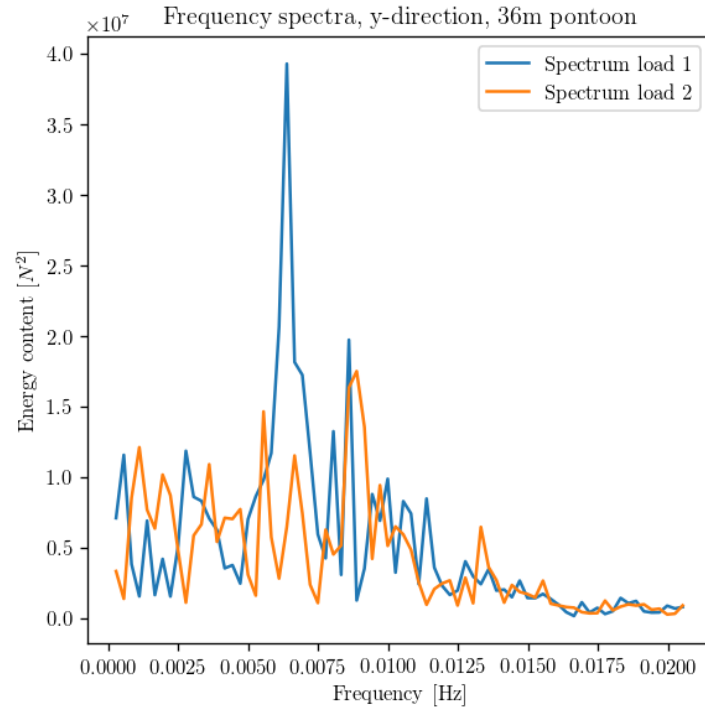


Figure J.32: Comparison of the cross-flow load spectrum for pontoon 6 (load 1) and pontoon 2 (load 2).

Error score	Value	Best possible value
R2 score	-0.624	1.0
Explained variance score	-0.623	1.0
Root mean squared error score	$6.678 \cdot 10^6$	0.0

Table J.19: Different metrics to compare data set similarity used on the cross-flow load spectra for pontoon 2 and 6.

J.3.5.3 Conclusions

Visual comparison of the spectra shown in Figure J.32 shows a large discrepancy in the location of the peaks - and thus in the energy content per load frequency. The error scores corroborate this, negative values for R2- and explained variance scores and a root mean squared error score of magnitude 10^6 , which is about as big as half of the biggest peak contained in the spectrum for pontoon 2, indicate very large differences in data sets that can't be explained by just the lower energy content due to the lower draught of pontoon 2. So it must be concluded that the assumption that the total load on a pontoon with a larger draught can be scaled to be used on a pontoon with a smaller draught is not valid for all draughts. Therefore it is recommended to further investigate the difference pontoon draught makes on cross-flow loading. Perhaps this means that all twenty-two pontoons must be included separately in vortex induced vibration analysis.

J.3.6 Coupled analysis using decoupling springs

To model the fluid-structure interaction, an attempt is made to calculate the fluid using a dynamic mesh in Fluent and the stiffness for the coupling springs calculated in appendix I as the boundary conditions. A dynamic mesh means that the mesh in the fluid flow region deforms according to the motion of the wall area designated as capable of movement. This analysis is performed to test this method of coupled analysis.

J.3.6.1 Set-up

The flow velocity profile used is the same as used in the 3D analysis in section J.3.4. The mesh parameters used for both analyses are depicted in Table J.20. It is clearly visible that the maximum mesh size is greatly increased compared to the maximum size set in the 3D analysis. This is due to the fact that problems arise when mesh element node movement between time steps is greater than the element size and the elements get a negative volume. To solve these problems, either the mesh element size has to be increased, or the time step decreased. An attempt has been made to prevent this problem by changing both. Therefore the time steps in this analysis are decreased to 0.5 s, while the simulation time is set at 1800 s.

Parameter	Value
Element shape	Tetrahedrons

Boundary layer	
Define by	Smooth transition
Transition ratio	0.21
Maximum layers	7
Growth rate	1.05

Size controls	
Max element face size	26 m

Table J.20: Mesh parameters used for the draught comparison 3D analysis.

A single coupling spring is used for this analysis in the cross-flow direction. Its spring stiffness is taken from the calculation performed in appendix I. The static value is taken for joint 'P63' located in pontoon 6.

Degree of freedom	Stiffness
cross-flow (y in SACS, z in Fluent)	26.02 kN m ⁻¹

Table J.21: Coupling spring stiffness pontoon 6.

J.3.6.2 Results

The results of this analysis in terms of cross-flow loading are shown in Figure J.33.

Figure ?? shows a contour plot of the fluid velocity magnitude during the analysis.

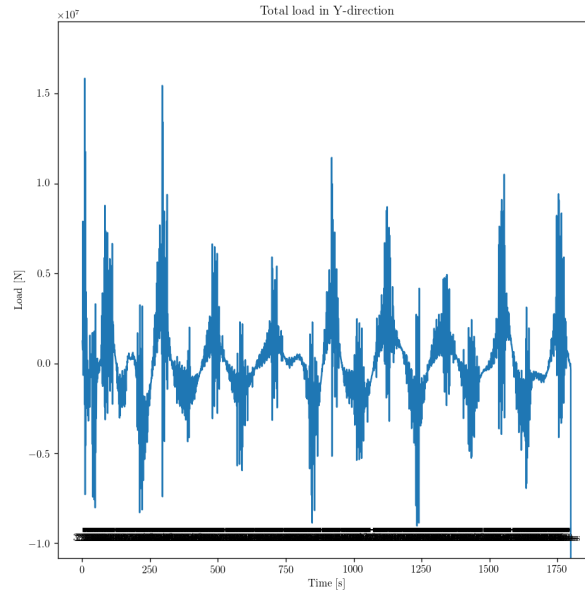


Figure J.33: Cross-flow load versus time for the dynamic mesh analysis of pontoon 6.

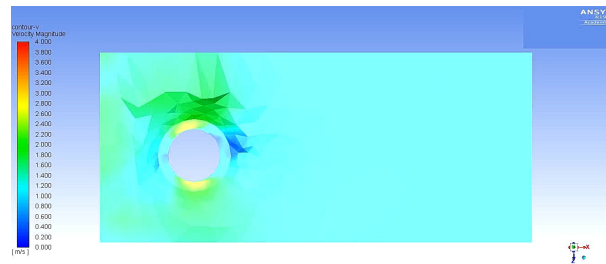


Figure J.34: Contour plot of the fluid velocity magnitude during the dynamic mesh analysis of pontoon 6.

J.3.6.3 Conclusions

The cross-flow loading calculated using this method displays huge peaks into values of magnitude 10^7 N. This is indicative of the time step being set too large.

Furthermore, the contour plot shows the irregular mesh pattern created during the analysis, the big 'jumps' in velocity magnitude between elements and the lack of a proper wake forming behind the pontoon. This is indicative of the mesh elements being too large.

Therefore it would be a logical step to decrease the time step and element size used for this analysis. However, this analysis of half the time span used in the other analyses already took approximately three times as long. Therefore, it is deemed this method of coupled analysis is not suitable for this study.

J.3.7 Coupled analysis

As the results of previous analyses clearly indicate that the bridge structure is sensitive to vortex induced vibrations, a coupled analysis is necessary to investigate the magnitude of the problem presented by vortex induced vibrations for the bridge structure.

J.3.7.1 Set-up

To investigate motion caused by vortex induced vibrations in the bridge structure, a coupled analysis is necessary.

First, the methodology of the coupled analysis performed in this thesis is presented. It is shown visually in Figure J.35.

The steps taken in the process are the following;

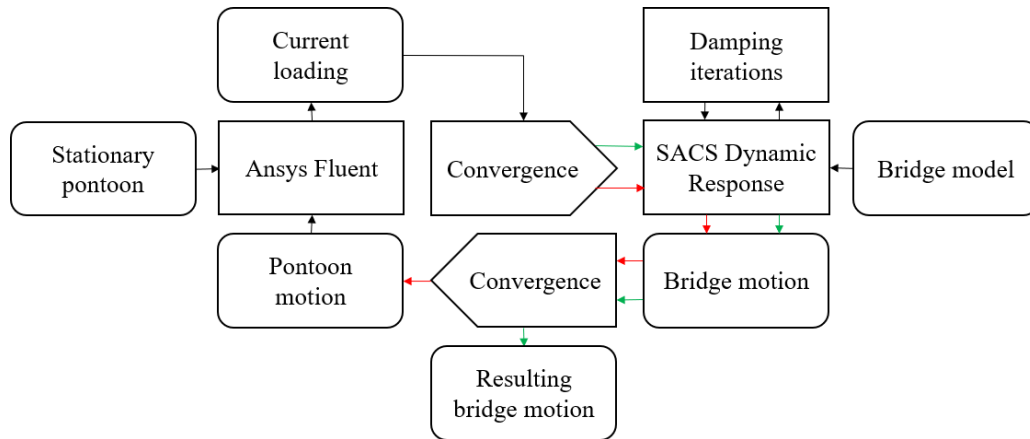


Figure J.35: Methodology for the coupled vortex induced vibration analysis.

First a 3D analysis is performed for four stationary pontoons as described in section J.3.4.

The resulting total cross-flow current load is transformed into distributed loading and applied to all pontoons in the complete bridge model using the Dynamic Response module. Reference is made to section H.3.

The resulting bridge motion is then sent through structural damping iterations, which are explained in more detail in this section.

The velocity of the motion of the center of buoyancy of the pontoon in both cross- and inflow direction is then applied as a velocity boundary condition to the pontoon walls in the Fluent calculation.

From this point the iterations continue, with convergence checks on both the current loading and subsequent bridge motion.

If both have converged, the end result is reached: The bridge motion due to vortex induced vibration caused by the current at the bridge location.

To include the pontoon motion in the Ansys Fluent calculation, the option to include a boundary condition in the form of a User Defined Function is used. A User Defined Function (UDF) is a small program coded in C++. An example of two user defined function templates created to set the velocity boundary conditions for the pontoon walls for this analysis are shown in Figures J.36 and J.37. The assignment of these boundary conditions to the pontoon in Fluent is shown in Figure J.38.

```

#include "udf.h"

static real x_vib[<len_x_vib>] =<x_vib_params>;

DEFINE_PROFILE(x_velocity,thread,position)
{
    face_t f;

    int i = N_TIME;

    begin_f_loop(f, thread)
    {
        F_PROFILE(f, thread, position) = x_vib[i];
    }
    end_f_loop(f, thread)
}
  
```

Figure J.36: User Defined Function template to define the in-flow direction velocity boundary condition for the pontoon walls in Fluent.

The structural damping iterations used for this analysis differ from the damping iterations used in section D. The methodology is the following;

```
#include "udf.h"

static real z_vib[<len_z_vib>] = <z_vib_params>;

DEFINE_PROFILE(z_velocity,thread,position)
{
    face_t f;

    int i = N_TIME;

    begin_f_loop(f, thread)
    {
        F_PROFILE(f, thread, position) = z_vib[i];
    }
    end_f_loop(f, thread)
}
```

Figure J.37: User Defined Function template to define the cross-flow direction velocity boundary condition for the pontoon walls in Fluent.

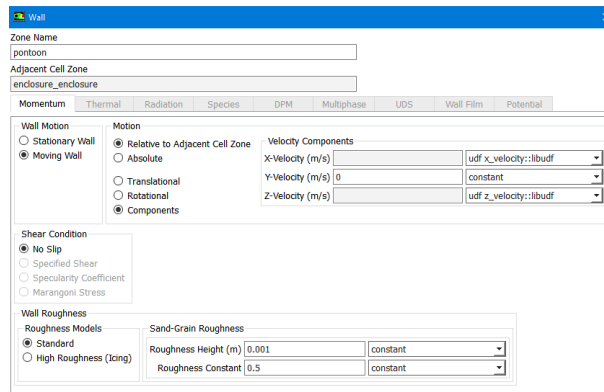


Figure J.38: Setting the pontoon boundary condition to the UDF's defined in Figures J.36 and J.37.

First the calculated displacements are imported into a Python program, together with the displacements calculated for the Steady State cases described in section D.

The maximum total displacement per node in the bridge model are compared using three error metrics; The R2-score, the Explained Variance score and the Root Mean Squared Error score [DS98] [KEN83] [MGB74].

Based on the results of the error metric scores, a new damping value is chosen and the calculation is re-run in SACS. This is continued until the error scores are minimized and convergence is reached in terms of displacement.

The iterations as stated above are performed in this manner to save time- and since the hydrodynamic fluid damping is the most important source of damping for this calculation, the relative error introduced by the approximation of the structural damping through this method will be small.

J.3.7.2 Results

This analysis has not led to a converged result. The iterations were stopped once it became clear that the structure is highly sensitive to vortex induced vibrations and the displacements kept increasing per iteration. To illustrate this, Figure J.39 displays the displacement in in- and cross-flow direction for pontoon 11 for the four iterations performed. It is illustrated further in Figure J.40, which displays the cross-flow loading plotted versus time for the same pontoon for the four iterations performed. It is visible in these Figures that with each iteration the observed load amplitudes increase.

The minimum and displacement per iteration for the cross- and inflow direction considered in are shown in the tables in section J.3.7.3 for each pontoon. From these results it is clear that from the very first iteration all pontoons vibrate in the eigenfrequency of the first mode of vibration of the bridge structure

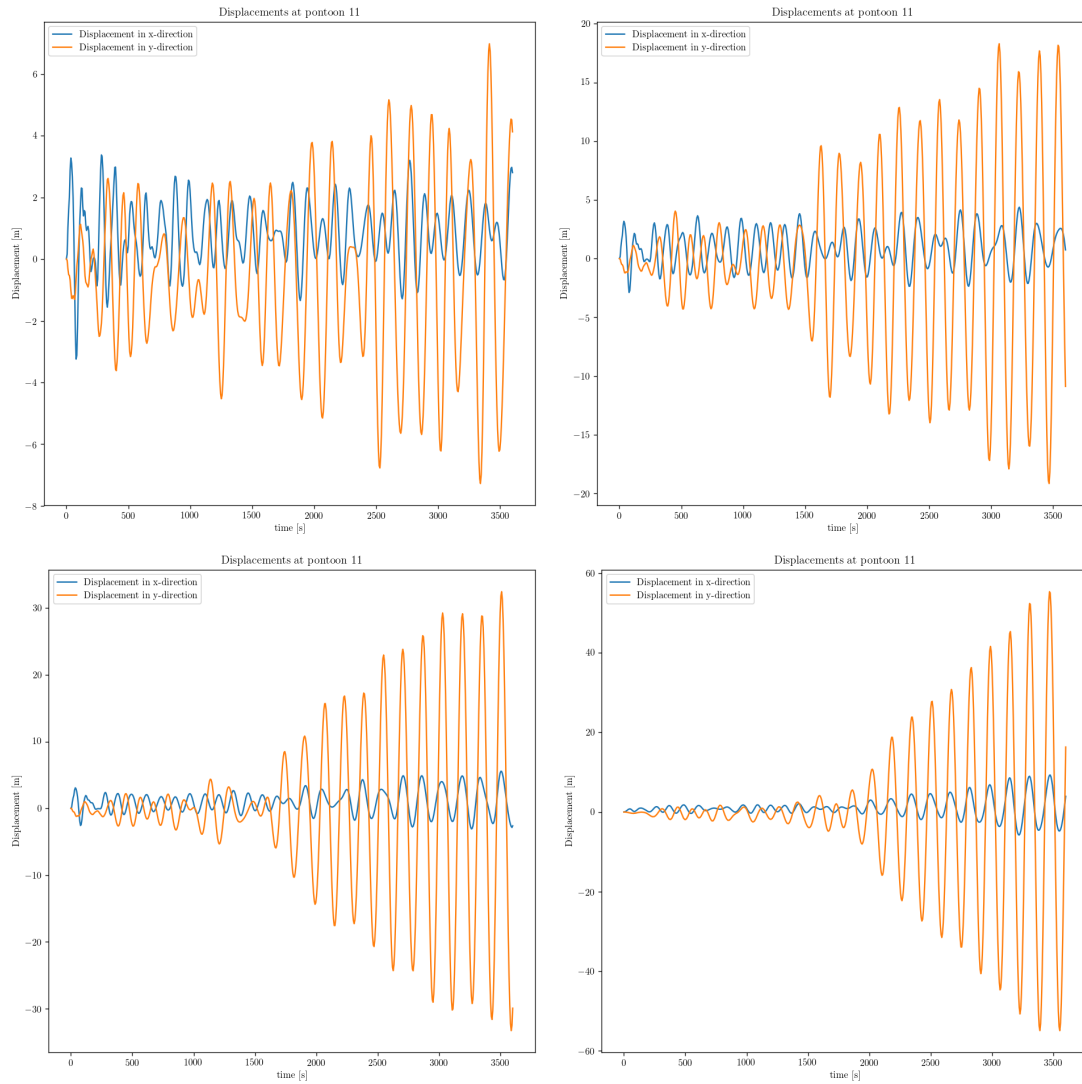


Figure J.39: Displacements plotted against time for pontoon 11 for the four coupled iterations performed.

in the cross-flow direction. By iteration four, the same can be said of the in-flow vibration frequency. Furthermore, it can be observed that the minimum and maximum cross- and in-flow displacements increase with each iteration.

The main frequencies of the cross-flow loading per pontoon diameter per iteration are shown in Table J.22. From this Table it is very clear that the fluid structure interaction has a big influence on the cross-flow loading frequency. In three iterations all cross-flow loading frequencies are moved to the frequency of cross-flow vibration of the pontoons, which coincide with the bridge structure's first modal eigenfrequency.

Diameter [m]	Iteration 1 [Hz]	Iteration 2 [Hz]	Iteration 3 [Hz]	Iteration 4 [Hz]
30	0.0072	0.0064	0.0061	0.0061
36	0.0064	0.0064	0.0064	0.0061
42	0.005	0.005	0.0064	0.0064
52	0.0053	0.0061	0.0061	0.0064

Table J.22: Cross flow load frequencies per pontoon diameter for four iterations

There is one result that indicates that a maximum may be reached in terms of the pontoon displacement and fluid forcing increasing each other with each iteration. It is found at pontoon 6, a 36 m diameter pontoon, at the tail end of the load calculation for iteration 4. The cross-flow loading for pontoon 6 in iteration 4 is depicted in Figure J.41. In this Figure it is clear that from about 3300 s, the cross-flow

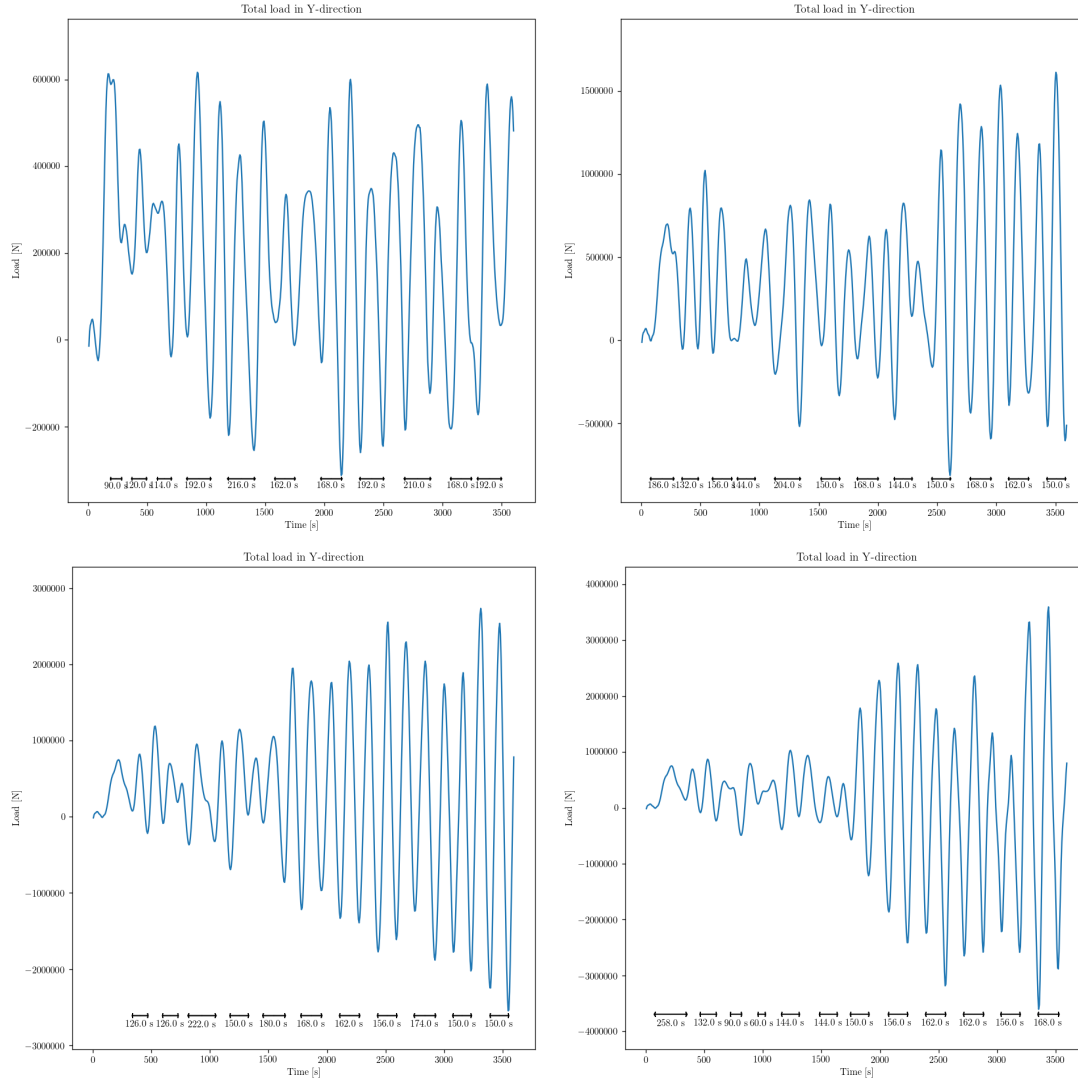


Figure J.40: Cross-flow loading plotted against time for pontoon 11 for the four coupled iterations performed.

load amplitude decreases sharply. When the velocity magnitude plot before this time period is reviewed it shows highly periodic vortex shedding, this is displayed in Figure J.42. Then from 3300 s first, the wake does not change sides and then a large disruption is visible, in which the wake separates from both sides of the pontoon. This is shown in Figure J.43. In these velocity magnitude plots, special attention is drawn to the red areas at the pontoon walls, and especially to the fact that they are visible in the first three images and is coloured yellow in the fourth image. This corresponds to the drop in cross-flow load amplitude observed in Figure J.41.

To see if the change in loading is visible in the displacement results, Figure J.44 displays the the displacement plot for pontoon 6 during iteration four. A visible flattening of the displacement increase with each cycle can be observed after 3300 s in the lower part of the plot.

This flattening, or in some cases even a slight decrease of the maximum deflection, from about 3300 s is observable in the displacements of all pontoons during iteration four. To illustrate this, Figure J.45 contains displacement plots for pontoons 1, 5, 10 and 12 during iteration four.

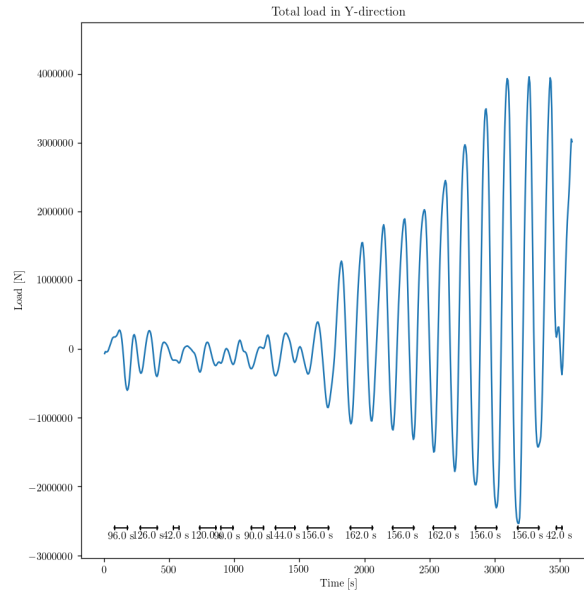


Figure J.41: Cross-flow loading plotted against time for pontoon 6 for the fourth coupled iteration performed.

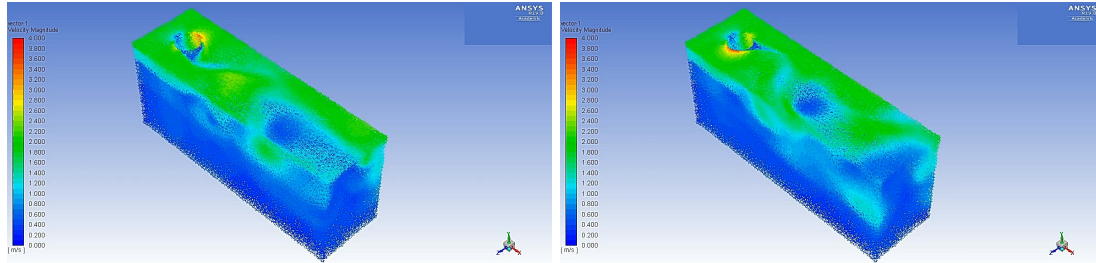


Figure J.42: Velocity magnitude plots for pontoon 6 showing the maximum and minimum periodic wake movement before 3300 s during iteration 4.

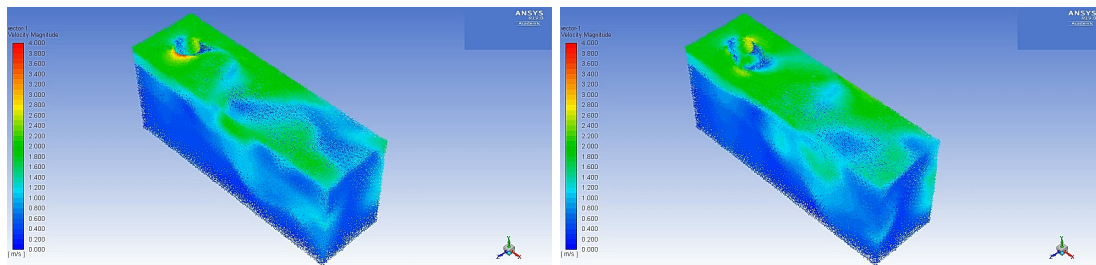


Figure J.43: Velocity magnitude for pontoon 6 plots showing the disruption of the periodic vortex shedding after 3300 s during iteration 4.

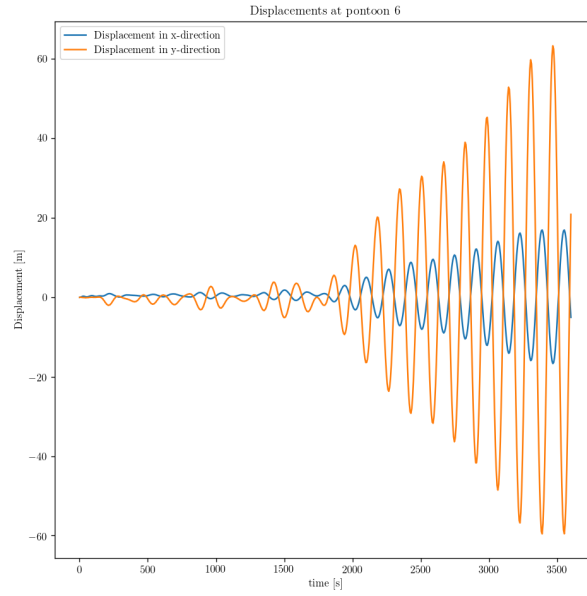


Figure J.44: Displacement plot for pontoon 6 during iteration four.

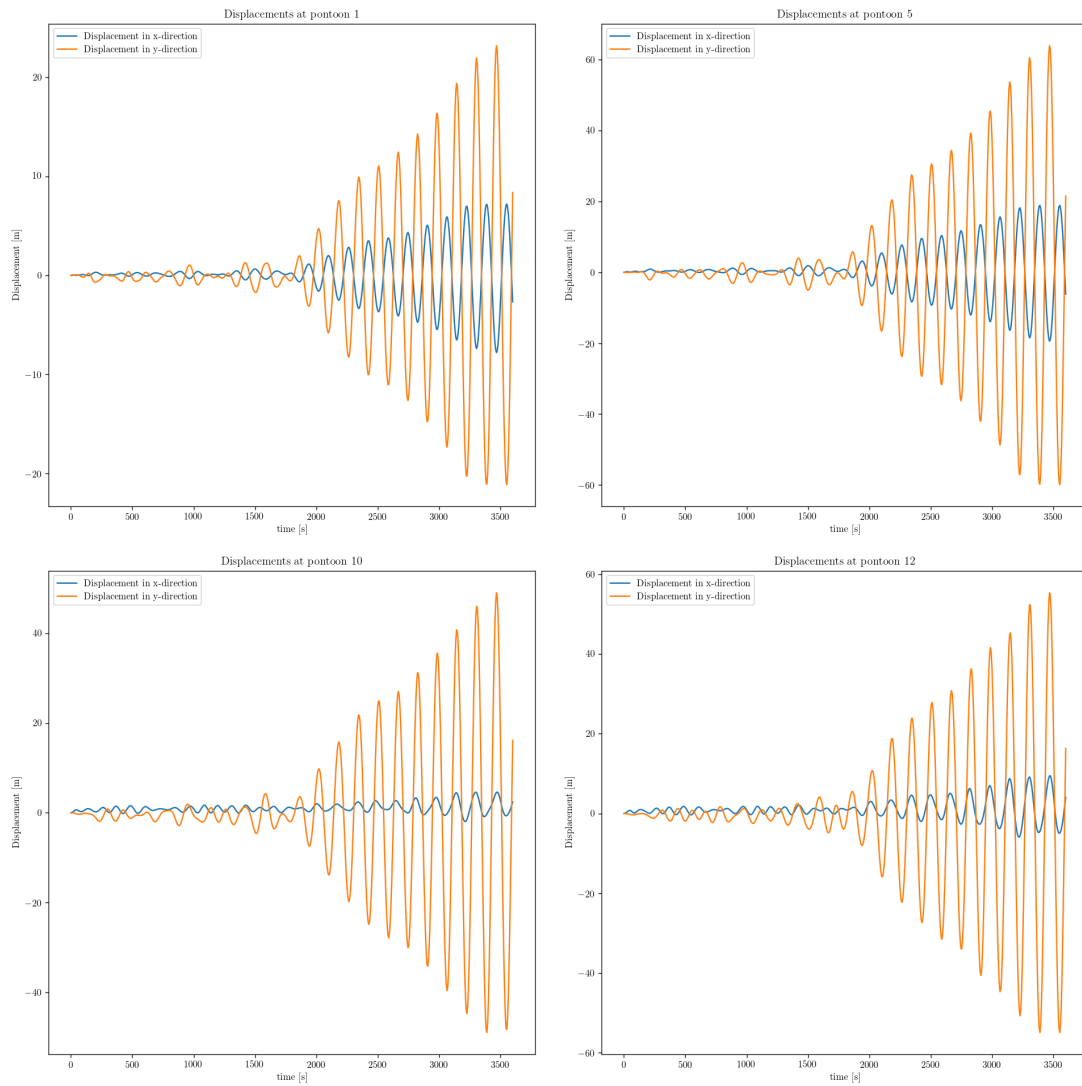


Figure J.45: Displacement plots for pontoons 1, 5, 10 and 12 during iteration four.

J.3.7.3 Displacement table

Pontoon Number	Iteration 1					
	Max u_y [m]	Min u_y [m]	Main freq. [Hz]	Max u_x [m]	Min u_x [m]	Main freq. [Hz]
1	2.533	-2.941	0.0061	1.062	-0.858	0.0061
2	4.283	-5.025	0.0061	1.767	-1.426	0.0061
3	5.648	-6.636	0.0061	2.379	-1.873	0.0061
4	6.627	-7.7	0.0061	2.725	-2.061	0.0061
5	6.987	-8.055	0.0061	2.75	-1.912	0.0061
6	6.781	-8.207	0.0061	2.585	-1.412	0.0061
7	6.563	-8.011	0.0061	2.293	-1.246	0.0061
8	5.216	-7.319	0.0061	2.244	-1.196	0.0064
9	5.644	-7.454	0.0061	2.655	-0.902	0.0083
10	5.606	-8.191	0.0061	2.944	-1.734	0.0083
11	6.986	-7.278	0.0061	3.38	-3.242	0.0083
12	6.979	-7.275	0.0061	3.372	-3.224	0.0083
13	5.613	-8.197	0.0061	2.912	-1.712	0.0083
14	5.668	-7.441	0.0061	2.621	-0.894	0.0083
15	5.221	-7.311	0.0061	2.219	-1.193	0.0064
16	6.564	-8.018	0.0061	2.252	-1.253	0.0061
17	6.816	-8.243	0.0061	2.562	-1.402	0.0061
18	7.022	-8.107	0.0061	2.746	-1.915	0.0061
19	6.658	-7.742	0.0061	2.729	-2.067	0.0061
20	5.681	-6.681	0.0061	2.389	-1.882	0.0061
21	4.304	-5.052	0.0061	1.777	-1.433	0.0061
22	2.515	-2.943	0.0061	1.068	-0.862	0.0061

Pontoon Number	Iteration 2					
	Max u_y [m]	Min u_y [m]	Main freq. [Hz]	Max u_x [m]	Min u_x [m]	Main freq. [Hz]
1	7.321	-7.111	0.0061	2.425	-2.486	0.0061
2	12.49	-11.873	0.0061	4.068	-4.173	0.0061
3	16.664	-15.736	0.0061	5.484	-5.57	0.0061
4	19.103	-18.256	0.0061	6.279	-6.267	0.0061
5	20.318	-19.647	0.0061	6.377	-6.117	0.0061
6	19.948	-19.549	0.0061	5.853	-5.131	0.0061
7	18.927	-19.685	0.0061	4.765	-3.571	0.0061
8	16.363	-17.363	0.0061	3.425	-2.031	0.0061
9	16.005	-17.196	0.0061	2.554	-0.786	0.0083
10	15.525	-16.357	0.0061	2.93	-1.469	0.0083
11	18.298	-19.156	0.0061	4.378	-2.881	0.0083
12	18.295	-19.151	0.0061	4.422	-2.865	0.0083
13	15.51	-16.35	0.0061	2.925	-1.449	0.0083
14	16.008	-17.192	0.0061	2.521	-0.762	0.0083

15	16.357	-17.349	0.0061	3.315	-1.933	0.0061
16	18.925	-19.701	0.0061	4.69	-3.499	0.0061
17	19.964	-19.57	0.0061	5.806	-5.091	0.0061
18	20.346	-19.694	0.0061	6.361	-6.105	0.0061
19	19.143	-18.317	0.0061	6.279	-6.267	0.0061
20	16.721	-15.81	0.0061	5.501	-5.583	0.0061
21	12.524	-11.92	0.0061	4.085	-4.187	0.0061
22	7.262	-7.082	0.0061	2.435	-2.493	0.0061

Pontoon Number	Iteration 3					
	Max u_y [m]	Min u_y [m]	Main freq. u_y [Hz]	Max u_x [m]	Min u_x [m]	Main freq. u_x [Hz]
1	12.985	-12.914	0.0064	4.417	-4.359	0.0064
2	22.29	-21.802	0.0064	7.459	-7.332	0.0064
3	29.597	-29.165	0.0064	10.104	-9.795	0.0064
4	33.427	-34.391	0.0064	11.608	-11.037	0.0064
5	35.71	-36.698	0.0064	11.739	-10.864	0.0064
6	35.392	-36.327	0.0064	10.549	-9.338	0.0064
7	33.775	-35.219	0.0064	8.357	-6.758	0.0064
8	29.68	-31.303	0.0064	5.545	-3.612	0.0064
9	29.168	-30.961	0.0064	3.078	-1.059	0.0064
10	27.463	-28.948	0.0064	2.88	-1.313	0.0086
11	32.463	-33.307	0.0064	5.562	-3.078	0.0064
12	32.455	-33.3	0.0064	5.656	-3.171	0.0064
13	27.444	-28.936	0.0064	3.032	-1.295	0.0086
14	29.153	-30.952	0.0064	2.923	-0.909	0.0061
15	29.666	-31.294	0.0064	5.35	-3.454	0.0064
16	33.786	-35.231	0.0064	8.212	-6.639	0.0064
17	35.445	-36.379	0.0064	10.459	-9.262	0.0064
18	35.799	-36.781	0.0064	11.707	-10.844	0.0064
19	33.54	-34.495	0.0064	11.608	-11.043	0.0064
20	29.728	-29.321	0.0064	10.137	-9.826	0.0064
21	22.371	-21.905	0.0064	7.494	-7.364	0.0064
22	12.911	-12.867	0.0064	4.437	-4.376	0.0064

Pontoon Number	Iteration 4					
	Max u_y [m]	Min u_y [m]	Main freq. u_y [Hz]	Max u_x [m]	Min u_x [m]	Main freq. u_x [Hz]
1	23.196	-21.137	0.0064	7.204	-7.806	0.0064
2	39.848	-36.358	0.0064	12.159	-13.115	0.0064
3	52.976	-47.94	0.0064	16.402	-17.516	0.0064
4	60.355	-55.446	0.0064	18.755	-19.728	0.0064
5	63.962	-59.893	0.0064	18.903	-19.399	0.0064
6	63.314	-59.547	0.0064	16.953	-16.67	0.0064

7	58.827	-58.215	0.0064	13.441	-12.126	0.0064
8	52.15	-51.857	0.0064	8.942	-6.554	0.0064
9	51.782	-51.736	0.0064	4.514	-1.269	0.0064
10	49.074	-48.991	0.0064	4.628	-1.943	0.0061
11	55.356	-54.938	0.0064	9.29	-5.766	0.0064
12	55.346	-54.929	0.0064	9.468	-5.931	0.0064
13	49.047	-48.957	0.0064	4.913	-2.188	0.0061
14	51.769	-51.713	0.0064	4.215	-1.105	0.0064
15	52.141	-51.832	0.0064	8.624	-6.254	0.0064
16	58.847	-58.205	0.0064	13.206	-11.901	0.0064
17	63.398	-59.636	0.0064	16.809	-16.526	0.0064
18	64.112	-60.048	0.0064	18.858	-19.355	0.0064
19	60.534	-55.652	0.0064	18.76	-19.734	0.0064
20	53.219	-48.19	0.0064	16.459	-17.571	0.0064
21	40.002	-36.52	0.0064	12.217	-13.172	0.0064
22	23.063	-21.062	0.0064	7.237	-7.837	0.0064

Table J.23: Pontoon minimum and maximum displacements and main displacement frequencies for four iterations

J.3.7.4 Conclusions

The first conclusion that must be drawn from this analysis is that the bridge structure is highly sensitive to vortex induced vibrations. This is clear from the fact that the fluid-structure interaction causes cross-flow loading frequencies over a wide band (0.005 Hz - 0.072 Hz) to move toward the structure's first modal eigenfrequency. Another indication of this problem is that the resulting main pontoon displacement frequencies after the first iteration, during which the pontoons were loaded with different frequencies, are all on the bridge systems first modal eigenfrequency. This may also be partially caused by the chosen load model, which is treated later.

The mode shape for the first eigenfrequency is shown in Figures J.46 and J.47. As is visible in these Figures, the shape first mode of vibration of the bridge structure is a slight deformation of the rigid bridge deck in which the pontoons mainly move in the cross-flow direction relative to the current. This contributes to the structure's sensitivity to cross-flow loading at frequencies in a range near the first eigenfrequency.

Despite the structure's high sensitivity to vortex induced vibrations, the fact that the vibrations are this pronounced casts doubt on the results obtained. Furthermore, the fact that the displacement reaches values that are larger than the pontoon diameters raises red flags, as experimental results indicate the maximum displacements in cross-flow direction should be in the range of 0.6 - 0.8 times the pontoon diameter [OM10]. Therefore, the results must be examined critically and reasons for the remarkable results must be found.

One recommendation for further research is to use a different model type to validate the calculation method used for the coupled analysis. One may think of a calculation of the vibration of a single pontoon compared to the results provided by the coupled analysis for a single pontoon. This can be found in section J.3.8.

Another point of attention is the fact that the fluid loading is calculated using the shape, and motion, of only four pontoons out of the twenty-two. After which it is scaled to the draught of the remaining pontoons of the same diameter. The assumption that this is a realistic model for the loading of stationary pontoons has been proven wrong for at least one combination of pontoons with the same diameter and different draughts in section J.3.5. Performing this operation leads to ten out of the twenty-two pontoons (all those with a 36 m diameter) being loaded at the first modal frequency of the bridge structure for the first iteration. Furthermore, due to the fact that the resulting motion of only four pontoons is taken into account for the calculation of the new fluid forces per iteration, this leads to a perfect line-up of forcing frequencies across all pontoons with the same diameter, which may be possible, but is improbable due to variations in structural boundary conditions for the different pontoons.

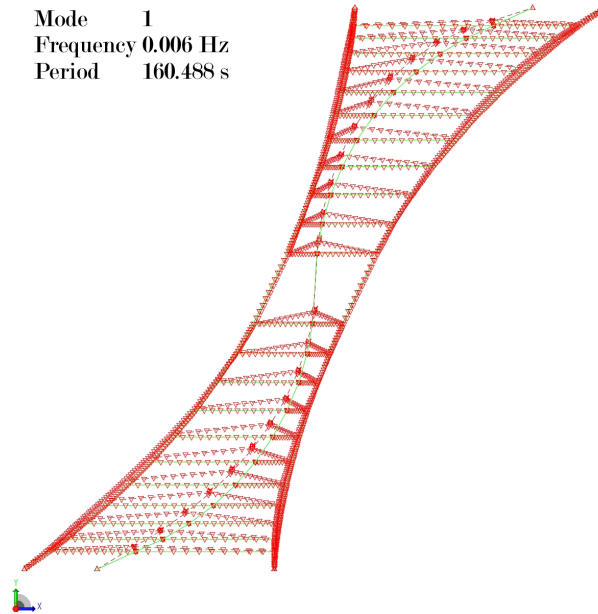


Figure J.46: Top view of the first eigenmode shape (in red) of the bridge structure and the undeformed structure (green).

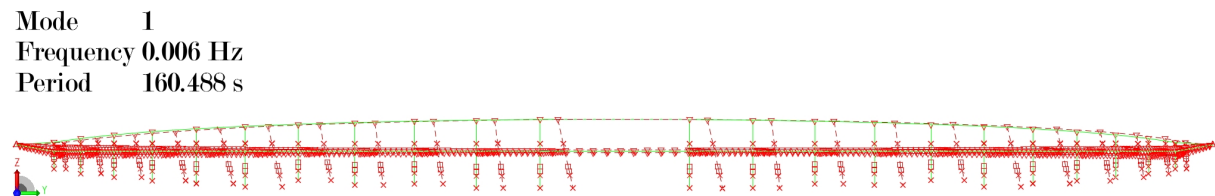


Figure J.47: Side view of the first eigenmode shape (in red) of the bridge structure and the undeformed structure (green).

For further research into this phenomenon, it is recommended to extend the calculation of fluid forces to all of the pontoons separately for each iteration, increasing the computation time by at least a factor five, but eliminating the assumptions leading to the issues described earlier.

Another remarkable element of the results is that the fluid force - structure interaction appears to increase each other with each iteration without an apparent maximum, although there are some clues in the results a maximum may have been reached. One of the reasons there is no conclusive result proving a maximum amplitude of vibration is the fact that the time-span for the analysis has been set too short. The first potential apparent 'plateauing' of the results appear after 3300s into the analysis and increasing the analysis time should lead to a conclusive answer to the question of the maximum amplitude's existence.

The following assumption made that will probably have had an influence on the results is the fact that only motions in the horizontal plane have been taken into account and the pontoons have been modelled as rigid vertical bodies translating through the fluid flow in cross- and in-flow directions. Pontoon rotations around the horizontal axes are neglected, which, based on the present results, are quite pronounced. The influence these rotations may have is based on the change of cross section in the horizontal plane the fluid has to pass. These cross section changes will influence the fluid flow, vortex shedding and resulting cross- and in-flow loading. It is expected that this influence is small, and perhaps even negligible in relation to the issues outlined earlier.

The simplified manner in which the structural damping is determined in this analysis may also contribute to the high amplitudes of the displacement results obtained. However, it is expected that the internal structural damping has a much lower influence on the obtained results compared to the hydrodynamic damping due to the fluid loading and therefore, although calculation of the model structural damping according to the method outlined in appendix D may lead to different results, the influence is expected to be small.

J.3.8 Model verification

In this section, the results produced for the motion of a single pontoon using the coupled analysis model presented in this thesis are compared to the results produced using a coupled wake oscillator model. The goal of this analysis is to show that the results calculated using the Fluent-SACS model are in the same range as the results calculated using this different model and thus verifying the Fluent-SACS model.

In this section, first the theory behind this coupled wake oscillator model is presented. Then the set-up for both the coupled wake oscillator model and the coupled analysis model are presented.

J.3.8.1 Coupled wake oscillator model

The wake oscillator model used in this thesis is based on work by Ogink and Metrikine (2010) [OM10]. A simplification has been made in that only the cross-flow motion of the structure is taken into account and in-flow motion has been restricted. Furthermore, the rigid body motion of the entire pontoon is modelled. The fluctuating wake and subsequent periodic lift force on the body is modelled using a wake oscillator model. This wake oscillator model is coupled to the motion of the body in the governing equations for both systems. This is shown in Equations J.14 and J.15 which show the governing equations for the wake oscillator model used in this thesis. In vortex induced vibration analysis it is common to use dimensionless governing equations. In this thesis it has been chosen not to make the equations dimensionless. This is mainly done to make it easier to tune the wake oscillator model to correspond to the pontoon loading calculated using Ansys Fluent through the scaling factors.

$$\frac{\partial^2 y}{\partial t^2} + 2 \zeta \omega_n \frac{\partial y}{\partial t} + \omega_n^2 y = \int_{z_D}^0 \frac{\rho D z}{2 (m + m_a)} \frac{C_{L,0} q(z, t)}{2} v^2(z) dz \quad (\text{J.14})$$

In which;

$y(t)$ is the cross-flow displacement of the pontoon

ζ is the structural damping ratio

ω_n is natural frequency of the cross-flow motion of the pontoon according to Equation J.16

z is the elevation below the water level

z_D is the pontoon draught

ρ is the water mass density

D is the pontoon diameter

m is the pontoon mass

m_a is the fluid added mass according to Equation J.17

$C_{L,0}$ is the lift coefficient for a circular body

$q(z, t)$ is the wake oscillator function

$v(z)$ is the fluid velocity at elevation z

$$\frac{\partial^2 q(z, t)}{\partial t^2} + \epsilon \omega_s(z) (q(z, t)^2 - 1) \frac{\partial q(z, t)}{\partial t} + \omega_s^2(z) q(z, t) = \frac{A}{D} \frac{\partial^2 y}{\partial t^2} \quad (\text{J.15})$$

In which;

$q(z, t)$ is the wake oscillator function

ϵ is a scaling factor

z is the elevation below the water level

$\omega_s(z)$ is the vortex shedding frequency at elevation z according to Equation J.18

A is a scaling factor

D is the pontoon diameter

$$\omega_n = \sqrt{\frac{k}{(m + m_a)}} \quad (\text{J.16})$$

In which;

ω_n is natural frequency of the cross-flow motion of the pontoon

k is the stiffness of the structure restraining the pontoon in the cross-flow direction

m is the pontoon mass

m_a is the fluid added mass according to Equation J.17

$$m_a = C_a \frac{\pi D^2}{4} \rho |z_D| \quad (\text{J.17})$$

In which;

m_a is the fluid added mass

C_a is the fluid added mass coefficient for a circular body

D is the pontoon diameter

ρ is the fluid mass density

z_D is the pontoon draught

$$\omega_s(z) = 2 \pi Str \frac{v(z)}{D} \quad (\text{J.18})$$

In which;

$\omega_s(z)$ is the vortex shedding frequency at elevation z

z is the elevation below the water level

Str is the Strouhal number for the structure and flow

$v(z)$ is the fluid velocity at elevation z

D is the pontoon diameter

As shown in the equations, the lift force coefficient is taken as constant. This is a simplification of reality. Another simplification is that the Strouhal number is taken as a single constant, while it is a function of the Reynolds number of the flow which varies over the draught of the pontoon.

J.3.8.2 Set-up

In this section, the set-up, preliminary actions and assumptions made for both the wake oscillator model and the Fluent-SACS model are presented. The fluid velocity profile used is the same as in the other analyses in this thesis and given in section J.3.1.

The coupled wake oscillator model is solved by numerical integration, using the Python function `solve_ivp` from the Scipy module. The integration method used is the 'RK45' method, an explicit Runge-Kutta method of the order 5 [DP80]. To numerically integrate the right hand side of the cross-flow displacement equation of motion, Romberg integration is used [Rom55]. This numerical integration method needs $2^k + 1$ samples to function, so the wake oscillator function is evaluated $2^k + 1$ evenly spaced locations along the pontoon's draught. After some testing, $2^7 + 1 = 129$ evenly spaced points provided a good trade-off between computation time and accuracy. The constant parameters used in the governing equations for the coupled wake oscillator model are shown in Table J.24. The initial values for the 129 wake oscillator functions are chosen randomly in the range (0.25, 0.5).

Parameter	Value
Pontoon diameter	52 m
Pontoon draught	−133.5 m
Pontoon mass	$2614.405 \cdot 10^3 \text{ t}$
Pontoon added mass	$290.519 \cdot 10^3 \text{ t}$
Pontoon cross-flow natural frequency	$0.0508 \text{ rad s}^{-1}$
Pontoon structural damping ratio	4.300 %

Table J.24: Parameters used in the coupled wake oscillator model.

The natural frequency of the cross-flow motion of the pontoon is calculated using the SACS Dynpac module, for more information on the methodology behind this reference is made to section H.1. The structural damping factor is the same as the one calculated in the coupled Ansys-SACS analysis.

The set-up for the coupled Ansys-SACS analysis is the same as in the coupled analysis performed in section J.3.7, apart from the fact that only the loading on a single pontoon is considered and the timespan is increased to 7200 s. The pontoon considered is pontoon 11, its defining characteristics are given in Table J.24.

One more important factor in the set-up of the coupled wake oscillator model is the Strouhal number and the scaling factor ϵ used. These two factors directly influence the governing equation for the wake oscillator thus the entire model. To determine the values to be used for these parameters, the loading on the stationary pontoon is calculated using Ansys Fluent. After this, the cross-flow loading is calculated using the wake oscillator model, but the cross-flow motion is set to zero. Then the Strouhal number and ϵ are iteratively scaled to fit the cross-flow loading calculated using the wake oscillator model to the one calculated by Fluent in both the frequency and time domain. The expression for the cross-flow loading on the pontoon in the wake oscillator model is given in Equation J.19.

$$F(t) = \int_{z_D}^0 \frac{\rho D z}{2} \frac{C_{L,0}}{2} \frac{q(z, t)}{2} v^2(z) dz \quad (\text{J.19})$$

In which;

$F(t)$ is the cross-flow lift force on the pontoon

z is the elevation below the water level

z_D is the pontoon draught

ρ is the water mass density

D is the pontoon diameter

m is the pontoon mass

m_a is the fluid added mass according to Equation J.17

$C_{L,0}$ is the lift coefficient for a circular body

$q(z, t)$ is the wake oscillator function

$v(z)$ is the fluid velocity at elevation z

The cross-flow loading calculated using Fluent are shown in Figure J.48 for both the time and frequency domain. The Strouhal number in the wake oscillator governing equation is set such that the shedding frequency of the fluid in the -10 to -30 elevation range with a velocity of 1.27 m s^{-1} is the same as the main shedding frequency calculated using Fluent. Doing this gives the best fit for the cross-flow loading in the frequency domain and is shown on the right in Figure J.49. As is visible, the wake oscillator model provides loading at four distinct frequencies. These are coupled to the four distinct fluid velocities found in the discrete fluid velocity profile used. This effect may be lessened by using different Strouhal numbers coupled to the different flow velocities (and thus different Reynolds numbers). However, this approximation is considered allowable for the purposes of this analysis. The ϵ value is found by iteratively trying different values, starting at the values found by Ogink and Metrikine (2010) [OM10], and comparing

the results, mainly in the time domain. In the end, the best fit was found at a value of 0.4 for ε . The resulting loading is shown in the time domain on the left in Figure J.49. The loading in the time domain is mainly consistent between the two models in terms of the amplitude of the load. For the coupled analysis, the scaling factor A is taken as 4.0, corresponding to the values found for the upper branch fitting by Ogink and Metrikine (2010) [OM10].

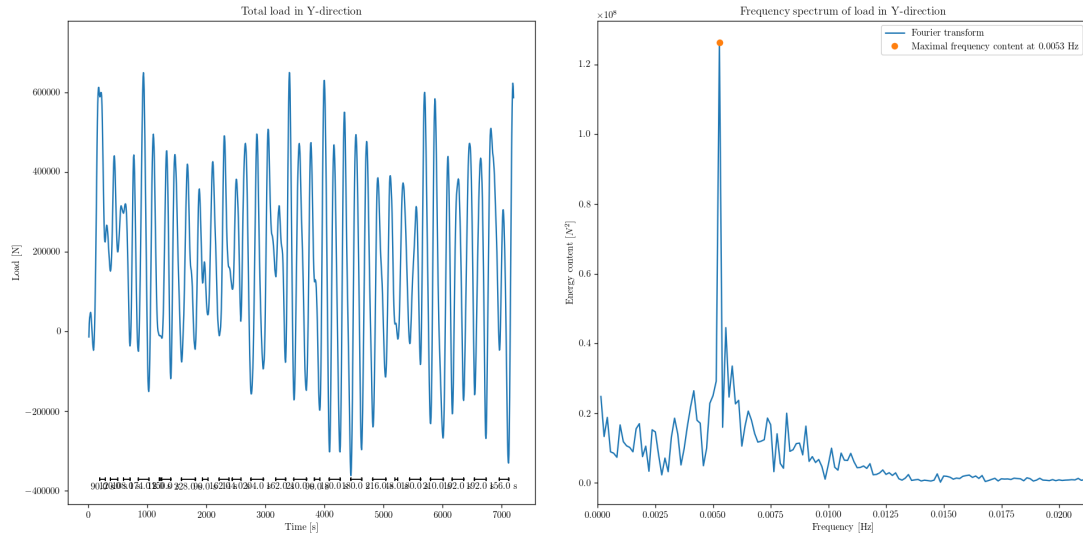


Figure J.48: Cross-flow loading calculated by Fluent for the stationary pontoon 11 in both the time (left) and frequency domain (right).

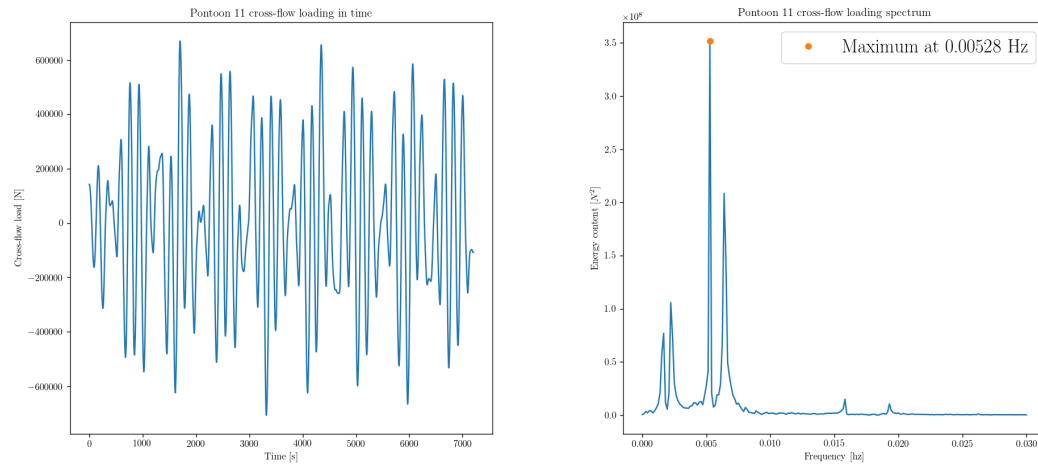


Figure J.49: Cross-flow loading calculated using the wake oscillator model for the stationary pontoon 11 in both the time (left) and frequency domain (right).

J.3.8.3 Results and conclusions

The results of the coupled wake oscillator model are shown in Figures J.50 and J.52 for the cross-flow loading and displacement.

Figures J.51 and J.53 show the results of the final iteration performed with the Fluent-SACS model. Once again, the solution has not converged and shows no signs of nearing convergence. The reason for this will be explained later.

The results show that the Ansys-Fluent model and the wake oscillator model calculate both loads and displacements with comparable amplitudes. Differences are found once the results in the are ex-

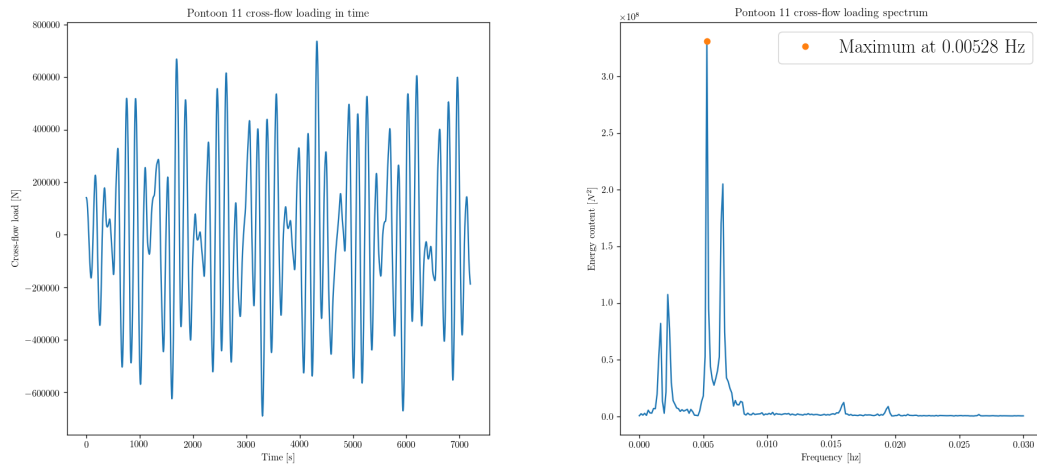


Figure J.50: Cross-flow loading calculated using the wake oscillator model for pontoon 11 in both the time (left) and frequency domain (right).

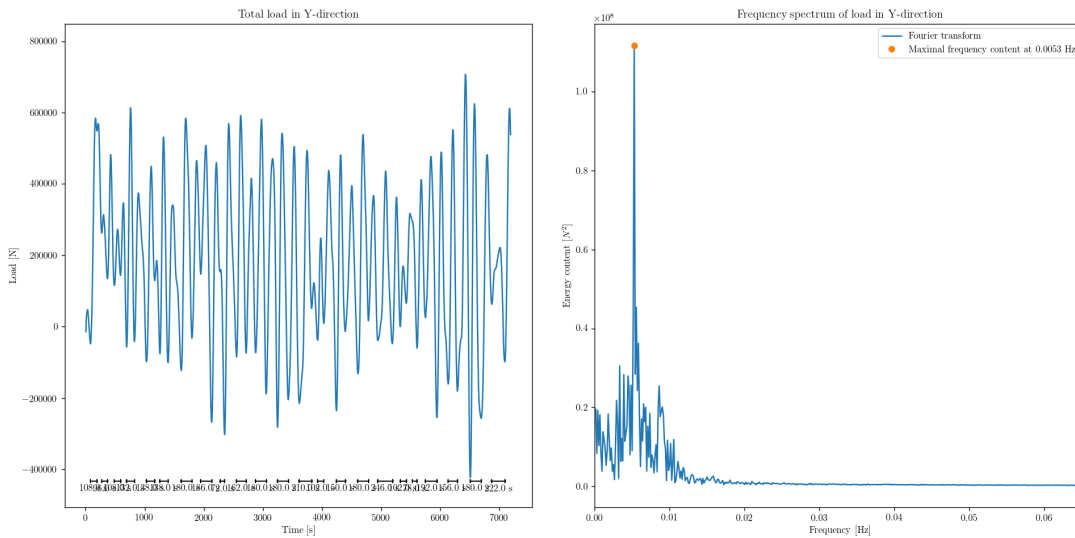


Figure J.51: Cross-flow loading calculated using the Ansys-Fluent model for pontoon 11 in both the time (left) and frequency domain (right).

amined in the frequency domain. The cross-flow loading using the wake oscillator model shows four distinct peaks, even in this coupled analysis, while the Fluent-SACS loading is mainly concentrated in one frequency. There are peaks near the same frequencies as in the wake oscillator model, but they are far less pronounced. For both the wake oscillator and the Fluent-SACS model the loading is not very different from the loading on a stationary pontoon. This is expected when the displacement amplitude is considered with respect to the pontoon diameter; 1.5 m versus 52 m, or a 0.029 amplitude over diameter ratio. The pontoon is nearly stationary. The wake oscillator model finds the pontoon's eigenfrequency as main frequency of vibration, while the Fluent-SACS model finds that the pontoon mainly vibrates at the amplitude of the loading and has a smaller peak at the pontoon eigenfrequency. This difference is explained by looking at the exciting frequencies for both models; the wake oscillator model has a pronounced peak close to the pontoon eigenfrequency, while the Fluent-SACS model is almost exclusively loaded at 0.0053 Hz. If further improvements are made to make the loading by the wake oscillator model more closely resemble the Fluent-SACS model loading, it is expected that the displacement results will also be more in line in terms of frequency. What can be concluded from this analysis is that both methods produce comparable results for this case.

Then there is the matter of the Fluent-SACS model not converging. The reason for this is found when

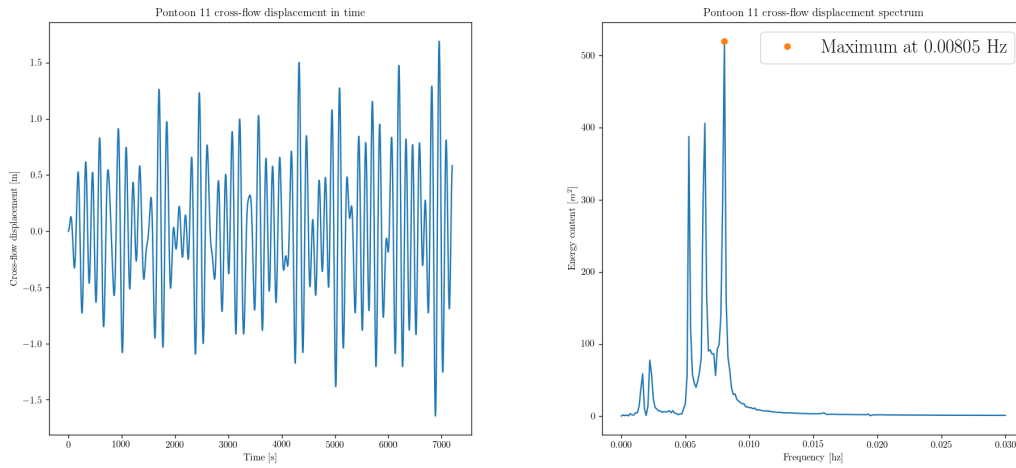


Figure J.52: Cross-flow displacement calculated using the wake oscillator model for pontoon 11 in both the time (left) and frequency domain (right).

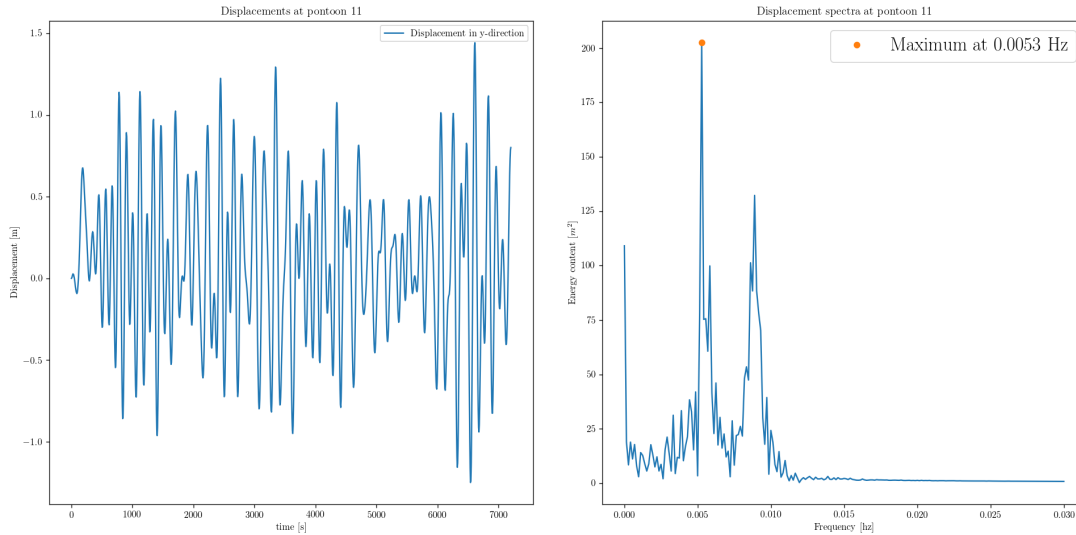


Figure J.53: Cross-flow displacement calculated using the Ansys-Fluent model for pontoon 11 in both the time (left) and frequency domain (right).

the simulation time of the wake oscillator model is extended. Figure J.54 shows the cross-flow motion of pontoon 11 over a time period of 28 800 s, or 8 hours. The figure shows that it takes about 22 500 s, or 6.25 hours, for the coupled system to reach a steady state in terms of vibration amplitude. This means that even at a simulation time of 2 hours, the modelled systems are still in the transient phase, making comparison of results and especially calculating convergence a futile effort.

One point of interest is the small peak near a frequency of 0.0063 Hz in the Fluent-SACS model's displacement in the frequency spectrum (shown on the right in Figure J.53). This value corresponds to the frequency of the first mode of vibration of the entire bridge structure and apparently it is already excited when only a single pontoon is loaded by cross-flow lift forces at mainly a very different frequency. This lends credence to the conclusion that the bridge is very susceptible to vortex induced vibrations.

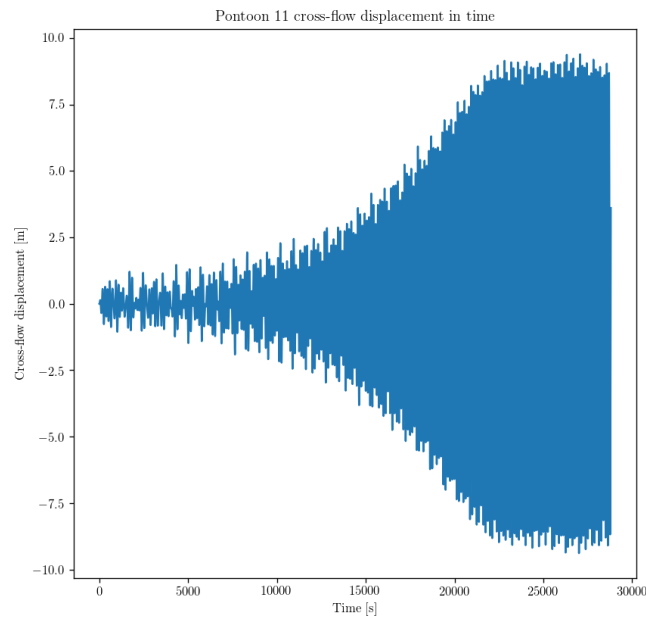


Figure J.54: Cross-flow displacement calculated using the wake oscillator model for pontoon 11 in time, for a period of 8 hours.

J.3.9 Possible solutions

The results of the coupled analysis detailed in section J.3.7 show that vortex induced vibrations will lead to problems at the bridge location. This chapter outlines possible solutions to this issue.

J.3.9.1 Helical strakes

One of the possible solutions to vortex induced vibrations is the use of helical strakes. An example of a helical strake applied to a pontoon is shown in Figure J.55.

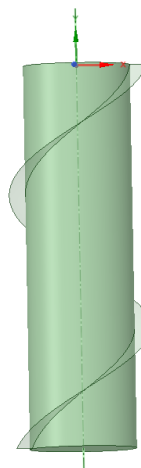


Figure J.55: Example of a helical strake attached to a pontoon.

Helical strakes function by providing clear locations along the pontoon for the fluid boundary layer to separate from the pontoon. This causes the phase of the vortex shedding to be slightly different at each horizontal cross section along the pontoon draught and, if applied well, this leads to both the frequencies of the shedding along the cylinder to be different and the amplitude of resulting in- and cross-flow forces

to be reduced. It is specified that for these strakes to work, they have to be applied well, meaning that a lot of modelling is required to achieve the desired effect. The spreading of shedding frequencies and reduction of fluid forcing amplitudes is, of course, positive, and based on these qualities of the strakes they are a welcome addition to the bridge design. One of the advantages of using helical strakes is that they 'work' for multiple flow directions of the fluid flow past the pontoon. Since the direction of the fluid flow at the bridge location is known, this is not relevant for the bridge design. One of the disadvantages of adding strakes to the pontoons is the increase in drag the strakes cause. Although this will probably not be as big an increase as the increase in drag caused by vortex induced vibrations, this is still an undesirable side effect of the use of strakes for the bridge design. One more point of attention with the use of strakes is their dependence on their shape to remain unchanged for their proper operation. This may be influenced by the growth of marine life on the surface of the strake. Since there will be a lot of marine growth occurring at the bridge location, this will mean having to either clean or treat the strakes on a regular basis.

J.3.9.2 Changing the pontoon shape

Changing the shape of the pontoons to something more aerodynamic may lead to reduction of vortex induced vibration effect. Due to the fact that the current direction and properties are known, it is possible to design a shape specifically for the current direction and properties at the bridge location.

To demonstrate a possibility for a different shape (with the same submerged volume as the corresponding pontoon to maintain buoyancy), a 3D fluid flow analysis, as described in section J.3.4 is performed on the stationary geometry shown in Figure J.56. This geometry has the dimensions specified in Table J.25.

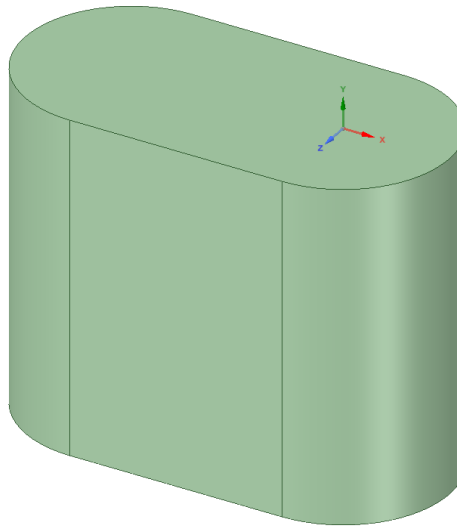


Figure J.56: Elongated pontoon geometry of with a 36 m cross-flow dimension.

Dimension	Size
Cross-flow length	36 m
In-flow length	72 m
Draught	57 m
Corresponding pontoon volume	Pontoon 6

Table J.25: Dimensions of the elongated pontoon used for the 3D analysis.

The analysis is run using the same properties for the mesh and flow velocity specified in section J.3.4. This leads to the mesh as depicted in Figure J.57.

The analysis is run for a timespan 3600 s. The resulting cross-flow loading is shown in Figure J.58. This figure clearly shows a huge drop in steady cross-flow loading amplitude when compared to the results obtained for pontoon 6 as depicted in Figure J.59.

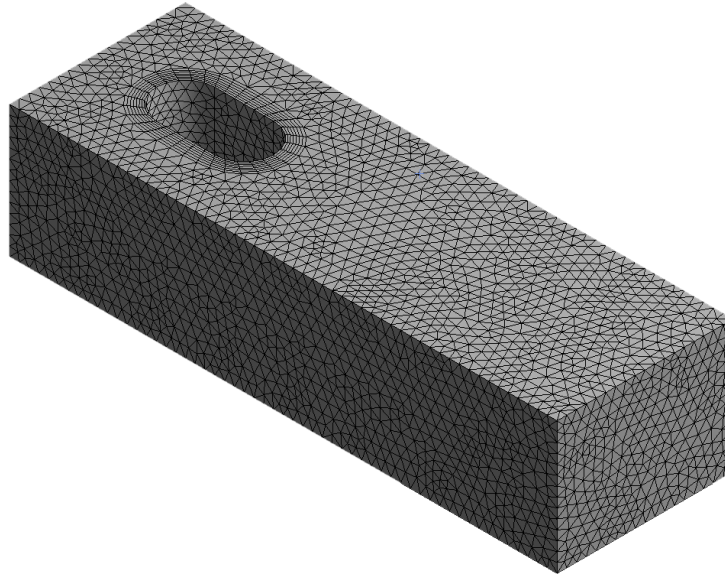


Figure J.57: Mesh used for the elongated pontoon geometry of with a 36 m cross-flow dimension.

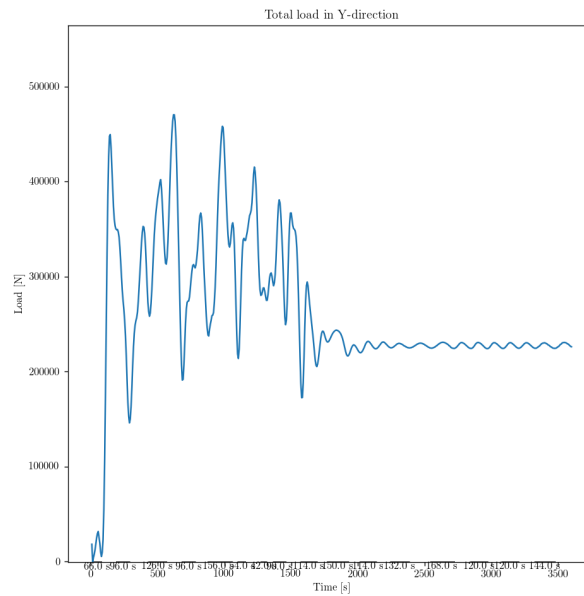


Figure J.58: Cross-flow loading versus time for the 3D-analysis of the elongated pontoon geometry.

The energy content per frequency also shows a large difference when compared to the reference pontoon. This is depicted in Figures J.60 and J.61. The Figures show that the cross-flow loading is spread across more frequencies for the elongated shape when compared to pontoon 6.

It is clear that changing the pontoon shape has advantages, even a simple change like the one analysed in this section already provides quite an improvement over the original situation. Changing the shape to a more elongated one is, however, not without risks. If the pontoons are not correctly aligned with respect to the current direction, there is a risk of galloping [DX16].

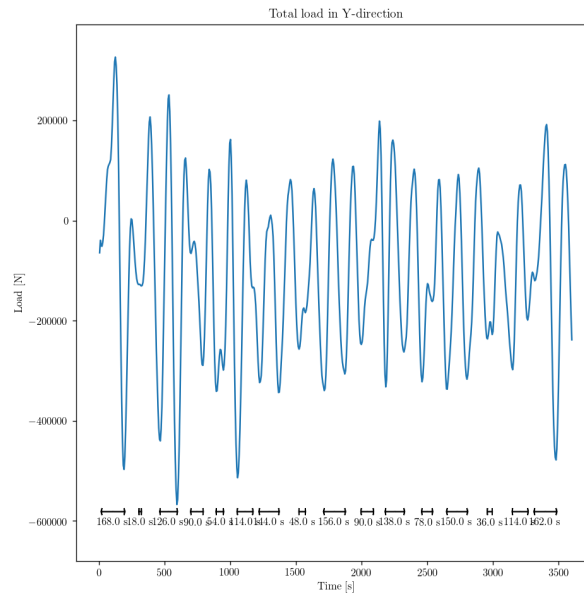


Figure J.59: Cross-flow loading versus time for the 3D-analysis of pontoon 6.

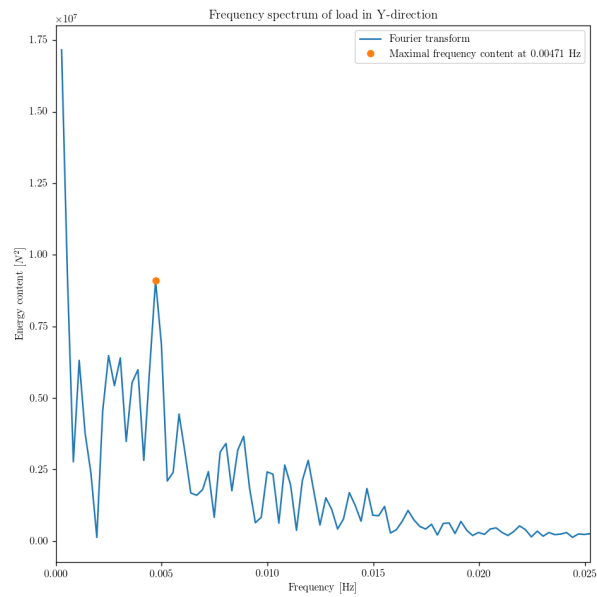


Figure J.60: Frequency spectrum of cross-flow load for the 3D-analysis of the elongated pontoon geometry.

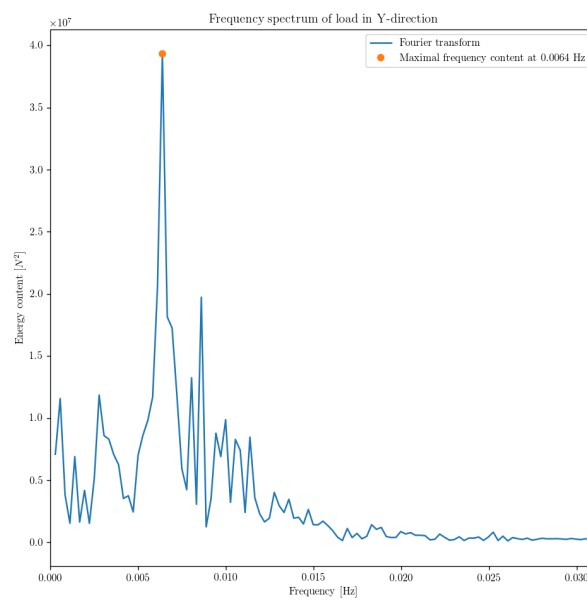


Figure J.61: Frequency spectrum of cross-flow load for the 3D-analysis of pontoon 6.

J.3.9.3 Dynamic absorber (tuned mass damper)

A dynamic absorber (or tuned mass damper) is an auxiliary mass, attached to the primary structure using springs and dampers or as a pendulum, used to 'absorb' the energy of certain vibrations from the primary structure by vibrating itself. Examples of how a dynamic absorber may be included in the pontoon design is shown in Figure J.62. From this image it is obvious that using a pendulum as a dynamic absorber is an extremely bad idea in this situation, since the pendulum load is applied above the pontoon center of buoyancy, increasing the destabilizing moment when the pontoon rotates. More information on this is found in section A.4.1. The option where the mass is located beneath the center of buoyancy makes more sense in this situation.

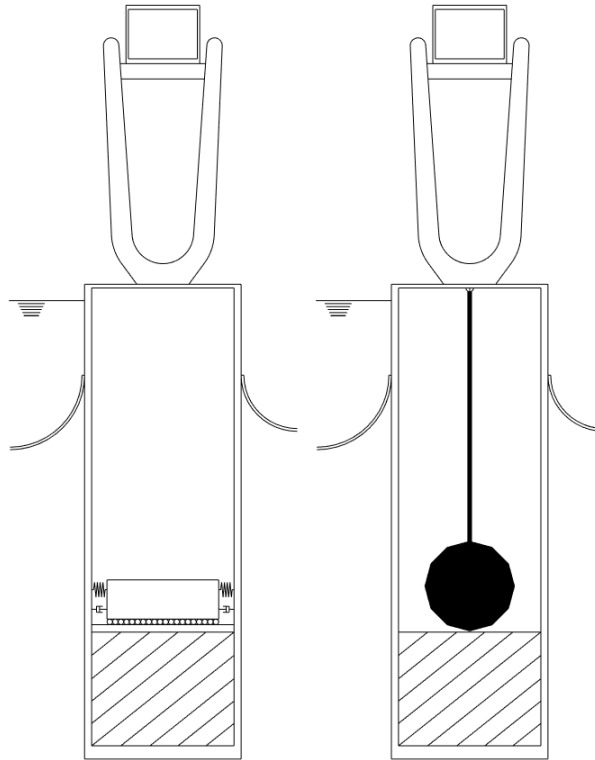


Figure J.62: Dynamic absorbers.

The goal for the dynamic absorber is to dimension the mass and spring stiffness in a manner that puts its eigenfrequency at the undesired frequency of vibration for the primary structure. The more energy the absorber can absorb from the vibration of the primary structure, the better. This can be achieved by maximizing the absorber mass and velocity during vibration within the confines of the pontoon structure.

J.4 Conclusions

The overall conclusions that can be drawn from the research into the bridge design in relation to vortex induced vibrations induced by the current at the bridge location are presented here.

The bridge system is highly sensitive to vortex induced vibrations induced by tidal current. Every analysis performed to investigate this sensitivity, from the 'semi-2D' to the coupled analysis, has shown that the structure is very sensitive. No precise measure of the extent of the vortex induced motions is provided, as results calculated in the coupled analysis seem to be outside the range reasonable results and need to be validated.

It is obvious a solution is necessary for the issue of vortex induced vibration and a few initial suggestions to this effect have been given.

Appendix K

Cable fatigue

This appendix contains research into fatigue of the cable system used to anchor the bridge design. For more information on the precise cable (system) design, reference is made to section A.5 and appendix C. This appendix contains a short introduction into the theory of fatigue damage and how it applies to steel cables. Then the research set-up used to investigate this phenomenon in the bridge model is described, after which the research results and conclusions are presented.

K.1 Theory

Fatigue is the accumulation of (at first) microscopic cracks in materials, mostly concentrated around small material imperfections or discontinuities. These cracks form due to stresses in the material peaking around these imperfections and thus causing small plastic (permanent) deformations of the material. This damage can occur at total stress levels much lower than the yield stress of the material. If this process occurs once, the effect is negligible and the structural element will be mostly unaffected. However, when the process is cyclical in nature, each cycle introduces more cracking and growth of the cracks until the structural element fails [Lal14].

This can be applied in structural design using rule called the Palmgren-Miner rule, for which the expression is shown in Equation K.1. The idea behind this rule is that a certain cyclical load introduces a certain amount of damage, which is a fraction of the damage at which the structural element fails. When there are enough cycles of the load, the damage reaches the damage level of failure. This simple model allows the combination of different load cycles and accompanying fractions of total damage to be identified and analysed to see if they, together, lead to structural failure [Cam12].

$$\sum_{i=1}^N D_i = D \quad (\text{K.1})$$

In which;

N is the number of load cycles of the load introducing damage D_i

D_i is the amount of damage per load cycle as a fraction of total damage D

D is the total damage at failure of the structural component

The relation between the loading and the amount of cycles until a structure fails can be shown visually using a Woehler diagram. An example of such a Woehler diagram for the axial loading of a steel cable is given in Figure K.1. In this diagram the load cycles are displayed as the normalized force range shown on the vertical axis and the black line shows the amount of cycles the cable can sustain under this loading before failure. The constant stress around which the load fluctuates is also an important factor, as is shown by the fact that changing this load changes the position of the lines. Figure K.2 shows a visualisation of the load amplitude, and minimum and maximum loading during a load cycle.

To determine the relations between axial minimum load, load amplitudes and cycles to failure, material tests have been performed, in which, in the case of cables, cables have been loaded to failure at different

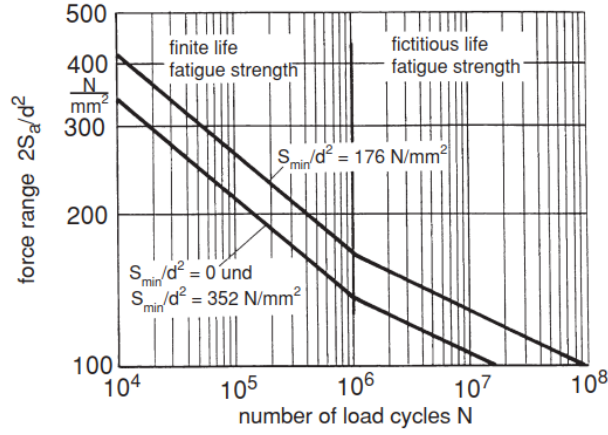


Figure K.1: Woehler diagram for a steel cable [Fey07].

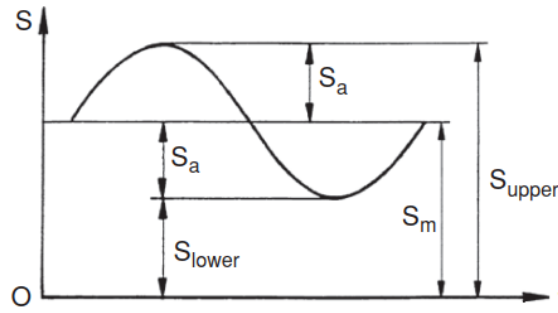


Figure K.2: One load cycle, with minimum, maximum and load amplitude indicated [Fey07].

values for all variables. The result of extensive testing has been the creation of an equation best fitting the test results [Fey07]. This expression is shown in Equation K.2.

$$\log N = a_0 + a_1 \cdot \log \frac{2 S_a d_e^2}{d^2 S_e} + a_2 \cdot \frac{S_{lower} d_e^2}{d^2 S_e} + a_3 \cdot \left(\frac{S_{lower} d_e^2}{d^2 S_e} \right)^2 + a_4 \cdot \log \frac{d}{d_e} + a_5 \cdot \log z \quad (\text{K.2})$$

In which;

N is the number of load cycles

a_i are scaling variables, determined through testing

S_a is the amplitude of the load cycle

d_e is a unit length, to make the expression dimensionless

d is the nominal rope diameter

S_e is a unit force, to make the expression dimensionless

S_{lower} is the lower limit of the force cycle

z is the number of wires in the rope

The a_i values have been determined from testing using regression calculations and differ for different wire rope dimensions and cross section designs. Using this expression, the Woehler diagram depicted in Figure K.1 is created, with the caveat that since no extensive testing has been performed beyond $2 \cdot 10^6$ cycles and the results do not allow for the derivation of a relation between the loading and the amount of cycles. Supposing that a constant fatigue strength does not exist, the line is continued using a fictitious

continuation of the fatigue strength line [Hai89]. The expression for the fictitious continuation is shown in Equation K.3.

$$N = N_D \left(\frac{2 \frac{S_a}{d^2}}{2 \frac{S_{aD}}{d^2}} \right)^{2 a_1 + 1} \quad (\text{K.3})$$

In which;

N is the number of load cycles

N_D is the number of load cycles from which the fictitious conservative continuation of the fatigue strength line starts, taken as $2 \cdot 10^6$ cycles

$\frac{S_{aD}}{d^2}$ is the force range at the number of load cycles N_D

S_a is the amplitude of the load cycle

a_1 is a scaling variable, determined through testing

d is the nominal rope diameter

K.2 Set-up

The set-up of the research performed in this appendix is described in this section. First the scope of the research is set. The scope is set at fatigue loading induced due to axial loads in the cables. Cable bending is not considered since the curvature changes of the cables in the cable system design are of a much smaller magnitude than the ones considered in empirical testing, where steel cables running along sheaves are considered [Fey07].

The scope is set further by limiting the investigation to the six critical wave load cases defined in section E and shown in Table K.1. These load cases correspond to storms occurring once in a 100 years and they should provide a maximum level of fatigue damage that the wave loading at the bridge location can induce (per cycle). Therefore the steady state analysis of the bridge structure as a result of these six load cases is taken as the basis for the calculation of the fatigue damage to the bridge structure. For more information on this analysis, reference is made to appendix E.

Loadcase	Wave direction - height - wavelength	Current direction
1	180° - 4.55 m - 33 m	Inwards
2	180° - 4.55 m - 33 m	Outwards
3	240° - 4.79 m - 36 m	Inwards
4	240° - 4.79 m - 36 m	Outwards
5	270° - 4.36 m - 36 m	Inwards
6	270° - 4.36 m - 36 m	Outwards

Table K.1: Wave load cases.

From the results of the steady state analyses, the minimum stress (S_{lower}) and stress amplitude (S_a) are determined per cable node in the system. Subsequently, the axial stresses in the cable strands are calculated using the expression shown in Equation K.4. Then the amount of load cycles until strand failure at these load levels is calculated per node using Equation K.2. The values used for the a_i variables in this thesis are taken from tests on ropes closely resembling the strands used in the main and lateral cable designs [Fey07]. Table K.2 compares the test ropes to the strand designs.

$$Z_{T,i} = \frac{E_i A_i \cos^2 \beta}{\sum_{all\ wires} E_i A_i \cos^3 \beta} T \quad (\text{K.4})$$

In which;

$Z_{T,i}$ is the tensile force in a single strand

E_i is the strand elasticity modulus

A_i is the strand sectional area

β is the lay angle of the wire or strand

T is the tensile force acting on the rope

	Nominal diameter [mm]	Wires	Layers	Nominal strength [N mm ⁻²]
Casey (1993) [Cas93]	40	135	6	1770
Lateral cable strand	42.3	61	4	1860

Wehking and Klopfer (2000) [Weh00]	127	292	10	1770
Main cable strand	123	1261	20	1860

Table K.2: Test and design cable properties.

The a_i values used for the main and lateral cable fatigue cycle calculations are displayed in Table K.3.

	a_0	a_1	a_2	a_3	a_4	a_5
Lateral cable strand	20.587	-5.420	-0.00019	-0.000024	-1.040	0
Main cable strand	15.401	-3.910	0.00118	-0.0000037	-0.793	0.399

Table K.3: a_i values for the main and lateral cable fatigue calculations

K.3 Results

The results of the analysis are in terms of cycles to strand failure at each node of the cable bending system. A distinction has been made between the main- and lateral cables due to their differing dimensions. The results are depicted in the Woehler diagrams shown in Figures K.3 and K.4 in which the results for all load cases are shown together. These Woehler diagrams also contain fatigue strength lines for the strands at two minimum stress levels to visually represent the cycle limits for the two cable designs.

To show the distribution of the stress amplitude across the cable system, colour-coded visualisations of the stress amplitudes for the different wave load cases are presented in Figure K.5. It should be noted that the colour-coding is different for each plot, so for direct comparison reference is made to the plot legends.

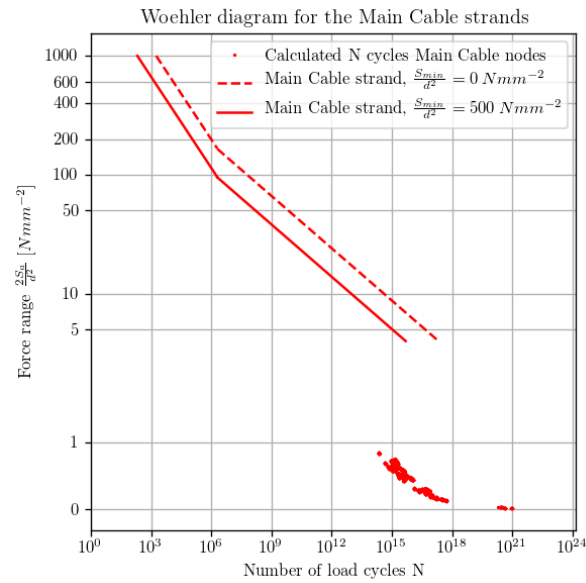


Figure K.3: Woehler diagram for the main cable strands with calculated cycles for the loads observed in the main cable nodes.

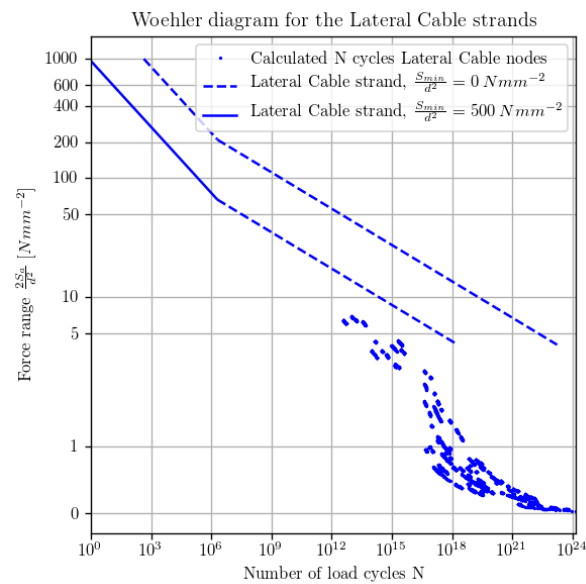


Figure K.4: Woehler diagram for the main cable strands with calculated cycles for the loads observed in the lateral cable nodes.

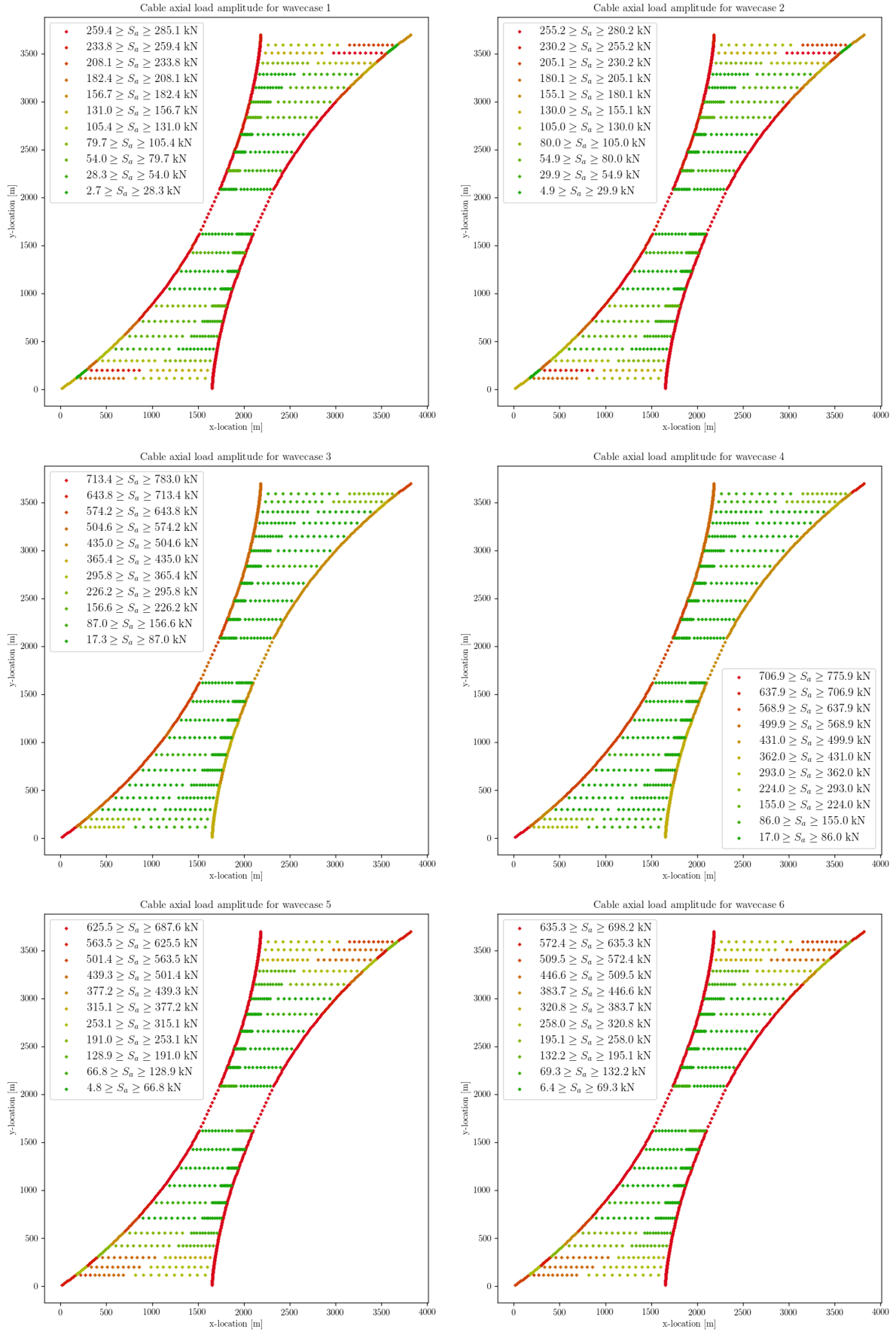


Figure K.5: Load amplitude values for the different load cases.

K.4 Conclusions

The conclusion to be drawn from this analysis is simple; based on the obtained results, fatigue induced by wave loading should not be an issue for the bridge design. This is clearly visible in the two Woehler diagrams presented in Figures K.3 and K.4. A quick calculation using the minimum cycles and minimum wave period shows that for the main cable to experience a single strand failure due to the wave loads would take, at minimum, approximately $10^{13} \cdot 4.6 \text{ s} = 1.46 \cdot 10^6$ years. For the lateral cable this number is slightly lower at approximately $10^{12} \cdot 4.6 \text{ s} = 1.46 \cdot 10^5$ years.

This is also explained by the load amplitudes calculated and depicted in Figure K.5. The maximal axial load amplitude calculated is 783 kN. Comparing this to the design static axial load values for the main- and lateral cables, 930 000 kN and 53 000 kN, respectively, shows the difference in order of magnitude.

Bending stresses have not been a part of the research presented here and will be an influence on the fatigue life. Their influence is, however, expected to be marginal and it is not expected that their inclusion will lead to cable fatigue being decisive in the bridge design.

Bibliography

- [Sto47] G.G. Stokes. “On the theory of oscillatory waves”. In: *Transactions of the Cambridge Philosophical Society* 8 (1847), pp. 441–455.
- [Rie51] B. Riemann. *Grundlagen für eine allgemeine Theorie der Functionen einer veränderlichen complexen Grösse*. Adalbert Rente, 1851.
- [Mac54] R.C. MacCamy. *Wave Forces on Piles: A Diffraction Theory*. U.S. Army Corps of Engineers Beach Erosion Board, 1954. URL: http://acwc.sdp.sirsi.net/client/en_US/default/index.assetbox.assetactionicon.view/1007800?rm=TECHNICAL+MEMO2%7C%7C%7C1%7C%7C%7C0%7C%7C%7Ctrue.
- [Rom55] W. Romberg. “Vereinfachte numerische Integration”. In: *Det Kongelige Norske Videnskabers Selskab Forhandlinger* 28 (1955), pp. 30–36.
- [CT65] J. W. Cooley and J. W. Turkey. “An algorithm for the machine calculation of complex Fourier series”. In: *Math. Comput.* 19 (1965), pp. 297–301.
- [Cha74] G. Chaikin. “An algorithm for high speed curve generation.” In: *Computer Graphics and Image Processing* 3 (1974), pp. 346–349.
- [MGB74] A. Mood, F. Graybill, and D. Boes. *Introduction to the Theory of Statistics (3rd ed.)*. 1974.
- [DP80] R. Dormand and P. J. Prince. “A family of embedded Runge-Kutta formulae”. In: *Journal of Computational and Applied Mathematics* 6 (1980), pp. 19–26.
- [KEN83] JOHN T. KENT. “Information gain and a general measure of correlation”. In: *Biometrika* 70.1 (1983), pp. 163–173. DOI: 10.1093/biomet/70.1.163. URL: <http://dx.doi.org/10.1093/biomet/70.1.163>.
- [Cha87] S. K. Chakrabarti. *Hydrodynamics of Offshore Structures*. Springer Verlag, 1987.
- [HH88] Chen Su Huan and Pan H. H. “Guyan reduction”. In: *Communications in Applied Numerical Methods* 4.4 (1988), pp. 549–556. DOI: 10.1002/cnm.1630040412. URL: <https://onlinelibrary.wiley.com/doi/abs/10.1002/cnm.1630040412>.
- [Hai89] E. Haibach. VDI-Verlag, 1989.
- [Cas93] N. F. Casey. “The fatigue endurance of wire ropes for mooring offshore structures.” In: *OIPEEC Round Table Conference 1993* (1993), pp. I.21–I.49. ISSN: 9037000916 9789037000917.
- [Zhu93] S. Zhu. “Diffraction of Short-Crested Waves Around a Circular Cylinder”. In: *Ocean Engineering* (1993). URL: http://www.sciencedirect.com.tudelft.idm.oclc.org/science/article/pii/002980189390003Z?_rdoc=1&_fmt=high&_origin=gateway&_docanchor=&md5=b8429449ccfc9c30159a5f9aeaa92ffb&ccp=y.
- [Men94] F. R. Menter. “Two-Equation Eddy-Viscosity Turbulence Models for Engineering Applications”. In: *AIAA Journal* 32 (1994), pp. 1598–1605.
- [al96] Feriani et al. “The Formation of Viscous Damping Matrices for the Dynamic Analysis of MDOF Systems”. In: *Earthquake Engineering and Structural Dynamics* (1996). URL: [http://onlinelibrary.wiley.com.tudelft.idm.oclc.org/doi/10.1002/\(SICI\)1096-9845\(199607\)25:7%3C689::AID-EQE575%3E3.0.CO;2-L/abstract](http://onlinelibrary.wiley.com.tudelft.idm.oclc.org/doi/10.1002/(SICI)1096-9845(199607)25:7%3C689::AID-EQE575%3E3.0.CO;2-L/abstract).
- [Pap97] K. O. Papailiou. “On the Bending Stiffness of Transmission Line Conductors”. In: *IEEE Transactions on Power Delivery* (1997). URL: <http://ieeexplore.ieee.org.tudelft.idm.oclc.org/document/634178/>.
- [DS98] N. R. Draper and H. Smith. *Applied regression analysis*. 1998.

- [Bel99] A. G. Belyaev. "A Note on Invariant Three-Point Curvature Approximations". In: (1999). URL: <http://www.kurims.kyoto-u.ac.jp/~kyodo/kokyuroku/contents/pdf/1111-16.pdf>.
- [Weh00] Klopfer Wehking K.-H. "Lebensdauer und Ablegereife von Drahtseilen unter Zugschwellbeanspruchung." In: *Abschlussbericht d. Forschungsprojekts AVIF und DRAHT 51* (2000), pp. 138–144.
- [ECS02] ECS. *Steel wire and wire products - steel wire for ropes*. EN 10264-1:2002. Design Code. European Committee for Standardization, 2002. URL: <https://www.nen.nl/NEN-Shop/Norm/NENEN-1026412012-en.htm>.
- [Fey07] K. Feyrer. *Wire Ropes*. Springer, 2007. ISBN: 978-3-540-33831-4. URL: <https://doi-org.tudelft.idm.oclc.org/10.1007/978-3-540-33831-4>.
- [Apo09] J. A. Apolinário. *QRD-RLS Adaptive Filtering*. 2009. ISBN: 978-0-387-09734-3. DOI: <https://doi-org.tudelft.idm.oclc.org/10.1007/978-0-387-09734-3>.
- [al10] Babuska et al. "Modeling and Experimental Validation of Space Structures with Wiring Harnesses". In: *Journal of Spacecraft and Rockets* (2010). URL: <https://doi.org/10.2514/1.48078>.
- [DNV10] DNV. *Environmental Conditions and Environmental Loads*. DNV-RP-C205. Recommended Practice. Det Norske Veritas, 2010. URL: <https://rules.dnvg1.com/docs/pdf/dnv/codes/docs/2010-10/rp-c205.pdf>.
- [ECS10] ECS. *Eurocode 1: Actions on structures - Part 1-4: General actions - Wind actions*. EN 1991-1-4:2005+A1. Design Code. European Committee for Standardization, 2010. URL: <http://www.phd.eng.br/wp-content/uploads/2015/12/en.1991.1.4.2005.pdf>.
- [OM10] R.H.M. Ogink and A.V. Metrikine. "A wake oscillator with frequency dependent coupling for the modeling of vortex-induced vibration". In: *Journal of Sound and Vibration* 329.26 (2010), pp. 5452–5473. ISSN: 0022-460X. DOI: <https://doi.org/10.1016/j.jsv.2010.07.008>. URL: <http://www.sciencedirect.com/science/article/pii/S0022460X10004621>.
- [al11] Lothe et al. *Mulighetsstudie for Kryssing av Sognefjorden Opedal - Lavik: Estimert På Bølger og Strøm*. Feasibility study. SINTEF, 2011.
- [Sim11] A. Simone. *An Introduction to the Analysis of Slender Structures*. 2011.
- [Cam12] F.C. Campbell. ASM International, 2012. ISBN: 978-1-61503-976-0. URL: <https://app.knovel.com/hotlink/toc/id:kpFFUB0001/fatigue-fracture-understanding/fatigue-fracture-understanding>.
- [Ell12] O. Ellefsen. *Project Overview Coastal Highway Route E39*. Statens vegvesen, 2012.
- [Fje12] A. Fjeld. *Feasibility Study for Crossing Sognefjorden - Submerged Floating Tunnel*. Feasibility Study. Reinertsen, 2012. URL: https://www.vegvesen.no/_attachment/513902/binary/828560?fast_title=Mulighetsstudie+for+kryssing+av+Sognefjorden+-+Neddykket+r%C3%B8rbru.pdf.
- [Adh13] S. Adhikari. *Structural Dynamic Analysis with Generalized Damping Models*. 1st ed. Mechanical Engineering and Solid Mechanics. Wiley-ISTE, 2013. ISBN: 9781848215214.
- [Spa13] K. et al. Spak. "Cable Modeling and Internal Damping Developments". In: *Applied Mechanics Reviews* (2013). URL: <http://appliedmechanicsreviews.asmedigitalcollection.asme.org.tudelft.idm.oclc.org/article.aspx?articleid=1678950>.
- [CGZ14] Xiangju Cheng, John S. Gulliver, and Dantong Zhu. "Application of Displacement Height and Surface Roughness Length to Determination Boundary Layer Development Length over Stepped Spillway". In: *Water* 6.12 (2014), pp. 3888–3912. ISSN: 2073-4441. DOI: 10.3390/w6123888. URL: <http://www.mdpi.com/2073-4441/6/12/3888>.
- [Her14] R. Hermans. "Buoyancy Aided Crossing for Bridging Extreme Widths". Delft University of Technology, 2014.
- [Lal14] Christian Lalanne. John Wiley and Sons, 2014. ISBN: 978-1-84821-647-1. URL: <https://app.knovel.com/hotlink/toc/id:kpMVSAVF03/mechanical-vibration/mechanical-vibration>.

- [DNV15a] DNV. *Offshore mooring steel wire ropes*. DNVGL-OS-E304. Offshore standard. Det Norske Veritas, 2015. URL: <https://rules.dnvgl.com/docs/pdf/dnvgl/os/2015-07/DNVGL-OS-E304.pdf>.
- [DNV15b] DNV. *Position mooring*. DNVGL-OS-E301. Offshore standard. Det Norske Veritas, 2015. URL: <https://rules.dnvgl.com/docs/pdf/dnvgl/os/2015-07/DNVGL-OS-E301.pdf>.
- [Yip15] T. Yip. “Long Span Buoyance Bridge with Submerged Cable Anchoring”. Delft University of Technology, 2015.
- [DX16] R. Dhanak and N. Xiros. *Springer Handbook of Ocean Engineering*. 2016. ISBN: 978-3-319-16649-0. DOI: <https://doi-org.tudelft.idm.oclc.org/10.1007/978-3-319-16649-0>.
- [al17] Visser et al. “Sognefjord Buoyancy Bridge Feasibility and Sensitivity Analysis”. In: *Proceedings of Eurosteel 2017* (2017).
- [Cij18] W. Cijssouw. “A continuous superstructure for the Sognefjord bridge”. Delft University of Technology, 2018.